UNIVERSITA' DEGLI STUDI DI PADOVA

Sede Amministrativa: Università degli Studi di Padova

Dipartimento di Scienze MM.FF.NN.

SCUOLA DI DOTTORATO DI RICERCA IN SCIENZA ED INGEGNERIA DEI MATERIALI

XX CICLO

NEW MAGNETRON CONFIGURATIONS FOR SPUTTERING NIOBIUM THIN FILMS INTO COPPER TESLA-TYPE SUPERCONDUCTING CAVITIES

Direttore della Scuola : Ch.mo Prof. Gaetano Granozzi

Supervisore :Ch.mo Prof. Vincenzo Palmieri

Dottoranda : Giulia Lanza

31 gennaio 2008

Para Indio,
meu sonho, meu amor.
Para todos os dias que passamos juntos.

Contents

Abstract

Superconducting radiofrequency resonators for particle acceleration have become a standard component for particle accelerators. This work proposes a deep study and development of an alternative to the more frequently used bulk niobium cavities: niobium thin film coated into a copper cavity. The first niobium-coated copper cavity was produced at CERN in the early eighties. The sputter technology was chosen first in the pure diode configuration and subsequently in the magnetron configuration. The last one was adopted for the successful series production of the LEP and LHC cavities.

In this work an intensive R&D effort has been undertaken to study the coating technique, to improve it with several equipments and understand the correlation between the coating system applied and the film morphology, the superconducting properties and the RF film quality. Four different coating configurations for sputtering niobium films into 1.5 GHz copper cavities has been explored. First of all, the standard technique applied for several years at CERN to coat the LEP cavities has been reproduced. Then, in order to improve the Nb film quality, the application of three main ideas to the sputtering process has been investigated: i) making niobium atoms imping perpendicularly to the substrate surface, ii) promoting the effect of plasma bombardment on the growing film, iii) increasing the sputtering rate. Therefore, three different and new sputtering configurations are described: the effect of Nb atoms arriving perpendicularly to the substrate is explored either by using a cathode that follows the cavity shape (Large Area Cavity Shaped Cathode) or by increasing the plasma confinement efficiency by means of a target parallel to the magnetic field lines (Ringed Shaped Cathode). The removal of adsorbed impurities from the film surface and the increase of the film density are investigated by a biased third electrode that promotes the positive ion bombardment of the growing film. A mixed Bias-Magnetron has been built using a positively charged metal grid positioned all around the cathode.

Different film characteristics have been studied and compared, focusing mainly on superconducting and resistive properties. Also morphological and microstructural properties have been analyzed with the very valuable collaboration of "Interdepartmental Laboratory of Electron Microscopy" (LIME), University of Rome "ROMA TRE", at the Mechanical and Industrial Engineering Department. Four RF test on different accelerating cavities are reported and commented. In addition a 3-cell bulk niobium 1.3 GHz cavity has been prepared and measured in order to compare bulk and thin film results.

Even if the work is still in progress every partial results have been analyzed and com-

mented, in order to extrapolate every possible information. The final result is a global overview of the sputtering coating techniques and OF their results, with at the end some suggestions for the future developments.

Estratto

Le cavità superconduttive in radiofrequenza sono diventate componenti standard degli acceleratori di particelle. Questo lavoro propone lo studio ed lo sviluppo approfondito di un'alterntiva alle usuali cavità di niobio: cavità di rame ricoperte internamente di un sottile film di niobio. Le prime cavità di niobio su rame sono state prodotte al CERN nei primi anni ottanta. Venne scelta la tecnologia dello sputtering, prima nella versione a diodo e poi in quella magnetron. Quest'ultima venne adottata per l'eccezionale produzione in serie delle cavità del LEP e dell'LHC.

In questo elaborato di tesi il lavoro di R&D si è concentrato sullo studio delle tecniche di deposizione, nel migliorare le strutture e la strumentazione e capire la correlazione tra il sistema di deposizione ultilizzato e la morfologia del film, le sue proprietà RF e superconduttive. Sono state esplorate quattro diverse configurazioni per depositare niobio nelle cavità 1.5 GHz di rame. Per prima cosa è stata riprodotta la tecnica standard utilizzata per molti anni per preparare la cavità del LEP presso il CERN. Nell'ottica di migliorare la qualità del film sono state investigate tre idee principali: i) far arrivare gli atomi di niobio perpendicolramente alla superficie del substrato, ii) promuovere l'effetto del bombardamento del film in crescita, iii) aumentare la resa di sputtering. Ciascuna di queste idee equivale ad una configurazione da sputtering: l'effetto degli atomi di niobio che arrivano perpendicolarmente alla superficie del substrato è stato studiato usando un catodo che segue la forma della cavità (Catodo ad area estesa) o aumentando l'efficienza di confinamento del plasma utilizzando un target parallelo alle linee di campo magnetico (Catodo sagomato ad anello). La rimozione delle impurezze adsorbite dalla superficie del film a l'aumento della densità del film sono state studiate aggiungendo alla configurazione magnetron un terzo elettrodo positivo che promuove il bombradmaneto ionico del film in crescita. Una configurazione mista Bias-Magnetron è stata costruita utilizzando una griglia metallica a potenziale positivo, posizionata tutto intorno al catodo.

Le diverse caratteristiche dei film prodotti, principalmente quelle superconduttive e resistive, sono state studiate e confrontate. Inoltre ne sono state analizzate le proprietà morfologiche e microstrutturali in collaborazione con il "Laboratorio Interdipartimentale di Microscopia Elettronica" dell'universita "Roma3", presso il Dipartimento di Ingegneria Meccanica ed Industriale. Sono stati effettuati quattro test in radiofrequenza di quattro diverse cavità, i cui risultati sono riportati e commentati. Come termine di paragone è stata preparata e misurata una cavità tre celle 1.3 GHz.

Anche se il lavoro è ancora in evoluzione, ogni risultato parziale è stato analizzato e commentato per poter estrapolare tutte le possibili informazioni. Il risultato è una visione generale di tutte le tecniche di deposizione per sputtering e i rispettivi risulati, che si conclude con alcuni suggerimenti per gli sviluppi futuri.

Introduction

Scientific context and thesis purpose

The scientific community has demonstrated clearly that superconducting accelerating cavities for particle accelerators involve several advantages both from a performance and an economic point of view. Particle bunches with high currents are accelerated with high efficiency because power dissipated in the cavity walls is very low compared to normal-conducting cavities. In this way the available radiofrequency power is almost completely converted to particle energy. Even considering cooling the power required to reach the liquid helium temperature, still there is a factor of one hundred gain.

The development of the sputtering technique for thin niobium films deposition onto copper cavities was started at CERN in 1980, the target application being the LEP collider, operating at 352 MHz. At that time, the main reasons for undertaking such an approach were the following: a) Better thermal stability (resistance to "quench") thanks to the much higher thermal conductivity of the Oxygen Free High Conductivity Copper (OFHC copper) substrate compared to the superconducting niobium; b) Reduced material cost; c)possibility of applying high Tc coatings (NbTiN, V3Si, Nb3Sn, HTS...). At the end of 2000, LEP was shut down and then dismantled in order to make room in the tunnel for the construction of the Large Hadron Collider (LHC). At the moment 52 quarter wave Nb/Cu resonators are mounted in ALPI, the super-conducting linac for heavy ions, in operation since 1994 at Legnaro[1]. R&D on thin niobium films for RF application is being developed in several laboratories all over the world: Cornell (USA), in collaboration with LNL-INFN and ACCEL on Nb/Cu Sputtering and biased Sputtering; CERN; Los Alamos (USA) on testing of MgB2; Peking University (China) on Nb/Cu Biased Sputtering; INFN/Roma for Cathodic Arc Process, Andrzej Soltan Institute (Poland) on Cathodic Arc Process; Jefferson LAB (USA) on Energy-Controlled ECR Plasma [2].

Unfortunately high energy gradients remain unachievable when using thin films. The main limit of the Nb/Cu cavity is the Q-slope, which means that the Q factor is decreasing with increasing accelerating fields.

This behavior was extremely costly for CERN, during LEP-II operation, due to the extra refrigeration power required.

Organization of the dissertation

The main aim of this work is to study different coating techniques in order to understand how they can influence the film morphology and consequently film superconducting properties and cavity RF performance.

This thesis is organized as follows: two chapters are dedicated to the theory of superconducting cavities and sputtering techniques, with a brief introduction of Nb/Cu benefits. The first chapter contains useful information on how superconducting cavities work and the state of the art, from bulk niobium to niobium on copper cavities. The second chapter is an overview of the sputtering techniques from the basic plasma to the different configurations applied in the coating apparatus.

After the theoretical part, the bulk of the work is discussed throughout the remaining chapters. In figure 2 the Work Breakdown Structure of this thesis is clearly summarized and in figure 1 a more detailed outline of the obtained results is shown.

The main idea is to focus on all of the Nb/Cu steps, from the substrate preparation, through the coating process, to the RF measurement. Four different coating configurations for sputtering niobium films into 1.5 GHz copper cavities has been explored. First of all the standard technique, applied for several years at CERN to coat the LEP cavities, has been studied. Then, in order to improve the Nb film quality for 1,5GHz cavity coatings, the application of three main ideas to the sputtering process has been investigated: i) making niobium atoms imping perpendicularly to the substrate surface, ii) promoting the effect of plasma bombardment on the growing film, iii) increasing the sputtering rate.

Therefore, three different and new sputtering configurations are described: the effect of Nb atoms arriving perpendicularly to the substrate is explored either by using a cathode that follows the cavity shape (Large Area Cavity Shaped Cathode) or by increasing the plasma confinement efficiency by means of a target parallel to the magnetic field lines (Ringed Cathode). The removal of adsorbed impurities from the film surface and the increase of the film density are investigated by a biased third electrode that promotes the positive ion bombardment of the growing film. A mixed Bias-Magnetron has been built using a positively charged metal grid positioned all around the cathode.

For developing this different but interrelated subjects, several apparati have been built and optimized. Different film characteristics have been studied and compared, mostly from superconducting and resistive properties. Also morphological and microstructural properties have been analyzed with the very valuable collaboration with the Mechanical and Industrial Engineering Department of "Rome 3" University led by prof. Bemporad. Morphological, microstructural and mechanical features of coatings have been experimentally determined by FIB-SEM, AFM, TEM and nanoindentation techniques and then correlated with the superconducting properties of the films.

Chapter 3 is entirely dedicated to surface treatments : copper and niobium cavities and samples are mechanically and chemically etched, heat treated and water cleaned with different methods. All plant built to optimize surface treatments are described in details.

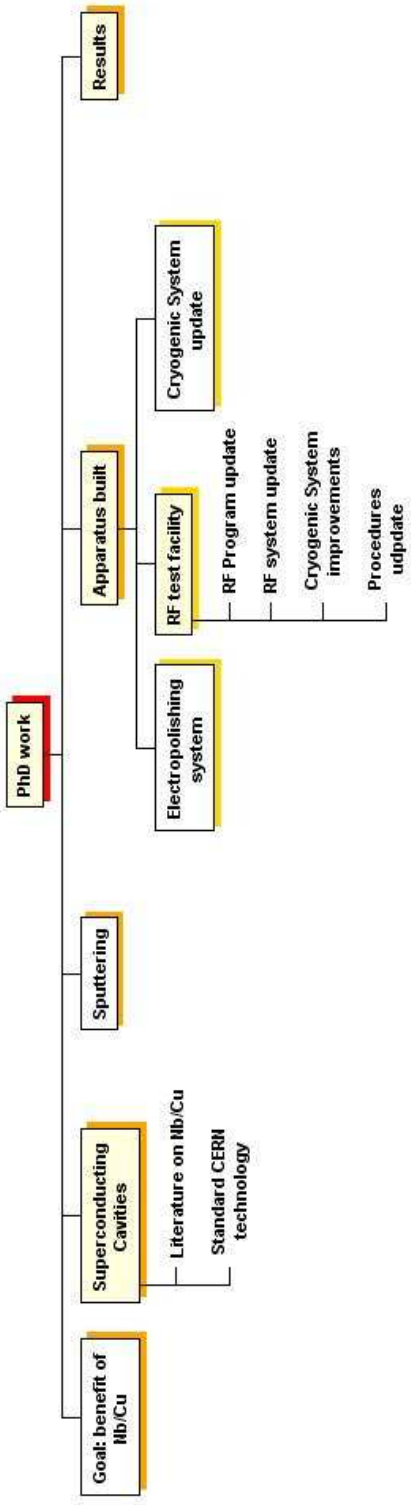

Figure 1: *Work Breakdown Structure of the PhD work*

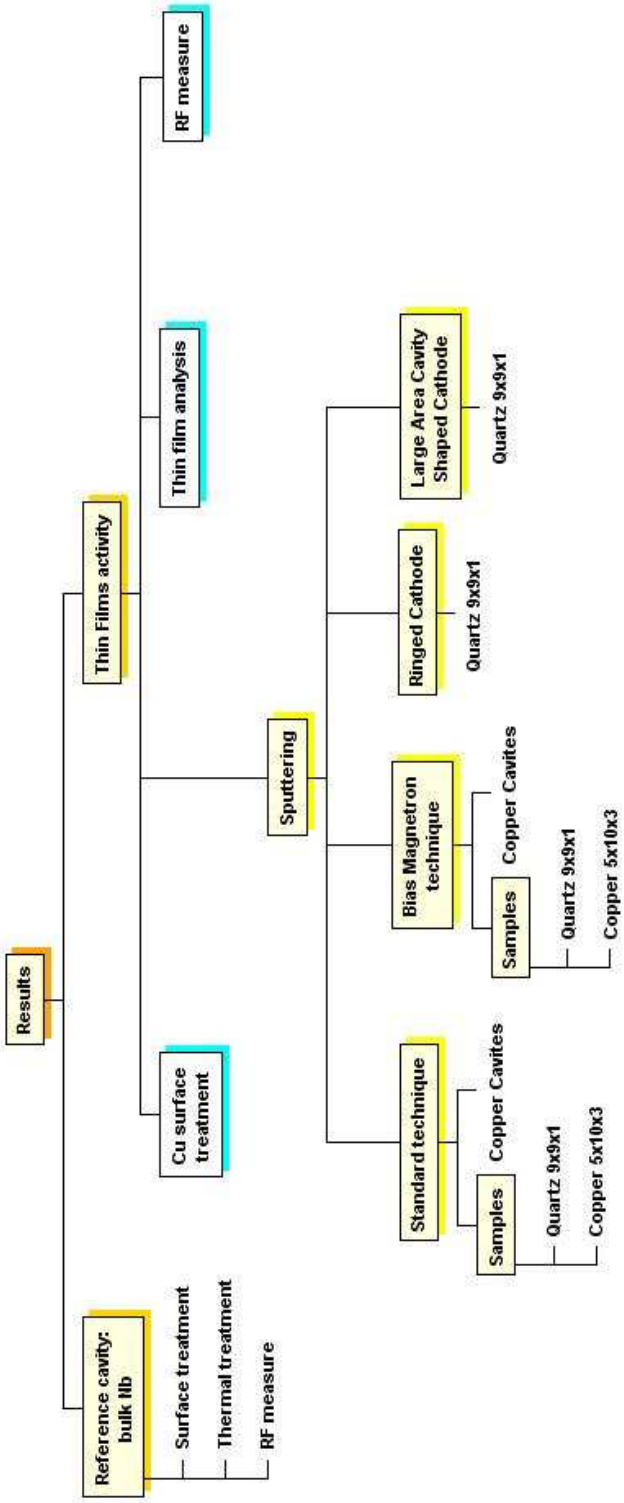

Figure 2: *Detail of the WBS about the obtained results*

One chapter is also entirely dedicated to the cryogenic and RF apparati adopted to test cavities. The RF system has been reorganized and updated in order to reduce errors and losses in the line. The program to monitor all parameters during cooling and measure have been modified and other instruments have been added. The cryogenic apparatus have been tested several time in order to optimize the cooling procedure. In addition the preparation and complete measure of a 3-cell bulk niobium 1.3 GHz cavity is discussed in order to compare bulk and thin film results.
In the last chapter, a complete summary of the work is given.

The whole work has been developed at the Superconductivity Laboratory of LNL-INFN in Legnaro.

Chapter 1

Basics of superconducting radiofrequency cavities

In this chapter the basic properties of radiofrequency cavities are reviewed [3] and the overview of Nb/Cu cavities status of art is provided. The surface resistance and its dependence on temperature and surface magnetic and electric field will be introduced. Niobium cavities different fabrications are presented and then some of the typical cavity problems are underlined. Nb/Cu cavities have several advantages thereby a summary of the ongoing works on Nb/Cu cavities subject spread all over the world concludes the chapter.

1.1 *Accelerating cavities - Figure of merit*

Accelerating cavities are used to increase the energy of a charged particle beam. Obviously, the energy gain per unit length is therefore an important parameter of accelerating cavities. This is conveniently derived from the accelerating voltage a particle with charge e experiences while traversing the cavity:

$$Vacc = \left| \frac{1}{e} \times \text{energy gain during transit} \right| \tag{1.1}$$

For particles travelling with the velocity of light c on the symmetry axis in z-direction ($\rho = 0$) and an accelerating mode with eigenfrequency ω this gives:

$$Vacc = \left| \int_0^d E_z(z) e^{\frac{i\omega z}{c}} dz \right| \tag{1.2}$$

The accelerating field is

$$Eacc = \frac{V_{acc}}{d} \tag{1.3}$$

Other two key parameters to characterize the accelerating structures are E_{pk} and H_{pk}, which denote the highest electric and magnetic field inside the resonant cavity. In an ideal situation, one can keep feeding the power to the resonant cavity until the peak magnetic field reaches the critical rf magnetic field, a little higher than the thermodynamic critical

magnetic field for niobium (a meta-stable superconducting state under superheated critical magnetic field). For a typical tesla-type cavity, the theoretical maximum accelerating gradient is about 55 MV/m [3]. At the moment the average Eacc is about 25-30 MV/m for working tesla-type accelerating cavities based on bulk niobium material.

To sustain the radiofrequency fields in the cavity, an alternating current is flowing in the cavity walls. This current dissipates power in the wall as it experiences a surface resistance. One can look at the power P_{diss} which is dissipated in the cavity to define the global surface resistance R_{surf}:

$$P_{diss} = \frac{1}{2} \oint_A R_{surf} H_{surf}^2 dA = R_{surf} \oint_A H_{surf}^2 dA \tag{1.4}$$

Here H_{surf} denotes the magnetic field amplitude. Usually, one measures the quality factor Q_0:

$$Q_0 = \frac{\omega U}{P_{diss}} \tag{1.5}$$

where

$$U = \frac{1}{2} \mu_0 \oint_V H^2 dV \tag{1.6}$$

is the energy stored in the electromagnetic field in the cavity. R_{surf} is an integral surface resistance for the cavity. The surface resistance and the quality factor are related via the geometrical constant G which depends only on the geometry of a cavity and field distribution of the excited mode, but not on the resistivity of the material:

$$G = \frac{\omega \mu_0 \oint_V H^2 dV}{\oint_A H^2 dA} \tag{1.7}$$

This gives:

$$Q_0 = \frac{\omega \mu_0 \oint_V H^2 dV}{R_{surf} \oint_A H^2 dA} = \frac{G}{R_{surf}} \tag{1.8}$$

The quality factor can also be defined as

$$Q_0 = \frac{f}{\Delta f} \tag{1.9}$$

where f is the resonance frequency and Δf the full width at half height of the resonance curve in an unloaded cavity. For the typical elliptical shape of superconducting cavities G = 270Ω. For a mono-cell TESLA niobium cavity the quality factor is typically $Q_0 = 1.2 \times 10^{10}$ at T = 2 K corresponding to a surface resistance of Rsurf = 10$n\Omega$.

One can see that the efficiency with which a particle beam can be accelerated in an radiofrequency cavity depends on the surface resistance. The smaller the resistance i.e. the lower the power dissipated in the walls, the higher the radiofrequency power available for the particle beam. This is the fundamental advantage of superconducting cavities as their surface resistance is much lower and outweighs the power needed to cool the cavities to liquid helium temperatures.

1.2 *Niobium properties*

Niobium is a transition metal of V group and fifth period. It is a chemical element that has the symbol Nb and atomic number 41. A rare, soft, gray, ductile transition metal, niobium is found in pyrochlore and columbite. It was first discovered in the latter mineral and so was initially named columbium; now that mineral is also called "niobite". Niobium is also used in special steel alloys as well as in welding, nuclear industries, electronics, optics and jewelry. In the family of superconducting element it has the highest critical temperature and its properties are collected in table 1.1.

Atomic number	41
Atomic weight	92,9 g/mol
Atomic radius	2.08
Density	8570 kg m^{-3}
Crystalline lattice	b.c.c.
Space group	Im3m
a	3,3033
Electrical resistivity (300K)	14.9 $\mu\Omega$·cm
Thermal conductivity (300K)	53.7 W $m^{-1}K^{-1}$
Debye Temperature	275K
Melting Point	2741K
Critical temperature	9.26K
Density	8570 kg m-3
Density	8570 kg m-3

Table 1.1: *List of the niobium properties*

1.2.1 *The Residual Resistivity Ratio (β)*

For a relatively impure Nb, the d.c. resistivity ($\rho \approx \frac{1}{\sigma}$) drops by a factor of 30 from its room temperature value of $1.4{\cdot}1^{-8}\Omega$ m^{-1} to its residual value. This factor by which resistivity drops to the residual value is called the *residual resistance ratio*, RRR, triple-R or β. The RRR is defined as the ratio of electrical resistivity at two temperatures: 273 K and 4.2 K. The value of RRR indicates the purity and the low-temperature thermal conductivity of a material, and is often used as a materials specification for superconductors. For pure Nb used in radio-frequency cavities of linear accelerators, the low temperature resistivity is defined as the normal-state value extrapolated to 4.2 K, but this value doesn't differ much from the 10K value.

$$\beta = \frac{\rho(273K)}{\rho_{extrap}(4.2K)} \tag{1.10}$$

RRR values serves as a convenient measure of the purity of the metal. High-purity niobium has higher RRR values; the theoretical limit is 35000 and is determined by scattering of electrons by lattice vibration.

Dissolved impurities serve as scattering sites for the electrons not condensed into Cooper pairs. These impurities lower the thermal conductivity and thereby limit the maximum tolerable surface magnetic field before the thermal breakdown occurs. Interstitial dissolved impurities in niobium, such as oxygen, carbon, nitrogen or hydrogen have a strong effect on the thermal conductivity and decrease the critical temperature of niobium. For example, oxygen decreases the T_c, of niobium by $\frac{1K}{atomic\%}$. Such looses are exponential and the decrease of the critical temperature with 1 K is a drastic decrease.

DeSorbo [4] studied the influence of oxygen and nitrogen concentration on niobium critical temperature and resistivity: concentrations of those two elements higher than the solubility limit cause a critical temperature decrease and an increase of the resistivity. At lower concentration the niobium creates interstitial solid solutions with both oxygen and nitrogen. The crystal lattice deformation is confirmed by the increasing of the lattice parameter and it causes superconducting properties variation of the material.

The natural niobium oxide presents a layered structure, comprising Nb_2O_5 as the outermost layer and reducing over a few nm to NbO_2 and NbO as the innermost layer. Since the rf penetration depth is a few tens of nanometers, the niobium oxide and the metal-oxide interface may play role in rf losses of superconducting niobium. To understand what's the role of niobium oxides in the high field Qslope, medium field Q-slope, and residual resistance, several studies are in progress [5, 6, 7]. For a sample of niobium with RRR = 300 with H_{c2} = 2400 Oe and the normal state surface resistance R_n = 1.5 mΩ at 1 GHz, the residual loss due to trapped magnetic flux will be given by the equation:

$$R_{mag} = 0.3(n\Omega) \cdot H_{ext}(mOe) \cdot f^{\frac{1}{2}}(GHz)(2.14) \tag{1.11}$$

In a sputtered cavity, the grain size and the purity of the thin film are such that the mean free path ℓ is very small (10-100 nm) and the Q_0 of such a cavity is twice that of a cavity made from high RRR bulk niobium. Experimental results show that surface resistance depends from the ratio $\frac{\xi_0}{\ell}$. When this ratio is $\frac{\xi_0}{\ell} \ll 1$ or $\frac{\xi_0}{\ell} \gg 1$ than the surface resistance is relatively high. For $\frac{\xi_0}{\ell} > 1$, the surface resistance reaches a minimum and this corresponds to RRR values 12-17. As regarding bulk niobium cavity, Kenji Saito in his work, presented during the 11th Workshop on RF Superconductivity showed that the higher RRR material has a benefit against frozen flux trapping. The experimental formulas:

$$R_0(\beta) = 3.15 \cdot \beta^{-0.394} \tag{1.12}$$

$$R_S(H_{ext})[n\Omega] = 3.15 \cdot \beta^{-0.394} \cdot H_{ext}[mGauss] \tag{1.13}$$

is valid for 1300MHz sc niobium cavity and if the niobium with β=500 is used for Nb/Cu clad tubes, then R_0 will be reduced to 0.27 nΩ/mG. The problem will be suppressed to one

half of that in the case of β=100. Of course making a tight magnetic shielding is another important cure.

1.3 *Superconductivity*

1.3.1 *Introduction*

Superconductivity was discovered in 1913 by Kammerlingh Omnes in Leiden. It was found that for mercury below a certain temperature (T = 4.2 K) no ohmic resistance could be measured. By now a large number of elements and compounds (mainly alloys and ceramics) have been found showing this behaviour. For superconducting cavities niobium shows the most interesting properties. The general features of superconductivity as well as the special properties of niobium are described.

1.3.2 *Characteristic length scales of superconductivity*

Meissner-Ochsenfeld effect

Two different types of superconductors were discovered. They have certain common features, but differ also in some important ways. When the material is cooled below the critical temperature Tc the ohmic resistance vanishes below the measurement limit. In addition, any external magnetic field up to a critical field B < B_{crit} is expelled. This magnetic field expulsion is called the Meissner-Ochsenfeld effect. This behaviour significantly differs from the properties of an ideal conductor where the field would be trapped inside the material. Even if the field is switched off, an ideal conductor would keep the magnetic field and become a permanent magnet as the currents induced by the field will continue to flow. From a thermodynamical point of view, one can define the thermodynamical critical field B_c:

$$G_n - G_s = \frac{1}{2\mu_0} V B_c^2 \tag{1.14}$$

Here one takes difference of the free enthalpy G in the normal and the superconducting state respectively. Experimentally, B_c can be determined from the area below the magnetization curve of the material. If the field exceeds a critical value B_c in a superconductors of type I the superconductivity breaks down and the normal conducting state is restored. This critical field depends on the critical temperature:

$$B_c(T) = B_c(0) \left[1 - \left(\frac{T}{T_c} \right)^2 \right] \tag{1.15}$$

For the second type of superconductor the magnetic field will start to penetrate the material above the lower critical field B_{c1}. Magnetic fluxons enter the material and their number increases with increasing field. If one raises the field further to a value of B_{c2} the material becomes normalconducting. The temperature dependence of the critical magnetic fields B_{c1} and B_{c2} is the same as for the B_c of a type I superconductor.

Coherence length in superconductors

For classical superconductors like lead or tin, a very successful microscopic theory was developed by Bardeen, Cooper and Schrieffer which is called BCStheory [8]. They assumed that electrons begin to condense below T_c to pairs of electrons, the so called Cooper pairs. The two electrons in a pair have opposite momentum and spin. They experience an attractive force mediated via quantized lattice vibrations called phonons. This bound state of the two electrons is energetically favourable. As the overall spin of these two paired electrons is zero, many of these pairs can co-exist coherently, just like other bosons. The coherence length describes the distance over which the electrons are correlated. It is given by:

$$\xi = \frac{\hbar v_F}{\Delta} \tag{1.16}$$

v_F denotes the velocity of the electrons near the Fermi energy and 2Δ is the energy necessary to break up a Cooper pair. Typical values for the coherence length in niobium are around 39 nm. If one interprets the coherence length as the size of a Cooper pair, one immediately sees that it spans over many lattice constants. Within the BCS theory the energy gap can be calculated:

$$\Delta = 1.76 k_B T \tag{1.17}$$

The exact value of factor (1.76) in the relation of the energy gap and the critical temperature is material dependent and for niobium one finds higher values of Δ=$1.9 k_B T_c$. The number of Cooper pairs $n_{cooper} = n_s/2$ is temperature dependent and only at T=0 K all conduction electrons are condensed into Cooper pairs. The superconducting electrons co-exist with their normalconducting counterparts. The number of normalconducting electrons is given by the Boltzmann factor:

$$n_e(T \longrightarrow 0) \approx n_s(0) \exp\left(-\frac{\Delta(T)}{k_B T}\right) \tag{1.18}$$

London penetration depth

Even in a type I superconductor the magnetic field is not completely expelled, but penetrates into the material over a small distance, as otherwise the shielding current density would have to be infinitely large. The so-called London penetration depth is given by the characteristic length of the exponential decay of the magnetic field into the superconductor.

$$B(x) = B(0) e^{-\frac{x}{\lambda_L}} \tag{1.19}$$

Its value is

$$\lambda_L = \sqrt{\frac{m}{\mu_0 n_s c^2}} \tag{1.20}$$

where e is the charge of an electron, m its mass and n_s the number of superconducting charge carriers per unit volume. A typical value for the penetration depth in niobium is

32 nm. The theory did not allow for impurities in the material nor for a temperature dependence of the penetration depth. Gorter and Casimir introduced the two-fluid model where a coexistence of a normal- and superconducting fluid of charge carriers is postulated.

$$n_c = n_n + n_s \tag{1.21}$$

They suggested a temperature dependence of the superconducting charge carriers.

$$n_s(T) = n_s(0)\left(1 - \left(\frac{T}{T_c}\right)^4\right) \tag{1.22}$$

Combining equations 1.20 and 1.22, the penetration depth shows the following temperature dependence:

$$\lambda_L(T) = \lambda_0\left(1 - \left(\frac{T}{T_c}\right)^4\right)^{-\frac{1}{2}} \tag{1.23}$$

The Ginzburg-Landau parameter is defined as:

$$\kappa = \frac{\lambda_L}{\xi_0} \tag{1.24}$$

κ allows to distinguish between the two types of superconductors:

$$\kappa < \frac{1}{\sqrt{2}} Superconductortype - I \tag{1.25}$$

$$\kappa > \frac{1}{\sqrt{2}} Superconductortype - II \tag{1.26}$$

Niobium has $\kappa \approx 1$ and is a weak type-II superconductor. The role of impurities was studied by Pippard [9] was based on the evidence that the penetration depth depends on the mean free path of the electrons ℓ in the material. The dependence of ξ on the mean free path is given by:

$$\frac{1}{\xi} = \frac{1}{\xi_0} + \frac{1}{\ell} \tag{1.27}$$

He introduced an effective penetration depth:

$$\lambda_{eff} = \lambda_L + \frac{\xi_0}{\xi} \tag{1.28}$$

Here again ξ_0 is the characteristic coherence length of the superconductor. This relation reflects that the superconducting penetration depth increases with a reduction of the mean free path [[10]]. For pure ("clean") superconductor ($\ell \longrightarrow \infty$) one has $\xi = \xi_0$. In the limit of very impure ("dirty") superconductors where $\ell \ll \xi_0$, the relation becomes

$$\xi = \ell \tag{1.29}$$

The mean free path in the niobium is strongly influenced by interstitial impurities like oxygen, nitrogen and carbon.

Microwave skin effect in normal metals

The shielding mechanism of a static magnetic field in a superconductor is analogous to the shielding of a microwave field in a normal metal. If a microwave of frequency ω is incident on a metal surface one can show that the field is decaying over a characteristic distance, the skin depth δ. For the case where the frequency is much lower than plasma frequency ($\omega << \omega_{plasma}$) the or the mean free path of the electrons ℓ is smaller than the penetration depth (or skin depth) δ one finds:

$$\delta = \sqrt{\frac{2}{\sigma \mu_0 \omega}} \tag{1.30}$$

σ is the conductivity of the metal. This is the regime of the normal skin effect. One can calculate the surface resistance

$$R_{surf} = \frac{1}{\sigma \delta} \tag{1.31}$$

According to this equation one would expect a strong reduction of the surface resistance at cryogenic temperature because σ grows for T $\longrightarrow$ 0. Unfortunately, for pure metals and at low temperatures ℓ may become larger than δ which leads to the anomalous skin effect. Then the electrons are not only scattered by phonons, but by impurities in the metal lattice. In the limit ($\ell \longrightarrow \infty$) the surface resistance becomes [3]:

$$R_{surf} = \left[\sqrt{3}\left(\frac{\mu_0}{4\pi}\right)^2\right]^{\frac{1}{3}} \omega^{\frac{2}{3}} \left(\frac{\ell}{\sigma}\right)^{\frac{1}{3}} \tag{1.32}$$

1.3.3 *Microwave surface resistance*

BCS resistance

For a direct current or low frequency alternating currents the superconducting electrons shield the normalconducting electrons from the electromagnetic field so that no power is dissipated. For alternating currents at microwave frequencies this is not true anymore. The inertia of the Cooper pairs prohibits them to follow the changing electromagnetic fields immediately, the shielding is not perfect anymore. The normalconducting electrons start to flow and dissipate power. This gives rise to a resistance which depends on the number of normalconducting electrons and the frequency of the alternating current. For temperatures T $< \frac{Tc}{2}$ and an energy of the microwave photons of $hf \ll \Delta$ the surface resistance can be approximated by:

$$R_{BCS}(T, f) = A\frac{f^2}{T} \exp\left(\frac{-\Delta}{k_B T}\right) \tag{1.33}$$

The factor A depends on material parameters like coherence length, electron mean free path, Fermi velocity and penetration depth. For niobium it is about 9x10^{-5} ΩK/(GHz)^2. Therefore the BCS resistance at 1.3 GHz is about 600 nΩ at 4.2 K and about 1 nΩ at 2 K. The result derived for R$_{BCS}$ from the two-fluid model will give [11]:

$$R_{BCS}(T,f) = C \cdot \sigma_{nc} \cdot \lambda_{eff}^3 \frac{f^2}{T} \exp\left(\frac{-\Delta}{k_B T}\right) \tag{1.34}$$

C is a constant, which does not depend on the material properties. σ_{nc} is the conductivity in the normalconducting state. The dependence of RBCS on the mean free path is therefore [12]:

$$R_{BCS}(\ell) \propto \left(1 + \frac{\xi_0}{\ell}\right)^{\frac{3}{2}} \cdot \ell \tag{1.35}$$

There exists a minimum of RBCS on the mean free path ℓ. A more detailed calculation of the BCS theory shows that the two-fluid model gives a good approximation for $\ell <$ 500nm [13].

Residual resistance

The total surface resistance contains in addition a temperature independent part, which is called residual resistance Rres. The residual resistance is usually dominated by lattice imperfections, chemical impurities, adsorbed gases and trapped magnetic field. Well prepared niobium surfaces show a residual resistance of a few nΩ.

Absorbed gases can lead to a high residual resistance.The dielectric properties of N_2 and O_2 are the reason for this behaviour. Minor contributions come from dielectric losses of the natural oxide Nb_2O_5. They have been estimated to be in the order of 1 nΩ [14] or below.

If a cavity is not shielded from the earth magnetic field its surface resistance is increased due to trapped magnetic fluxons. Those fluxons are trapped at impurities called pinning centers even though the superconductor tries to expel the magnetic field. The losses from fluxons can be calculated:

$$R_{fl} = \eta \frac{B_{ext}}{B_{c2}} R_{surf,nc} \tag{1.36}$$

Bext is the external magnetic field and Rsurf,nc is resistivity of the material in the normalconducting state. $\eta \leq 1$ is a correction factor for the field expulsion. Measurements have shown that the trapping efficiency is very close to 1 even in high purity niobium [15]. Any contamination of the surface with metallic parts (from screws, gaskets, etc.) or dielectric remnant from the surface treatment has to be avoided. It can enhance the residual rf losses to an intolerable level.

1.4 *Cavity fabrication*

The traditional fabrication procedure of elliptical SRF cavities consists of deep drawing and electron beam welding (EB) of the half cells. This procedure is well established and has about 30 year of industrial fabrication experience. It is well known that RRR degradation in welding areas of conventional cavities can be critical for the performance [16]. In

the last few years improvement of the material quality control, preparation for EB welding and the welding parameters allowed to reach accelerating gradients close to the theoretical limit by applying advanced cavity treatment techniques such as electropolishing (EP) [17].

Nevertheless not only the progressive achievement of higher accelerating fields, but also the drastic reduction in resonator production time and costs (K$ per MV/m) is compulsorily for the feasibility of more and more powerful accelerators, as for instance the ILC. This is the motivation under the research toward simpler and cheaper fabrication techniques as for instance seamless cavities. In fact a fabrication method which will avoid the welding is very complementary from two aspects:

- the seamless cavity does not have the risk of equator weld contamination;
- a lower cost of fabrication can be expected.

The development of the seamless technique mostly for the TESLA shape cavity was pursued in the last years at INFN by V. Palmieri (spinning) [18, 19], and at DESY (hydroforming) [20].

1.4.1 *Spinning*

Plastic deformation of metals by spinning is a powerful technique, in fact it has been shown that seamless resonators can be cold formed starting either from circular at blanks or from tubes without need of any intermediate annealing. In the optics of a low cost resonator mass production, a strong effort on fabrication times reduction (around 4 hours per resonator) has been spent in last two years at INFN. Much shorter fabrication times are however possible and are under study at the moment. Several years of development were necessary to build the TESLA shape multicell cavities, with a ratio of equator diameter to iris diameter of about three.

The spinning fabrication technique and performance of the spun cavities is described in details in ref. [18]. A 9-cell cavity was produced. A new spinning machine was introduced [19]. The spinning process [21, 22, 23] of a copper mono-cell from blank is mainly divided in four steps:

- a circular disk of 400 mm diameter and 3 mm thickness is first preformed onto a frustum shaped mandrel;
- the first half-cell is formed and a cylindrical shape is given to the remaining part of the piece, by means of a second pre-mandrel;
- spinning the obtained manufact onto a collapsible mandrel that has exactly the same shape of the cavity interior, up to when the roller overcomes the equator and fixes the piece to spin onto the mandrel;
- inserting a further frustum-shaped collapsible mandrel in order to guide the material when spinning the second halfcell.

Both collapsible mandrels are then removed. The presence of an internal mandrel insures the high respect of tolerances on internal dimensions, and as a consequence of the resonant

frequency.

Generally the most part of the working time is spent in order to set-up the machine. The whole forming operation for a monocell takes less than 10 minutes, a time absolutely competitive in comparison with the standard half-cell drawing, edge trimming, positioning into the EB- Chamber, vacuum pumping and welding. The dismounting operation of the mandrel takes a few minute time.

Cavities after spinning must be internally tumbled or mechanically grinded, then simply chemical and electro-polishied.

Low temperature radiofrequency tests have proofed that the seamless approach and in particular spinning is a solution worthwhile to pursue. Q-values over 10^{10} and accelerating fields over 40 MV/m have been reproduced on all the last spun prototypes fabricated at LNL of the INFN, treated and measured in different laboratories. The most significant and representative result obtained by K. Saito at KEK at 1,6 K onto a bulk Niobium 1,3 GHz monocell, spun at LNL of the INFN, is reported in figure 1.1 [18].

Multi-cell cavities either in Niobium or Copper can be formed both directly from

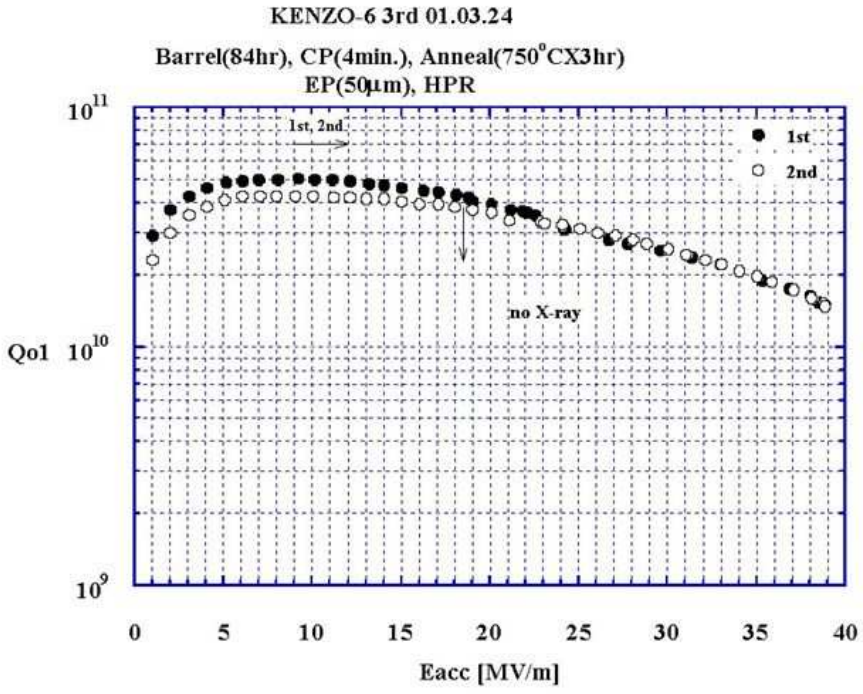

Figure 1.1: *Bulk Niobium 1,3 GHz monocell spun at LNL. The cavity has been mechanically grinded for 100 microns, then barrel finished for 84 hours, vacuum annealed at 750 C for 3 hours, electropolished for 50 microns and then high pressure rinsed [18].*

circular blanks and from tubes. When forming a cavity from a tube, each cell is formed exactly in the same way but the tube hardening indeed grows progressively along the tube axis depending on the tube forming solution we choose. The spinning procedure remains unchanged from cell to cell only if the cavity is spun under high pressure between

lathe headstock and tailstock; in alternative it is always possible to anneal the tube before spinning.

Niobium seamless tubes however are not commercial and in order to get seamless tubes suitable for the further spinning process, three different methods are being simultaneously developed: forward flowturning and deep-drawing both direct and reversal. Both Niobium and Niobium clad Copper have been successfully formed by flowturning.

Spinning of seamless Niobium nine-cell cavities is not a problem. It starts from

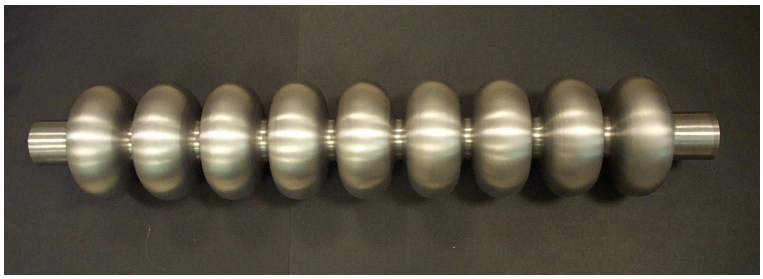

Figure 1.2: *The first Niobium seamless 9-cell cavity ever fabricated [18].*

a circular Nb blank 550 mm in diameter, 12 mm thick, then a seamless tube has been flowturned and from it, the cavity has been spun following the usual procedure. The procedure indeed is still manual and it has been not yet automatized. The time dedicated to spinning indeed is of the order of less than two hours for a nine-cell, the other 28 hours are dedicated to the machine setting up, the internal die extraction and other operations due to the fact that the roller can be pushed only forward and not also backward. The cavity is displayed in 1.2, and the thickness distribution is plotted in 1.3.

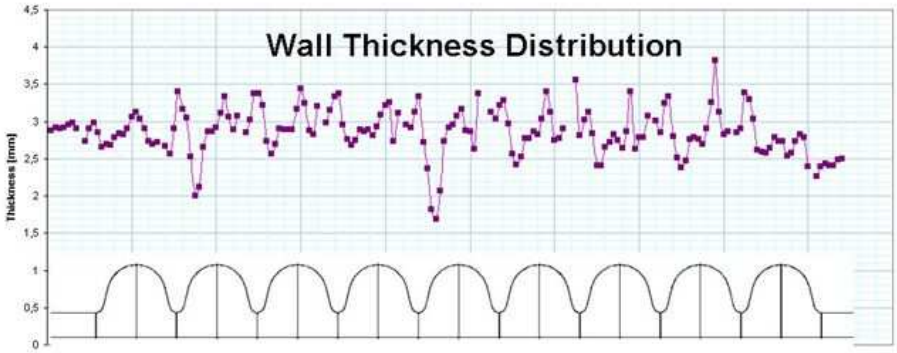

Figure 1.3: *Wall thickness distribution for the nine-cell cavity [18].*

1.4.2 *Hydroforming*

For the hydroforming of a seamless bulk niobium cavity of the TESLA shape, with a ratio of equator diameter to iris diameter about three, one starts with tube of a diameter intermediate between iris and equator. The forming procedure consists of two stages: reduction of the tube diameter in the iris area followed by expansion of the tube in the

equator area. For the choice of the initial tube diameter two aspects should be taken into consideration. On the one hand the work hardening at the equator should be moderate and during the expansion remain below the yield strength of the material. Therefore a larger initial tube diameter is preferred, easing the second stage of hydroforming. On the other hand enlargement of the tube diameter increases the roughness at the iris area.

The hydroforming experiment consists generally of three steps:

- determination of the strain-stress properties of the tube material;
- computer simulation of the forming;
- the hydroforming test itself.

During hydroforming experiments an internal pressure is applied to the tube and simultaneously an axial displacement, forming the tube into an external mold.

At DESY the hydroforming machine is provided with a water hydraulic system for the internal pressure in the tube and with a oil hydraulic system for the cylinder movements. The developed computer control system for the hydroforming allows the hydraulic expansion in stepwise as well as in continuous regime. The maincriterion for the hydraulic expansion is the theoretically determined relation between internal pressure and axial displacement. Further correction of the expansion parameters can be done on the basis of comparison of the theoretical and experimental growth of the tube diameter.

The developed technology allows to fabricate not only single cell but also multi cell cavities and several two and three cell Cu cavities of the TESLA shape and first bulk Nb double cell cavity were recently successfully produced at DESY (figure 1.4). Development

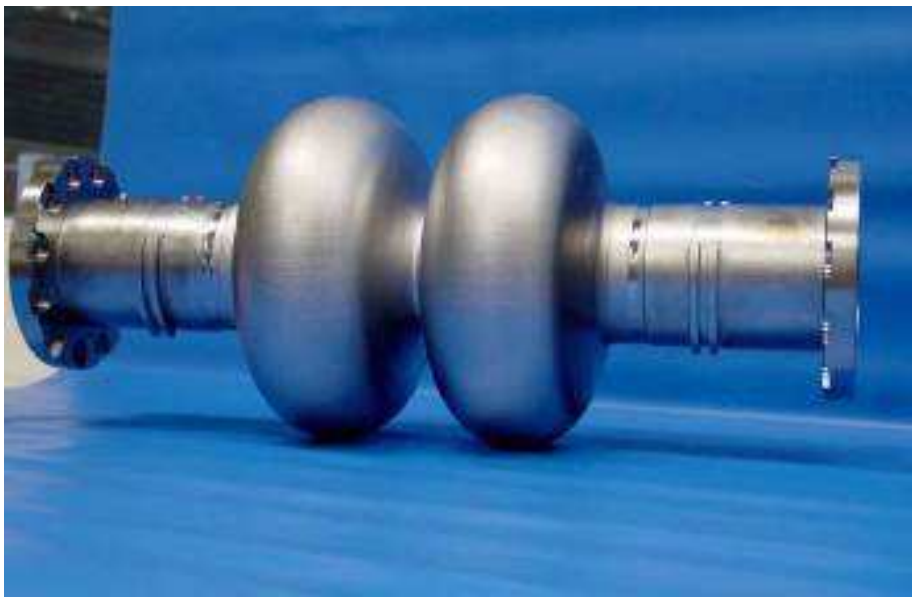

Figure 1.4: *First Nb double cell cavity produced at DESY by hydroforming. [20]*

of the production of seamless Nb tubes for hydroforming was done and is being continued in collaboration with several companies. The combination of spinning or deep drawing with

flow forming allows to improve the surface and significantly reduce the tube wall thickness variations. A good reproducibility of the cavity shape can be easily reached. The arithmetic mean roughness Ra inside the cavity is a few μm larger compared to that of deep drawn cells, but this difference becomes negligible after standard BCP or EP treatment.

1.5 *Problems in the bulk niobium cavities operation*

1.5.1 *Thermal rf heating*

While one can make a perfect resonant cavity by extensive effort in the laboratory, there will be defects in real manufacturing, especially microscopic defects. The defects will heat up the local area by high surface current induced by the electromagnetic field. The thermal conductivity of the resonant cavity limits the amount of heat that can be dissipated to the cooling agent.

Eventually, before the magnetic field exceeds the critical value, the temperature will exceed the transition temperature T_c, if one keeps increasing the stored energy. The local area loses the superconducting state, and then it becomes a run away process (quench). The increased temperature certainly reduces the critical magnetic field, which in turn will cause the quench. To efficiently cool the resonant cavities, one can try to reduce the wall thickness while maintaining sufficient mechanical strength, improve the thermal conductivity of the cavity material, use thin film technology, or use a different material with higher T_c and higher critical magnetic fields.

1.5.2 *Multipacting*

In rf resonant cavities, stray electrons can hit the cavity surface, creating secondary electrons. The secondary electrons, which in turn, can be accelerated by rf fields, absorb the rf energy and hit the wall surface to create more secondary electrons. When these secondary electrons happen to hit the same area, the absorbed rf energy heats the surface, thus creating a local hot spot. That not only limits the accelerating gradient, but also creates more rf surface loss eventually leading to a thermal quench. By adjusting the resonant cavity shape, the multipacting can be reduced. It can't be totally eliminated, and whenever it happens, the thermal efficiency surely would help. Also, some resonant cavities such as quarter wave resonators can't change their geometry shape to fully overcome the multipacting.

1.5.3 *Field Emission*

Another important phenomenon limiting the Eacc from reaching its maximum, is field emission. When the surface electrical field is strong enough for that small area, the electrons will start to tunnel out of the metal surface to form a steady current. The field emission current increases rapidly as the field is increased. Like the multipacting phenomenon, it absorbs a great amount of rf power, depositing the heat wherever the electrons hit. Some

of the heating is strong enough to cause the resonant cavity to lose the superconducting state.

1.6 *Advantages and disadvantages of Nb Thin Film Cavity*

1.6.1 *Thermal stability*

Bulk niobium has a typical heat conductance of about 75W/mK if the purity is high, while copper is as high as 300 - 2000 W/mK. For a typical hot spot inside a SC cavity, say, 50-micron size defect, the amount of heat is about 10mW if the magnetic field at the defect area is 400 Oe. It is very easy for the copper substrate cavity to conduct the excessive heat to the helium bath. A more accurate simulation using thermal breakdown model for defects inside the resonant cavity [24] sufficiently illustrates the effect of the defect's size and the niobium purity level (represented by RRR, residual resistivity ratio). As we have seen in the previous section, multipacting and field emission could cause problems to resonant cavities. The large thermal conductivity of copper helps the thin film cavity to be more resilient in those situations.

1.6.2 *Low cost*

The copper is a lot cheaper than niobium, about 1/10 the cost of the niobium. Since the dimension of the rf cavity is inversely proportional to its resonant frequency, a typical 500MHz cavity needs more than 9 times the material required for a 1,500MHz cavity with the same cavity thickness. If the thickness is made proportional to diameter, the material per cell would be 27 times. The material itself is not the only cost advantage: it is widely believed that the manufacturing cost associated with copper can be substantially lower than that of niobium.

1.6.3 *Insensitivity to earth magnetic field trapping*

Residual resistance of the niobium surface is caused by many different sources. For an ideally cleaned cavity, the residual resistance can be caused by trapped magnetic flux, hydrogen dissolved in the surface layer, surface oxides and even some surface roughness. Films showed a further unexpected advantage, in that their surface resistance is almost insensitive to the Earth's magnetic field. As an order of magnitude the effect is 100 nΩ/Gauss of external magnetic field for bulk Nb, and only 1 nΩ/Gauss for films. This allows for the fabrication of much simpler and cheaper cryostats without the need of complex magnetic shielding of cavities [25, 3].

1.6.4 *Freedom from undissolved inclusions*

During the pressing, rolling and melting, etc., the niobium sheet or the copper sheet will have some kind of micro-inclusions. Typical inclusions can be elements such as steel, nickel, and some compound oxides. They don't necessarily decrease the RRR of the metal

sheet, but they show up from time to time, even with vigorous etching.

Although they can be controlled well, they do increase the cost for better raw material and also the cost for extra processing during the cavity manufacturing. One simple example is that the inclusions are very easily introduced to the niobium sample from machine tools [26]. Although that kind of inclusions can be etched away, the inclusions caused by precipitation during cooling process can be deep inside the niobium material. That can happen when the amount of some compound dissolved while the Nb is molten exceeds the solubility during cooling. Vacuum deposition of thin film is known to produce excellent surface quality except the possible degradation of performance due to the increased BCS surface resistance.

1.6.5 *Non-Quadratic rf losses*

At 1.7 K the BCS component of the surface resistance reduces exponentially and the residual term remains dominant. Although of comparable order of magnitude between sputtered film and bulk at zero-field, the residual resistance had a stronger increase with field in the case of films, thus showing a "slope" in Q. The Q-degradation caused by the increased external rf field actually exists in both bulk niobium and in thin film cavities but in the second case it limits the cavity operation to low field. This anomalous rf loss is known as Non-Quadratic Loss(NQL), As named by the Durand and Weingarton in their pioneer work [27].

One should underline first that some models predict that such a "slope" is inherent in films because of the limited electron mean free path compared to bulk. This should manifest either in a reduction of Hc1 and thus nucleation of (Abrikosov)fluxons [28] in a rather low rf field, effect possibly enhanced by demagnetization due to surface roughness. Or it could manifest itself in a depression of the superconducting gap due to a reduction of the critical superfluid velocity [29], this transforming directly in an increase of the BCS surface resistance. Both phenomena do clearly happen in films, however their importance is difficult to estimate a priori. It is then important to study in depth the film material parameters and all possible methods to alter them in a way that can be correlated to changes to the "slope".

Hydrogen and Oxygen

The hydrogen trapped in the film is a possible cause of the "slope", since this has always been a primary source of losses in bulk Nb cavities. The quantity of hydrogen contained in the films, depending on the coating procedure, has been measured accurately at CERN, as well as its binding state. The largest possible sources,i.e. the Nb cathode and the copper substrate, have also been characterised fully and suitable means to reduce their hydrogen content have been found [30]. Further ways of reducing the hydrogen content of films by means of NEGs have been devised. Unfortunately hydrogen reduction was not effective [31].

Malev and Weisser analyzed the data available from CERN's Nb thin film and revealed that the stimulated desorption mainly contributes to the oxygen and carbon oxide partial pressure to 10^{-7} mbar during the argon discharge sputtering [32]. However, several analysis methods show no concentrated oxygen migrated to the grain boundary and the interface between the thin film and substrate [27]. Whether there is oxygen or not is still in dispute [33, 6].

Thermal barrier

Efforts have been devoted in determining whether the Nb/Cu interface introduces a thermal barrier, such that the "slope" would be produced by a thermal runaway effect [7]. Accurate measurements on samples showed that Nb coated specimens have the same thermal conductivity (in the direction normal to the surface) at 1.7 K as the naked substrate, be it Cu or Nb [31].

Roughness

The roughness of the substrate has strong influence on the roughness of the film, and self-shadowing effects during film growth may lead to poorly connected Nb film grains, possibly enhanced by a non-normal angle of incidence. Granularity effects have always been seen as a major source of trouble in literature, either because of possible losses in weak-links [34], or because of easier penetration of (Josephson) fluxons [28].

Intergrain losses

Another possibility for the Q-slope is intergrain losses, a basic effect for fine-grained superconductors. Counter evidence for this mechanism comes from the fact that films grown on oxidized copper have a grain size of 100 nm, but when grown on an oxide-free surface the grain size is of the order of micrometres. However, the Q-slope does not decrease with the larger grain size. Other possibilities are impurities in the film and surface roughness. Irregularities on the substrate can result in film inhomogeneities.

There is no strong proof showing whether the intrinsic defects are filled with oxygen or not. The intrinsic defects are believed to be conducting nanometer size junctions, and they decrease the critical magnetic field of the superconducting thin film [27]. It resembles the intragranular weak links in the superconductor. The intrinsic defects are also believed to trap the rf magnetic flux, which contributes significantly to the NQL.

1.7 *Current status of thin film cavities*

Superconducting cavities produced by the magnetron sputtering technology have been successfully used at CERN, and are also employed in several other present or future accelerator facilities, such as ALPI (INFN,Legnaro, Italy) or SOLEIL (St-Aubin, Gif-sur-Yvette, France) for acceleration, or ELETTRA (Trieste, Italy) and SLS (Paul Scherrer Institut,

Villigen, Swiss) for 3rd harmonic bunch lengthening. There are clearly defined sets of accelerator machine parameters where films show a clear advantage compared to bulk niobium, in particular for low frequencies or for operation at 4.2 K. Niobium films have however not yet achieved their possible ultimate performance, contrary to what has been obtained with niobium sheet cavities, and this hinders at present their use for electron linacs although their cost is far inferior.

Several novel developments in coating technology are however under study which, on the grounds of the present understanding, may produce an important leap forward. A first simple step towards improving film quality is adding a bias to the classical magnetron configuration for having an ion bombardment during film growth. This should produce smoother films and has been first tested at CERN with no significant changes in rf performance. A further possibility is to create the film using Nb ions, instead of neutrals such as in sputtering, attracted to the substrate by a bias, thereby allowing conformal deposition with a normal angle of incidence everywhere and thus suppress self-shadowing. The most promising techniques have been selected by different Laboratories and are under development or are being tested [35]. For niobium thin films, there are DC post magnetron processes, biased DC magnetron deposition, vacuum arc coating, ECR.

1.7.1 *Italy INFN DC-post magnetron*

It is quite true that increasing the deposition rate during the sputtering process can reduce the impurities in the growing film. The DC-post magnetron method adopts a simple target Niobium pole together with a tunable magnetic field to achieve a uniform film deposition. The experiment has not obtained a uniform quality film yet, while the increased incident flux of Niobium does not improve the RRR very much either. The sputtered single cell cavity has a large residual resistance resulting in a low quality factor. ($2x10^8$ at 4.2K). The result did show the plasma influenced the film growth greatly[36, 37].

1.7.2 *ALPI experience on Nb thin films*

ALPI is the Legnaro super-conducting linac for heavy ions, in operation since 1994 [1]. Originally the sputtered medium β cavities installed in ALPI were Pb plated and only later they were renewed by substituting the original metal coating with a Nb layer deposited by DC bias sputtering. The bias voltage applied to the substrate promotes the ionic bombardment of the growing film and the desorption and breakup of the surface adsorbed species. Since the very beginning of the ALPI project two R&D programmes were launched, one on the sputtering of Cu bases with Nb and the other on the realization of full Nb cavities [38]. ALPI accelerating structures are Quarter Wave Resonators (QWR) of three different β. ALPI medium β section consists of 44 $\beta = 0.110$ and f = 160 MHz QWRs contained in 12 cryostats. The resonators with electroplated Pb were installed in 1992-1993 and were operated, at their best, at an average Ea of 2.7 MV/m. ALPI first beam was accelerated in May 1994 and since then the cavities have been routinely used

to provide beams to nuclear physics experiments under scheduled beam runs [39]. In the frame of a cryostat maintenance programme started in 1998, 9 medium β cryostats were removed from the beam line and had their cavity upgraded, as later described, substituting the Pb layer by a Nb film. The refurbishing of the remaining 12 cavities is foreseen soon, compatibly with ALPI operation. The high β section (β= 0.13) includes only 8 Nb/Cu QWRs. Their shape, optimized for the sputtering process, permits the establishment of an accelerating field exceeding 7 MV/m at 7 W [40].
In the same year (1993) these programmes, which proceeded in parallel, brought ALPI to the outstanding result of an accelerating field of ∼6 MV/m. At the moment 52 quarter wave Nb/Cu resonators (Figure 1.5) are mounted.

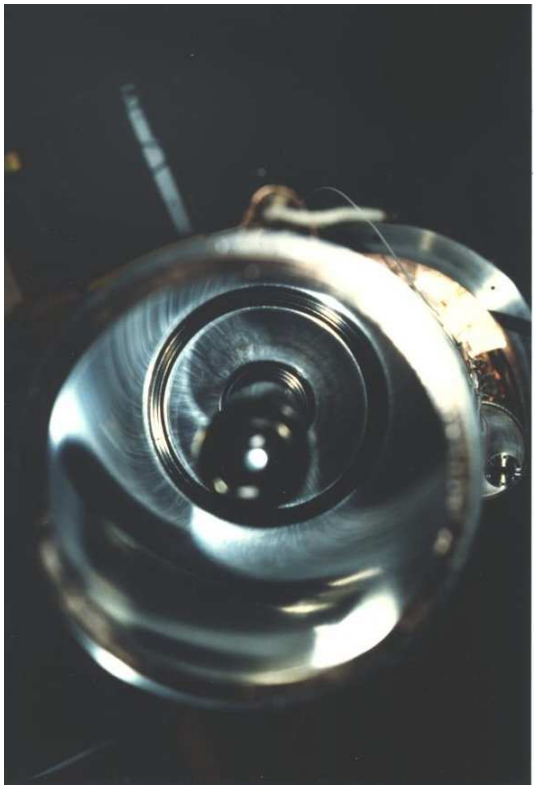

Figure 1.5: *Upgraded medium β resonators; by replacing its Pb layer with a sputtered Nb film it could reach an accelerating field exceeding 4 MV/m at 7W dissipated power.*

1.7.3 *Vacuum arc coating*

INFN Roma and Soltan Institute formed a joint coating project to investigate the feasibility of a vacuum arc technique [41]. In this coating technique an electric arc is established over the cathode's surface by a suitable trigger (high voltage or laser pulse). The arc is sustained by an adequate power supply, with the plasma plume containing Nb atoms at such a high density that they are fully ionized. Discharge gas is not needed in this case, contrary to classical sputtering, resulting in no trapped impurities. The technique provides a high coating rate, and of course the coating flux can be attracted at the desired energy

towards the substrate.

A strong disadvantage is however the formation of macroparticles because of the explosive nature of the process. Magnetic filtering and steering of the ion flux is then needed, in order to remove macroparticles from the flux and to obtain a defect-free coating, adding complexity to the coating system.[42]. Nb coatings have already been performed on Cu samples which have been fully characterized. An important difference of "energetic" coatings compared to sputtered films is the absence of preferential orientation of the crystallites, whose growth in the case of sputtering is instead dominated by the lattice free energy resulting in a (110) texture.

Moreover the grains are several microns in size, compared to a few hundred nm in the case of sputtering, and completely free from defects and microstrain, which are a major source of electron scattering in sputtered films. In addition, the depositing energy varies from 10-100 eV. The transition temperature ranged randomly from 8.7K to 9.26K and the niobium thin film with the best result cannot be reproduced for larger thickness.

Work is progressing towards the construction of a filtered UHV arc coating system for rf cavities, either with a planar arc as a source (figure 1.6), or using a cylindrical arc which is somewhat similar in geometry to the standard DC magnetron system.

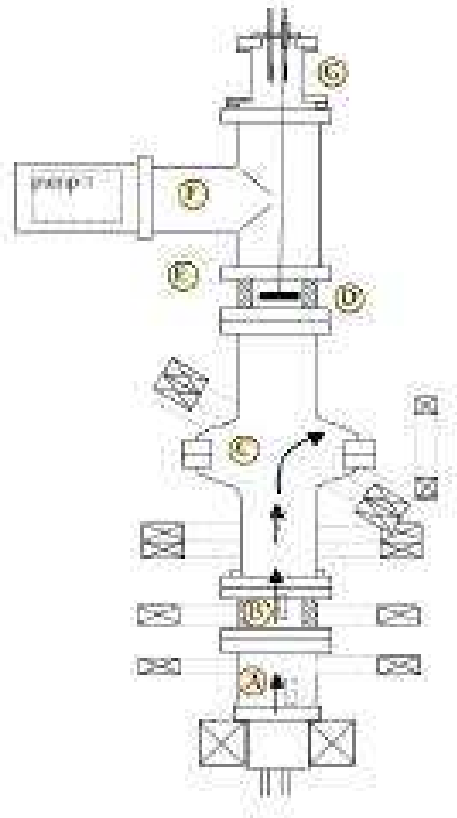

Figure 1.6: *Magnetic configurations for cavity arc coating. The uppermost coil can rotate around the cavity axis to produce an uniform coating in the upper cell [43]*

1.7.4 *ECR post-ionization of evaporated Nb*

A different approach, pursued at JLAB [44], consists in first creating a flux of Nb atoms by e-beam evaporation, and then ionize it by an ECR process. The ions can then be steered to the suitably biased substrate by magnetic guidance [45]. The advantage compared to arc deposition is the total absence of macroparticles, albeit at the expense of a much lower coating rate which calls for an extremely clean XHV environment. The vacuum conditions, and in particular the hydrogen partial pressure during the process, must anyway be kept under tight control in "energetic" coatings. The virtually defect-free films produced by these techniques will in fact result in a much higher mobility of hydrogen that may reflect in a degradation of rf performance. Encouraging results in terms of film quality have been obtained on small samples by this technique, and work is progressing towards the coating of a full cavity (figure 1.7).

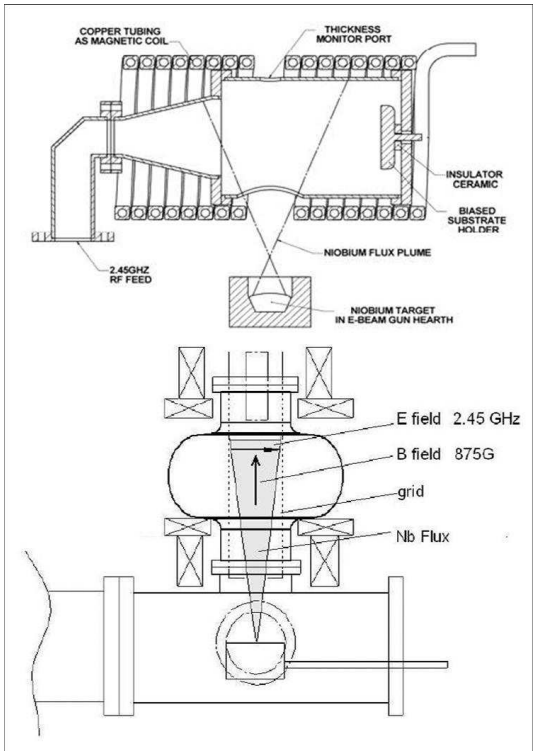

Figure 1.7: *Schematic set-ups of evaporation + ECR coating system for small samples and for cavities [45]*

1.7.5 *High Power Pulsed Magnetron Sputtering (HPPMS)*

HPPMS is an evolution of the magnetron technique which relies on ∼100 μs high-voltage pulses of the order of ∼1 kV compared to the ∼300 V of the standard DC magnetron process . During the pulse a huge power density is deposited onto the target, of the order of a few kW/cm^2 compared to a few W/cm^2 of the standard DC process, producing a highly dense plasma in which also the Nb atoms are partially ionized. These can in turn

be attracted to the substrate with a suitable bias. A further advantage of the technique lies in the fact that no hardware changes are required compared to a standard DC biased magnetron system, except for the obvious replacement of the power supply. Experiments have been pursued by CERN in a classical planar magnetron system using a low repetition rate power supply.

Chapter 2

Sputtering generalities

Basic informations on what is sputtering, how it happens and sputtering techniques are briefly introduced. Cylindrical Magnetron sputtering is the technique used for 1,5 GHz cavity coating and, for this reason, a detailed description of this configuration, as well as sputtering parameters that influence film quality, is given. At the end the status of art of niobium on copper accelerating cavities is reported.

2.1 *Fundamentals*

A material-bombarding particle, like a single atom, ion or molecule with a relatively high potential energy can give rise to the ejection of γ electrons (secondary electrons) or other phenomenon, like breaking or rearranging chemical bonds. If the kinetic energy of the bombarding particles exceeds the binding energy of the atoms, atoms of the lattice are pushed into new position; surface migration of the atoms and surface damage can arise. At energies exceeding roughly 4H (where H is the sublimation heat of target material that coincide with the binding energy of atoms) ejection of atoms into the gas phase or their dislodging start to play an important role [46].

The new phenomenon that arises is called *physical sputtering*. In physical sputtering, ions rather that neutral atoms are used for bombardment, as with ions ones can have the desired kinetic energy accelerating them with electrical fields.

Sputtering is always associated with temporary or permanent lattice damage and surface migration of atoms. For this reason sputtering is often considered as an inconvenience as it causes erosion of the electrodes, damage to active surface layers in thermionic low-work-function cathodes, undesirable deposits on walls and observation windows etc. One can say that sputtering is responsible for limiting the useful life of a lot of devices including old electronic vacuum triodes (television) valves or even gas lasers.

The sputtering with high kinetic energy can be considered as three dimensional billiard game with atoms. A bombarding ion is reflected or scattered backward from the collision event with the target atoms and the number of collisions depend on the atomic mass relation between the bombarding ion and the target atom. Embedding of bombarding ions

into the lattice appears when the kinetic energy exceeds 100eV. For example Ar^+ in Cu has an average of penetration depth of roughly 1 nm/keV. Of course, this penetration depth depends mainly on the crystal structure and orientation. Sputtering experiment with energy higher that 8keV can cause X-ray hazard coming from the high amount of γ electrons. Maximum sputtering yields (atoms emitted per incident ion) occurs at different energies for different ions, being proportional to the ion mass. For example H^+ reaches maximum at 2keV while Hg^+ reaches the maximum sputtering yield at $50-100$ keV. Anyway at very high ion or particle energies, the process is more a radiation damage than a sputtering one. Sputtering deposition of thin films has energy region of primary interest, which are from threshold to about 5keV (for example bias sputtering). During sputtering the atom may be ejected as excited atoms or as negative or as positive ions. For this reason, there is a distinguishable difference between ion beam in a field free space and plasma sputtering in which the target is negative with respect to the surrounding plasma. In plasma sputtering, the ejected positive ions are pulled back to the negatively charged target, while the negative ions and γ electrons are accelerated away from the target surface. The energy of these negative ions can be so high that can cause resputtering of the material that they reach (substrate).

In a sputtering process, parameters such as kinetic energy of the ions, electronic structure of the collision partners, binding energy of the lattice atoms, lattice structure and orientation are involved and play an important role to the sputtering yield.

2.2 *Sputtering techniques*

There are two methods of sputtering: a) plasma sputtering and b) ion beam sputtering.

Plasma sputtering can be arranged in a triode system, in which the discharge is fed and maintained by the electrons of the thermionic cathode and not by γ electrons from the glow discharge cold cathode. The advantage of this is that sputtering can be maintained without a magnetic field even at low gas pressure (low mTorr region). In d.c. glow discharge pressure is p>30 mTorr. Applying a negative voltage with respect to plasma or anode results in creating a positive ion-sheath, through which the ions stream from the plasma toward the electrode. The sheath thickness d is given by Langmuirs space-charge equation 2.1

$$J^+ \sim \frac{U^{\frac{3}{2}}}{d^2} \tag{2.1}$$

where J^+ is the ion current density at the sheath edge, d is the sheath thickness and U the voltage difference between target and plasma. Plasma electrons in the electrode vicinity are repelled so there is no excitation of gas atoms; the sheath is dark and clearly visible. Increasing the applied voltage will result in pushing the sheath edge farther away from the electrode. Ion-sheath thickness is independent of gas pressure as long as the ion current density remain constant.

2.3 *The self sustained glow discharge*

If a d.c. voltage is applied between two electrodes spaced at some distance d apart in a gas at low pressure (10^{-2}-1 mbar), a small current will flow. This is caused by small number of ions and electrons, which are always present in a gas due ionization , by cosmic radiation. On their way from the cathode to the anode, the electrons make a fixed number of ionizing collisions per unit length. Each ionization process produces further electrons, while resulting ions are accelerated toward the cathode. If the applied voltage is enough, ions striking the cathode can eject secondary electrons from its surface. Emission ratio of secondary electrons of most materials is of the order of 0.1, so several ions are needed to bombard a given area of the cathode and to release secondary electrons. If the power supplied is not high enough, the bombardment is concentrated near the edges of the cathode. When the power supplied increases, the bombardment covers the entire cathode surface and a constant current is achieved.

The two processes of ionization by electron impact and secondary emission of electrons by ions, control the current I in the system, described by equation

$$I = \frac{I_0 e^{\alpha d}}{1 - \gamma[e^{\alpha d} - 1]} \tag{2.2}$$

where I_0 is the primary electron current generated at the cathode by the external source; α is the number of ions per unit length produced by the electrons; d is the spacing between the electrodes and γ is the number of secondary electrons emitted per incident ion.

According to *Townsend criteria*, $\gamma[e^{\alpha d} - 1] = 1$ if the voltage between the electrodes is raised, the current becomes infinite (see equation 2.2). Gas breakdown it is said to have occurred; the glow discharge burns self-sustained, as the number of secondary electrons produced at the cathode is sufficient to maintain the discharge. Breakdown voltage is a function of the product of pressure p and electrode distance d *(Paschen's law).* Distribution of potential, field, space charge and current density in a glow discharge are visually seen as region of varied luminosity. From a cross sectional view of a glow discharge we see as of primary interest the region marked as *Crookes Dark Space* (Cathode Dark Space) (see figure 2.1).

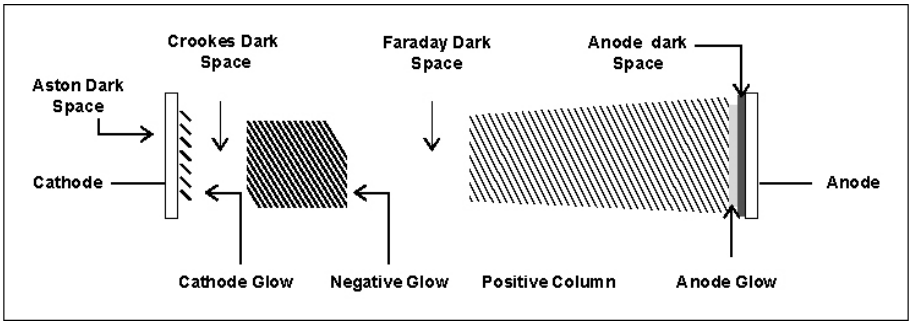

Figure 2.1: *Cross sectional view of a glow discharge.*

In this region, the positive ions have accumulated and have formed the space charge. Its thickness is approximately the mean distance travelled by an electron from the cathode before it makes an ionizing collision. Usually this distance is 5-10 times longer than the electronic mean free path ℓ. The electron energies are over the maximum excitation potential which is insufficient to ionize gas molecules, so that no visible light is emitted. Electrons that leave the cathode with energy of the order of 1eV are accelerated to sufficient ionizing energies in a region called *Aston's dark space*. The luminous region closest to the cathode is the *cathode glow* where the electrons reach energies corresponding to the ionization potential. When the electrons reach the edge of the *negative glow*, they begin to produce significant numbers of ion-electron pairs. The number of slow electrons (i.e. those produced by ionizing collisions) has become very large. The energy they posses is enough to cause only excitation and can't produce new ionization. Excitations caused by slow electrons are the reason of the appearance of the negative glow. In Faraday dark space the electrons have insufficient energy to cause either ionization or excitation, consequently is a dark space. Faraday dark space and the positive column are nearly field-free regions with nearly equivalent numbers of ions and electrons. For glow discharges applied as sputtering sources, the positive column and the Faraday dark space usually do not exist, as the electrode separation needs to be small and the anode is located in the negative glow.

2.4 *Sputtering configurations*

Sputtering is a technique by which atoms and ions of argon or other gases from plasma bombard a target thereby knocking atoms off the target. These material atoms travel to a substrate where they are deposited and form a thin film. The simplest configuration of a sputtering source is shown in figure 2.2. Diode sputtering configurations consist of two electrodes placed in a vacuum chamber.

An anomalous glow discharge between two electrodes is created if a d.c. voltage of around 500V is applied. The substrate where the film is deposited is placed on the anode, while the target that will be sputtered represents the cathode (the negative electrode). High or ultrahigh vacuum is necessary to achieve thin film purity. After evacuation to high vacuum or ultra high vacuum (UHV), the chamber is filled with the sputtering gas, usually Argon, at the pressure of 10^{-2}-10^{-1} mbar. Applying a d.c. voltage of ca. 500V between electrodes will create a glow discharge that will ionize the argon gas. Positive ions of argon will be accelerated towards the cathode and due to their kinetic energy will eject atoms from the target surface. The ejected atoms have energies of the range of several eV. They will diffuse in chamber, following the $\cos^{-1}$ law till they condense on the surface of the substrate. The high kinetic energy of the sputtered atoms leads to a better adhesion and higher density of the sputtered thin film.

The number of ejected atoms per incident ion is called *the sputtering yield Y*. The

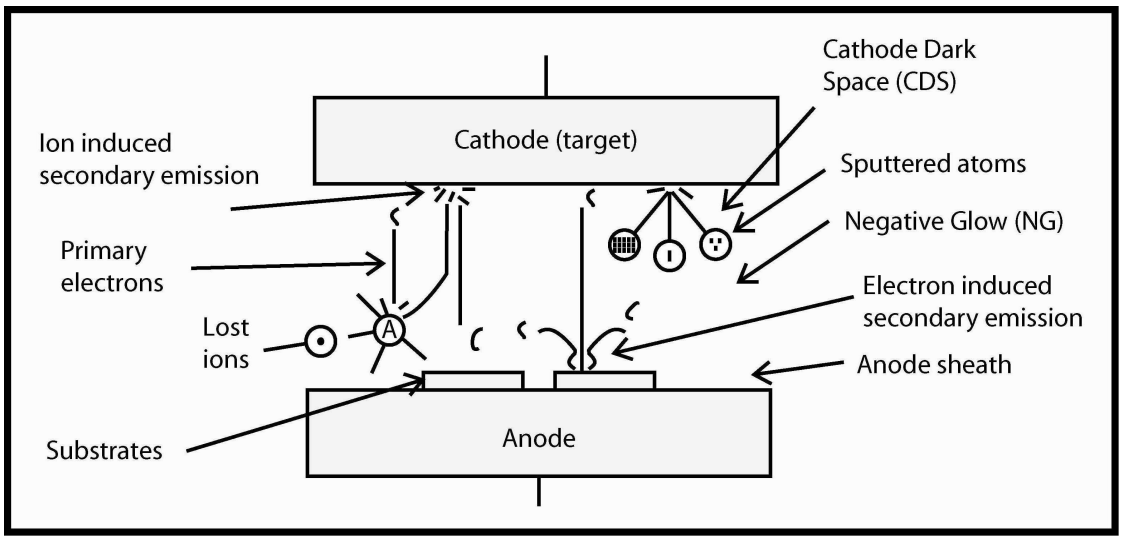

Figure 2.2: *Schematic representation of the sputtering process in the planar diode configuration [47].*

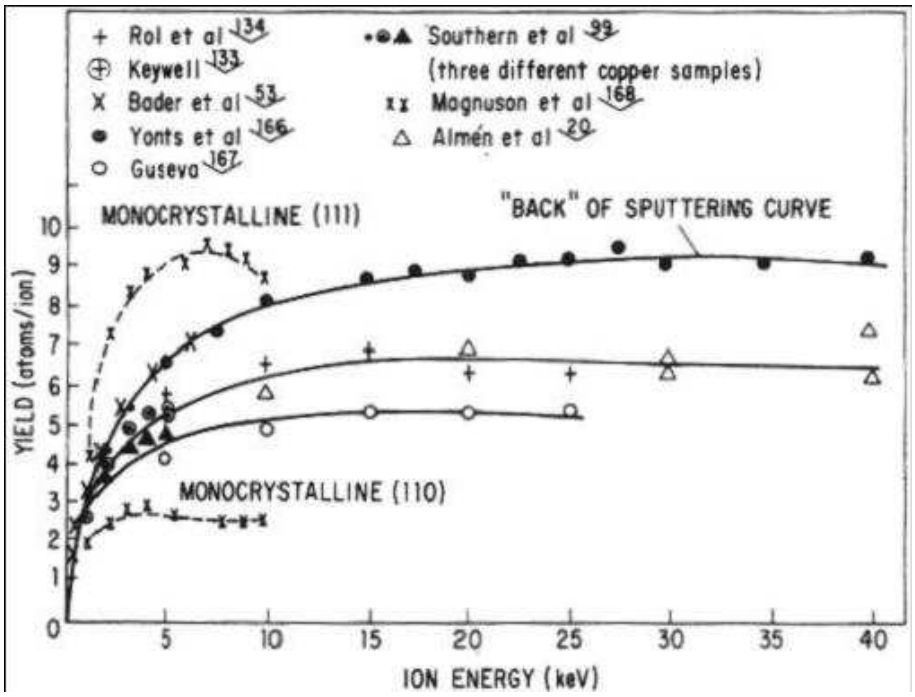

Figure 2.3: *Variations of sputtering yield with energy for argon ions bombarding copper (high energy region)[46].*

minimum ion energy required to dislodge target atoms is called *sputtering threshold*. The sputtering yield increase first exponentially above the sputtering threshold (10-30 eV), then linearly, then less linearly till it approaches a flat maximum at energies of 10 keV (see figure 2.3). With further increasing of ion energy, ion implantation effect takes place and sputtering yield decreases. Sputtering yield depends on the following parameters:

- *Bombarding ion energy* influence the sputtering yield as explained above;
- *The atomic number of colliding atoms*: the atomic masses of target element or compound influence the energy transfer as follow

$$E = \frac{4mM}{(m+M)^2} \tag{2.3}$$

  where m is the mass of the target atoms and M is the incident ion mass. It's evident that for high sputtering yield the mass of target atom should be not very different from the mass of the bombarding ion.

- The experiments show clearly that the *noble gas* ions give the highest sputtering yield. This for the fact that the inert gases are not interested in "stealing" the electrons needed to make ionization collision near the cathode.
- *Angle of incidence of the ions*: The sputtering yield increases when less directional change of the momentum is required for ejecting atoms. This happens at more oblique incidence. The sputtering yield follow the $\cos\Omega^{-1}$ law and arrive a maximum for angles 45° - 50° from the surface, but for values near 90° (perpendicular to the surface) the effect of ion reflection becomes dominant and sputtering yield decreases.

2.4.1 *Magnetron Sputtering*

For an effective sputtering, primary electrons must be used effectively to make sufficient ionization collisions in the vicinity of the cathode. The efficiency of the available electrons can be increased if the plasma is confined by a magnetic field parallel to the cathode surface. A general rule for the shape of the magnetic field is: *Magnetic field must born from the cathode and die onto the target.* A plasma confinement is achieved, while magnetic and/or electrostatic mirrors trap the electrons. Magnetic field traps and forces electrons to describe helical paths around the lines of magnetic force (see figure 2.4). When $\overrightarrow{B}$ is parallel to $\overrightarrow{E}$ the particles are freely accelerated, while when there is an electric field component $E_\perp$(Volts/cm) perpendicular to B, a drift of speed V_E occurs.

$$V_E = 10^8 \frac{E_\perp}{B}\left(\frac{cm}{s}\right) = \frac{\overrightarrow{E}\times\overrightarrow{B}}{B^2} \tag{2.4}$$

When B is uniform and E is zero, the electrons drift along the magnetic field lines orbiting them with a cyclotron frequency ω_c and the gyro or Larmor radius r_g.

$$\omega_c = \frac{eB}{m_e} = 1.76 \cdot 10^7 \cdot B \left(\frac{rad}{sec}\right) \tag{2.5}$$

$$r_g = \frac{V_E}{\omega_c} = \frac{m_e}{e}\left(\frac{V_E}{B}\right) = 3.37\frac{\sqrt{W_\perp}}{B}\,(cm) \tag{2.6}$$

Where B is in Gauss and $W_\perp$ is the energy associated with the electron motion perpendicular to the field in eV.

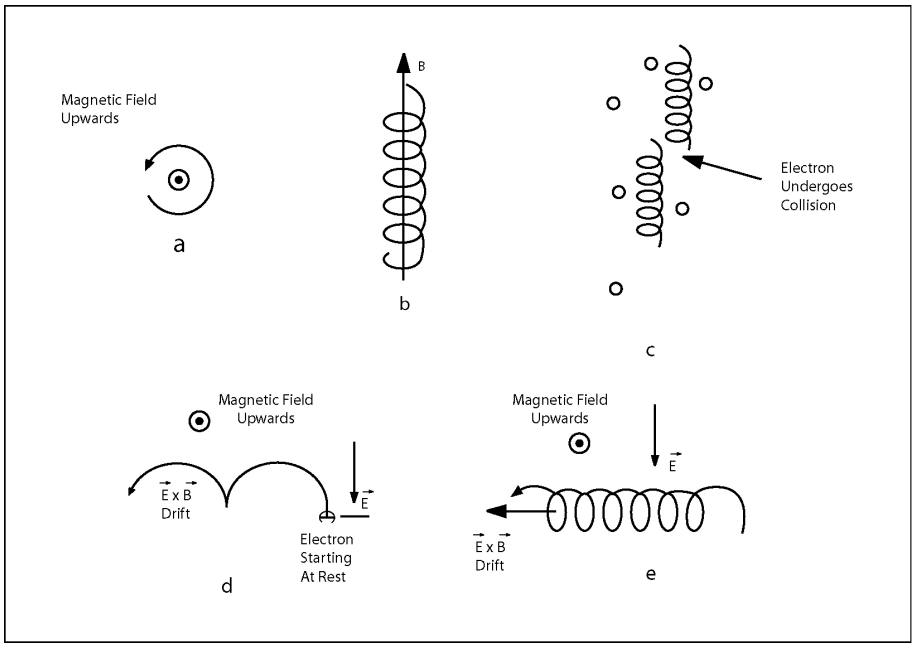

Figure 2.4: *Electron trajectories in static electric and magnetic field [48]. a)electron motion in static magnetic field seen from up to down. b) electron drift along the magnetic field lines. c) movement of the electron when undergoes a collision. d) movement of the electron in an electromagnetic field when there is electric field component E⊥ (Volts/cm) perpendicular to B. e)* electron has a drift speed $\overrightarrow{E} \times \overrightarrow{B}$ in an electromagnetic field

If the charge is immersed in both and electric field $\overrightarrow{E}$ and magnetic field $\overrightarrow{B}$, its equation of motion is:

$$\frac{dv}{dt} = \frac{e}{m}(\overrightarrow{E} + \overrightarrow{v} \times \overrightarrow{B}) \tag{2.7}$$

or rather

$$\overrightarrow{F} = e(\overrightarrow{E} + \overrightarrow{v} \times \overrightarrow{B}) \tag{2.8}$$

only the electron motion (not the ions) is influenced by the magnetic fields of the strengths used in sputtering source operating in the magnetron mode.
The force acting on charged particles is perpendicular to the electric and the magnetic field, and itreaches its maximum intensity when both fields are orthogonal:

$$|v \times B| = |v| \cdot |B| \cdot \sin\theta_{vB} \tag{2.9}$$

With the introduction of a magnetic field the electrons run along longer path, thus increasing the probability of collision. The same effect can be achieved increasing the gas pressure. With a magnetic field, sputtering at lower pressure (10^{-3} mbar)is possible; on the other way, if the pressure in not reduced, it is possible to obtain greater current for a given applied voltage. This, on the other hand, causes strong target heating and a target cooling system is necessary.

As the electrons can move freely along the field lines, end losses are possible. The problem is eliminated installing reflecting surface wings (mirrors) maintained at the cathode potential or by causing the magnetic field lines intersect that cathode. In order to complete the electrical circuit, the low energy electrons must be removed from the trap and migrate to the anode. It is believed that plasma oscillations assist in this process. Anode placement, size and design are of an important role and should take into account the poor mobility of the low-energy electrons. Proper anode placement and design can greatly reduce spurious electrical activity.

2.4.2 *Magnetic mirror and wings*

A spool formed from a cylindrical barrel and two wings is called a cylindrical post magnetron cathode. In a relatively uniform magnetic field, a uniform intense plasma will form along the barrel and will extend outward a distance W. The smallest wing size W should be at least three times larger that the gyro radius of the primary electrons emitted from the cathode. An empirical formula that calculates the wing size W is given by field strength B and operation voltage V in the equation 2.10:

$$B \cdot W = 10\sqrt{V} \quad (Gauss \cdot cm) \tag{2.10}$$

In our experimental investigation, we use magnetic field ca 150 Gauss and voltage of the range 500 V. That means, the wing size for our cathode should be at least

$$W = \frac{10 \cdot \sqrt{V}}{B} = \frac{10 \cdot \sqrt{500}}{150} = 1.49\, cm \tag{2.11}$$

2.4.3 *Cylindrical magnetron sputtering*

When a planar cathode is used, the longitudinal magnetic field is the preferred mode for sputtering purposes. If a cylindrical cathode is used, a transverse magnetic field is applied along the axis of the cylinder. Cylindrical configuration is post magnetrons or hollow cathode (see figure 2.5). In the *post magnetron* case, the cylinder is the cathode and the outer cylinder is the anode (substrate), while in the *hollow cathode* case it's vice versa. In both cases, cathode wings (mirrors) are necessary to achieve plasma confinement.

The advantage of using magnetic field is that in a field of about 300 Gauss a current of several amperes at 500V could be obtained. This is a great improvement as compared with a current of only a few tenths of an ampere at 1500V without a magnetic field. The

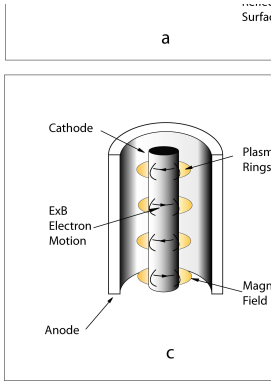

Figure 2.5: *The configuration of various magnetron sputtering source: a) and c) are cylindrical magnetrons; b) and d) are called inverted magnetrons; a) is referred as cylindrical-post magnetron and b)as cylindrical-hollow magnetron [47].*

magnetic field used in sputtering sources is of the range of 10^{-2}T (100 Gauss) and does not influence the ions but only the electrons.

2.5 *Film growth in the sputtering environment*

In a sputtering process a minimum accumulation-rate below which the sputtered film can not be deposited does not exist, instead in the evaporation process it does. During sputtering process deposition of the film material is done atom by atom on the substrate. One of the advantages of the sputtering versus thermal evaporation is that sputtering yield of different materials do not vary that much. Thus refractory materials, which require high temperature and low vapour pressure, sputter almost as readily as any other material. Anyway, the sedentary nature of sputtered refractory materials appears at the point of deposition. The diffusion from the random point of impingement onto energetically favourable sites is restricted form the low mobility of the sputtered material. The microstructure and properties of coating deposited is, however, influenced a lot from the plasma sputtering environment, which can be manipulated [49]. Without any modification of the plasma environment one can obtain primitive growth structures that are not strongly interbonded.

The deposition of thermally evaporated metals in the form of tapered grains was determined by Movchan and Demchishin [50] to occur at temperatures below about 1/3 of the respective melting temperature. Thornton adapted their zone diagram for metal coating deposited by plasma sputtering just adding a second axis for sputtering gas pressure (fig-

ure 2.6). The diagram adapted by Thornton indicates that the microstructure properties of the sputtered film depend not only on the substrate temperature, but also on the gas pressure. The Zone 2 that appears at 1/3 of melting temperature in thermal evaporation occurs first at $\frac{1}{2}T_m$ (melting temperature) at the deposition by plasma sputtering.

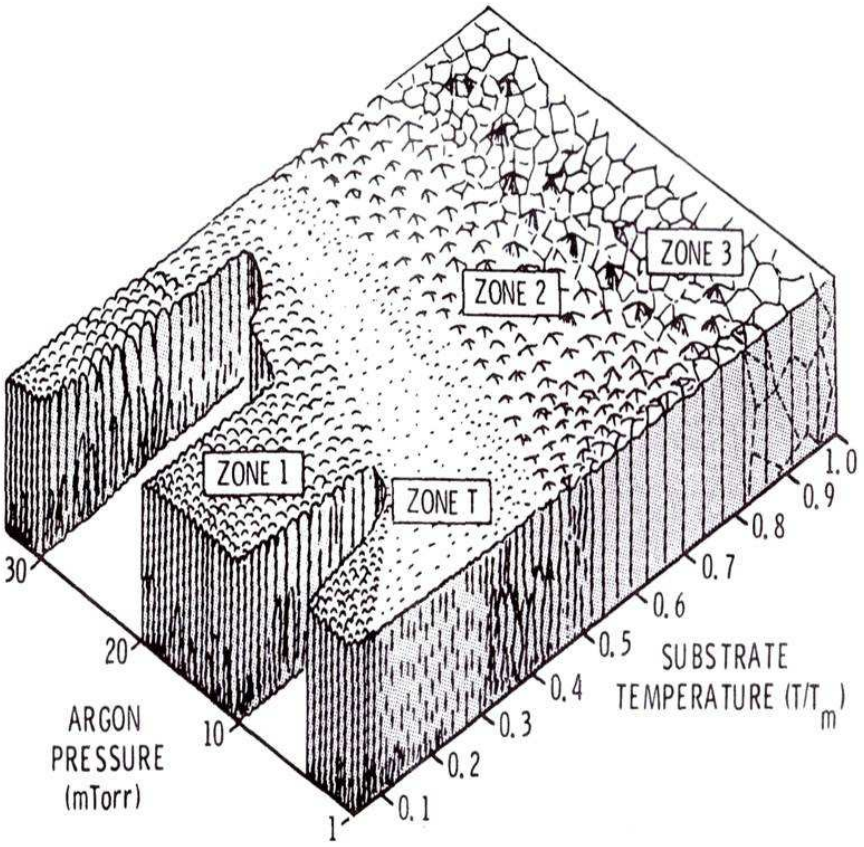

Figure 2.6: *Structural zone model proposed by Thornton for metal coatings grown by sputtering.*

2.5.1 *Influence of plasma bombardment on the growing film*

A positive bias applied between target and substrates promotes ion bombardment of the growing film. If the film is given a negative potential with respect to the plasma, the resulting technique is referred to as bias sputtering. In this way films are subjected to a certain amount of resputtering that causes the desorption and breakup by ion bombardment of the surface adsorbed species; whether or not this will occur depends on the relative strengths of the metal-to-impurity and the metal-to-metal bonds. The fraction f_i of impurities of species i trapped in a film is given by

$$f_i = \frac{\alpha_i N_i}{\alpha_i N_i + R} \tag{2.12}$$

where N_i is the number of atoms of species i bombarding unit area of film in unit time during deposition, α_i is the effective sticking coefficient of the species i during deposition

and R is the deposition rate of the film [46, 51]. It is clear from Eq.1 that f_i can be reduced by increasing R.

Considering the bias process equation 2.12 is modified as

$$f_i = \frac{\alpha_i N_i - \beta}{\alpha_i N_i - \beta + R} \tag{2.13}$$

where β is a function of the bias current due to impurities ions.
The main advantages of the insertion of a biased electrode are: removal of most impurities during resputtering; rearrangement of atoms during film growing; densification of the crystal structure; higher sputtering rate; lattice rearrangement; films quality improvement; increasing of the coating hardness; similar defect annealing as does an elevated substrate temperature [52]; electrons bombardment reduction; adhesion improvement. On the contrary applying the wrong bias voltage can cause noble gas atoms embedding, lattice defects, thickness reduction and still the hydrogen removal rate is low, due to the high sticking coefficient of this molecule [52].

Ballistic stimulation using oblique incidence from two opposing angles were carried out by Dirks and Leamy [53, 54] (see figure 2.7). Elongated microvoids oriented normal to the plane of the substrate appear near the centre of the finite simulated structure. The microstructure of coating plasma sputtered is a sponge-like one with a low physical density and near-zero residual stress. This primitive microstructure can be modified and densified during discharge sputter deposition by stimulated bombardment (bias sputtering) or coincidence control.
Leamy et al. [54] have given some other supporting evidence shown by molecular dynamics simulation. From this simulation was proved that particle energies sufficient to densify normal - incidence deposit were insufficient to densify oblique deposits accumulated under otherwise identical conditions. Not randomized angular deposit of the film will produce a porous-spongy like film, while a well randomized sputtering (high pressure) will result to a densified and less porous film property. For this reason, a high pressure magnetron sputtering is preferred than a low pressure one, which can result to a porous and bad quality thin film deposited.

2.5.2 *Coating temperature and gas mixture effect*

From early morphology studies, the film structure is highly correlated with the deposition rate and the adatom surface mobility [55, 56]. By increasing the incident atom energy and incident flux, we can expect increased substrate temperature right at the surface, and higher adatom surface mobility, which leads to the larger grain size. Based on this and the findings in [57], Schucan et. al., have tried to use Ar/He mixture as working gas to increase the adatom surface mobility during niobium deposition [58]. Unfortunately rare gas trapping reduces the grain size and affects the grain growth. The investigation of the rare gas trapping of Ar, Ke and Xe is reported in [59]. Sputtering film technique has the

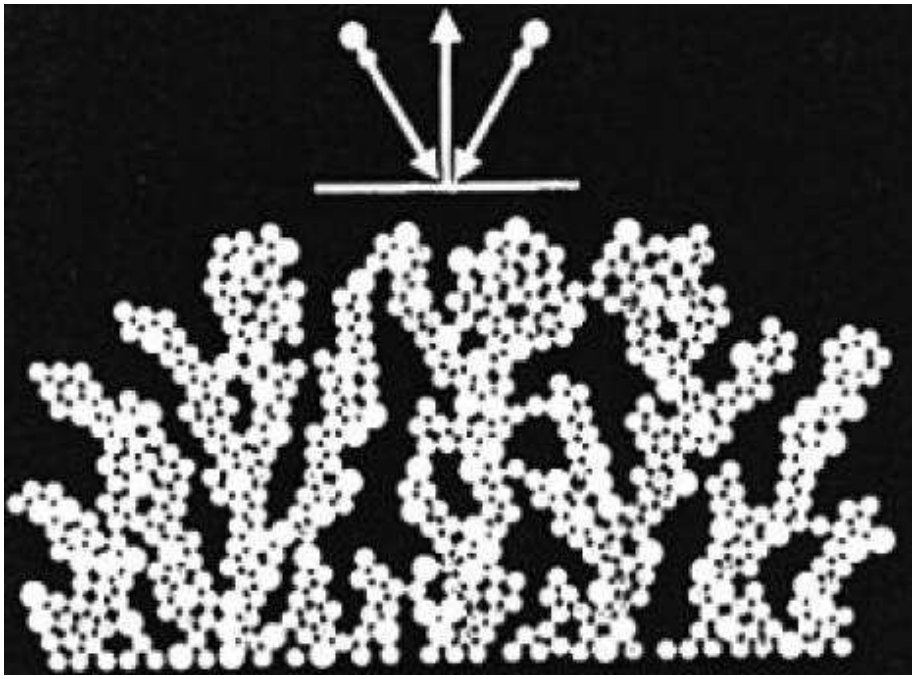

Figure 2.7: *Structure formed by oblique incidence deposition of hard disk from two directions at ±30° relative to the substrate normal. Disk were allow to relax at the nearest point of contact with two others disk.*

following drawbacks:

- The working gas is trapped in the film; it may cause intrinsic defects inside of the grain.;
- The impurities of the working gas are not good for the thin film.;
- The deposition energy is low, which does not help to avoid columnar grains.;

The RRR of magnetron sputtered film ranged from 5-10, later improved to 10-20 after using krypton as working gas instead of argon. The transition temperature usually occurs at 9.6K while many films had unusually wide transition width.

Chapter 3

Surface treatments

In this chapter all the surface treatments that cavities and samples underwent during this work are presented. Copper, niobium and quartz surfaces are mechanically polished and chemically etched, heat treated and water cleaned with different methods.

3.1 *The importance of surface treatment*

In both cases of niobium or copper cavities, surface treatments play a fundamental role in cavity performances. With improvements in fabrication (see section 1.4) and ultra cleanliness techniques, the limitation on SC cavity performance now seems to be the surface state generated by the etching process. The influences of various surface treatments are now being studied at several laboratories (KEK, DESY, CERN).
Spinned cavities present a damaged internal surface and microcracks. The problem arising from the crack presence is twofold: on one hand rf currents are obstacled in their path, on the other hand, the well of a crack is practically impossible to clean even by means of high pressure water rinsing. A crack is a receptacle of contamination from BCP residuals, water and so on. To fight this problem spinned cavities preparation consists in surface mechanical treatments, chemical etching, heat treatment and surface cleaning. In fact 100 microns of previous mechanical grinding succeed making the Q-value versus field flat. After BCP and an in situ baking at 115°C, a monocell 1,5 GHz cavity has reached a Q_0 of 5×10^{-9} at a gradient of 33 MV/m [60].

The same for the EBW niobium cavities: "Experience has shown that a damage layer in the order of 100 μm has to be removed from the inner cavity surface to obtain good rf performance in the superconducting state" [61].
Saito have analyzed the Q_0-Eacc excitation curves of electropolished niobium cavities based on the global heating and rf magnetic field penetration models, in addition to rf magnetic field enhancement model. He deduced the relationship between the surface roughness and the field enhancement. "The remarkable field enhancement starts from about 2 μm of the surface roughness in Rz. To get the high gradient Eacc $>$ 30 MV/m, the surface roughness should be smoother than 2μm" [62]. At the moment mechanical grinding and electropol-

ishing are necessary base processes. After having removed 100 microns or even more from the surface, one can adopt any other clean polishing technique from chemical polishing, water rinsing, heat treatment, atmospheric plasma, ecc.
In the following sections each cleaning technique is described in details.

My role in this part of the work has been: assembling and adapting the EP system for copper and niobium cavities; assembling and adapting the system for SUBU and passivation of copper cavities. New flanges and cathode for the 3-cell niobium cavities have been designed and the copper cathode for Nb electropolishing have been substituted with a pure aluminium tube. In addition several samples, with a variety of shapes, have been treated and different anode-cathode system for electropolishing and chemical polishing have been built and tested.

3.1.1 *Copper*

Copper cavities need a peculiar attention to surface treatment because it has been proved that a reduction in roughness allows for a consistent reduction in film defect density. In many cases niobium film seems to replicate the copper substrate morphology as the result of an heteroepitaxial growth mechanism, which favors the growth of some niobium planes parallel to particular copper planes for which there is a good lattice match[63].
Generally the copper cavities described in this work undergo the following sequence of treatments (if not else specified) and processes:

- Stripping from the previous coating
- 1 hour electropolishing
- 10 minutes chemical etching
- 10 minutes passivation
- High Pressure Water Rinsing (HPWR) 1 hour at 100 bar
- Coating keeping the cavity at 150°C
- HPWR 1 hour at 100 bar
- rf test

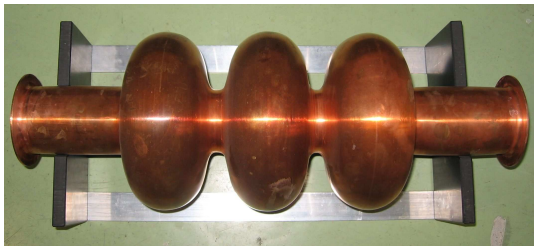

Figure 3.1: *Spinned 3-cell copper cavity*

In some cases washing in ultrasonic bath have been tried, mainly to remove the chemistry residuals. Of course each cavity has its own treatments history, that will be specified before showing the rf test results.

Copper samples, usually 10x5x1mm have been prepared with the same cavity chemical treatments but with various processing time.

3.1.2 *Niobium*

The 3-cell cavity described in this work has been treated as follows:

- mechanical polishing with Scotch Brite^{TM} (various grains) for 6 hours
- Degreasing in ultrasonic bath with soap and double rinsing in deionized water
- 2 hour and 15 minutes electropolishing, approximate thickness removed: 60μm.
- High Pressure Water Rinsing (HPWR) 45 minutes at 100 bar
- rf test n.1
- 1 hour chemical etching in the 1:1:2 solution
- High Pressure Water Rinsing (HPWR) 30 minutes at 100 bar
- Heat treatment at 750°C for 3 hours
- 1 hour and 20 minutes electropolishing
- High Pressure Water Rinsing (HPWR) 3 hours at 100 bar
- rf test n.2
- High Pressure Water Rinsing (HPWR) 2 hours at 100 bar
- rf test n.3

The 3-cell spinned niobium cavity has two wings at the end of the beam-pipe (figure 3.2). Vacuum flanges for rf test and all the other flanges, for chemical treatments and water cleaning, have been designed in order to seal the system using those wings. For vacuum test, indium wire is necessary, while during surface processes vyton o-rings have been used. In this way electron beam welding of stainless steel flanges has been avoided.

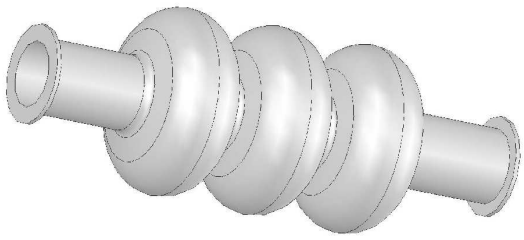

Figure 3.2: *A 3D technical drawing of the niobium 3-cell 1.3GHz cavity*

3.2 *Mechanical polishing*

The first essential treatment that cavities undergo is a mechanical brushing of the surface. At the very beginning the mechanical grinding of monocell cavities have been made with Scotch Brite^{TM} rotating tools. The abrasive showed in figure ... can be inserted easily inside the cell of a monocell cavity and they are great for creating an uniform surface

finish or blending surface imperfections. In this way both the iris and the equator are mechanically finished.

Figure 3.3: *Scotch Brite^{TM} tool used for mechanical grinding inside monocell cavities*

Manual grinding is possible only for monocell, from three cells to nine cells is practically impossible. Slow and automatic barrel polishing is the alternative to manual surface finishing. Different media and different velocities have been tested and this method is still applied to ALPI quarter wave resonators. Due to the fact that mechanical grinding is a powerful method to remove surface defects from superconducting niobium cavities, at KEK a simple and faster mechanical grinding method has been developed: CBP (Centrifugal Barrel Polishing)[64], as the pre-treatment for EP[65]. This method, combined with the right choose of the polishing media, is a perfect solution for removing the surface roughness due to the spinning. Unfortunately, to apply this intense centrifugal force the cavity should be stiff enough to support the stress all along its surface. Both the nine-cell spinned cavity that has been treated with this method were indeed too thin at the iris and suffered serious damages.At the moment all cavities described in this work underwent a manual mechanical treatment.
Copper samples have been mechanically prepared to chemical treatment with sandpapers of different size, from the biggest size to the finest one.

3.2.1 *Diamond turning*

Diamond turning is a process of mechanical machining of precision elements using Computer Numerical Control (CNC)lathes equipped with natural or synthetic diamond-tipped cutting elements. This process is also known as single-point diamond turning (SPDT). The process of diamond turning is widely used to manufacture high-quality aspheric optical elements from glass, crystals, metals, acrylic, and other materials. Optical elements produced by the means of diamond turning are used in optical assemblies in telescopes, TV projectors, missile guidance systems, scientific research instruments, and numerous other systems and devices.

Diamond turning is a multi-stage process. Initial stages of machining are carried out

using a series of CNC lathes of increasing accuracy. A diamond-tipped lathe tool is used in the final stages of the manufacturing process to achieve sub-nanometer level surface finishes and sub-micrometer shape accuracies. The surface finish quality is measured as the peak-to-valley distance of the grooves left by the lathe. The shape accuracy is measured as a mean deviation from the ideal target form. Quality of surface finish and form accuracy is monitored throughout the manufacturing process using such equipment as contact and laser profilometers, laser interferometers, optical and electron microscopes.

The SPDT manufacturing process produces a relatively high percentage of defective parts, which must be discarded. As a result, the manufacturing costs are high compared to conventional polishing methods. Even with the relatively high volume of optical components manufactured using the SPDT process, this process cannot be classified as mass production, especially when compared with production of polished optics. Each diamond-turned optical element is manufactured on an individual basis with extensive manual labor.

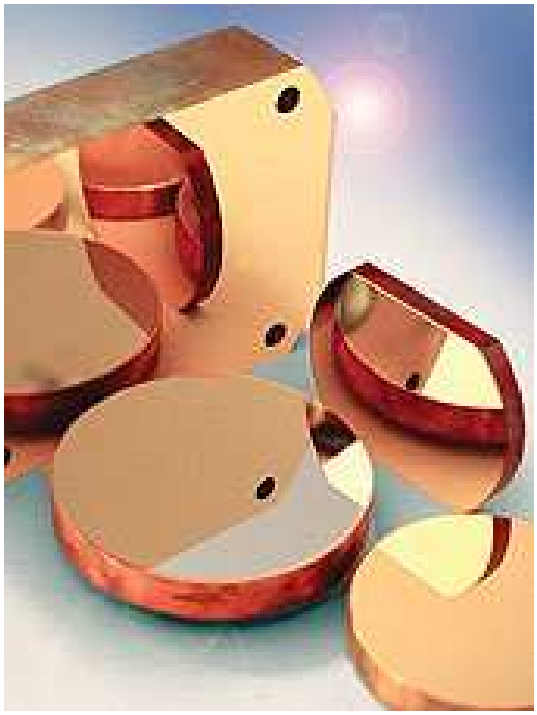

Figure 3.4: *Examples of diamond turned plates.*

This technique have been applied to two copper plates in collaboration with LTultra, Herdwangen-Schönach Germany. We managed to obtain also ultra pure aluminium plates but all tests on niobium plates failed due to the softness of the metal.

3.3 *Electropolishing*

Within the sequence of surface finishing operations, electropolishing just follows mechanical polishing. It is well-known indeed that mechanical polishing produces an altered microstructure of the outermost layer. As already mentioned, for both bulk Niobium cav-

ities and for Niobium sputtered cavities, the amount of Niobium or Copper that has to be removed by electrolytic polishing, is usually around 100 μm. Palmieri, during the tutorial of the 11th workshop of rf superconductivity, gave an exhaustive talk concerning the electropolishing mechanism and all theories adopted to explain it. In this section I'll try to summarize the most important concepts[17].

Looking at experimental results already existing in literature about mechanically polished Copper surfaces, Turley and Samuels [66, 67] reported for an OFHC Copper surface abraded by P1200 grade silicon carbide abrasive paper, that the outermost layer, for a depth of around 1500Å, is constituted by very small subgrains approximately equiaxed. The small subgrains have sharp boundaries and part of them got recrystallization due to plastic strain and/or to a local increase of temperature. Recrystallized grains were most identifiable by the presence of annealing twins. No evidence was found of the presence of an amorphous-like layer. At depths lower than 1500Å, subgrains get larger up to when they are replaced by cells having a slab morphology and sharp boundaries. Getting deeper, the boundaries of the slab-shaped cells became diffuse. The plastically deformed layer matches smoothly the virgin structure of Copper, its thickness depending on the degree of polishing.

In the case of Niobium sputter-coated Copper cavities, it is clear that an altered Copper superficial layer at the interface between Cu and Nb should be removed because it can influence thermal boundary. In fact, it is well known that dislocations induced by plastic deformations can decrease thermal conductivity even of an order of magnitude. Even from the point of view of contamination trapped on the Copper surface, this altered layer should be removed. Indeed, all the mechanically polished samples that have been examined [17], even after deionized water rinsing, display foreign inclusions such as Al, Ca, Mg, coming from the abrasive media.

3.3.1 *EP Process*

Several hypotheses exist for explaining the mechanism of electropolishing of Copper in phosphoric acid solutions. All of them concern with the existence of the thin bluish viscous layer of electrolyte forming in proximity of the anode.

In an electrolytic cell we can have anodic reactions and cathodic reactions. Anodic reactions are all the oxidation reactions and in general all reaction that produce electrons. Cathodic Reactions are all the reduction reactions and in general all reaction that consume electrons. Anodic reactions in electrolytic polishing depend mainly on the nature of the dissolving metal, the electrolyte composition, the temperature, the current density and the degree of agitation.

The electrolytes used in electropolishing should satisfy a number of requirements, for instance:

1) the electrolyte should contain complex ions;

2) the electrolyte should contain anions with large radii and a small charge, e.g., ClO_4^-, $H_2PO_4^-$, $H_3P_2O_7^-$,

3) a viscous liquid layer should be formed on the anode during the process.

Important work has been prepared around the end of the late thirties by Jacquet [68], that first investigated the electropolishing of Copper in phosphoric acid by observing the I-V Characteristics. He found that, depending of the voltage applied, it is possible to obtain pitting, polishing or gas evolution, as shown in fig. 3.5.

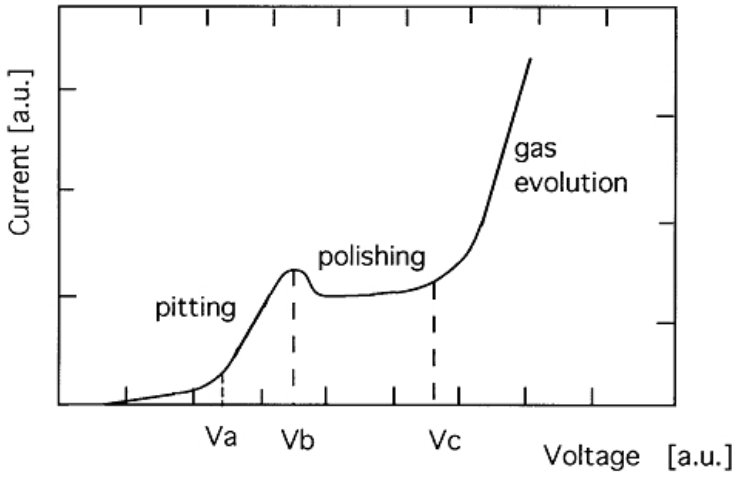

Figure 3.5: *Current density vs. voltage for Copper electropolishing in phosphoric acid*

In particular he found that up to the point VB, the surface conserves its mechanically worked appearance and shows some signs of pitting. Fluctuations in both voltage and current and a simultaneous drop in current density are found just after V_B. Over the horizontal range (V_B - V_C), the current density remains constant although the voltage increases. A polishing effect is observed between V_B and V_C , but the best results are obtained near point V_C. The first bubbles of gaseous oxygen appear on the anode at a voltage corresponding to point V_C. At higher voltages than V_C, the dissolution of metal is accompanied by evolution of oxygen, but there is some pitting as a result of contact with oxygen bubbles trapped on the surface. At potentials much higher than V_C, the quality of polishing improves, since the oxygen bubbles cannot be trapped on the surface and there is no pitting. A solid, brown film is formed on the anode surface for voltages between V_A and V_B, the film adheres to the metal but is destroyed at higher current densities.

The thin layer of electrolyte in the vicinity of the anode assumes a bluish color. Moderate agitation of the solution reduces the thickness of the bluish layer while voltage drops. Vigorous agitation reduces the thickness to a few tenth of a mm and voltage drops even more. Jacquet assumed that a relationship exists between the formation of the viscous layer in the electrolyte and the polishing effect. According to Jacquet, the process should be controlled by maintaining a constant voltage rather than a constant current density; in this case it is not necessary to calculate the total surface area of the sample to be polished. Rigorously speaking, it would be not possible to control the electropolishing process solely on the basis of voltage or current density measurements.

The Applied Voltage V is a function of the anode and cathode potentials, the Voltage

Drop in the electrolyte (I R_{electr}) and the voltage drops in the conductors and contacts (I $R_{Conduct}$), i.e.

$$V = (V_{anode} - V_{cathode}) + IR_{electrol} + IR_{Conduct} \tag{3.1}$$

Thus V depends on the electrode potentials, the electrolyte concentration, the anode and cathode surfaces, the arrangement of electrodes, shape and size of the bath. Hence, the "applied voltage" used by Jacquet as a control parameter would not always correspond to the optimum polishing conditions. The electropolishing process could be controlled on the basis of the anode potential through the use of a special non-polarizing auxiliary reference probe (for example a saturated calomel third electrode). On the other hand, the potentials of the anode and of the auxiliary electrode do not remain constant - they change as a function of the time of electrolysis and the composition of the electrolyte. For this reason, the reading of the auxiliary electrode should be corrected from time to time.

If the plateau region in the I-V characteristics gives the best polishing conditions, it is important to look at the effect that process parameters have on the plateau. The four most important parameters are the electrolyte Temperature, Acid Concentration, Viscosity and Stirring. The temperature does not affect the plateau voltage range, but only the current density; the same holds for acid concentration, the plateau voltage remains unchanged, while the current density increases; the current density is inversely proportional to viscosity; while stirring increases almost linearly the current density.

3.3.2 *EP software*

At LNL a method for controlling the electropolishing process have been developed; this method has been used for all the electropolishing of cavities and samples described in this work.

The idea is trying to minimize parasitic problems as gas evolution, by searching the best working point of the I-V characteristic and by following it during the whole process. The method consists in computer monitoring the I-V characteristic. The process is driven in voltage.

An HP Instrument automatic program controls the Power System Supply HP 6032 (0-60V, 0-50A, 1000W) is used for monocell electropolishing (figure 3.6). The program displays the numeric derivative of I versus V. The working point is chosen as the minimum of such derivative, i.e. the minimum of bath differential conductance that corresponds to the point of maximum resistance of the viscous layer [69]. Computer control helps in finding this ideal working point and constantly tuning the process following the evolution of this point. Figure 3.7 displays the differential conductance compared to the ratio I-V and together with the I-V characteristic. The first minimum in differential conductance is due to edge effects and to the not uniform distance between electrodes. Some literature approximates the second minimum of dI/dV with the minimum of I/V. Already from fig. 3.7, it is visible that the two minima differ quite substantially in voltage. In any case that of an electrolytic cell is a nonlinear circuit, hence the solution conductivity is a differential

quantity while, the ratio I/V has no any physical sense in such a case. This method has been applied successfully for the electropolishing of materials such as Copper and Niobium.

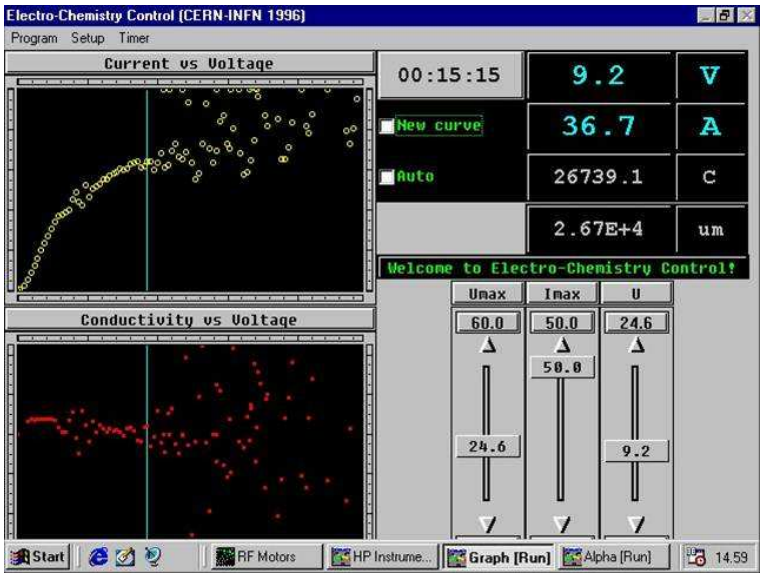

Figure 3.6: *Screenshot of the HP Instrument software for automated EP of monocell cavities.*

The I-V characteristic evolves with time and the current plateau evolves too, changing the working point. The reason for this is twofold: the leveling action decreases the roughness, but also the surface area decreases. Moreover in the hypotheses of an anodic passivating oxide film, the longer is the process, the more stable is the film, the weaker is the etching. By locking the minimum of the differential conductance, we could follow the plateau up to very low values of Copper dissolution rate. Hence the removal of large thicknesses cannot be obtained by simply increasing the process time. In addition all electropolishing experiments have shown that the voltage has to be adjusted carefully with changing temperature of the electrolytic bath. The bath is heated due to electrical power dissipation.

The Automatized Program for Electropolishing of 3-cell cavities is written in Labview® 7.1 RT instead 3.8. It can work in connection with the PC or stand alone into the physical memory of NI Field Point®. When the program works in connection with the computer, all the parameters can be changed during the process and the display refreshes the polarization curve [70]. The controlled power supply is Alintel mod. HCED125/80 (0-80V, 0-125A).

3.3.3 *EP apparatus*

The facility allows for the treatment of single cell cavities as well as TESLA 3-cell structures, and it is also possible to treat two cavities (one of copper and one of niobium) at the same time3.11. In fact, under the extractor fan, there are two completed circuits, one dedicated to the electropolishing and the chemical polishing of niobium cavities and the other one for copper cavities[71].

The power supply for monocell cavities is the Power System Supply HP 6032 (0-60V, 0-

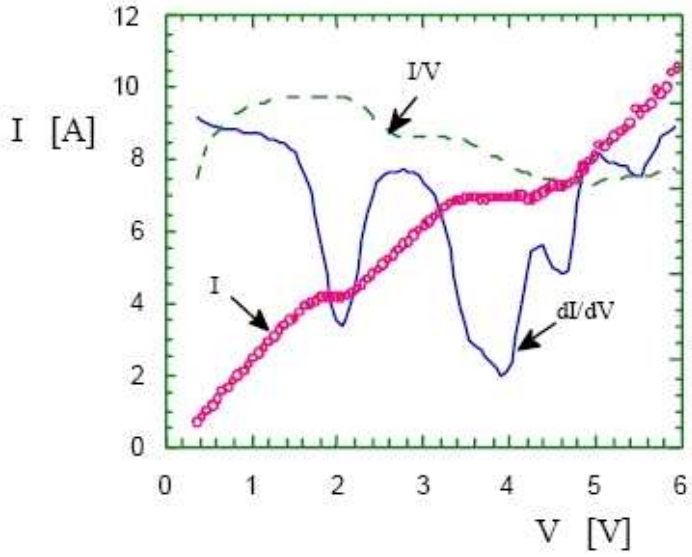

Figure 3.7: *I-V characteristic for a standard electropolishing process(circles), the differential conductivity dI/dV(continuous line) and the ratio I/V (shaded line) are displayed versus voltage*

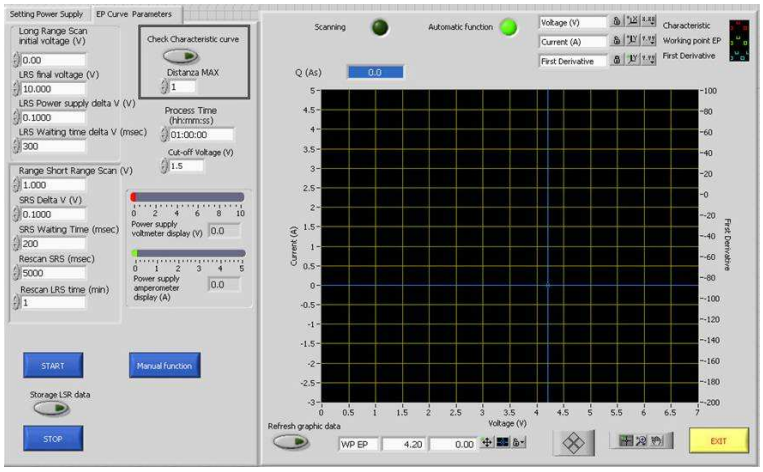

Figure 3.8: *Screenshot of the Labview® software for automated EP of monocell cavities.*

50A, 1000W) and it is controlled by the Visual Basic software. Cavities are polished in horizontal orientation and are filled with acid at a level of 65%. All rotating flanges and the fixed structure connected to the cavity are made of PVDF. The pump chosen is air powered, self priming, diaphragm pumps with a maximum capacity of 50 l/min at 6 bar made of PTFE. After the pump the acid flow through a filter (0,2 μm) The tubes, fittings and valves are industrial standard for pure fluid handling and made of PFA. To force the acid flow, the system is under pressure by a nitrogen flux visible in figure 3.9.
It has been observed that it is advantageous to inject the acid downwards in the individual cells, indeed acid flows inside the cathode and get into the cavity passing through its holes, positioned in correspondence of each cell. This helps also to obtain a better mixing of "fresh" and "older" acid in the cavity. The acid is then drained on both sides of the cavity into 1 inch pipes.
While the cathode is kept still, the outer part of the flanges rotates and so does the cavity. An electrical stepping motor controlled by a computer program provides the rotation. The operator can select the speed, the duration and the direction of the motion. In all EP processes, the cavity rotates at about 1rpm.

At the end of the process, the power supply and the membrane pump is stopped. The acid is removed from the cavity volume, by putting the cavity upright. The gravity and the nitrogen gas overpressure make the acids flow to the acid tank. When the cavity is empty, the cathode is removed from the upper flange and a water inlet is mounted instead of it. Thus, the cavity is rinsed until the pH of exiting water is neutral. Furthermore, the pump and the filter are emptied, and both are connected to the water line for rinsing. Due to the potential chemical hazard the whole EP system is mounted inside a fume hood, which also holds inside the exhaust acid tank and the nitric acid solution tank. In this way any acid droplets that may come out from the EP system is kept inside the hood. The acid vapor is sucked up through a couple of apertures, by using a 3000 lt/h ventilator. However, the operator must wear chemical resistant overalls along with a pair of PVDF gloves and a gas mask.

Cavity	Current (A)	Voltage (V)
1,5 GHz monocell Cu	17.7	2.81
1,3 GHz monocell Nb	50	4
1,3 GHz 3-cell Nb	71	10

Table 3.1: EP process starting parameters for all cavities studied in this work.

As concerning samples, experience teaches that just the surface to be treated should be exposed to the solution. For this reason every sample shape needs an appropriate cathode and a material resistant to acid should be adapted to screen the rest of the surface. In fact the cathode usually "feels" also the back side of samples and leave them all exposed to the solutions could mean doubling the metallic surface. Results are a wrong I-V curve and the erroneous choice of the the processing parameters. The metallic wire connecting the

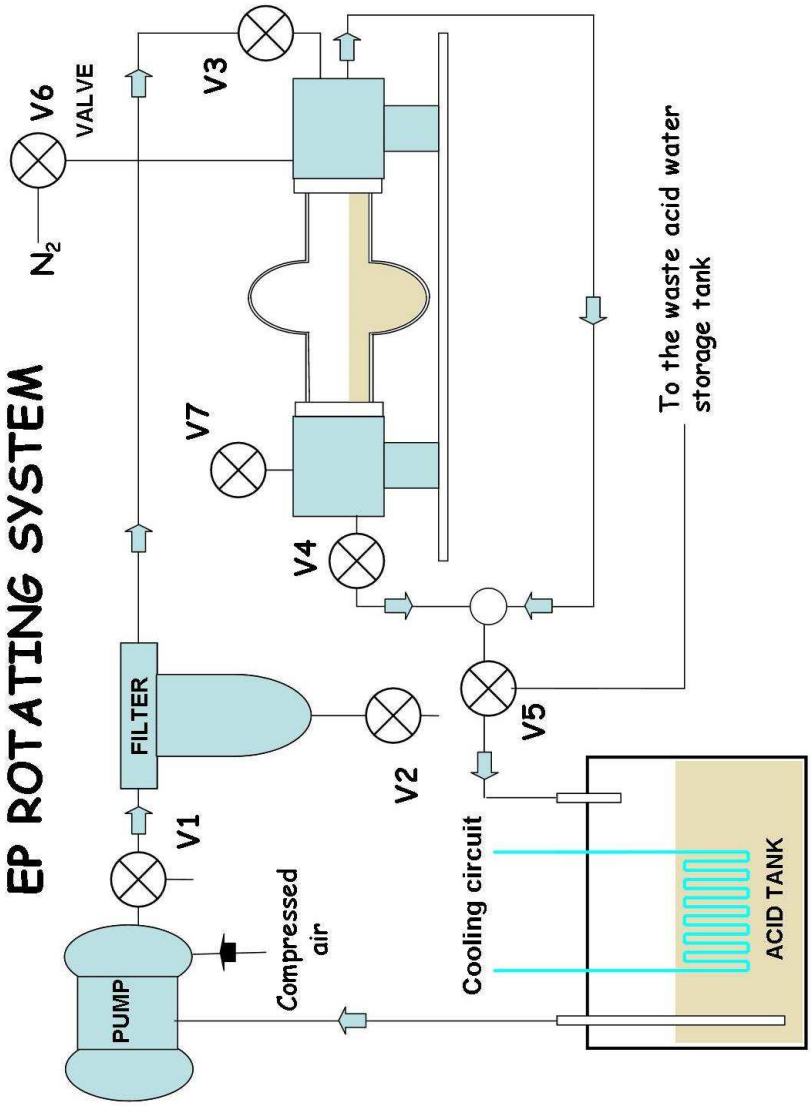

Figure 3.9: *Scheme of the horizontal EP apparatus for copper and niobium cavities*

sample to the power supply should be screened to, especially if its surface is not negligible respect to the sample one. In figure 3.10 there is a clear example of a sample not being screened on the back side.

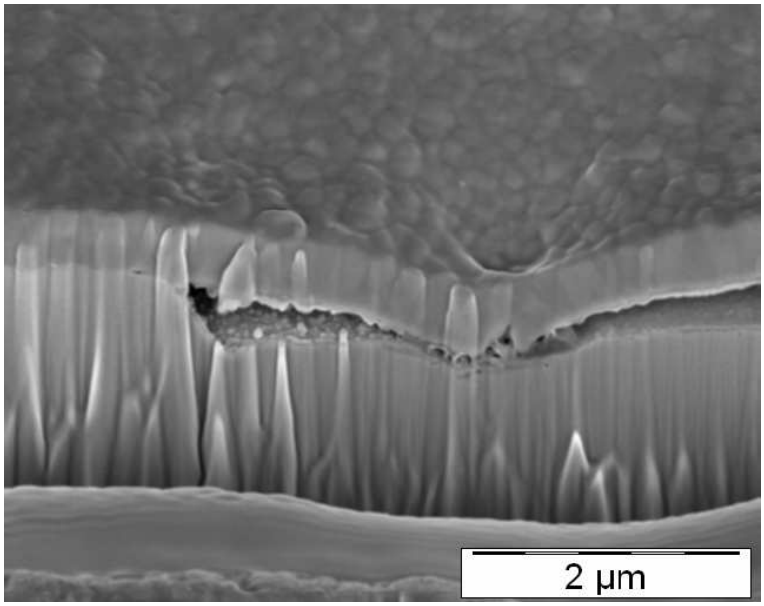

Figure 3.10: *Detail of a surface defect due to a wrong choice of EP parameters*

3.3.4 *Copper*

The cathode is OFHC copper with a purity of 99.9%, an outer diameter of 25 mm and a wall thickness of 1 mm. Samples and cavities described in this work have been treated with the standard electro-polishing in a Phosphoric acid (85%) and Buthanol (99%) mixture, in the ratio 3:2. The acid storage tank is made of PVDF and the doesn't need a water cooling circuit.

3.3.5 *Niobium*

The cathode is aluminium with a purity of 99.5%, an inner diameter of 30 mm and a wall thickness of 2 mm. For the 3-cell cavity its outer diameter is 22 mm and a wall thickness of 3 mm. The total length depend on the treated cavity. According to the electrochemical series aluminium is less noble than niobium which avoids the concentration of aluminium impurities on the niobium surface.

The niobium cavity has two electrical connections. The voltage decays over the cavity, due to the finite resistance of the niobium. Since the cavity is rotating during the process and connections are fixed, long cables are used, that can rotate with it.

We assume that 35°C is the maximum acceptable cavity temperature. Limitation of the temperature is necessary to reduce out-gassing of HF and to keep the working point stable. Temperature is monitored in different places by using a remote IR thermometer. A constant temperature distribution in the cavity is essential for an equal removal of the

Figure 3.11: *The double horizontal EP apparatus for copper and niobium cavities*

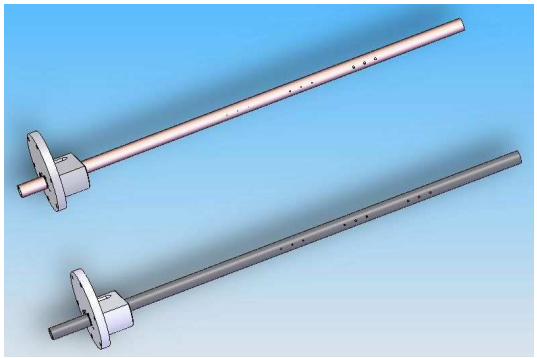

Figure 3.12: *Technical drawing of two cathodes for the EP of niobium and copper 3-call cavities.*

Niobium in the individual cells. To achieve that the acid storage tank, made of PVDF, is water cooled with a close circuit inserted in the acid tank and it is constantly stirred.

The acid is a mixture of sulphuric acid (98%) and hydrofluoric acid (40%) with a ratio of 9:1. The chosen working points are summarized in table 3.1.

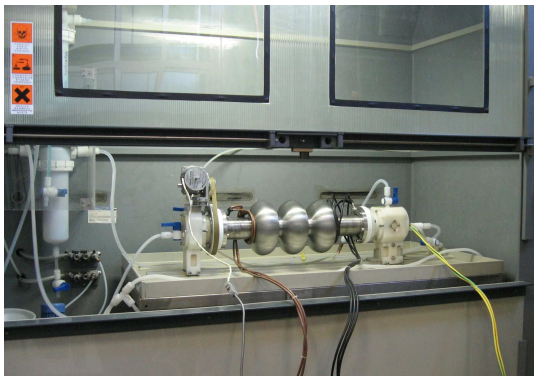

Figure 3.13: *Electropolishing of the 3-cell niobium cavity*

3.4 *Chemical Polishing*

Chemical polishing (CP) is easier and cheaper then electropolishing, so it is widely used in many laboratories, but it doesn't grant good performances at high gradients. The drawback of BCP as commonly applied is that it etches rather than polishes the surface. After heavy etching, BCP tends to etch preferentially at grain boundaries, leaving some crevices, which are difficult to rinse correctly and which enhance the surface roughness. Moreover, ortho-phosphoric acid is known to incorporate into the oxide layer in the form of POx (x∼2) ions [72], and is regularly found at the metal-oxide interface during chemical analysis [73, 74].

3.4.1 *Copper*

Prior to coating, the copper substrate is chemically polished in order to obtain a clean and smooth surface. For hydroformed cavities the removal of 40 μm is usually sufficient, whereas for spun cavities optical microscopy has indicated that at least 120 μm must be removed in order to eliminate the flaws generated by the spinning process. On electroformed cavities the initial polishing is of approximately 25 μm in order to remove the remnants of the chemical dissolution of the mandrel and the initial layer deposited under dc conditions without unduly affecting the smoothness of the surface [75]. The polishing agent (SUBU) is a mixture of sulfamic acid (5g/l), hydrogen peroxide (32%, 50ml/l), n-butanol(99%, 50ml/l) and ammonium citrate (1g/l) [76] and the working temperature is around 70°C. For subsequent coatings, after having stripped the preceding niobium film with a solution containing hydrofluoric acid and sodium benzoate, the removal of 10 to 20 μm of copper is usually sufficient. After SUBU the cavity is passivated with a diluite solution of of sulfamic

acid.

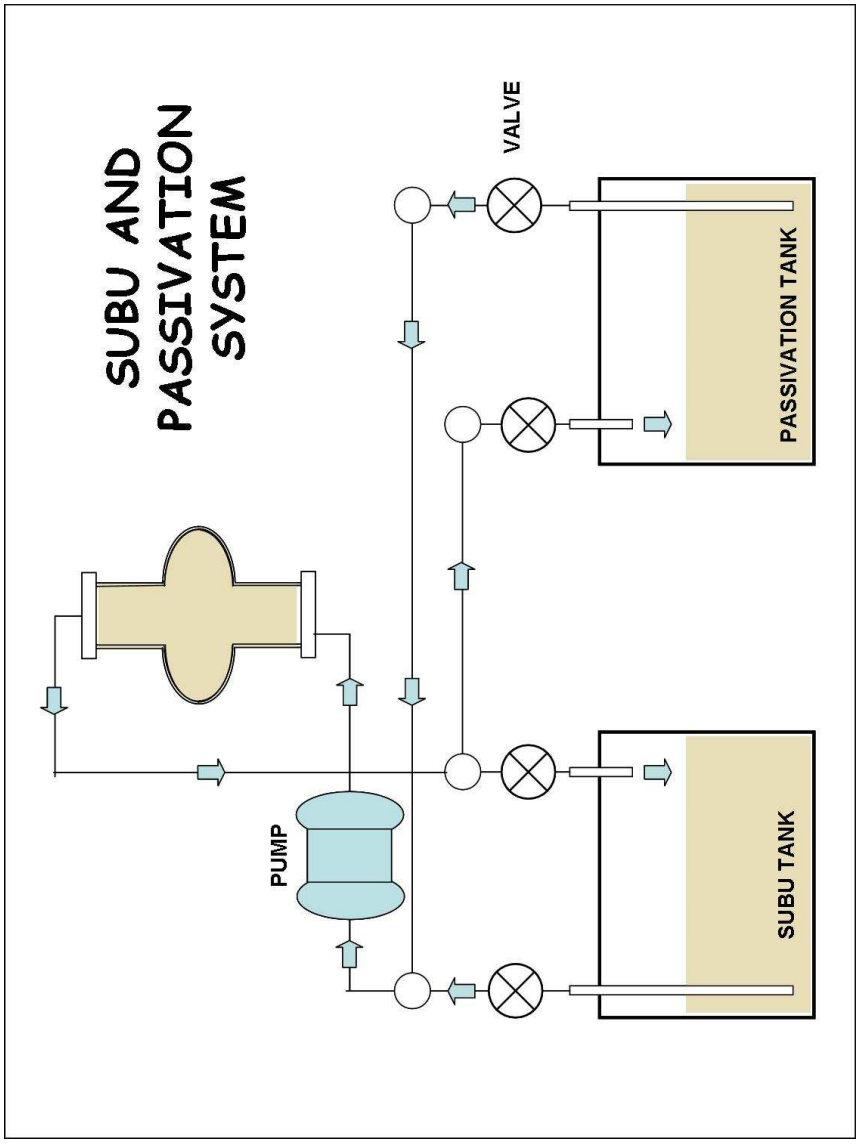

Figure 3.14: *Scheme of the vertical apparatus for the SUBU and passivation of copper cavities*

All copper samples analyzed during this work have been chemically etched after electropolishing; usually the etching time have been 10 minutes of SUBU and 10 minutes of passivation. In figure 3.15 the SUBU of 2 inches copper plate is shown and the energetic stirring is visible. During SUBU the solution should be energetically stirred in order to avoid the formation of a viscous layer on the substrate surface that reduce and finally blocks the etching.

3.4.2 *Niobium*

There are many "recipes" in the literature for etching niobium, see for example [77] or [78]. In all these mixtures we can find the same basic constituents:

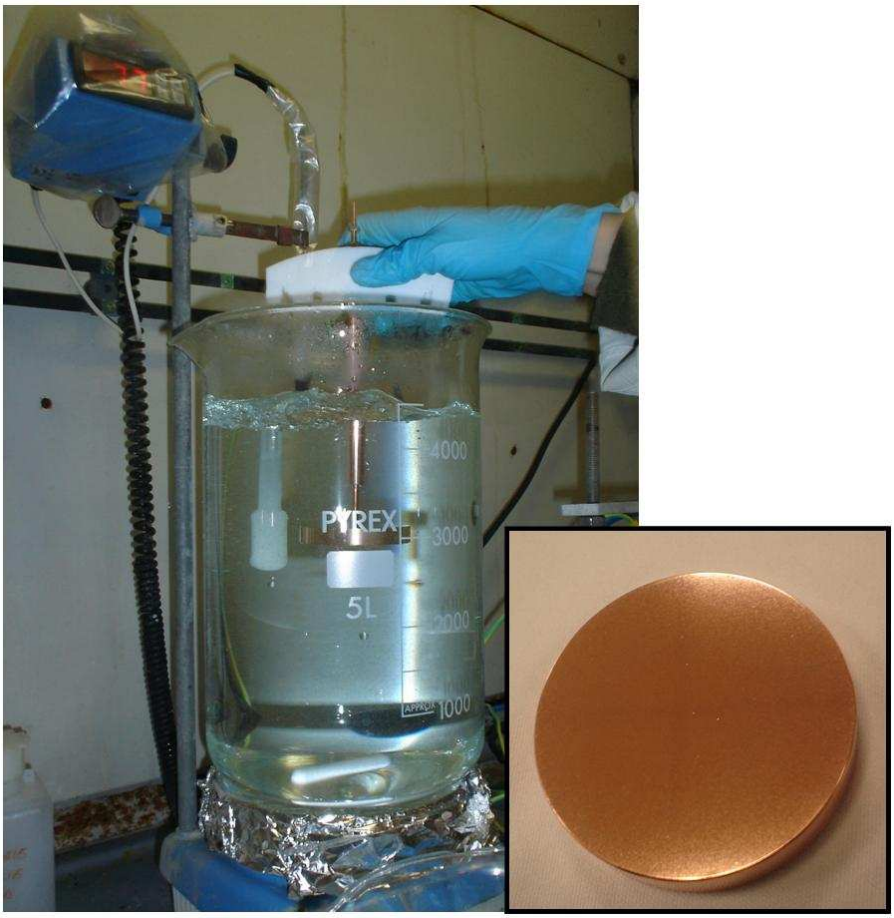

Figure 3.15: *During SUBU the solution should be energetically stirred in order to avoid the formation of a viscous layer that reduce and finally blocks the etching. The surface finishing after EP, SUBU and passivation is visible on the plate down to the right.*

- A niobium complexant, i.e. a chemical species that reacts with ions Nb^{5+} and forms a compound soluble in water.
- An oxidant, which reacts with metallic niobium Nb^0 and turns it into the oxidized form Nb^{5+}, which in its turn will be soluble.
- Additional compounds like buffer or brightening agents.

Note that in the case of electro-polishing, there is no need for an oxidant since a high potential (= oxidant) is already imposed on the niobium by the means of the electrodes and the solution. The drawback of BCP as commonly applied is that it etches rather than polishes the niobium surface, After heavy etching, BCP tends to etch preferentially at grain boundaries, leaving some crevices, which are difficult to rinse correctly and which enhance the surface roughness. Moreover, ortho-phosphoric acid is known to incorporate into the oxide layer in the form of POx (x∼2) ions [72], and is regularly found at the metal-oxide interface during chemical analysis [73, 74]. The Niobium chemical etchings, commonly called BCP 1:1:1 or BCP 1:1:2, are a mixture of Hydrofluoric, Nitric and Phosphoric acids, respectively in the ratio 1:1:1 or in the ratio 1:1:2. Nitric acid plays the role to oxide the Niobium surface. Hydrofluoric acid reduces the Niobium Pentaoxide into a salt that is soluble in water. Phosphoric acid acts as a moderator for the chemical reaction giving rises to a less turbulent and more controllable reaction. That's why often 1:1:2 is preferred to 1:1:1 for treating cavities. The main reaction happening at the Niobium surface is:

$$6\ Nb + 10\ HNO_3 = 3\ Nb_2O_5 + 10\ NO + 5H_2O$$

and

$$Nb_2O_5 + 10\ HF = 2\ NbF_5 + 5\ H_2O$$

then

$$3Nb + 5\ HNO_3 + 15\ HF = 3\ NbF_5 + 5\ NO + 10\ H_2O$$

Other baths were also developed in order to change the chemical environment where the oxide layer starts to grow.

The study proposed by Antoine et al. [79] investigates the possibility to substitute phosphoric acid with sulphuric acid. The Niobium oxidation takes place as well, while in addition sulphuric acid has a brightening action. In addition it presents a well characterization of the surface morphology at different scales: roughness seems a second order factor as the recrystallization brings a lot of change to the niobium surface while it is does not change the Q- slope (even if the quench field is improved). Cavities with very different surface aspects due to their previous "history" exhibit the same type of Q variation, providing an indication that the overall surface roughness does not play a noticeable role. The oxide thickness and its sensitivity to air exposure produced the only noticeable difference that could be observed on samples. Another aspect also explored is the apparent "memory" effect. Indeed, evidence can be found in literature that, depending on the electrochemical media, impurities are likely to dissolve much more slowly than the metal because of the ionic field assisted diffusion mechanism of the latter.

The ternary diagram of figure 3.16 have been built by Palmieri at al. [69] by measuring

the Niobium etching rate versus different percentages of Hydrofluoric, Nitric and Phosphoric acids. The same etching rate of the 1:1:1 mixture can be obtained by decreasing the nitric percentage vs the hydrofluoric content if we increased the phosphoric percentage or vice versa. In other words, the reduction effect of Hydrofluoric acid is so high that a little fraction of the oxidant agent (Nitric) is needed in order to solute Niobium; more Phosphoric in this case is needed for smoothing the reaction. The numbered lines inside the triangle are the curves of equal etching rate (removed micron per minute) in the three-dimensional space determined by the three acids. The dot serials instead correspond to points obtained by varying the phosphoric percentage leaving unchanged the hydrofluoric-nitric ratios.

The same work propose alternative recipes for Niobium chemical etching: among the

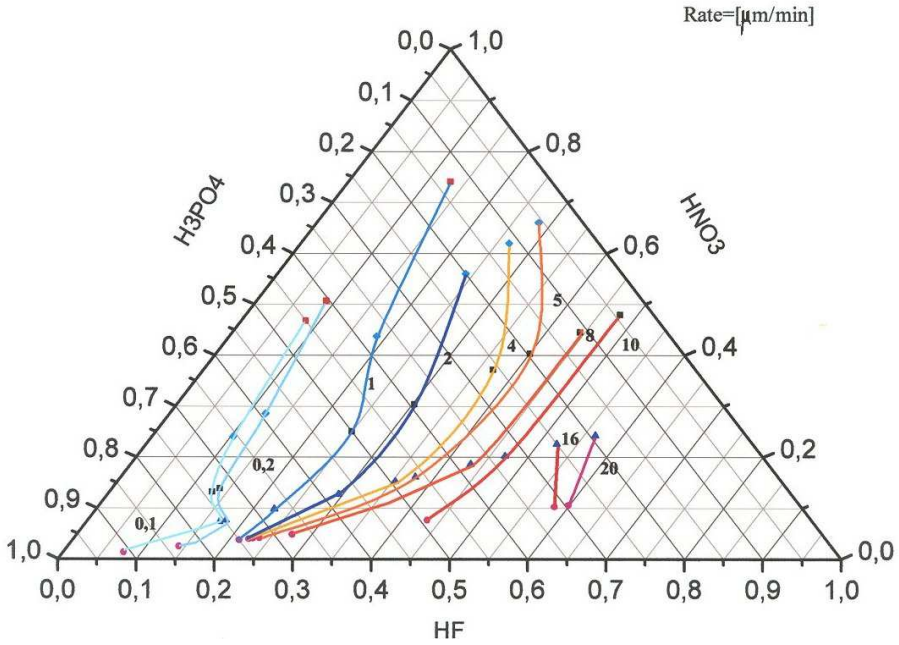

Figure 3.16: *Curves of equal etching rate in the three-dimensional space of BCP. The number reported close to each curve corresponds to the etching rate (removed micron per minute) [69].*

several recipes, best results were found at room temperature by the following mixtures:

$$NH_4F + HCl + H_2O_2 + H_3PO_4$$

in the ratio 2:2:4:1 with (60g/lt) of NH_4F. Ammonium fluoride does not bring into the solution the same amount of Fluorine ions than Hydrofluoric acid, so Hydrochloric acid is added since Niobium Oxy-chloride is both stable and soluble in water too. It is possible to get rid of Hydrochloric acid by increasing the concentration of NH_4F, even up to 700 g/lt. The etching rate in this way can be modulated up to 1 μm/min, giving rise to a brilliant surface.

Niobium cavities are chemically etched in the same system used for electropolishing,but using different pipes and by-passing the filters after the pump. As listed in section 3.1.2

the 3-cell cavity has been treated with the 1:1:2 solution using Hydrofluoric (40%), Nitric (65%) and Phosphoric acids (85%) .

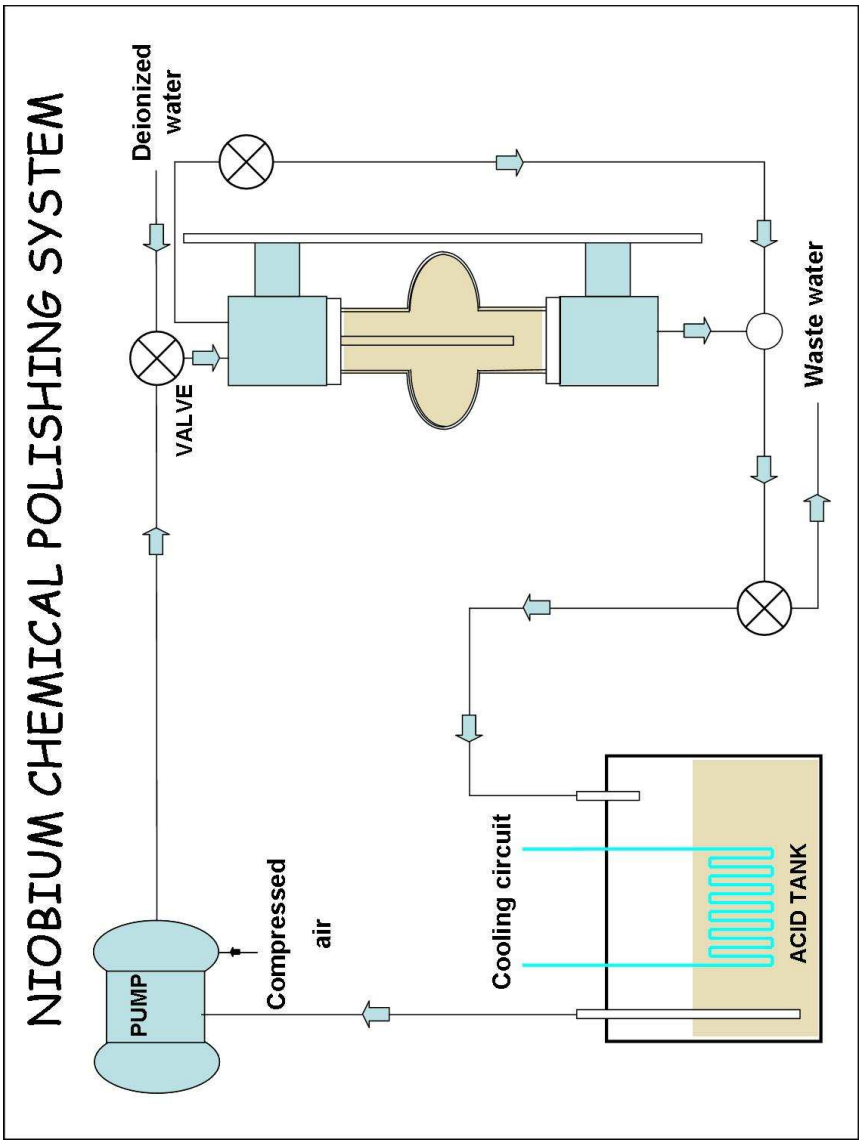

Figure 3.17: *Scheme of the vertical CP apparatus for niobium cavities.*

3.5 *Heat treatment*

Presently, the cavities are rinsed with clean water after the 800°C treatment and then immediately transferred to another UHV oven in which they are heated to 1350−1400°C [61]. To capture the oxygen coming out of the niobium and to prevent oxidation by the residual gas in the oven (pressure < 10.7mbar) a thin titanium layer is evaporated on the inner and outer cavity surface, Ti being a stronger getter than Nb. The high-temperature treatment with Ti getter is often called post-purification.

At these temperatures the interstitial impurity atoms are quite mobile. When they

arrive at the surface they sink into the foreign metal coating. Both coating and purification operations can be combined into one step because, at the diffusion temperature, the vapour pressure of the getter metal is also high enough to evaporate the necessary layer. The high-temperature treatment removes nearly all of the dominant oxygen impurity.

Since, at 1350 °C, titanium diffuses into niobium to a substantial depth (100 μm) along the grain boundaries, heavy chemical etching becomes necessary after the post-purification step. The titanium layer is removed by a 80 μm BCP of the inner surface. A BCP of about 50 μm is applied at the outer surface since the thermal interface resistance ("Kapitza resistance") of titanium-coated niobium immersed in superfluid helium is about a factor of 2 larger than that of pure niobium [80]. Commercial niobium of RRR = 250-300 has been improved to RRR = 500-700. Since the vapour pressure of titanium is lower than that of yttrium, higher temperatures or longer times are needed with titanium. However, titanium does have the intrinsic capability to remove nitrogen and carbon by solid state gettering because of its appreciable affinity for these impurities. Since the diffusion rates of nitrogen and carbon are much lower than the rate of oxygen, very long gettering times are necessary. Using titanium for more than 50 h, an RRR of 1000 was achieved in samples of starting RRR = 200 [81].

Regarding copper cavities, the substrate temperature is one of the most interesting parameters during the argon discharge sputtering process. There is a focused description of temperature effects on cavity sputtering at CERN, Geneva [82]. An optimum range for the sputtering temperature is at 150°C-175°C for better Rs. There is no other information like the film morphology available for further discussion. In [57], the Orlandi group has reported that sputtering on substrate temperature of 550°C leads to a quite large grain size, 0.2μm, and a RRR of 35. From the report, we also know the deposition rate was higher than the lower temperature case [57].

3.6 *High Pressure Water Rinsing*

The High Pressure Water Rinsing is commonly used as final step to get rid off dust particles from the cavity's surface. This technique [83] has already shown its fundamental importance to reach high accelerating gradient without Field Emission. Therefore, a system for high pressure water rinsing has been built and tested at Legnaro [71]. In figures refUgello HPWRUno2 and 3.21 the technical drawing and a picture of the HPWR cap used at Legnaro is shown, mounted at the end of the moving bar. On the cap there are two spray nozzles from which water comes out at high pressure (100 Bar max).

The cap rotates along the moving bar vertical axis. Thus the two spray nozzles located on both side of the cap move so that they can rinse the whole inner surface of the cavity. Moreover, while the cap is rotating, a mechanism moves the bar along a vertical path to allow the water jets to scan the entire cavity's surface. The vertical motion is repeated

Figure 3.18: *The 3-cell niobium cavity in the titanium box, waiting for the high temperature baking.*

many times, changing its direction when the cap is close to one end of the cavity. The system is designed for 1.3 GHz 9-cells TESLA-type cavity [84] and it can rinse cavity with a total length of 1256 mm. The minimum beam pipe's aperture diameter should be at least 50 mm.

The Visual Basic computer program allows to control the vertical position and the speed of the head very precisely. In fact, the electrical motor is equipped with a double channel encoder for measuring the rate and the number of steps the shaft makes. And therefore the computer program gives the possibility also to rinse cavity with a particular sequence.

A 0.1 μm particle filter, which is located close to the motion system, (working pressure 100 Bar) makes sure that the ultra pure water is free of dust. The cavity at the upper end is closed by a flange, whereas at the bottom is mounted on a flange. A flow of filtered nitrogen creates a little overpressure inside the cavity to help the water to exit from the four outlets at the bottom. Typically the rinsing lasts a couple of hours; after that the cavity is disconnected from the system and brought in a 100 class clean room for the assembly of the RF antennas and pumping line.

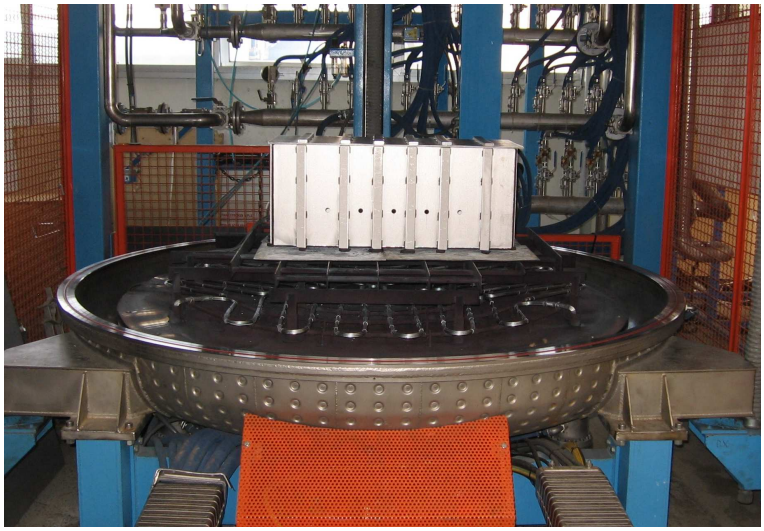

Figure 3.19: *The ultra high vacuum oven for cavity baking in LNL site.*

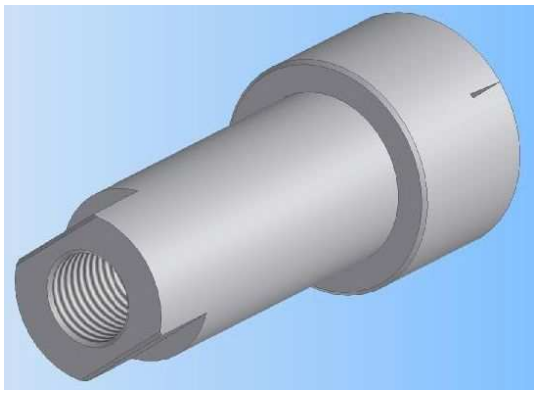

Figure 3.20: *Technical 3D drawing of the HPWR cap.*

3.7 *Ultrasonic cleaning*

Ultrasonics is the application of mechanical sound waves to the cleaning process. This technique utilizes a digital generator powering transducers submerged in a tank of hot water. The piezo electric transducers vibrate at a frequency of 40 KHz creating millions of tiny bubbles that form and implode. This repeated formation and implosion creates a gentle cleaning action known as Cavitation. Cavitation has the ability to not only clean the surfaces of items, but also penetrate into the difficult to clean internal and crevice areas. Millions of tiny bubbles implode within the solution and penetrate into every orifice of the item being cleaned, removing dirt and grime within seconds. It is safe and gentle. Ultrasonics will not scratch, pit or damage items the way that conventional cleaning methods can.

Ultrasound is used widely throughout industry for removing contamination problems from all forms of hard surfaces, such as metals, plastics and ceramics. Its unique properties can be harnessed to clean items of all shapes, sizes and technical complexity, penetrating

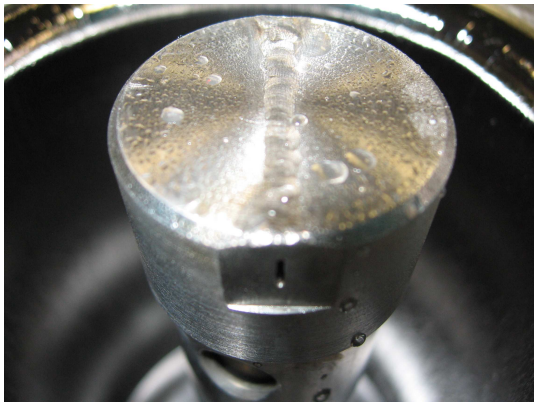

Figure 3.21: *Picture of the HPWR cap rotating inside the cavity. It goes up and down ejecting water at 100 bar.*

holes and cavities that are impossible to reach using ordinary cleaning methods.

In an ultrasonic cleaner, the object to be cleaned is placed in a chamber containing a suitable ultrasound conducting fluid (an aqueous or organic solvent, depending on the application). In Aqueous cleaners, the chemical added is a surfactant which breaks down the surface tension of the water base. An ultrasound generating transducer is built into the chamber, or may be lowered into the fluid. It is electronically activated to produce ultrasonic waves in the fluid. The main mechanism of cleaning action is by energy released from the creation and collapse of microscopic cavitation bubbles, which break up and lift off dirt and contaminants from the surface to be cleaned. The higher the frequency, the smaller the nodes between the cavitation points which allows for more precise cleaning. The bubbles created can be as hot as 10,000 degrees and 50,000 lbs per square inch, but are so small that cleaning and removal of dirt is the main result.

Figure 3.22: *Picture of the 3-cell spinned niobium cavity monted on the HPWR system.*

Chapter 4

Microstructural analysis

4.1 *Surface Morphology and Coatings Microstructure*

Thickness measurements were performed using a Dektak® 8 Advanced Development Profiler Veeco. The profiler scans the surface with a constant load fixed at 10 mg. Six different scans, 2 mm long, has been executed for each sample in three different positions near the area where the quartz substrate is exposed. Here each step from niobium to quartz gives the film thickness. The average of the six measurements is considered as the film thickness and the root mean square as its error.

In-plane morphological characterisation of coatings were performed using Atomic Force (AFM) and Scanning Electron Microscopy (SEM) techniques. Surface roughness measurement was also carried out by Contact-Mode AFM analysis: roughness parameters (Roughness Average, Ra, Root Mean Square, RMS, Peak to Peak) were obtained after statistical analysis on a total scanned area of about 750 μm^2.

Cross-section coating investigations (coating thickness, microstructure and crystallite size measurements, surface and layer interface analyses) was investigated by using Focused Ion Beam (FIB) techniques: FIB systems [Lucille A. Giannuzzi, Fred A. Stenie, Introduction to Focused Ion Beams - Instrumentation,Theory, Techniques and Practice, Springer editor.] utilize a finely focused beam of gallium ions (Ga+) operating at low beam currents for imaging and at high beam currents for site-specific milling. By controlling the location, beam size and current density of the ion beam, material can be selectively removed from sub-micron areas. Most apparatus nowadays available in the market also contains in situ scanning electron microscopy (SEM) capabilities for real time imaging of the ion milling site and even 3D tomography. The capability of high-resolution imaging using both secondary electron and secondary ion signals has made the FIB microscope a unique imaging tool. Stress-free cross sectioning using the primary gallium ion beam provides valuable microstructure information beneath the specimen surface. FIB techniques can be also used for TEM specimen preparation: a finished electron transparent portion of the sample (usually 5 ìm x 20 ìm) is obtained by FIB micro-milling and then placed by a micromanipulator on a sample holder to be inserted into the TEM microscope: this proce-

dure at present represents the one site-specific and artefact-less outstanding TEM sample preparation techniques.

While FIB techniques therefore appear to be an ideal tool for microstructural investigations of thin films, such as superconducting Nb coatings, they have so far been used for microstructural investigations of sputtered Nb thin films only rarely [7]. One example of FIB applications is the study to reveal the difference in the structure of "standard" polycrystalline Nb films grown on oxidized copper surface and epitaxially grown ones deposited on oxide-free copper [7].

In the present study, SEM microstructural investigations have been performed after FIB sectioning, while interfaces structure and microstructure and thickness of the surface oxide layer have been investigated by TEM after FIB sample preparation.

4.2 *Coatings Intrinsic Hardness and Elastic properties evaluation*

Composite Hardness measurements were performed using Vickers standard indentation tests, with loads ranging from 100g (1N) down to 0,5g (0,005N). The obtained value for each load corresponds to the mean of six measures.

In case of soft coatings on hard substrate (which is the case of Nb on Quartz), the application of models for intrinsic hardness evaluation is not straightforward [85]: for this reason and considering previous results available in literature [86, 87, 88], the Korsunsky [89] model has been applied for coatings' intrinsic hardness and hardening coefficient evaluation after composite hardness measurements: previous experimental works [85] have observed how this model, based on a energetic approach, can be much more reliable in fitting experimental data than other models [86, 87], in case of soft-on-hard configuration. The same model was applied to Nb coatings on OFHC Cu substrate, in order to have consistent and comparable data for intrinsic hardness of coatings.

AFM analysis of the residual indentation marks shape was also performed in order to have more reliable data for low-load ($<$ 10 gf) indentations. Work hardening behaviour was taken into account as well, by adopting the Indentation Size Effect (ISE) Meyer's law [88], which describes the relation between load and size of indentation:

$$P = k \cdot d^n \tag{4.1}$$

Where P is the applied load, d is the indentation size, k and n are constants. Eq. 4.3 can be rewritten as a function of Vickers hardness:

$$HV = HV\Delta d^{n-2} \tag{4.2}$$

Coefficient n is known as Meyer's or hardening index, generally lower than 2,0 for pyramidal indenters [86].

Surface mechanical properties (intrinsic hardness, elastic modulus, surface oxide layer

properties) were analysed by means of nano-indentation testing [90]: 5 tests (MTS XP-Nanoindenter equipped with Continuous Stiffness Measurement) were performed for each coating adopting the following test parameters: Berkovich indenter (calibrated on Silica reference sample), 100 nm maximum penetration depth, 0,05 s-1 constant strain rate, 10 s hold at peak load for creep, 20 s hold at 90% for thermal drift correction, allowable drift rate 0,05 nm/s. Oliver and Pharr method [90] was adopted for hardness and elastic modulus evaluation.

It has to be underlined that elastic properties of coatings are always strongly microstructure dependent [91], being elastic response correlated to columnar grain dimension and orientation, film density, pores, micro-cracks, residual stress. For these reason calculated values have to be considered as an estimation of the Elastic response of the coatings. In the case of MS-PVD Nb coatings for superconducting application, the evaluation of coating Elastic properties is performed with the main aim of describing the correlation between coating Elastic properties, microstructural aspects (such as density and grain dimension) and coating functional properties.

4.3 *Superconducting Properties*

RF measurements to evaluate the quality factor of accelerating cavities coated with thin films are complex and they need a well calibrated RF and cryogenic apparatus. Preliminary studies on samples are needed to understand if the modified coating technique is valid and if it introduces significant changes of the film quality [92].

The Residual Resistivity Ratio β and the transition temperature Tc of sputtered films on insulating quartz is measured with the four point method to eliminate the effect of possible contact resistance at the contact point between niobium films and the pins of the measuring device. A Visual Basic program has been written to acquire the resistance curve from 300 K to the transition temperature. Applying to the sample a current of 10mA the voltage is measured. The same method is used for the temperature probe, applying a direct current of 10mA the resistance is measured and the temperature is obtain from the calibration curve.

The low temperature resistance of the sample is fixed at 10K and the RRR calculated with the following formula:

$$\beta = \frac{R(300K)}{R(10K)} = 1 + \frac{R_{ph}(300K)}{R_{res}} = 1 + \frac{\rho_{ph}(300K)}{\rho_{res}} \tag{4.3}$$

ρ_{ph}(T) is the resistivity due to the electrons-phonons collision, decreasing with the temperature; ρ_{res} is the residual resistivity and it doesn't depend on the temperature. ρ_{ph}(300K) is 15 $\mu\Omega$·cm and it is a constant while the phononic resistance at 10 K is negligible. RRR is an immediate estimate of the film quality: the higher is the value, the more pure is the material. In addition it's an adimensional parameter that doesn't care of the geometric dimensions that stay constant with the temperature so they get eliminated in the ratio.
The transition temperature Tc $\pm\Delta$Tc is calculated from the resistance curve with the

following formula

$$Tc = \frac{T_{(90\%)} + T_{(10\%)}}{2} \qquad \Delta Tc = T_{(90\%)} - T_{(10\%)} \tag{4.4}$$

T(90%) is the temperature corresponding to the 90% of the resistance before the transition; T(10%) is the temperature corresponding to the 30% of the resistance before the transition. ΔTc is the error on the critical temperature estimation.

Chapter 5

Radiofrequency test system

In this chapter all information about the developed rf test system are exposed. After a summary of the rf measurement theory, all structure is describe in details, from the hardware to all softwares specially conceived for the system set up. Then the rf test need of a well functioning cryogenic apparatus and a constant monitoring of all important parameters like pressures, temperature and possible radiation emissions. In the end three rf measure on a 3-cell 1.3 GHz tesla-type cavity have been completed to test the whole apparatus and procedure step by step. This chapter is entirely written in collaboration with Silvia Deambrosis.

5.1 *Fundamental equations for rf test*

During the rf tests on cold cavities the basic rf properties such as maximum accelerating gradient, field emission onset, and quality factor Q_0, as a function of gradient are determined. These tests are done in test cryostats where the cavities are held vertically. Ideally, these tests are done at or near critical coupling. In this way the rf source requirements are only a few hundred watts, which is just enough power to overcome the wall and field emission losses. The critical variable for calculating the rf parameters of a superconducting cavity is the shunt impedance, which relates the stored energy to the effective accelerating gradient, peak electric field, and peak magnetic field for any given mode. In our case is determined using the electromagnetic simulation tool Superfish and all important parameters determined for 1.5 and 1.3 GHz cavities are collected in table 5.1.

When a cavity mode oscillates with a resonant frequency ω, a stored energy U and rf losses on the cavity walls, P_{diss}, the quality factor can be defined as:

$$Q_0 = \frac{\omega U}{P_{diss}} \tag{5.1}$$

Q_0 is roughly, 2π times the ratio of the stored energy and the energy consumed in one period. In the frequency domain the Q_0can also be expressed as

Symbol	Variable name	Units
r/q	Geometric shunt impedance	Ω/m
G	Geometry factor	Ω
E	Electric field	V/m
L	Electrical lenght	m
ω_0	cavity frequency	s^{-1}
U	Stored energy name	J
R_s	Surface resistance	Ω
Tc	Critical temperature	K
P_{emit}	Emitted power	W
R	Shunt impedance	Ω
T	Operational temperature	K
R_{res}	Residual surface resistance	Ω
Q_0	Intrinsic quality factor	Units
Q_{cpl}	Fundamental Power coupler coupling factor	Units
Q_{pk}	Field probe coupling factor	Units
R_C	Coupling impedance	Ω/m
P_{diss}	Dissipated power	W
τ	Decay time	s
r	Shunt impedance per unit length	Ω/m

Table 5.1: Common variables when discussing rf cavities [93].

$$Q_0 = \frac{\omega}{\Delta\omega} \tag{5.2}$$

where $\Delta\omega$ is the 3-dB band. Unfortunately, the direct measurement of the 3-dB band of a superconducting cavity is practically impossible, because it can attain very small values (some Hz or fractions of Hz), in any case much less that the resolution of a network or spectrum analyzer. For this reason, a time domain method must be used.

The cavity receives the rf power via an input cable and a short input antenna (coupler) from a power amplifier driven by a signal generator which is locked, as explained in the following chapters, exactly onto the resonant frequency of the cavity mode.

The transmitted power is extracted from the cavity by the output antenna (pickup probe).

All antennas are connected to calibrated power meters and it is possible to calculate the total power lost P_L with the following power balance:

$$P_L = P_d + P_{cpl} + P_{pk} \qquad P_{cpl} = P_i - P_{ref} \tag{5.3}$$

where P_d is the power dissipated in the cavity walls, P_i is the incident power, P_{ref} is the reflected power and P_{pk} is the transmitted power.
In this condition the so called "Q loaded" is introduced because it takes into account the resonant circuit behaviour when it is coupled with an external line:

$$Q_L = \frac{\omega U}{P_L} \tag{5.4}$$

Introducing the quality factor for each dissipated power:

$$Q_0 = \frac{\omega U}{P_d} \qquad Q_{cpl} = \frac{\omega U}{P_{cpl}} \qquad Q_{pk} = \frac{\omega U}{P_{pk}} \tag{5.5}$$

Those Q values are proportional to the number of cycles the system needs to dissipate all the energy on the considered transmission line. It's also important to understand if the dissipated power in the couplers is higher or lower that the power dissipated on the cavity walls.
It follows that:

$$\frac{1}{Q_L} = \frac{1}{Q_0} + \frac{1}{Q_{cpl}} + \frac{1}{Q_{pk}} \tag{5.6}$$

Each transmission line has its own external coupling factor β defined by:

$$\beta_x = \frac{Q_0}{Q_x} = \frac{P_d}{P_x} \qquad (x = cpl, pk) \tag{5.7}$$

The transmission antenna should be sized in order to avoid perturbation of the cavity operation, this condition is reached when $\beta_{pk} \ll 1$; in this way the antenna pickup the bare minimum energy requested for the measure. Moreover its position respect to the coupler antenna is far enough to avoid the signal transmission without resonance inside the cavity

(cross-talking). On the other side, to be able to transfer all the input power to the cavity, the coupler should satisfy the condition $\beta_{cpl}= 1$. That conditions assure a perfect match of the system and the cavity electrical impedances (coupling). In fact when $\beta_{cpl}= 1$ the input power equals the power dissipated in the cavity:

$$P_d = P_i - P_{ref} \tag{5.8}$$

Impedance matching is essential otherwise a mismatch causes power to be reflected back to the source from the boundary between the high impedance and the low impedance. The reflection creates a standing wave, which leads to further power waste. As described in the following chapter, the impedance matching device is the antenna tuner. β doesn't vary with temperature so the matching at room temperature is still valid for liquid helium temperature.

When switching off the power supply, the cavity enters into a state of free decay, loosing energy due to dissipation on the power flowing through the input and the output antennas. During a free decay, the power lost corresponds to the variation with time of the stored energy, thus:

$$\frac{dU}{dt} = -P_L = -\frac{\omega U}{Q_L} \tag{5.9}$$

the solution (assuming that Q_L is independent of U) is an exponential decay, with

$$U = U(0) \cdot e^{-\frac{t}{\tau}} \qquad \tau = \frac{Q_L}{\omega} \tag{5.10}$$

The decay time constant τ is experimentally measured and it is used to calculate a value fore the loaded-Q, Q_L. Then Q_L, P_i, P_{ref}, P_{pk} are used to calculate Q_0 In fact when the cavity is critically coupled:

$$Q_0 = (1 + \beta_{cpl} + \beta_{pk})Q_L = 2Q_L = 2\omega\tau \tag{5.11}$$

$$Q_{pk}\frac{2\omega\tau(P_i - P_{ref}}{P_{pk}} \tag{5.12}$$

In summary, measuring P_i, P_{ref}, P_{pk} and τ consent to derive Q_L and Q_{pk}. Next step is increasing the power P_{cpl} in order to raise the energy value U. The Q_0 and E values, then can be derived from the only measure of P_i, P_{ref}, P_{pk} because Q_{pk} is constant:

$$Q_0 = \frac{Q_{pk}P_{pk}}{P_i - P_{ref}} \tag{5.13}$$

The gradient may then be calculated as:

$$E = \sqrt{P_d Q_0 \frac{r/Q}{L}} \tag{5.14}$$

Parameter		Tesla-type cavity	
		1.5 GHz	1.3 GHz
ω	frequency (Hz)	$9.425 \cdot 10^{-9}$	$8.168 \cdot 10^{-9}$
r/q	Geometric shunt impedance (Ω/m)	82.7	82.7
L	Electrical length (m)	0.1	0.1154
G	Geometry factor (Ω)	287	287

Table 5.2: *Important parameters when calculating the cavity excitation curve. In this work bothy mono-cell 1.5 GHz and 3-cell 1.3 GHz have been tested.*

5.2 *RF system*

The Q measurement and rf processing of superconducting resonator can take advantage of computer-controlled procedures, which control the devices, collect data and assist the operator during the measurements [94]. The procedures are similar for different resonators operating in a wide range of frequencies.

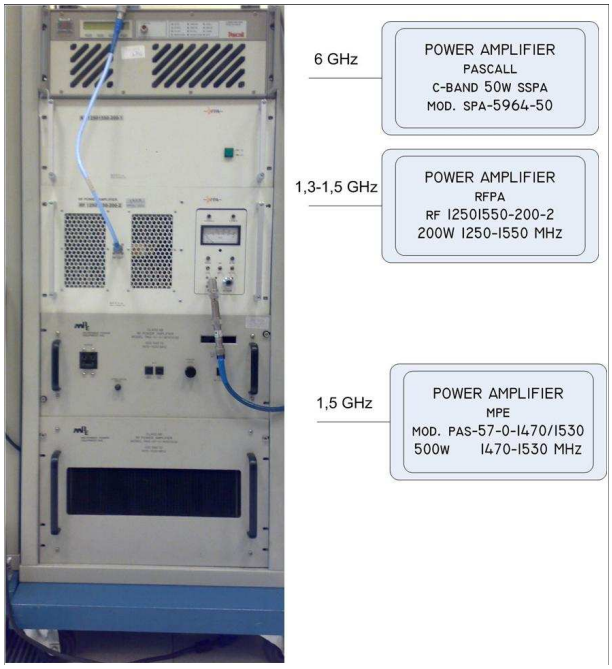

Figure 5.1: *The power amplifiers available in the Superconductivity Laboratory at LNL-INFN.*

Also most of the costly part of the equipment can be shared, the only things that differ being elements that have a small frequency range [95, 96]. The general structure of the measurement apparatus is presented in figure 5.2. The computer is interfaced with the signal generator (HP 83620A), power meter (HP 437 B), peak power analyzer (HP 8991A) and frequency counter (hp, 5350B) via IEEE 488 bus. A dedicated computer board allows the acquisition of analog and digital inputs and the setting of digital and analog outputs.

The rf generator signal is divided into three paths (figure 5.3). One goes through the

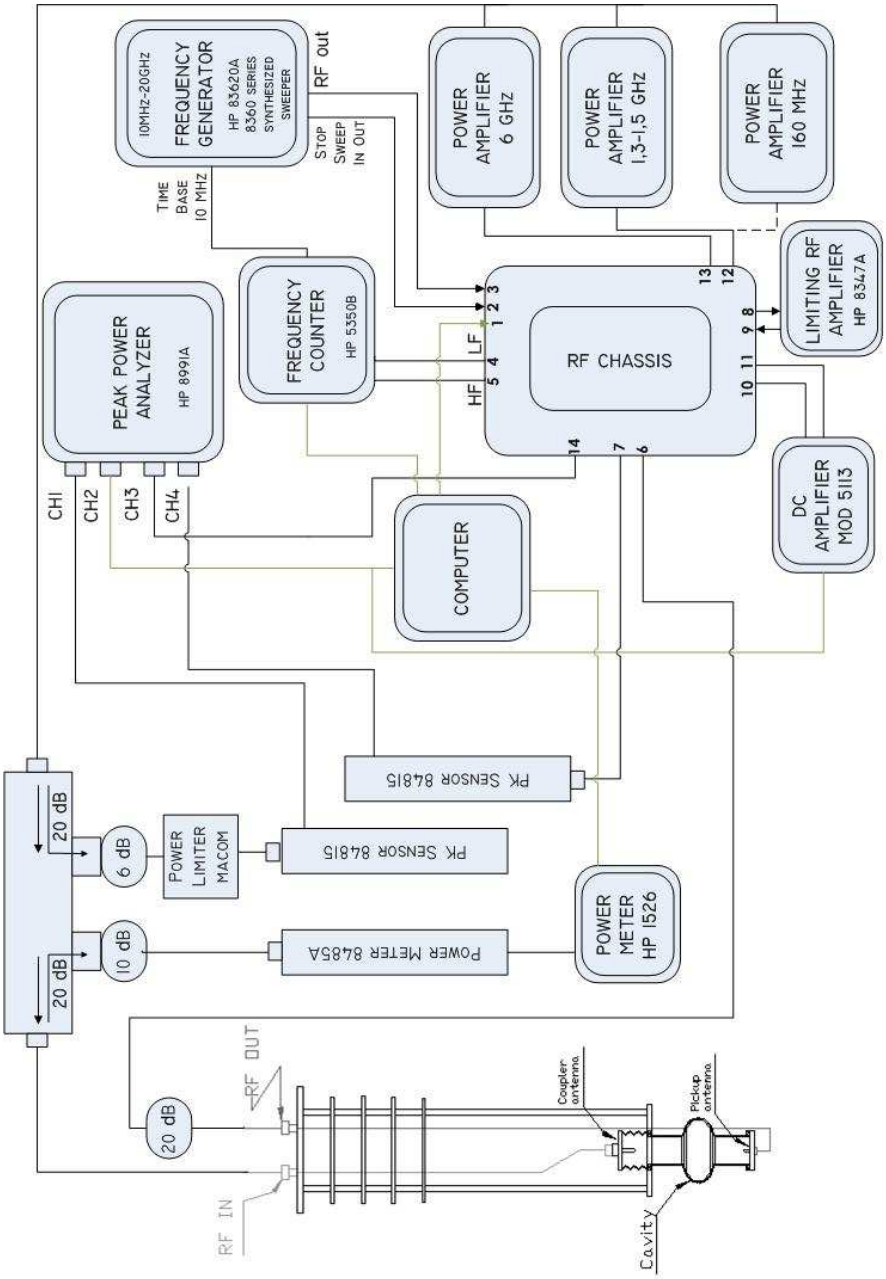

Figure 5.2: *A schematic of the rf test apparatus.*

programmable phase shifter to feed the LO mixer input.This line is attenuated to give always nominal +7 dBm at the mixer input. A second line goes to the frequency counter. The third one arrives at the power amplifier (its choice depends on the cavity frequency as summarized in figure 5.1) through a PIN diode switch and a variable attenuator, and then is sent to the main coupler of the cavity. The cavity reacts as mismatch in the circuit and reflects back to the amplifier part of the incident power. Both P_r and P_i are separated by the bi-directional coupler (Narda, model 3022) that allows monitoring the forward (Agilent, 8485A power sensor) and reflected power (Agilent, 84815A peak power sensor) traveling on the feeding line. The Peak Power Analyzer and the Power Meter convert the rf power in a digital signal for the computerized data acquisition system.

Connected to the cavity there is a pickup which withdraw a small part of the rf signal transmitted by the first coupler. This signal is properly amplified and measured by the power head. The level of this signal is related to the amount of energy stored inside the cavity. As mentioned above, this signal is shifted in phase respect to the incident one. The pick-up signal passes through a PIN diode switch and an amplifier before being splitted into two parts. One of them reaches a limiting amplifier before going to the second mixer input, the latter arrives directly to the Pickup peak power sensor (Agilent, 84815A).

Finally the frequency is measured with a Frequency Counter.

The first operation is finding the value of ω_0 using the computer program developed for the tests. The operator looks at the input-output phase difference $\triangle\phi$ versus frequency swept by the generator. The signal proportional to $\triangle\phi$ is used as a retroaction to correct the delivered frequency and it shows a fast variation around ω_0. Near the set frequency, the phase loop will keep the cavity locked (Section 5.2.3).

The retroaction takes place at the mixer.The output is a dc signal proportional to the phase difference between P_t and P_i. The limiting amplifier (cavity output line) and the phase shifter (cavity input line) correct the initial value and keep low the difference of phase. Thus, the working point of the sweep generator is controlled by the output of the mixer to close the loop. Finally the frequency is measured with a Frequency Counter. The pick-up signal passes through a computer-controlled attenuator and a low noise 30 dB amplifier, and is measured by a power meter. A part of this signal, amplified and limited is used to drive the RF input of the mixers at the nominal level +7 dBm. A DC amplifier with programmable gain closes the frequency loop

5.2.1 *Power sensor calibration*

Power meter and peak power analyzer sensors are easy to calibrate: connecting the heads directly to the corresponding instrument, it corrects the acquired data through its *one point calibration*. Our equipment is out of date so we need to check the responses linearity once more and eventually correct the power sensors readings through the software. For each value, the computer program calculates the difference between the measured one

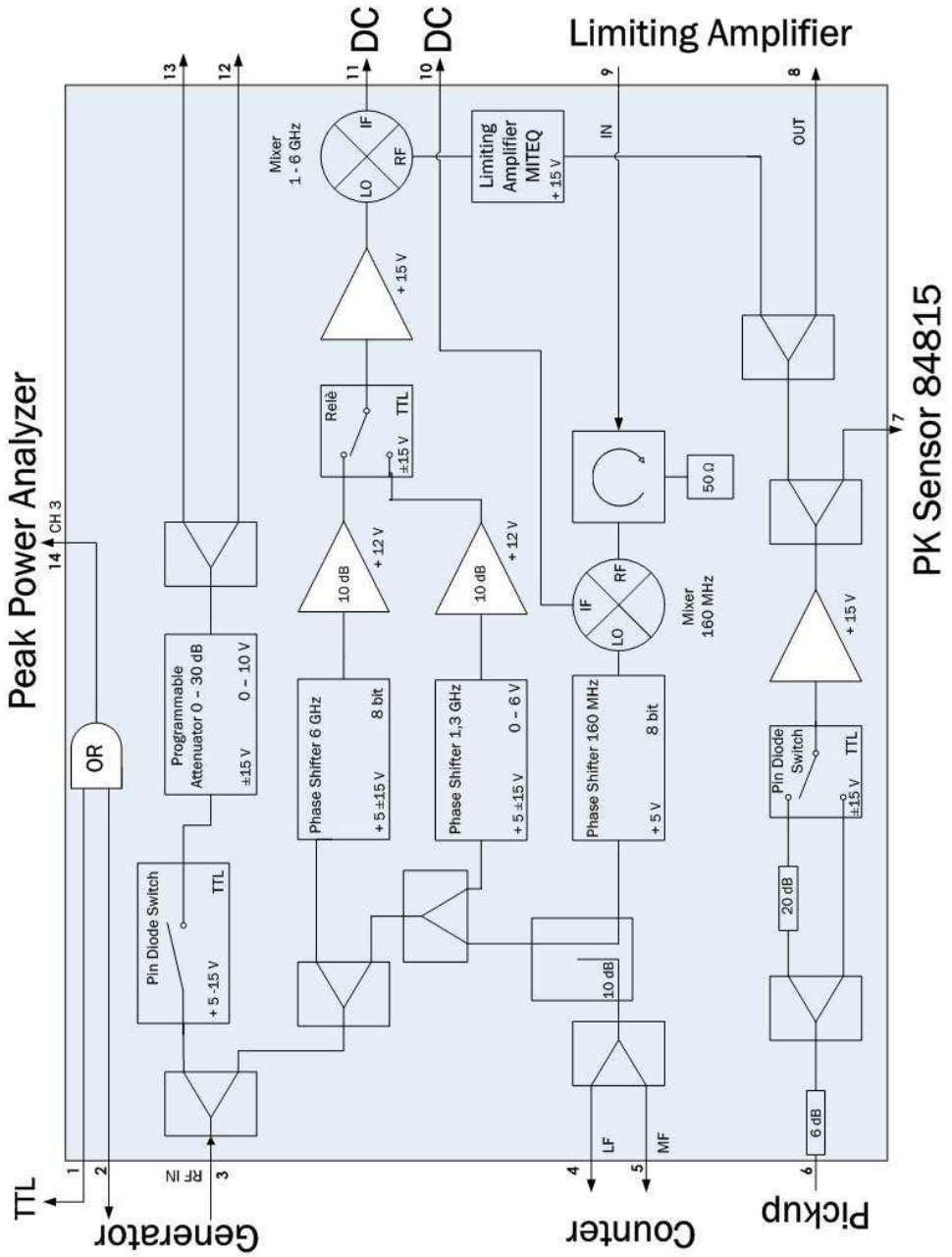

Figure 5.3: *A schematic of the built rf test box.*

and the one we should expect using the rf generator as a reference: in this way a calibration curve is obtained.

Effectively a three ports circulator (depending on the frequency of the cavity) has to be connected (port 1) to the generator rf output (previously set at the correct frequency value). Then the head to be calibrated is fixed to the circulator (port 2) while a load is attached to port 3. The circulator avoids the possible reflections caused by the head-generator direct attachment (not exactly 50 Ω). When all the connections are well tight, calibrating procedure can be run. This practice is performed for the power meter sensor 8485A and for the two 84815A peak power heads.

5.2.2 *Cable calibration*

The program calculates the Q value of the cavity by means of a balance of power: one needs to know exactly the forward power input to the superconducting cavity, to discriminate between the reflected power due to the resonant structure and the parasitic ones, to measure the power collected by the pickup antenna, excluding all the circuit contributions. To reach this purpose, it becomes mandatory to evaluate all the power dissipated in the various parts of the loop.

Figure 5.4 is used as a reference to clarify the followed procedure. In particular, the positions called as A, B (on the top plate of the cryostat), C (peak power sensor 84815A connected to the bidirectional coupler) and D (peak power sensor 84815A connected to the RF chassis) are clearly evidenced.

Forward power calibration
The reflected power head (peak power sensor HP 84815A + MACOM power limiter) is connected to the forward cable (A - C) while a 50 Ω load is attached to the bidirectional coupler in the place of the sensor (position C). Then, knowing the power supplied, the effective power level arriving at point A is measured to evaluate the forward cable attenuation. The calibration procedure can be activated through the dedicated section of the rf control software.

Reflected power calibration
To calibrate the reflected signal, the peak power sensor HP 84815A (+ MACOM power limiter) is fixed back to the bidirectional coupler (C) while a short-hat is connected to the forward cable (A). Now the power level at the end of the forward cable (A) is known (the forward power calibration has already been performed). The short hat make the rf signal to be completely reflected backward giving us the possibility to measure the attenuation when the signal travels from A to C. After setting up the right connections, the only thing to do is to allow the computer program to go on with the second calibration step.

Transmitted power calibration

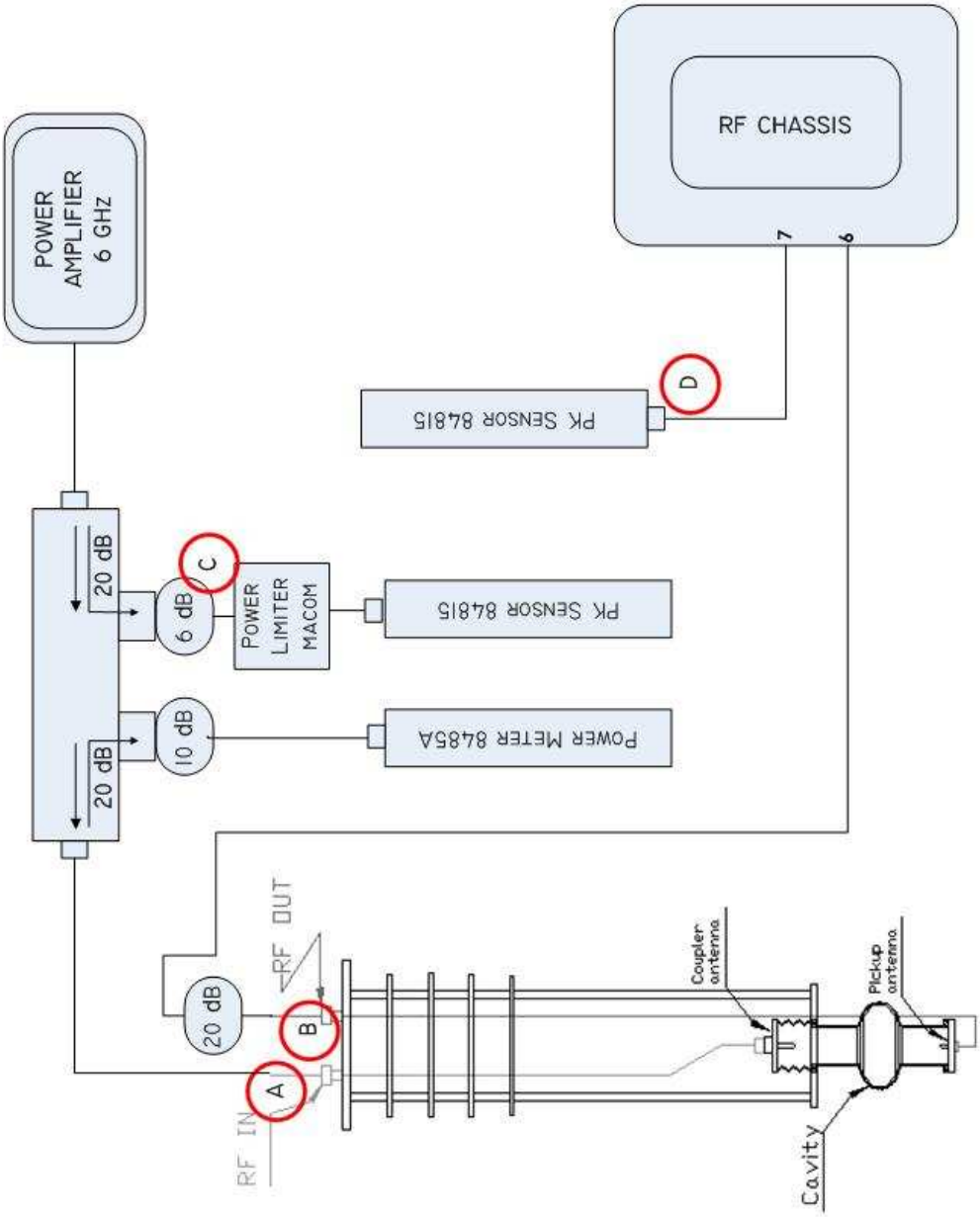

Figure 5.4: *Block diagram explaining the cable calibration.*

It is done simply connecting the forward cable free edge (A) to the transmitted cable one (B): the circuit is closed without connecting the cavity. Along the pickup line a sensitivity PIN diode switch is inserted (see Figure 5.3): a 20 dB attenuator can be placed in or not, depending on the power level measured by peak power sensor HP 84815A (D). The transmitted power calibration starting point can be selected: it has to guarantee the calibration range (5 dBm) includes the sensitivity switching. We need to know the transmitted circuit gain/attenuation with and without the attenuator adding. At the end of the procedure, the rf control system returns two values: one of them corresponds to the high sensitivity correction, the other to the low sensitivity one (20 dB attenuator placed in).

Internal cables calibration

Input and output ports (on the top plate of the cryostat) are connected to the cavity's antennas through two cables (Figure 5.2): they are defined as "*internal*" because they have to be closed in the cryostat with the cavity. After the cavity cooling down, its frequency is found (see chapter 5.2.4). Then forward, reflected and transmitted signals calibrations are performed through the procedures described above. Obviously it is fundamental to measure the internal cables dissipations too, before starting the rf test.

Transmitted cable attenuation

The forward cable has to be fixed to the pickup port on the top plate of the cryostat. If the rf generator frequency is changed to be out of the cavity band, the forward power is completely reflected backward (the resonator is under - coupled, as described in Section **??**). The reflected signal one can read on the computer screen doesn't correspond to this situation (it is $< 100\%$) because of the presence of the transmitted internal cable attenuation (still not considered). The internal cable attenuation can be evaluated looking at the reflected power percentage. It is necessary to adjust the correction (in dB units) writing it on the dedicated software window. We know the correction to be the cable attenuation when the reflected power percentage rises to 100%.

Forward cable attenuation

The rf generator frequency has to be changed to be out of the cavity band: if the generator frequency is exactly the cavity one, the reflected power is low (or $\sim$ zero if the coupling is critical) and the internal cable loss cannot be evaluated. The forward cable has to be connected to the input port on the top plate of the cryostat and the procedure previously described for the transmitted cable attenuation has to be followed (100% reflected power).

5.2.3 *PLL*

In this section the Phase Locked Loop circuit is described: its basic components, operation and application to the superconducting resonant cavities rf vertical test are briefly summarized.

PLL BASICS
A basic phase locked loop, PLL, consists of three elements:

✓ Phase comparator (mixer): It is a device that compares two input frequencies, generating an output that is a measure of their phase difference (if, for example, they differ in frequency, it gives a periodic output at the difference frequency).

✓ Loop filter: It is used to filter the mixer output in the PLL. It governs many of the properties of the loop and removes any high frequency elements on the signal.

✓ Voltage controlled oscillator (VCO): The voltage controlled oscillator is the circuit block that generates the output radio frequency signal. Its frequency (ω) can be controlled and swung over the operational frequency band for the loop.

PLL OPERATION
The concept of the operation of the PLL is relatively simple, although the mathematical analysis can become more complicated.

The Voltage Controlled Oscillator, VCO, within the PLL produces a signal which enters the mixer: this signal frequency is ω. If ω_0 (reference signal) doesn't equal ω, the phase error signal, after being filtered and amplified, causes the VCO frequency to deviate in the direction of ω_0 . If conditions are right, the VCO will quickly "lock" to ω_0 maintaining a fixed relationship with the reference signal.
If two signals are fed into a mixer, being equal in phase and frequency, there will be no output from it. However, if these signals are not in phase and frequency, the difference is converted to a DC output signal. The greater the frequency/phase difference in the two signals, the larger the output voltage. The phase locked loop or PLL is a particularly flexible circuit building block. It can be used for a variety of radio frequency applications, and accordingly the PLL is found in many radio receivers as well as other pieces of equipment.

As mentioned above, when the PLL is in lock a steady state error voltage is produced. By using an amplifier between the mixer and the VCO, the actual error between the signals can be reduced to very small levels. However some voltage must always be present at the control terminal of the VCO as this is what puts onto the correct frequency.

rf VERTICAL TEST
The rf signal frequency (ω) that feeds the cavity, is set through the rf generator . Since it can be different form the resonant cavity one (ω_0), it becomes mandatory to set up a circuit able to provide a signal at the correct frequency and to follow its variations in time: such a device is the so called Phase Locked Loop (PLL). Its working principle has been described above. Figure 5.2.3 is the block diagram of the PLL we use for our cavities testing.
If $\omega_0 = \omega$, the DC amplifier (mainly the low pass filter and the loop amplifier) output is

a constant error signal (depending on the phase difference). In other words, if the rf generator signal (cavity forward signal) is correct ($\omega_0 = \omega$), it is maintained as such through the PLL circuit. If the cavity transmetted signal (ω_0) changes ($\omega_0 \neq \omega$), the DC amplifier output isn't constant anymore: when entering the frequency modulation port of the rf generator (containing a Voltage Control Oscillator, VCO), it's frequency is modified to restore the fundamental condition $\omega_0 = \omega$.

The primary function of the limiting amplifier and the PIN diode switch (bottom part of the circuit) is to ensure that the rf input to the mixer is not power starved or over driven. For all of these devices the phase shift must be accounted for.
The limiting amplifier section is followed by a mixer. The two major considerations are that the intermediate frequency (IF) output must be DC coupled and the operating level of the local oscillator input port (LO) should be as high as practical. The low pass filter (of the DC amplifier) stage serves two purposes. The first is to eliminate the frequency content at the fundamental frequency or its second harmonic. The other purpose is to limit the loop bandwidth to about 300 kHz which reduces the system noise. The variable gain amplifier (of the DC amplifier) provides the way to adjust loop gain that is independent of loop phase. The rf generator has an option for an external frequency modulation (FM) control which can be DC coupled (connected to the DC amplifier). Between the generator and the LO mixer port a phase shifter is inserted: it compensates all the undesired phase differences.

5.2.4 *Cavity measurements procedure*

Once the superconducting state of the material is reached, the cavity is ready for the rf test. Two main parameters are measured - namely the Q_0 or quality factor of the equivalent resonant circuit vs. the accelerating field Eacc. These parameters are determined from a measurement of the incident, reflected and transmitted power (respectively Pi Pr and Pt) and the resonant frequency of the cavity ω_0. In order to search the cavity resonant frequency, the input-output phase difference versus frequencies swept by the generator is observed. This value, which is used as a retroaction to correct the frequency delivered by the generator, shows a visible variation around the resonant frequency; following the cavity impedance variation.

Searching of the resonant frequency is done at low power (1 W) with two 10dbB attenuators connected at the amplifier output. It is possible to work in loco but, anyway, the amplifier is interlocked with the plug connected to ionizing radiation monitor (see section 5.5). The DC amplifier gain varies between 25-50 and 200.

Changing the span value the frequency axis scales differently. In the superconducting state, the cavity band will be of a few Hertz so usually it is advisable to lock the cavity before it gets superconducting, so that it is easier to find it in the cold state. After each sweep, the above mentioned phase difference is displayed on the front panel as a function of frequency. It appears as a continuous line with many different peaks and plateaux. The resonant frequency corresponds to a sharp variation which looks like a discontinuity (figure

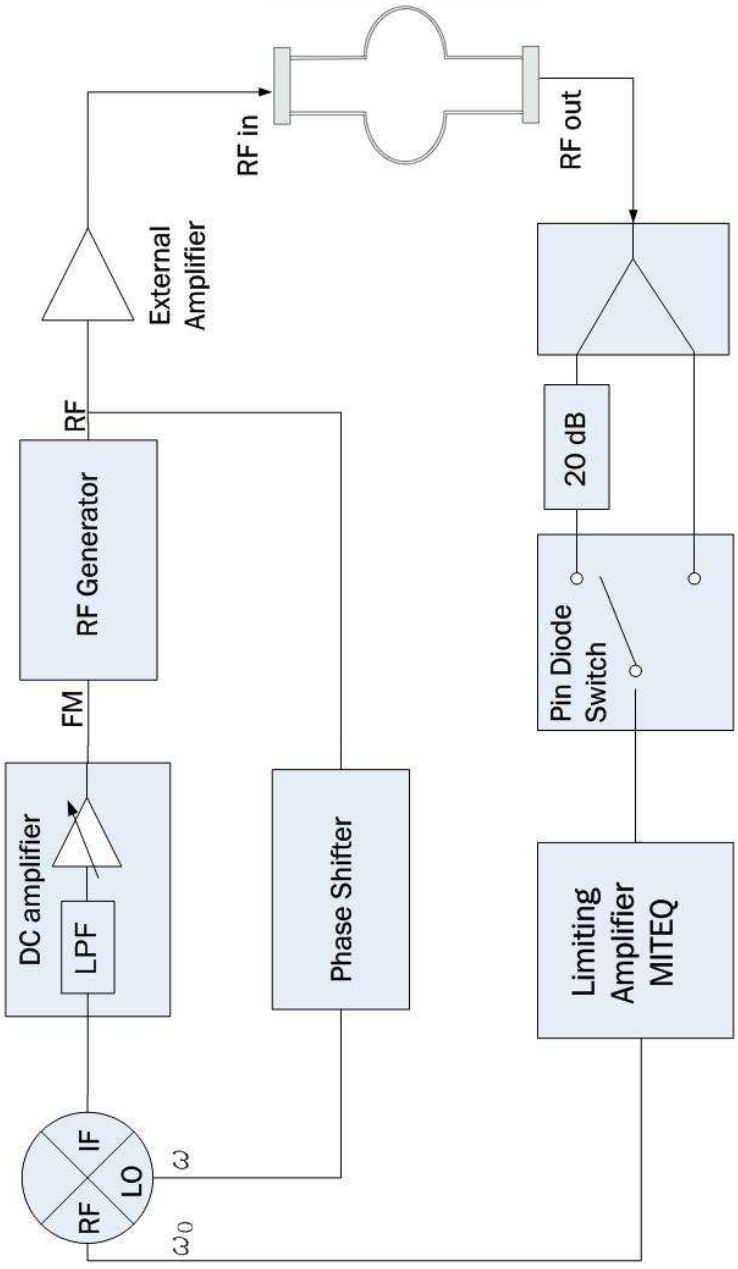

Figure 5.5: *Block diagram of a typical VCO-PLL system: it includes the cavity structure.*

5.6). Once this point is set the phase should be adjusted, looking at the mixer curve

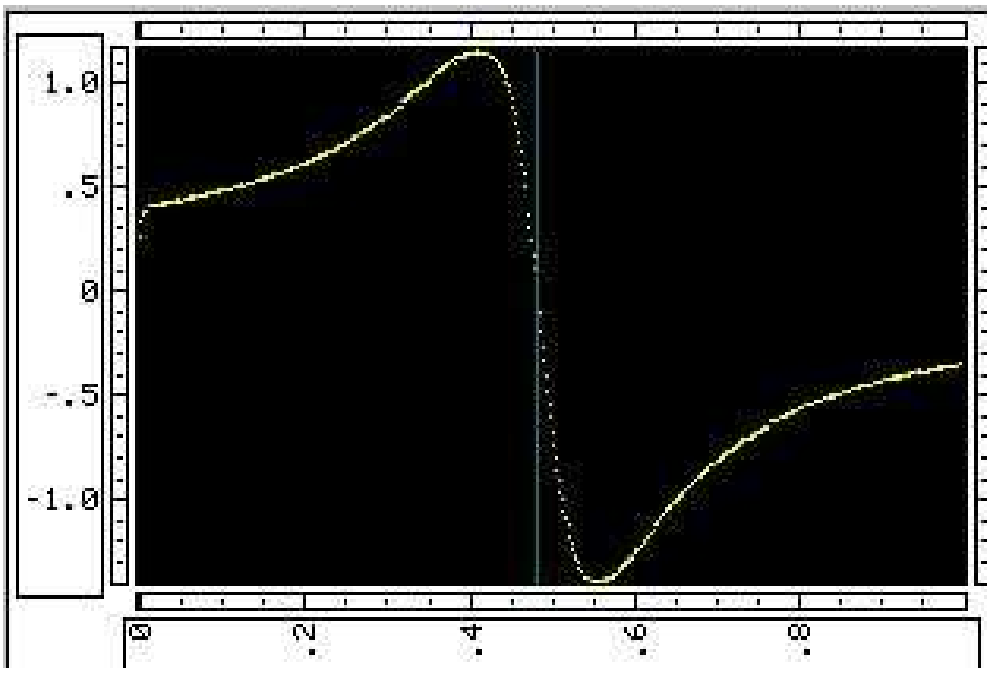

Figure 5.6: *Input-output phase difference versus frequencies. The sharp variation appears in correspondence to the resonant frequency.*

discontinuity, in order to obtain a negative retroaction, which will give us a stable loop (figure 5.6).

Now the cavity can be locked (Once the phase has been adjusted in this way, the cavity could be locked.) and it's necessary to work as close as possible to the critical coupling, where the reflected power is zero. The phase changing and the coupler motion have the the aim to minimize the reflected power. Acceptable value of reflected power are under 10%.

When the critical coupling is set, the decay time procedure perform the Q_0 measurement and all values are saved automatically. After that, the two attenuators could be removed from the amplifier, the laboratory is evacuated and all measurements are executed remotely by two computer station placed in the office, outside the controlled ionizing radiation area.

The following steps should be repeated to records the Q-E curve:

1. turn on the amplifier;
2. turn on rf on the control panel;
3. search and lock the cavity, according to the above given procedure;
4. perform a Q_0 (decay) measurement, and save the set up file (*.set);
5. click on the "Q(E)" button: the curve begins to be displayed on the control panel;
6. increase gradually the power, always saving the recorded points when they are believed to be stable.

During cooling down from 4,2 K to 1,8 K the cavity band continues to shrink and it is better to leave it locked in the phase lock loop.

5.3 *Software*

The control program, developed in Visual Basic 3, allows to:

- calibrate the rf lines,
- find the resonant frequency,
- set the loop phase,
- lock the generator to the resonator frequency,
- adjust suitable coupling conditions and the forward power level,
- measure the levels of pick-up, forward and reflected power signals,
- measure of the decay time,
- compute the Q and plot it as a function of the accelerating field allowing both a fast data analysis and recording (figure 5.7).

All these procedures are started from the program panel: the main control panel is designed to give complete manual control of the measurement, indicating all the crucial system parameters in real time. The automatic procedures are activated by the buttons and after fulfilling them the system always returns to the manual mode. It is always possible to stop the automatic procedure and to operate manually the devices if necessary, resuming the automatic process later if required. The control panel is composed of numeric controls

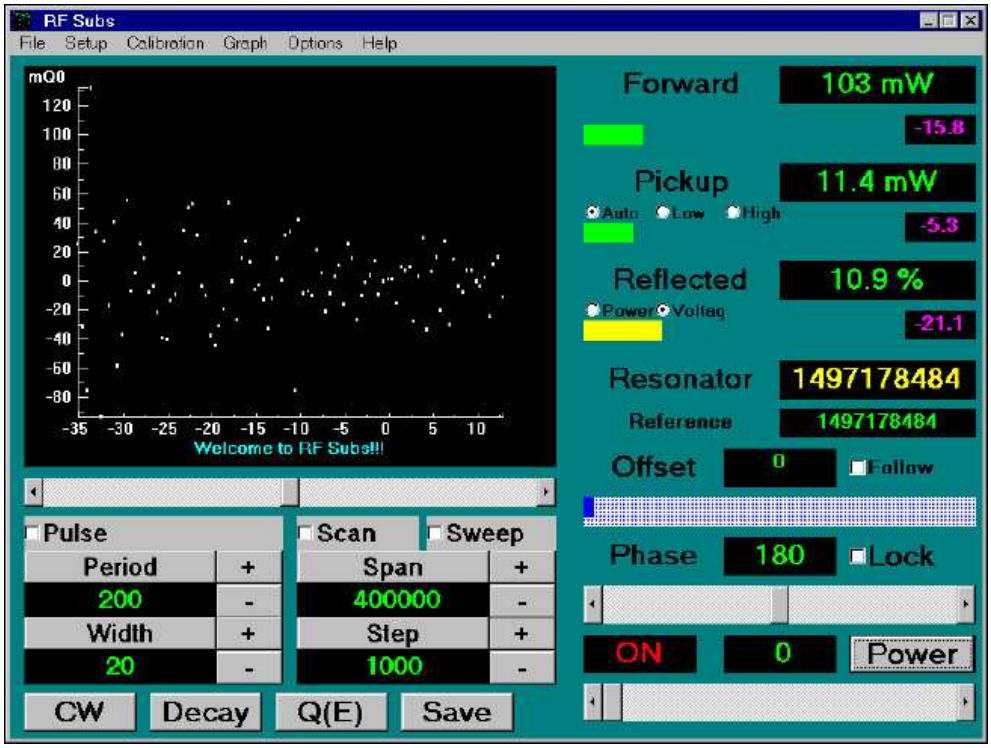

Figure 5.7: *Screen shot of the rf control program page developed in Visual Basic .....*

and indicators, two sliders, one indicator bars, several scroll bar and a custom scroll menu. Starting from the right part of the screen of the screen (figure 5.7):

- the direct power indicator ("Forward") gives the power delivered to the cavity. The operator should always be aware of this number, particularly when the amplifier is on, because in that situation it is possible to exceed the power ratings of several components, leading to permanent damages.
- The "Pickup" indicator shows the power level transmitted by the resonator. It gives hints of the loop effectiveness. It is possible to change the sensibility of the pickup power head between "High" and "Low" or left it in the automatic way.
- The Reflected power indicator ("Reflected") is very important as well, since this is the quantity to minimize in order to improve the measure accuracy. It can be expressed in "Power" or "Voltage" percentage.

Each power indicators display a value, expressed in Watt, that take into account all the calibration of the system. The slider below each box change length and color when the displayed values enters three different range. In the boxes below the power indicators, the violet value expressed in dB, indicates the power read directly from the power heads.

- The frequency delivered by the generator ("Reference") is in the text box displayed under the "Reflected" indicator. It is the sweep center frequency, in the graph box placed on the left and it can be changed just writing in the box.
- The "Resonance" box display the cavity resonance frequency.
- The "Offset" appears as number and position of the cursor in the indicator bar. It is the phase error signal coming out from the DC amplifier.
- The "Phase" slider can be changed clicking on the two arrows on both sides or just dragging the cursor.
- The "Power" slider is in logarithmic scale and it allows to increase or decrease the power from the amplifier.
- The "Follow" box adapt the frequency generators to the resonant frequency of the cavity.
- The "Lock" box close the loop (see section 5.2.3).
- On the graph box on the left the frequency range, spanned by the sweep, is selected with the scroll bar of the "Span" buttons, and, accordingly, the step width (of course the sweep is a discrete sequence in the frequency domain, with a given step).
- The "Scan" modality show the pickup signal intensity versus frequency on the graph box.
- The "Pulse" modality switch on the pulse power for the cavity conditioning. "Period" and "With" of the pulse can be selected.

- The "Q(E)" button change the graph box to display the Q versus E curve. Each point of the curve can be registered in a file with the "Save" button.
- The "Decay" button starts the decay time calculations.
- The CW button go back to the normal procedure and it is used to go out from the "Decay" and "Q(E)" modality.

Another simpler but important software have been developed for the coupler motion. The stepping motor could be controlled acting on the "Speed", the number of "Steps" and the movement direction (up or down). These two software allows to complete an rf measure remotely, controlling each instruments and measure parameters. Both software are programmed to display several warnings in case of problems occurring during the test.

5.4 *Cryogenic apparatus and cavity stand*

During the test, the cavity has to be cooled at cryogenic temperatures to reach the superconducting state. The cryostat has been designed for measuring at 4.2K and 1.8K at a maximum power of 60 W. In the rf testing facility there are four apertures which can host a cryostat. Three of them are used to test QWRs and single cell TESLA type cavity. This kind of cryostat can hold 100 liters of helium. The last one is for the multicells TESLA type cavity with a volume of 400 liters of helium.
The Helium vessel is constituted by three successive chambers containing respectively air, liquid nitrogen, the inner being under vacuum to thermally insulate the sides. At the top, the insulation is ensured by several copper screens cooled with the recovery helium cold gas. The cryogenic insert with a multicells cavity is shown in figure 5.8. In order to reduce the cooling cost, a preliminary cooling is achieved by using the liquid nitrogen of the second chamber. Thus the He vessel is filled with Helium gas at a pressure of 1000mBar, and a thermal contact is created between the He vessel and the liquid N_2 chamber by filling the inner chamber with 200mBar. Once the temperature reaches 80K, the He in the third chamber is removed and the transfer of liquid He at 4.2K is started. The transfer does not stop until the liquid level reaches 1000 or 1400 mm, depending on the cavity size.

The cavity is tested at 4.2K and then at 1.8K. The temperature of liquid helium can be lowered by using the heat of evaporation. A pumping line takes away the vapour over the liquid and hence some liquid helium evaporates to compensate the drop of pressure. Furthermore, a liquid helium supply at 1.8K must occur to keep the level constant. This task is carried out by a heat exchanger, which utilizes the cooling capacity of the return gas stream to cool down the incoming liquid. The cooled fluid is sent into a liquid/gas separator. The low temperature portion is taken apart by a sinter brass plate in the middle of the separator. The liquid flows by capillarity towards the lower side while the gaseous phase remains on the upper part and it is used to refrigerate the copper screen. The stream of liquid is regulated by two valves which can be operated manually from the outside. By changing the pumping speed it is possible to set the evaporation rate and, in turn, the

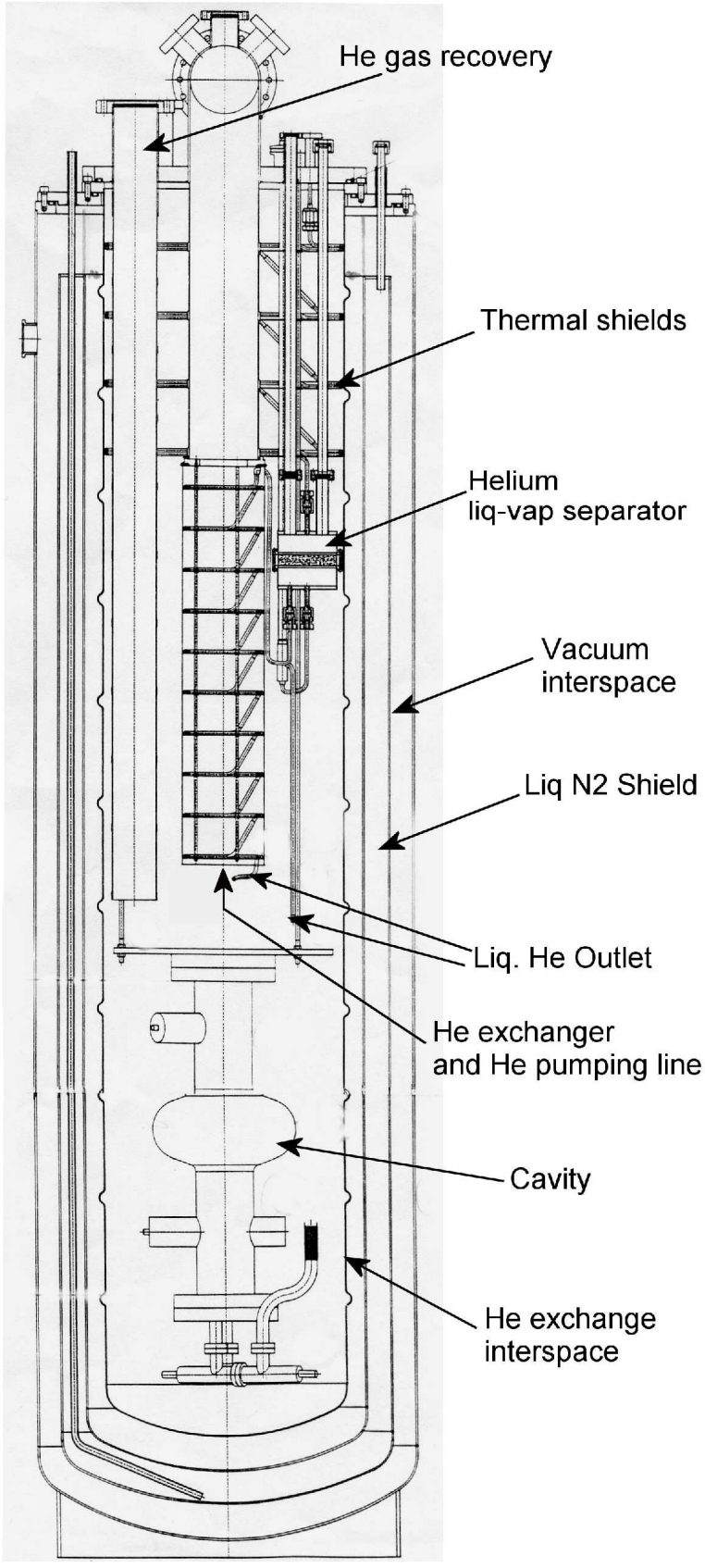

Figure 5.8: *Cryogenic insert designed to hold a 9-cells cavity.*

amount of power removed from the dewar. Besides, the temperature of the bath depends on the pressure inside the dewar which is again regulated by the pumping speed.

Typically, a single cell cavity dissipates only few tens of watts during the test. The rf tests

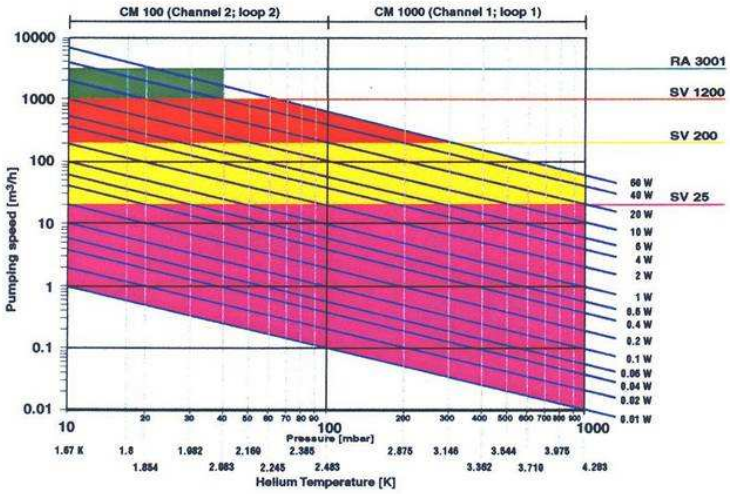

Figure 5.9: *Plot of the pumping speed as a function of the temperature for different power dissipated.*

are performed at 4.2K and at 1.8K with the result of making the pumping speed range very large as it is shown in figure 5.9. This plot illustrates the pumping speed needed to remove a given power as a function of the temperature of the liquid helium.

Figure 5.10 shows that the whole range is covered by using four pumps - namely RA3001, SV1200, SV200, SV25 which work at different speed ranges. The first pump is a Roots pump while the others are rotative pumps.The operator can set on the pumping control system the working pressure in the cryostat in a range between 16 and 1000mBar. The system initially tries to pump the cryostat with the smallest pump (SV25). If the selected pressure is not reached, a bigger pump (SV200) is automatically activated. In the case that also this one cannot attain the selected pressure, also the third pump (SV1200) is activated. If an adequate pumping speed is still not achieved, at 40mbar the Roots pump (RA3001) starts pumping. Along the line of gas pumped there are several sensors connected to the automatic control device. The pressure control (PC) automatically opens the three valves VR1, VR2, VR3 to select the working point of the pumps. In addition, each rotative pump can be excluded from the line by the intercepting valve that precede them. There is also a gas cooler in the line, because the Roots tends to be damaged by the hot gas present at the exit of the pump itself. At the exit of the pumping line, the helium gas is stored and subsequently sent to the liquefier when the tank is full.

A stepping motor lift up and bring down a tube connected to the lamellar bellow of the antenna.

As the purpose of a cryogenic system is to generate and maintain very low temperatures, a suitable network of temperature sensors and heaters is needed. The temperature

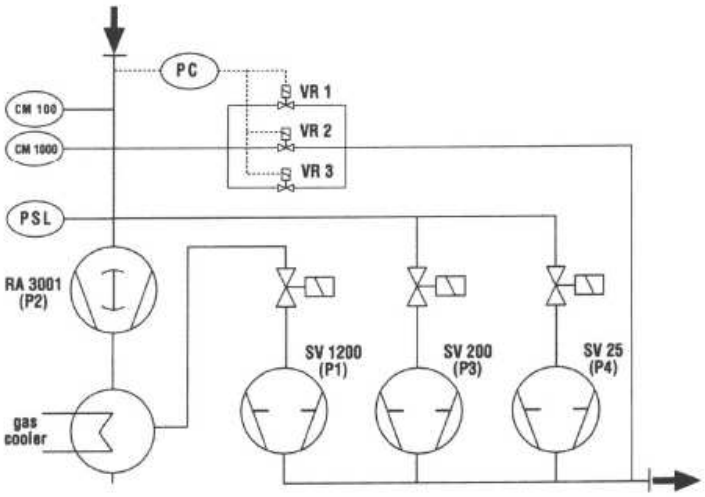

Figure 5.10: *Arrangement of the cryostat pumping system.*

monitoring in the cryostat is undertaken by three kinds of sensors: Diode thermometers, carbon glass resistor and germanium resistance thermometers. The diodes are substantially used as an additional level probe, while the carbon glass and germanium are employed for the temperature region between 4,2 and 1,8 K.

After the preliminary evacuation, the cavity is mounted on the vacuum system for the cold test. The layout of this system is sketched in fig 1. Staring from the exhaust line, there is an oil free backing pump and a turbo-molecular pump. Valve V5 is used to insulate the turbo in case of power failure. V6 is foreseen for the leak detection. V4 is the main gate. V7 allows venting the system, with the gate closed. V8 and V9 are for the helium conditioning. V3 allows leaving under vacuum the "fixed" part of the system, which is connected to the cavity by the VCR between V2 and V3

The cryostat vacuum chamber has a long pipe connecting the pumps, at room temperature, to the cavity immersed in the liquid helium. In this situation the cavity itself act as a cryogenic pump, while the low conductance of the pipe makes it difficult the work of the upper pumps. It is thus advisable to evacuate the cavity before the mounting on the cryostat insert. This job is done by means of a separated vacuum facility, sketched in figure 5.11. The cavity is pumped leaving it on the movable support used for the chemistry stage. We prefer to carry out baking at low temperatures (less than 100 °C) in order not to interfere with the process eventually occurred during sputtering, anyhow this is a possible matter of discussion. After overnight baking and 8 hours pumping the pressure will be in the high 10^{-8} mbar range. It is time to put the cavity on the cryostat.

5.5 *Radiation Safety System*

During the rf test, a cavity can become a source of ionizing radiations. Electrons are extracted from the walls of the cavity and then accelerated by the presence of the high

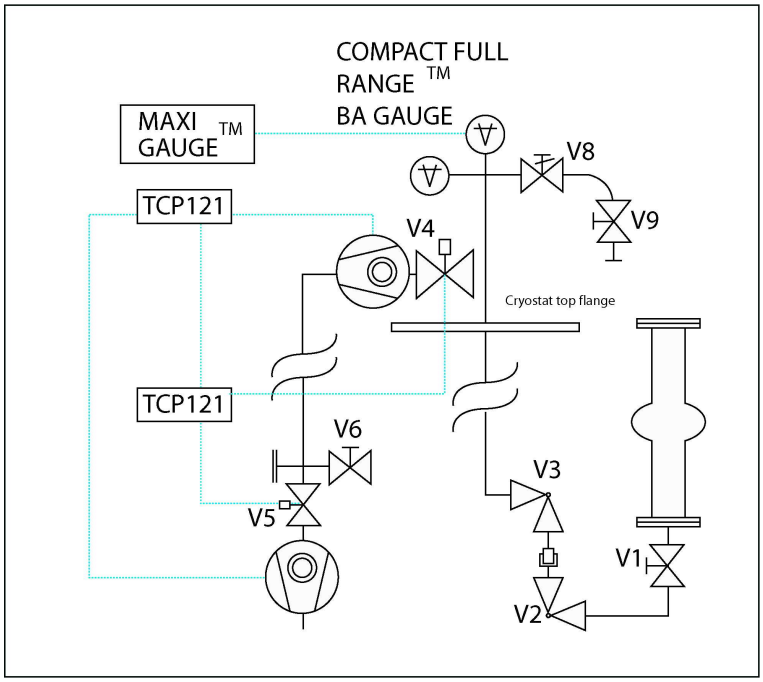

Figure 5.11: *Sketch of the cavity pumping system when it is mounted on the cryogenic stand.*

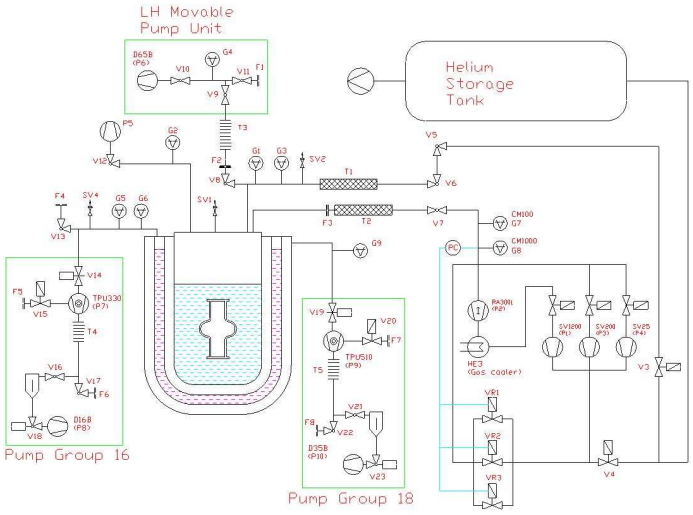

Figure 5.12: *Global view of the cryostat pumping system and gas lines.*

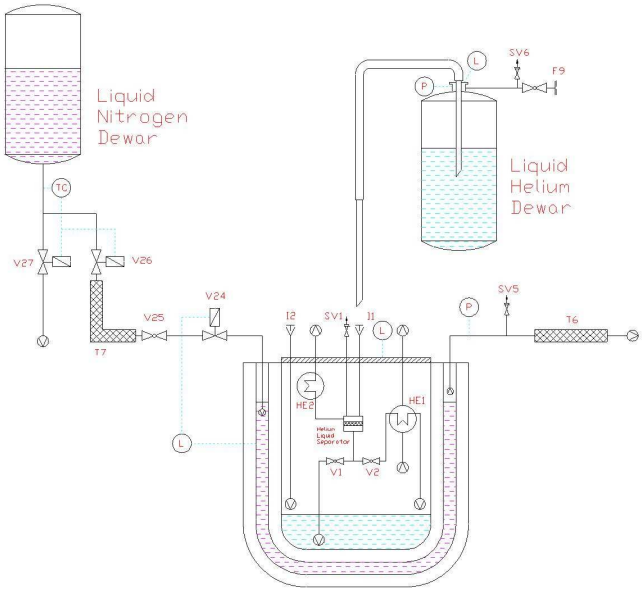

Figure 5.13: *The local lines for liquid nitrogen and helium. Both are connected to the system and monitored by a control panel located in the laboratory.*

intensity electric field. This electron current generally hits the wall of the cavity and some X-rays are produced by Breemsstrahlung effect. The electrons heat the material destroying the superconducting state. The performance of the resonator drops exponentially and the test stops. The occurrences for this event have been deeply studied in the last decades and it turned out that they are strictly connected to the cleanliness of the surface and many procedures have successfully been developed to exclude this problem. Anyway a safety system is mandatory to monitor the emitted radiation dose. Each of the cryostats stays in a hole in the ground made of concrete wall with at least 15 cm of thickness and they are laterally shielded with 1.5 cm lead. The cryostat top plate is made of 2.5 cm of stainless steel and 4 mm of Aluminium. A further movable shielding provides of 1.5 cm of lead. In figure 5.14 is illustrated a map of the Radiation Safety System. Three detectors are interlocked to the main rf Power Amplifier and continuously monitor the radiation emitted during the measurement. The trespassing of the security threshold value automatically turns off the amplifiers. Once there is no power to the cavity, the radiation emission stops and, since there is no process of activation, the access to lab is safe again. Thus the activation of the rf power is subordinated to the evacuation of all the personnel from lab. Before starting any kind of test the operator has to check the presence of any possible worker and advise them to leave the room. In addition, an acoustic alarm and some flashing signals warn the people outside the lab that a production of radiation may occur.

In the map are shown several check-point buttons which the operator has to press in the right order with the aim to control all the rooms. The amplifier can switch on only when all the check-points are done and the door to the external corridor is closed. For

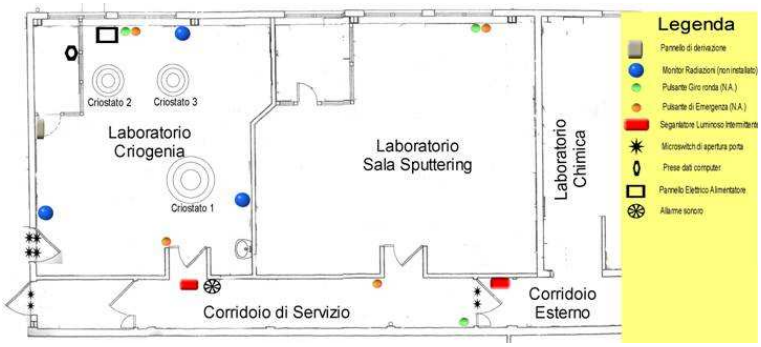

Figure 5.14: *Map of the Radiation Safety System.*

security reasons, there are also thirty seconds before the activation. This allows anyone still inside the laboratory to be able to press the emergency button and stop the power. Once the amplifier turns on, nobody can go into the lab. All the doors are interlocked to the main power by making use of several micro-switches. The operator can control the test in remote by a computer program.

5.6 *System monitoring and data sharing*

The setting of experimental apparatus requires keeping a large number of parameters under control. A large variety of test devices, which have to be quickly set and configured according to the different situations have to be used. Since for safety reason the operators have to work in remote control during measurements, a software tool was developed to make the acquisition and visualization process easier for users without any further programming, in order to allow configuring the system, to get readings from all the connected devices, to register and visualize the data on the main computer and share them in the local net. The software is compatible with most Windows versions and is written in the way to minimize the load on the local net. The acquisition program GUARD running on a computer located nearby the acquiring instruments makes the data available through the local net and the user can have real time visualization of data using the program CHARTS (figure 5.15)[97].
GUARD presently supports data acquisition from the most typical instruments used in the lab for thermometry, cryogenics, vacuum, pressure, radiation, frequency, RF, AC, DC measurements and data available from other computers through the local net. By this software tool, users can also get the information about accelerator status or any other critical processes without big risks of uncontrolled access to the main accelerator control system.

Coming to the left side of the screen, we have indicators for the liquid helium level, in the cryostat and in the dewar, and for the temperatures red by all the thermometers: the latter can be configured according to the location of the sensors in the cryostat.

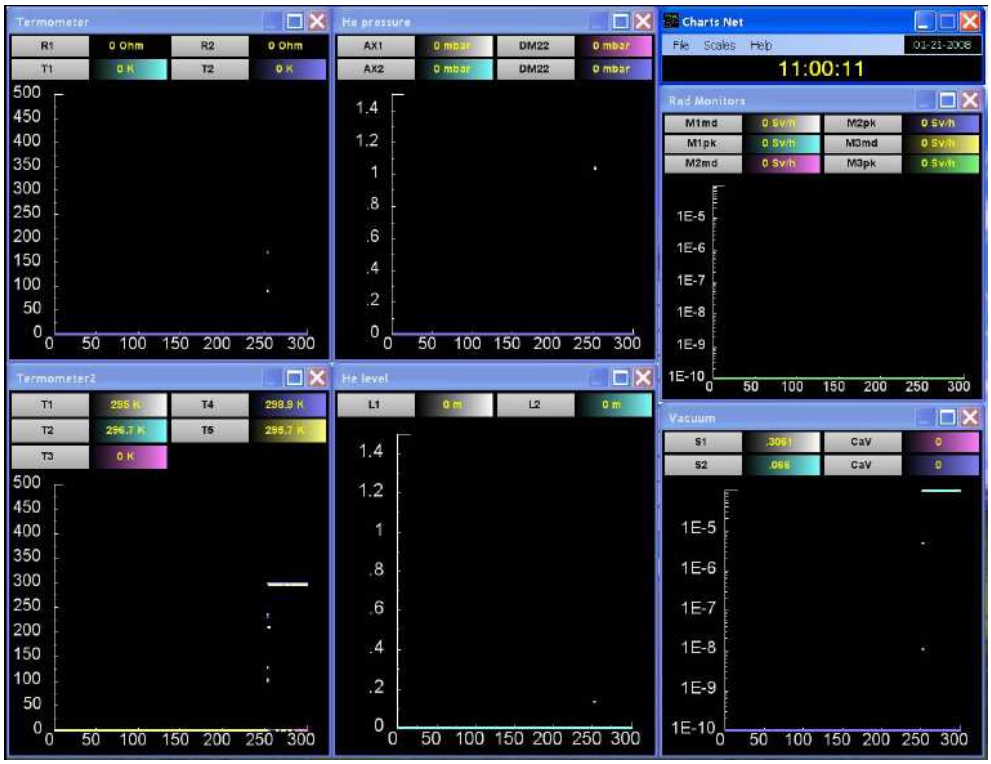

Figure 5.15: *Screen shot of the monitoring real time visualization of data software CHARTS, developed in Visual Basic ..... in order to draw all monitored data collected by the software GUARD.*

Hardware and software

Typically, the computer used for data acquisition and registration is equipped with RS232 serial ports, IEEE488 interface card, LAN connection and USB 2.0 ports. It is possible in this way to employ up to 10 serial instruments, 31 IEEE488 instruments and gather and share the data through LAN. Mainly the number of channels and the acquisition rate determine the choice of the computer. For the simple and/or slow configurations even the old PC's starting from 486 can be recovered to perform this task. GUARD code (Server) and CHARTS code (Client) are written in Visual Basic 2005. The GUARD program, that depends on hardware (mainly IEEE488 cards and corresponding libraries), is actually operating on **95/98/ME/XP/** platforms. CHARTS has been tested to work with all versions of Windows from 95 to XP. Both codes have their setup (configuration) files in text format that can be loaded through command line and give the user the possibility to organize the set of instruments for GUARD and personalize the visualization of corresponding strip charts on the screen with CHARTS program. The GUARD setup file contains the list of instruments, particular device configurations or data channels that can be read through RS232/IEEE488/LAN/USB2.0 interfaces. The type of IEEE488 card (NI, HP, Keithley) installed is detected automatically. Every instrument or data channel has a dedicated subroutine that performs initialization and takes readings when requested. The first time interval in the GUARD setup file corresponds to the refresh rate of the shared exchange file that is generally saved on the virtual disc and contains tab-delimited string of the last data gathered from the whole set of instruments. With the second specified time interval the software adds new line to the registration file that represents tab-delimited table saved to hard disc for future elaboration. The file is reopened every 300 lines with date-time stamp as a filename. The CHARTS setup permits to define the exchange file address over the local net, to set the access period and to organize the data in order to create a set of synchronous strip charts. Every chart can contain up to 8 curves. The setup parameters include panel title, number of curves, size and position of the panel in the fractions of the screen, Y-scale (min-max), scale type (lin-log) and for every chart curve - state (on-off), title, units and comment. Due to the screen area limits, multiple CHARTS instances with corresponding setups were made possible in order to permit the contemporary connection to several GUARD servers inside LNL.

5.7 *RF test of a Nb spinned 3-cell 1,3GHz cavity*

The whole system for cavity rf characterization has been tested step by step during preparation and measure of a Nb-bulk 1.3 GHz 3-cell TESLA type cavity. The cavity was formed with the spinning technique [23]. The characteristic parameters are listed in the table 5.2. The cavity has been tested at room temperature firstly, to have a preliminary estimation on the correct length of the rf antennas (see section **??**). It has been chosen to work with a Q variable coupler which covers the range between 10^7 and 10^{10}. On the contrary a fixed antenna was chosen for the pick up with a value around $7{\cdot}10^{11}$.

The cavity has been treated as follows:

- mechanical polishing with Scotch Brite^{TM} (various grains) for 6 hours
- Degreasing in ultrasonic bath with soap and double rinsing in deionized water
- 2 hour and 15 minutes electropolishing, approximate thickness removed: 60μm.
- High Pressure Water Rinsing (HPWR) 45 minutes at 100 bar
- rf test n.1
- 1 hour chemical etching in the 1:1:2 solution
- High Pressure Water Rinsing (HPWR) 30 minutes at 100 bar
- Heat treatment at 750°C for 3 hours
- 1 hour and 20 ,minutes electropolishing
- High Pressure Water Rinsing (HPWR) 3 hours at 100 bar
- baking at 80°C for 20h
- rf test n.2
- High Pressure Water Rinsing (HPWR) 2 hours at 100 bar
- baking at 80°C for 20h
- rf test n.3

After the assembling in clean room, the cavity is mounted on a vacuum system for pumping down. This step removes the air and the water that may still be present inside the cavity. A gentle thermal treatment at 80°C is performed during this step [98]. The final pressure is around $2{\cdot}10^{-9}$mbar. Cavity vacuum pressure is monitored during the whole test and data are collected in figure 5.16. No x-rays have been produced during none of the three test.

The cavity is mounted on the test stand and inserted in the cryostat. The cooling

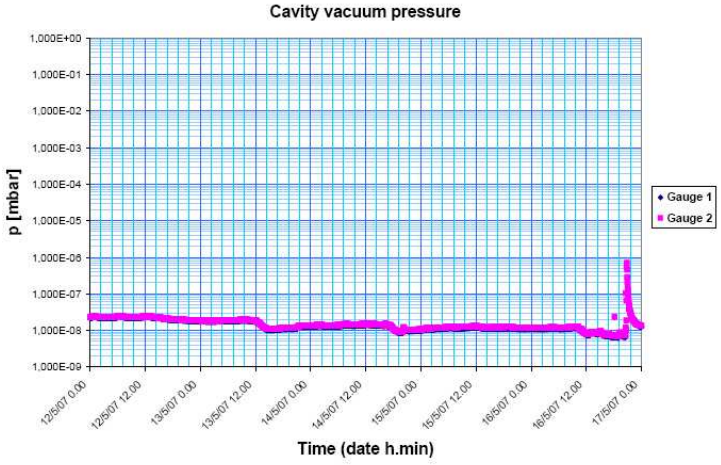

Figure 5.16: *Monitoring of the cavity vacuum during the whole rf measurement process.*

procedures is explained in section 5.4 and temperatures, liquid helium level and cryostat pressure are monitored as showed in figures 5.17, 5.19 and 5.20. Once the He level exceed the cavity height all cavity thermometers signs 4.2K and a preliminary Q curve is measured.

Then the pressure of the helium bath is slowly lowered to cool the cavity down to 1.8K. At the same time the Qfactor is measured at different temperatures. The rf power is roughly 10mW to avoid anomalous losses. After that the temperature of 1.8K is reached and the system is stabilized, the Q curve is measured. Due to the high Q factor of the resonator, the field inside the cavity can produce non resonant losses such as the Field Emission.

Figure 5.17: *Monitoring of the cavity and shields temperatures. The stand shields are cooled just pumping the helium gas from the cryostat through a tube welded on the external circumference of all shields. The pumping starts manually and it doesn't work constantly to save helium.*

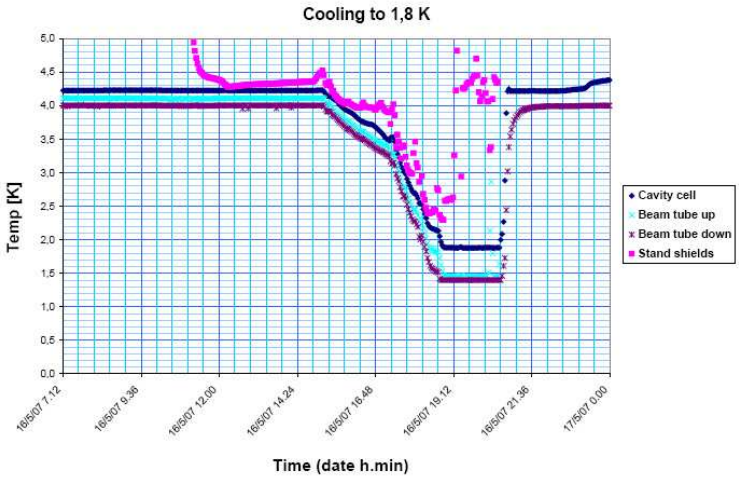

Figure 5.18: *Details of the cavity temperatures during cooling to 1,8K. Some thermometers are old and not perfectly calibrated, anyway the reference thermometer is positioned on the cavity cell.*

Results of the three rf tests are summarized in figure 5.21. Errors bars have been calculated with the software created by Powers [93], with the following conditions:

- the linearity of the power meter is $\pm$ 2%
- percentage error on the pickup-Q Q_{pk} 11%

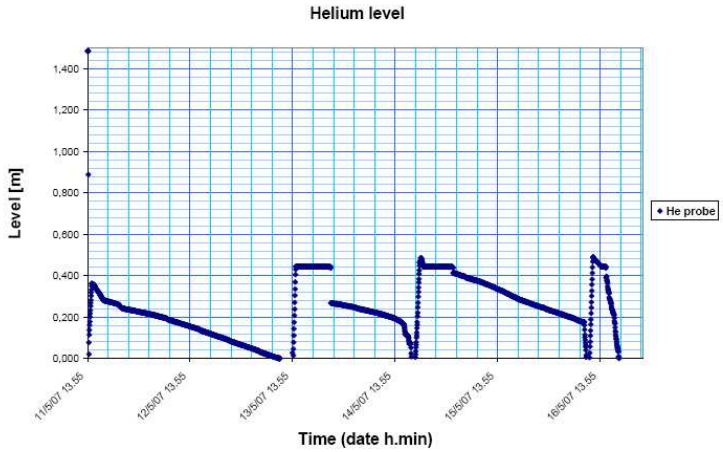

Figure 5.19: *Monitoring of the He level in the cryostat: four refilling have been carry-out during this test.*

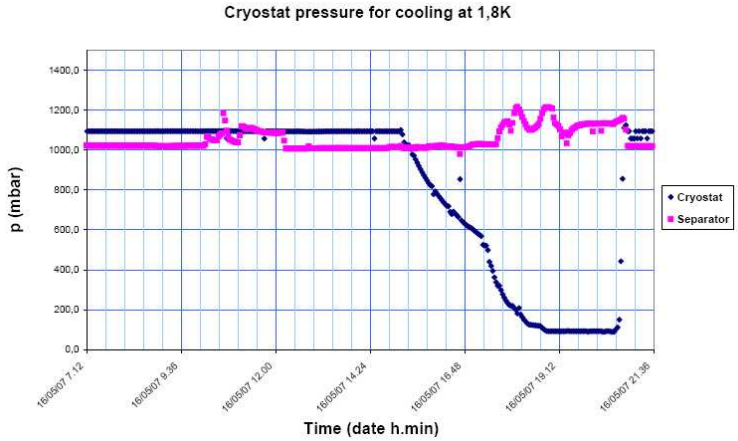

Figure 5.20: *Details of the cryostat pressure during cooling to 1,8K. While the whole cryostat pressure decrease, the separator pressure is 200 bar over the atmospheric pressure because the cryostat re-filling is still going on.*

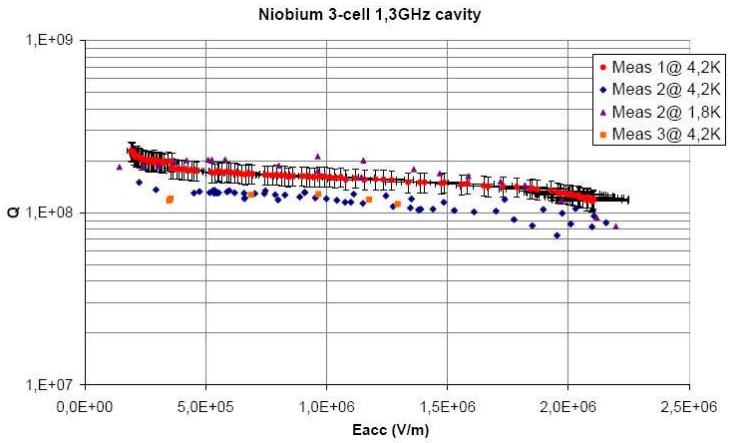

Figure 5.21: *Excitation curves of electropolished niobium three-cell 1.3 GHz cavity after three different internal surface treatments.*

Unfortunately no improvement was found after the second and the third treatment. After four etching the cavity still shows a bad surface and results are far from the actual normal values of Nb bulk cavities. One way to improve the inner surface of this cavity is the Centrifugal Barrel Polishing [64] developed at KEK and successfully applied to mono-cell spinned cavities [18]. The construction of a similar polishing machine at Legnaro is in progress and could be the first solution to improve the 3-cell spinned cavity performances.

Field emission has not been detected because the cavity quenches at very low field. Anyway surface contamination by foreign particles probably plays a role in the 3rd measure quench. It may be inferred that they could come from the step after the HPR, namely assembling and pumping down. These two steps have not been refined yet but it is also necessary to install a liquid particle counter at the outlet of water in the HPR system to monitor the amount of particles over the time. Thus, it would be possible to decide when the cavity is effectively clean, by looking at the minimum number of particles at the exit.

Another required improvement is in the cryogenic system. The thermal stability of 1.8K has to be longer than 30min, to let the helium conditioning working. In addition to, the safety value of the radiation monitors has to be revised. It is necessary to find the correct trade off between the safety conditions and the maximum power delivered to the cavity to reduce the time for conditioning. A better xray shield might be necessary.

Chapter 6

Apparatus

This chapter illustrates the structures and the features of the vacuum system in use and contains one paragraph dealing with the cathode assembly. The section dedicated to the standard coating focus the attention on just some of the obtained samples. They will be used in the following chapter as comparison with all the other results. All morphological characterization have been performed in collaboration with the "Interdepartmental Laboratory of Electron Microscopy" (LIME), University of Rome "ROMA TRE".

6.1 *Vacuum System*

The vacuum system used for depositions has been built and improved to cover the 1,5 GHz copper cavity during previous works of thesis (figure 6.1) [37]. The work implemented on the pumping system during this study have come out to be simple ordinary maintenance (substitution of instruments, cleaning of some parts of the camera). There have been, on the contrary, some implementations of the cathode assembly and the cooling system.

Looking at the figure 6.2 we can start describing the system from the exhaust pipe. The system is made up of a double stage Edwards E2M18 rotary pump (RP) that reaches the maximum vacuum of 10^{-3}mbar and uses the TW Edwards low vapor tension oil. The rotary pump is closed by an electropneumatic valve, named V1 that opens when the pump is switched-on and closes with the switching off. The system is provided with an absorption trap (ZT) to avoid the backstreaming problem, that means the oil and air reflux from the low vacuum towards the high vacuum camera. The trap is followed by another valve at VAT angle (V2) that, isolating the rotary from the system, is used during the leak test.

A sequence of two crosses, situated between the valve V2 and the turbomolecular pump, complete the low vacuum zone: to one of the crosses is connected the VAT (V3)linear valve for the leak detection without stopping the pumping; to the other is connected the valve V4 of the first nitrogen line for the venting of the zone situated behind the gate (GT).

The turbomelecular pump Seiko Seiki TP300 (TP) is the magnetic levitation, so it doesn't use any oil. The control panel of the pump is relatively simple but it doesn't foresee an automatic reduction of the pumping speed (Stand-by): this inconvenience has

been overcome, by giving the system a by-pass (BP) that directly connects the pump to the chamber through a tombak and a valve (V5) UHV All-Metal Bakeable Varian, with a very low conductance. Thus, it permits working in the chamber at pressure of 10^{-3}-10^{-1} mbar during the sputtering stage, keeping the pump at the maximum pumping speed, without damaging or tiring it.

The turbo pump doesn't work if electricity breaks off for a period longer than 50ms, in this case the pump panel is provided with some batteries that supply the magnetic bearing coils and make the blades slowing down. The slowdown of the pump, in case of blackout, represents a hard problem because the pumping arrests and, although the system remains sealed and there are no problems of contaminations, it is stopped until the pump isn't re-started up.

The turbo panel is connected to a control panel that command the opening and

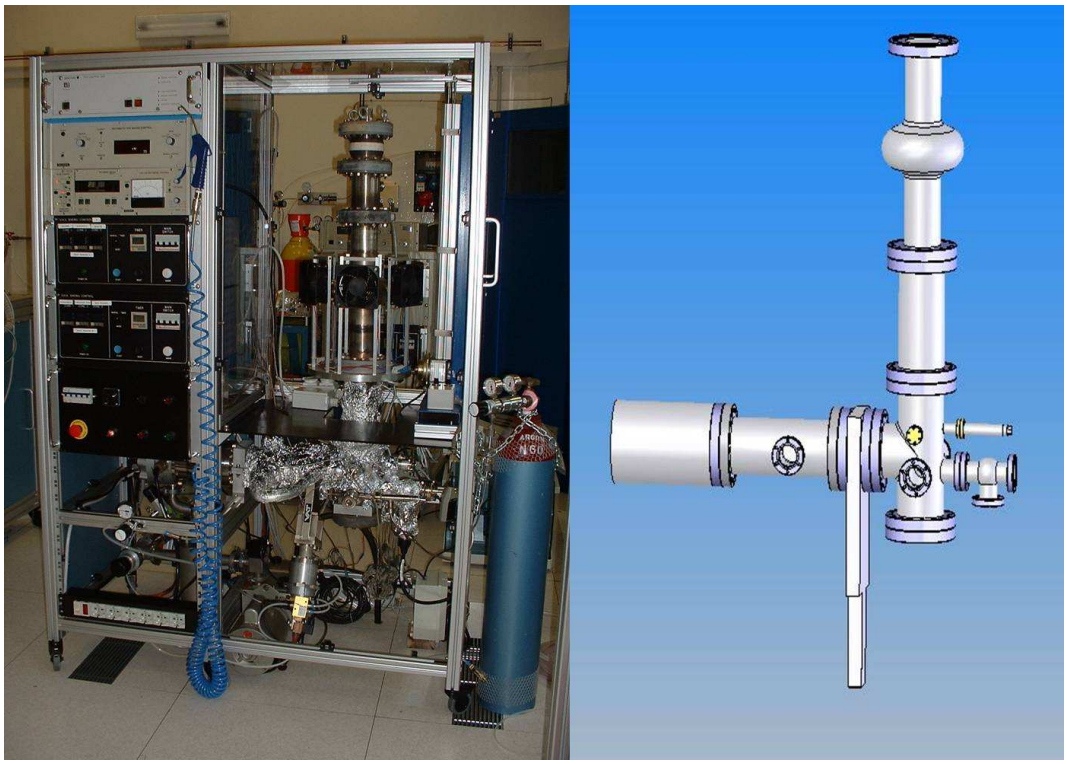

Figure 6.1: *Picture and drawing of the system used for depositions.*

closing of the gate. This panel is programmed in a way that the gate opens only when the pump has reached the maximum speed. This is not a problem if it is possible to reach a preliminary vacuum in the chamber using the bypass, so when the pumping is switched-on, the bypass has to be opened. The gate remains closed during the acceleration of the turbo because a good evacuation of the sputtering system has to be very slow; especially during the phase of viscous flux (1-10^{-3} mbar), when it is very easy to raise some dust or particles in the system.

The sputtering chamber has been ideally divided into three zones: the base, the cavity and the cathode. The base is connected to the pumping system through the gate valve and

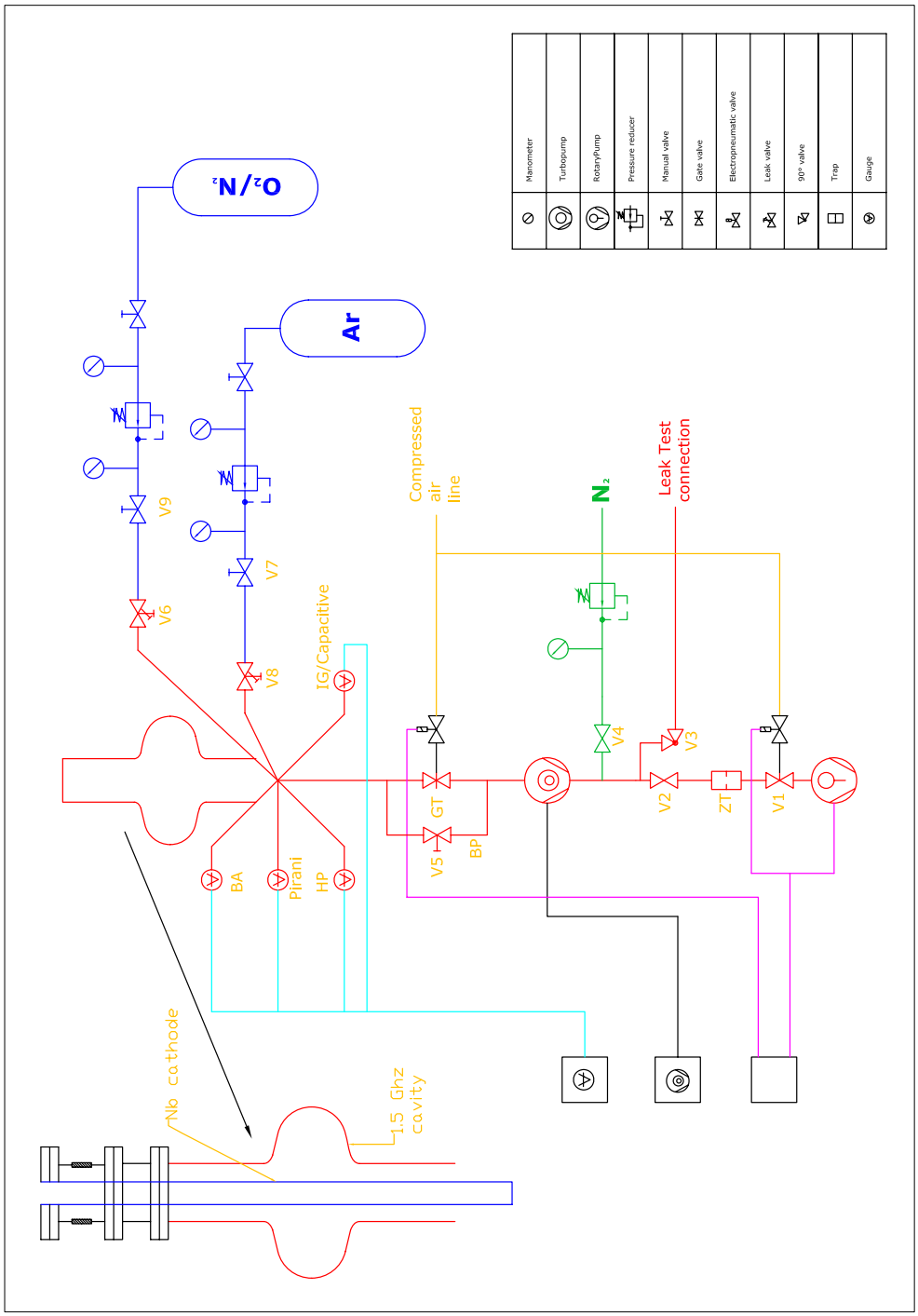

Figure 6.2: *Complete structure of the vacuum system.*

it is provided with a porthole through which visual monitoring to the plasma is possible. Several safety valves are placed all along the system and at the bottom of the vacuum chamber the following pressure gauges are connected:

1. Bayard-Alpert IMR112 Balzers (10^{-3}-10^{-8} mbar) BA,
2. Ion Gauge IMR 132 Balzers(10^{-6}-10^{-13} mbar) IG,
3. Pirani TPR018 (10^{3}-10^{-3} mbar) PG,
4. Capacitive CMR264 Pfeiffer(10^{1}-10^{-4} mbar) CG.

Three gas lines arrive to the base: the nitrogen one for the venting of the low vacuum area, the mixed oxygen-nitrogen one for the venting of the high vacuum chamber, and the pure argon one for the sputtering. The mixture oxygen-nitrogen (only used for the last depositions) enters the chamber passing through a valve (V6) UHV All-Metal: it is used to guarantee a controlled oxidation of the surface without humidity ($H_2O < 1$ ppm). The nitrogen, whose pressure is controlled through a pressure regulator at double stage, enters, through V4, the area behind the gate, while the argon N60 (purity 99,9999%) is "stocked" in a 15l bottle fixed in the system. The connection between the bottle and the line uses a Cajon system, followed by a all-metal angled valve (V7) and by an all-metal dosing valve precision valve(V8). During pumping and baking, the precision valve always remains opened while the all metal valve that precedes it, opens only during the sputtering. To place a precision valve to regulate the flux of argon at the base of the chamber means that the most part of the gas is immediately pumped and only a little fraction of gas is changed with the chamber. In this way, the pressure in the chamber is more stable and, moreover, the film contamination, due to the gas impurities, is reduced.

Most test have been executed using a stainless steel cavity, instead of a copper cavity. The steel cavity has some special sampleholders formed by two strips 120mm large, made of stainless steel and shaped in order to assume the inner form of the cavity (figure 6.3). The sampleholders are hooked to a screw welded on the wall of the inferior cut off; they are drilled on their length and to each hole corresponds a substrate position. The cavity zones are indicated in figure 6.4

The stainless steel chamber has the standard dimensions of a mono-cell cavity 1,5 GHz and at the end two CF100 flanges have been brazed to connect it to the vacuum system. At the equatorial level the cavity is provided with a CF35 flange on which a viewport can be fixed. Above and under the cavity two chambers, 25cm high, have been inserted to separate the cavity from the base and the cathode system. This precaution helps to avoid sputtering of valves and gauges. In addition using a cathode longer than the usual mono-cell cavity length it is possible to coat different cavities all along their surface.

All the flanges of the high vacuum area are Conflat or Cajon type with copper or silver gaskets. It's important to remind that each surface that is in touch with the vacuum shows a gas emission essentially due to four reasons:

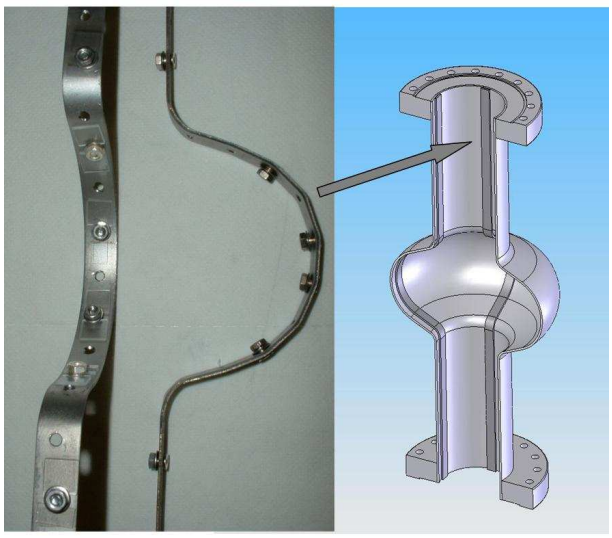

Figure 6.3: *Picture of the sampleholders used for the deposition of substrates and their positions in the chamber.*

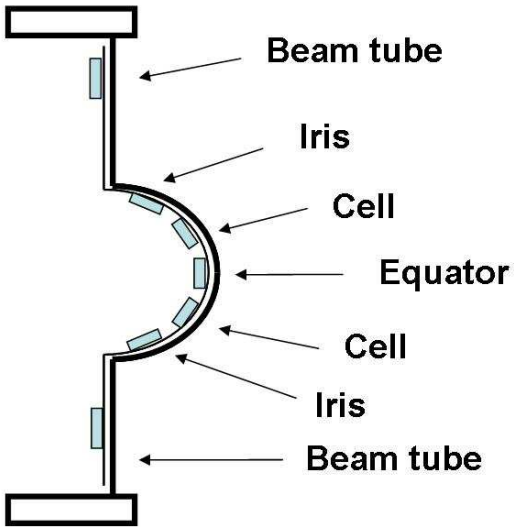

Figure 6.4: *The cavity is divided mainly in two zones: the beam tubes and the cell. The iris is the connection between the beam tube and the cell, meanwhile the equator is the central part of the cell.*

- Permeation, that is the passing of gas through the separation wall from an environment at a major pressure to one at a lower pressure;
- Diffusion from the bulk material, that can be of an interstitial type or through the vacancies;
- Desorption of molecules previously adsorbed;
- Vapour pressure of the material that composes the surface itself.

The combined effect of these phenomena is labeled "degassing" and represents (together with possible leaks) the main limit to the minimum pressure that can be reached in a Ultra High Vacuum system.

The specific degassing speed of a system is expressed in terms of quantity of gas per unit time per unit surface, expressed in $(Pa{\cdot}m^3)/(s{\cdot}\ m^2)$ or in $(mbar{\cdot}l)/(s{\cdot}\ cm^2)$ and it depends on the kind of material considered and its history. The following procedure has been used to estimate the degassing rate of the complete system: the gate is closed in order to seal the chamber, and the chamber pressure is monitored with time. The basic pressure is $1.7{\cdot}10^{-9}$ mbar. With an inner estimated surface equal to 0.4 m^2 and a volume of 8.3 lt, the degassing rate has been calculated:

$$\frac{dP}{dT} \cdot \frac{V}{A} \tag{6.1}$$

The value dP/dt is the pressure speed increasing in the chamber, obtained interpolating linearly the pressure variation with time. After a baking of 35h at 150°C a degassing rate equal to $8.4{\cdot}10^{-14}$ $(mbar{\cdot}lt)/(s{\cdot}cm^2)$ has been obtained. That value is good to obtain superconducting Nb films.

6.2 *The cathode*

The cathode is located on the axis of the system (figure 6.5). It consists of a vacuum tight stainless steel tube (liner) surrounded by a niobium tube. The niobium tube is a rolled niobium sheet, welded by the electron beam technique. It has an RRR superior to 250 because a high purity is necessary to reduce the contaminations of the film due to the cathode.

The liner is welded to a flange CF100 and closed at the base with a TIG welded plate. It supports the Nb cathode (cathodes of different diameters have been used) and the screen of quartz; the thermic and electrical contact with the niobium cathode occurs through nine steel tensioned tabs that can open or close to irreversibly increase the diameter of the steel tube (figure 6.6). A Nb disc, fixed by a screw to the steel tube, prevent the falling of the cathode, while the quartz screen avoids the insulator metallization. If not used, the whole system of the cathode is left in a clean room class 1000, to maintain it clean and avoid that some dust deposits on it.

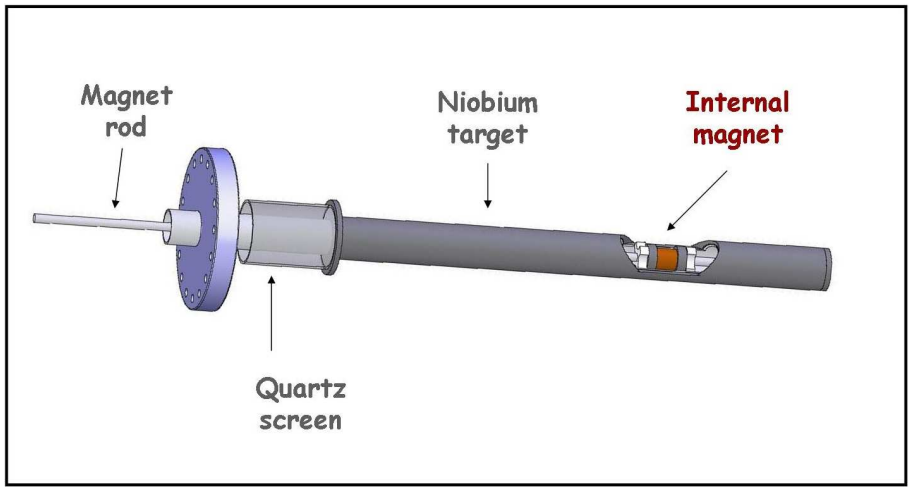

Figure 6.5: *Cylindrical Standard Cathode.*

The Nd-Fe-B magnet is kept between two little iron circles that concentrate the magnetic field lines. The whole assembly of magnets and irons are fixed on a stainless steel tube of 9mm diameter that assure the movements up and down inside the liner. The magnet and bar assembly movements inside the cathode occurs through an electro-mechanic actuator mounted on the side of the sputtering camera. It is controlled by a remote control and it moves at a user controlled speed. In order to know the magnet position, a dashboard that reproduces the shape of the cavity is mounted on the top of the system. To avoid some current flowing from the cathode liner walls, through the magnet to the actuator, the magnet is isolated from the moving 9mm diameter bar.

If not specified, the configurations described in this work are all developments of new

Figure 6.6: *Detail of the steel tabs built up to guarantee the electric contact between the stainless steel tube and the Niobium target.*

cathodes keeping the characteristics described in this paragraph.

6.3 *The cooling system*

During the sputtering the cathode is subjected to an ionic bombardment and can reach temperatures of 1000-1500°C in function of the power. To avoid the overcoming of the temperature of demagnetization, called temperature of Curie and equal to only 80 °C, it is indispensable that the magnet inside the cathode is efficiently cooled during sputtering. Originally the magnet was cooled by a flux of compressed air forced at 7 bar through the small tube that sustain the magnet. Then the cooling system have been modified to increase the cooling efficiency. At the moment the magnetron cathode is cooled by a water closed circuit. The water flows down through the tube that sustains the magnet; then it flows back inside the stainless steel tube and goes out from the aperture above the cathode flange as described in figure 6.7.

6.4 *Standard coating technique*

To plan some magnetron configurations and coating thin films with the requested qualities, the first step has been the CERN standard procedure sputtering schematized in Figure 6.8.

6.4.1 *Results of the Standard coating technique*

In the Cylindrical Magnetron (CM) configuration the standard procedure is:
"the extension tubes are coated first in an argon atmosphere of $1x10^{-2}$ mbar; a stable current of 1A is set between the cathode and the grounded sample holders. The magnet is moved in 14 steps over the cathode length in order to coat each tube uniformly. The cell is coated with slightly different discharge parameters, leaving the magnet fixed in its center for 15 minutes: the argon pressure is reduced to $1.5x10^{-3}$ mbar so as to increase the mean free path of the atoms ejected from the cathode and the current is increased to 3A (400V) to rise the sputtering rate."[75]

Niobium films have been coated both on quartz and copper samples. Deposition on quartz was a method adopted at CERN 25 years ago [99]. From this method its not possible to extrapolate conclusions about cavity quality but it gives threshold parameters because, if niobium on quartz shows bad results, it won't likely have better results on copper. In addition, film on quartz could be tested with the four contacts method in order to evaluate the resistive properties varying the temperature, thereby deposition on quartz alert about possible problems. Measuring the resistive properties also allows to compare different coating techniques and help to establish which one has the better application for coating resonant cavities.

More than 30 runs have been tested for coating samples and cavities with the standard cylindrical magnetron. Some variations from the standard method, especially in current

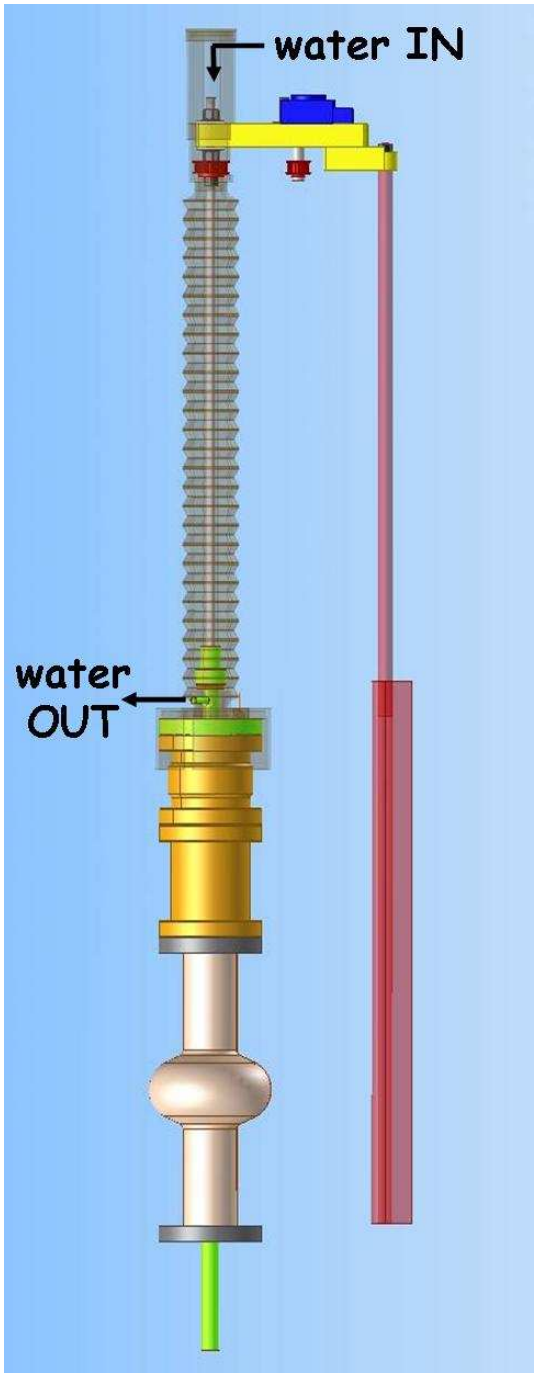

Figure 6.7: *The cathode and the magnet are cooled by a water closed circuit and the water flows through the tube that sustains the magnet to the stainless steel tube.*

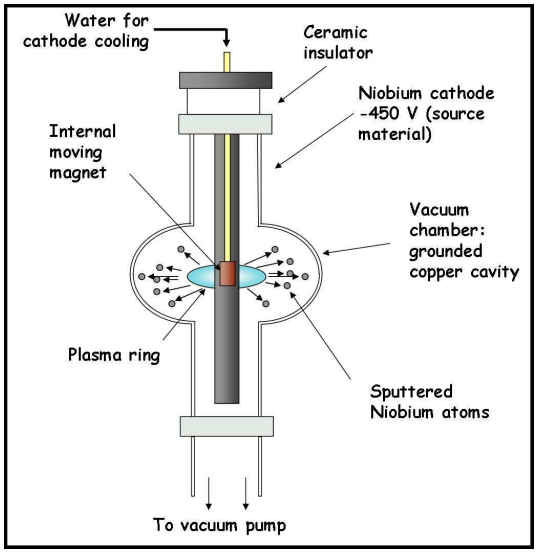

Figure 6.8: *Simplified structure of the standard CERN configuration for sputtering niobium into 1,5 GHz copper cavities.*

and pressure values, have been studied [100]. This section focus the attention on just some of the obtained samples, that have been characterized looking at the superconducting properties and the morphological properties collected with the collaboration of "Rome3" "Interdepartmental Laboratory of Electron Microscopy" (LIME).

Morphological characterization of coatings (in-plane and cross-section coating investigations, coating thickness, microstructure and crystallite size measurements, surface and layer interface analyses) were performed using Digital Optical Microscopy and Scanning Electron Microscopy techniques. Surface roughness measurement was carried out by Contact-Mode Atomic Force Microscopy analysis: roughness parameters (Roughness Average, Ra, Root Mean Square, RMS, Peak to Peak) were obtained after statistical analysis on a total scanned area of about $750\mu m^2$.

Each subsection describe one or more runs, the coating parameters applied, the used characterization technique and the respective result properties. Last subsection deal with the coating of two 1,5 GHz copper cavities.
Composite Hardness measurements were performed using Vickers standard indentation tests, with loads ranging from 100g (1N) down to 0,5g (0,005N). The obtained value for each load corresponds to the mean of six measures.

In order to extrapolate film intrinsic hardness, the Jonsson & Hogmark [86], the Chicot & Lesage [87] and the Korsunsky [89] models have been used. Work hardening behaviour was taken into account as well, by adopting the Indentation Size Effect (ISE) Meyer's law [87, 88]. More details on that models and their application range are collected in Chapter 4. AFM analysis of the residual indentation marks shape was also performed in order to have more reliable data for low-load ($<$ 10 gf) indentations.

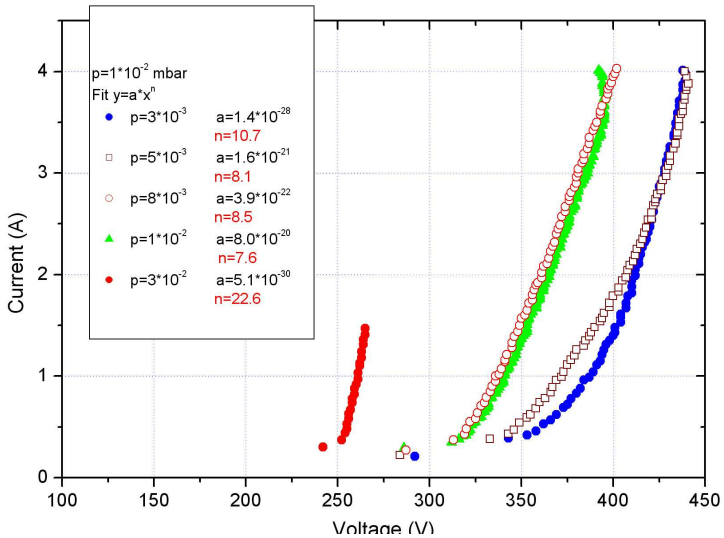

Figure 6.9: *I-V curves at different pressure for the standard coating configuration. The magnet is left leveled with the cavity cell.*

Thin films on copper substrates and morphological analysis

Run 10 is one of the few deposition executed on copper substrates. Samples have been processed as follows:

- grinding with Scotch Brite^{TM}
- 10 minutes electropolishing
- 5 minutes chemical etching (SUBU)
- Ultrasonic rinsing
- 5 minutes passivation
- Ultrasonic rinsing

Five substrates have been placed in different positions inside the cavity cell. Sample 765 and 766 are positioned exactly above and belove the equator and they have been deeply characterized. In table 6.1 the coating parameters are summarized.

Figure 6.10 shows on the left and electropolished copper substrate. On the right the substrates is electropolished and chemical polished. The EP process left a smooth surface where grains are barely visible. On the contrary CP reacts on defects and grain boundary (high surface energy zones) and expose a cleaner but rougher surface.

In figure 6.11 coated and plane copper surfaces of samples 765 and 766 are put side by side; the mean crystallite area vary between 590 and 290 μm^2 while the equivalent diameter vary between 27 and 19 μm. The film morphology reflects the substrate structure perfectly; this is evident also, with higher magnitude, in figure 6.12 obtained with the optical microscope. The coated surface is never perfectly plane.

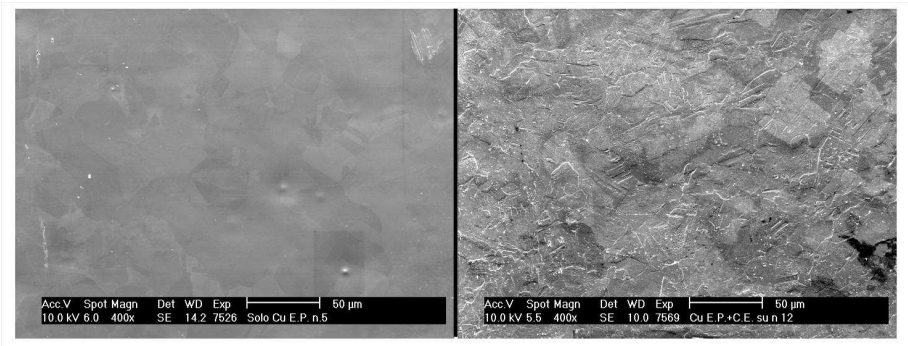

Figure 6.10: *SEM images of an electropolished copper sample (on the left). On the right the same sample have been chemical polished after EP.*

Run	I_{cell} (A)	p_{cell} (mbar)	$time_{cell}$ (min)	I_{tube} (A)	p_{tube} (mbar)	$time_{tube}$ (min)	details
10	3	$1.5 \cdot 10^{-3}$	15	1	$1 \cdot 10^{-2}$	1.45	copper substrates

Table 6.1: *Summary of the coating parameters used in Run10, applying the standard technique.*

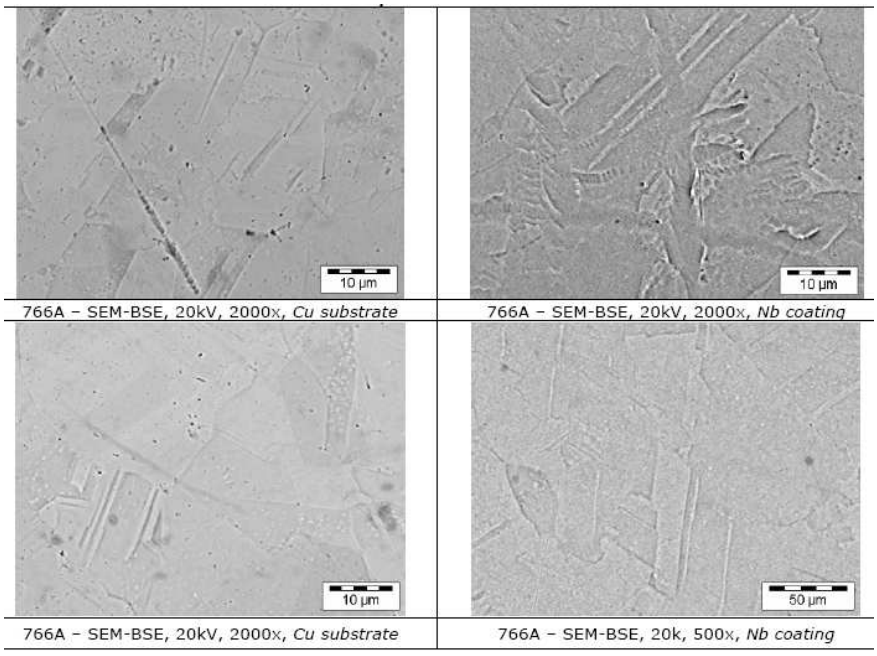

Figure 6.11: *SEM images of the plane copper surfaces (on the left) and the niobium coating (on the right) for samples 765 and 766 positioned on the equator during Run10.*

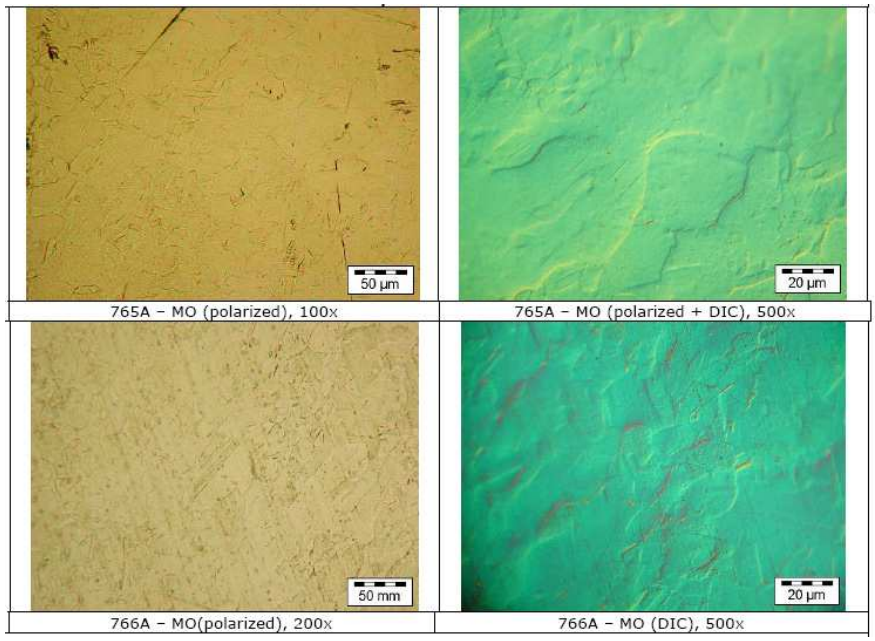

Figure 6.12: *Images of the niobium coating (on the right) for samples 765 and 766 positioned on the equator during Run10. They are obtained with the optical microscope.*

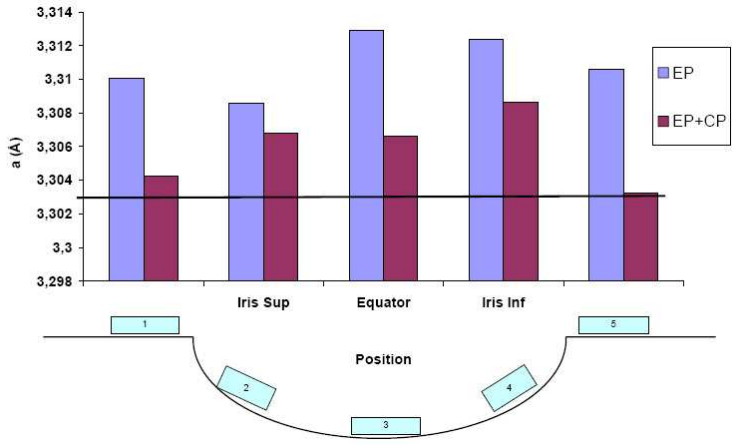

Figure 6.13: *Lattice parameter value versus position for the standard coating of niobium thin film on copper samples. a is calculated with the Bragg formula from X-ray diffraction spectra. The black line is leveled with the a lattice parameter of bulk niobium.*

X-ray diffraction spectra on niobium coated films have been analyzed. Lattice parameters and grain dimension have been estimated with the Bragg formula. Results are showed in figure 6.13. It is the typical behaviour of standard cylindrical magnetron coatings on copper substrates of the cell area: a increases on the equator and all samples show a stressed lattice parameters, higher that the bulk niobium. Lattice stress is due to the impact energy of the atoms arriving on the growing film and to the lattice parameter difference between film and substrate. From this analysis niobium film growing on an electropolished and chemical polished substrate seem to be less stressed.

AFM and high magnitude SEM images (figure 6.15) reveals an homogeneous structure

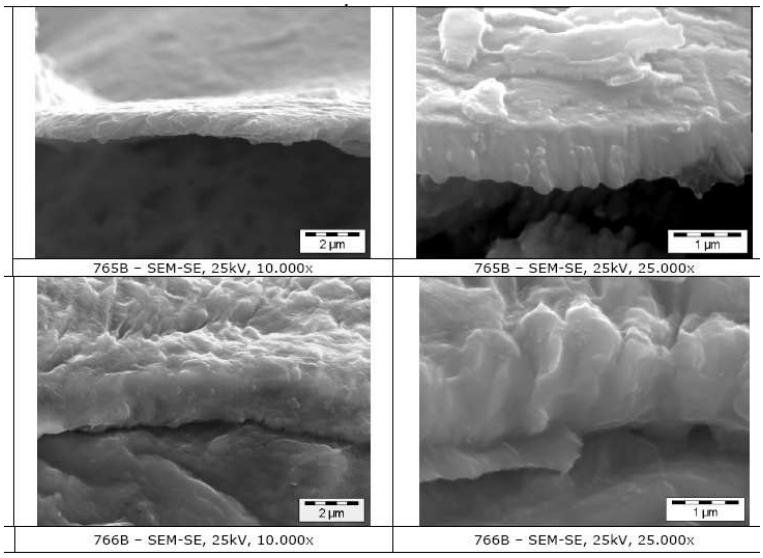

Figure 6.14: *SEM-SE-BSE cross section images of Nb films. Samples have been sectioned by brittle fracture in liquid nitrogen.*

with a mean grain dimension of 150-200nm. The mean height difference between grains is about 200nm. No preferential growth are observed. Roughness results are summarized in table 6.2.

Coating thickness have been observed with the SEM-SE-BSE technique. Images 6.14

Properties	**Samples**	
ID sample Run10	765	766
Thickness (μm)	1 ($\pm$0.1)	1.9 ($\pm$0.2)
Roughness:RMS-R_a-Peak to peak [nm]	7.6 - 6.1 - 46	8.2 - 6.6 - 43.5
Growth angle	11.3°	14.7°

Table 6.2: *Summary of the coating parameters used in Run10,applying the standard technique.*

show the preferential growth of coating crystal columns, the shadow effect allows to measure the growth angle respect to the substrate: samples 765 and 766 of run10 have growth angles less then 15° with the normal to the substrate.

Indentation size effect curve and the intrinsic hardness of run10 samples have been extrapolated using the Jonsson & Hogmark [86] and the Chicot & Lesage [87] models. Coating Elastic recovery was evaluated by 3D AFM reconstruction [101] of residual indent volume and applying Lesage model [102], by which an evaluation of the elastic recovery is performed after comparison between the actual volume of the residual indent and its theoretical value on Vickers indentation marks. Results are summarized in table 6.3.

From SEM images analysis (figure 6.16) a marked elastic recovery, after the indenter removal, is evident. In fact the pyramidal marks show the typical bending on each sides. The total absence of cracks all around each mark, even for the higher load, confirm that the film has a ductile behaviour. Intrinsic hardness calculated with the two models clearly differ, this fact is explained in chapter 4.

Model	**Samples**	
	765	**766**
Chicot & Lesage Intr. hard. (kg/mm^2)	561.5	400.5
Jonsson & Hogmark Intr. hard. (kg/mm^2)	329.3	255.3
Vickers hardness (kg/mm^2)	163.9	303.38
hardening index	0.3209	0.4782

Table 6.3: *Intrinsic hardness calculated with the Chicot & Lesage and Jonsson & Hogmark models, Vickers hardness and hardening index,of sample 765 and 766 (niobium on copper) Run10.*

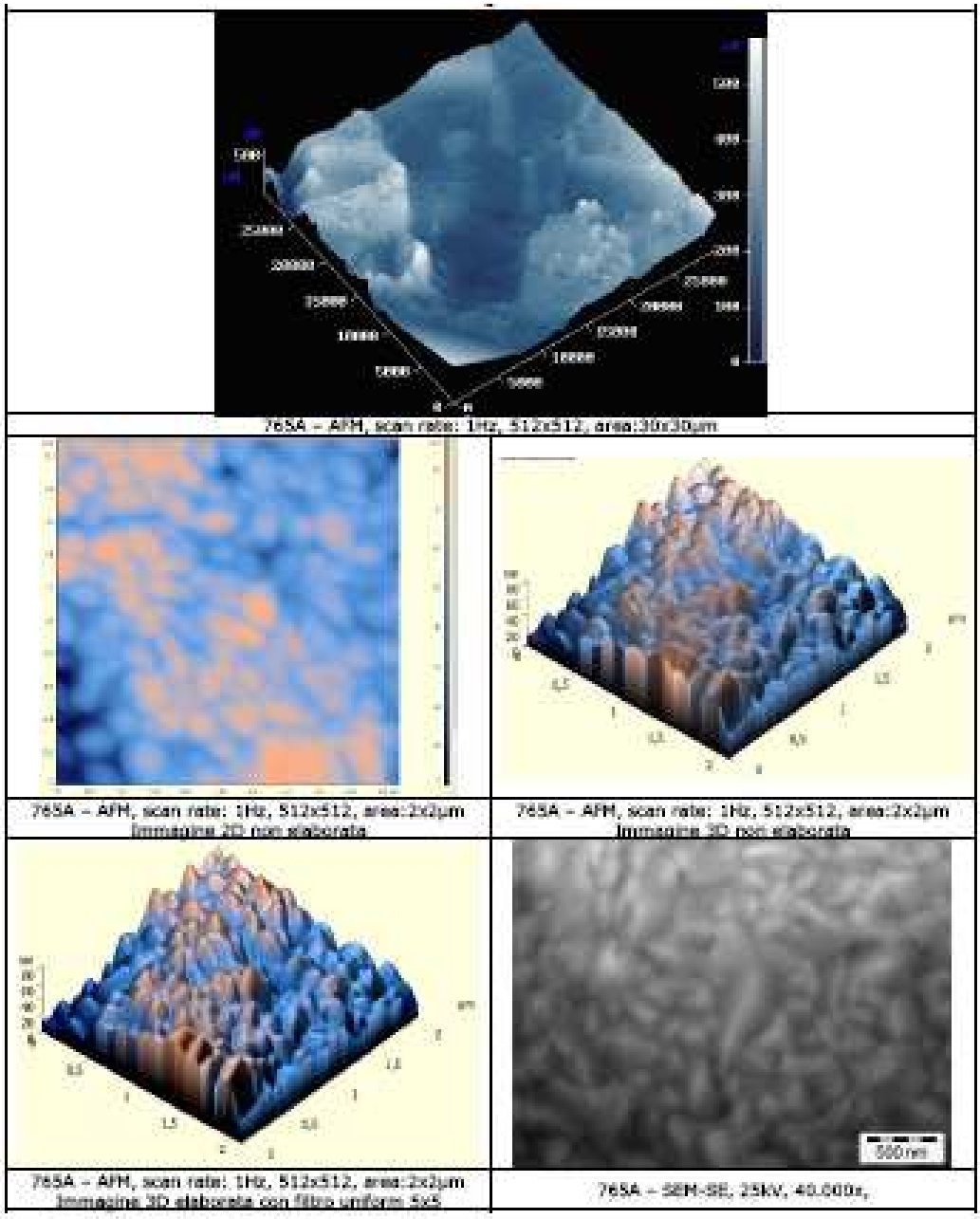

Figure 6.15: *AFM and high magnitude SEM-SE images of Nb film on copper.*

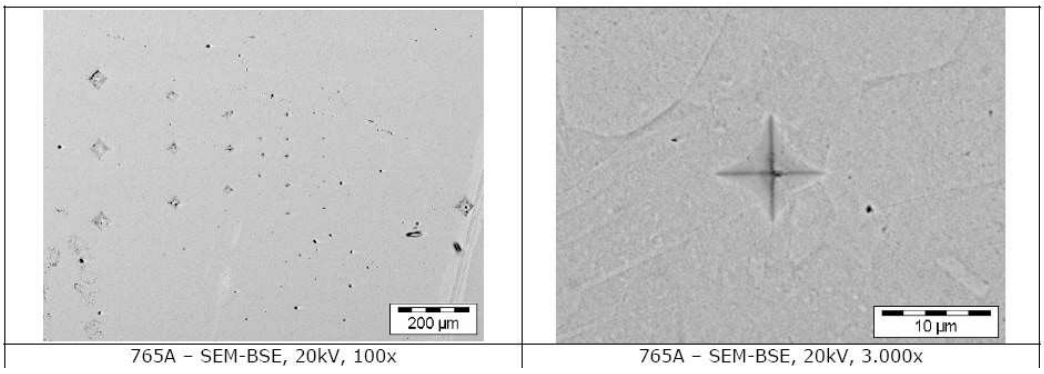

Figure 6.16: *SEM images of the microindentation maps (on the left) and one indentation mark.*

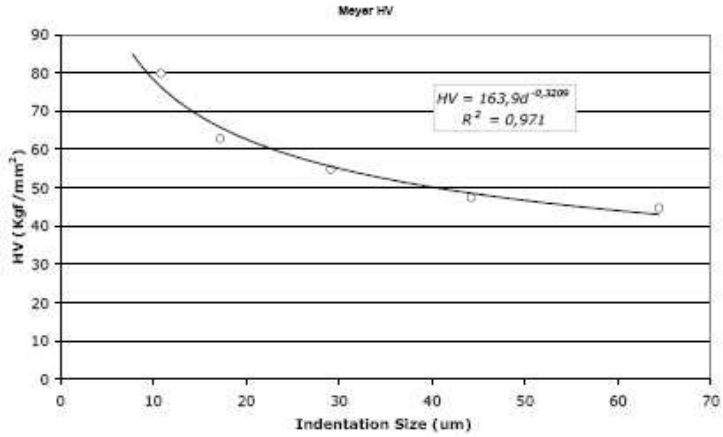

Figure 6.17: *Indentation size effect curve (Mayer model) to determine the Vickers microhardness.*

Thin films on quartz substrates and superconducting properties

In this section niobium thin films on quartz substrates properties are enumerated. considerations about the differences between thin films coated on copper or quartz substrates are developed in chapter 9, and several analysis are compared and discussed.

Quartz substrate allows to execute easily the electrical analysis with the four probe method. In chapter 4 the two four probe methods applied to obtain the following results are briefly mentioned. Sputtering rate depends on pressure, cathode current and mag-

Run	I_{cell} (A)	p_{cell} (mbar)	$time_{cell}$ (min)	I_{tube} (A)	p_{tube} (mbar)	$time_{tube}$ (min)	details
23	3	$1.5{\cdot}10^{-3}$	15	1	$1{\cdot}10^{-2}$	1.45	
24	3	$1.5{\cdot}10^{-3}$	15	1	$1{\cdot}10^{-2}$	1.45	
25	3	$1.5{\cdot}10^{-3}$	15	1	$1.5{\cdot}10^{-3}$	1.30	the same p for all cavity
26	3	$1.5{\cdot}10^{-3}$	15	1	$1.5{\cdot}10^{-3}$	2	beam tube with 2 min. step
30	7	$2{\cdot}10^{-3}$	15	2	$3.4{\cdot}10^{-3}$	1.20	water cooling
31	7	$2{\cdot}10^{-3}$	20	3	$3.4{\cdot}10^{-3}$	1.20	increased $time_{cell}$

Table 6.4: *Summary of the coating parameters used in Runs 23-24-25-26, applying the standard technique.*

netic field intensity. Actually the sputtering rate decreasing was unexpected, because the pressure was nearly constant and the current is more than doubled. Actually the only explanation could be the magnet degradation. As explained in section 6.3 during run 24, 25 and 26 the magnet was still cooled with compressed air forced in the cathode liner. Run 30 and 31 have been executed after the cooling system upgrading with the water closed circuit. After this improvement still the sputtering rate is low because the current have been doubled respect to the previous test so the produced heat is higher. In addition the magnet degradation is not completely reversible. To compensate the sputtering rate decreasing the coating time have been increased to 20 minutes in run 31.

Figures 6.19 and 6.20 collects all RRR and Tc results of the five runs. Estimated errors for RRR and Tc are respectively 5 and 0.05K . The RRR at the equator vary from 16 to 34 and for the first three run there is gradual improvement as long as the cathode is sputtered. Then Best RRR and Tc results at the equator are 34.5 and 9.42K that correspond to Run 31 where the cell have been sputtered 20 minutes instead of 15 minutes. Time of sputtering has a strong influence on the film purity and consequently on RRR: the higher is the sputtering time, the purer is the gas in the chamber and the cleaner is the atoms flux arriving on the substrate, due to the getter property of the growing niobium.

Tc higher than Nb bulk means a compressive stress of the crystal lattice, confirmed also by X-ray diffraction cell parameter measure a = 3.29Å respect to the bulk value a_0 =3.303Å (figure 6.21). In table 6.5 RRR and Tc result, measured with the second four probe method mentioned in chapter 4, are collected for run 30 and 31. Values dif-

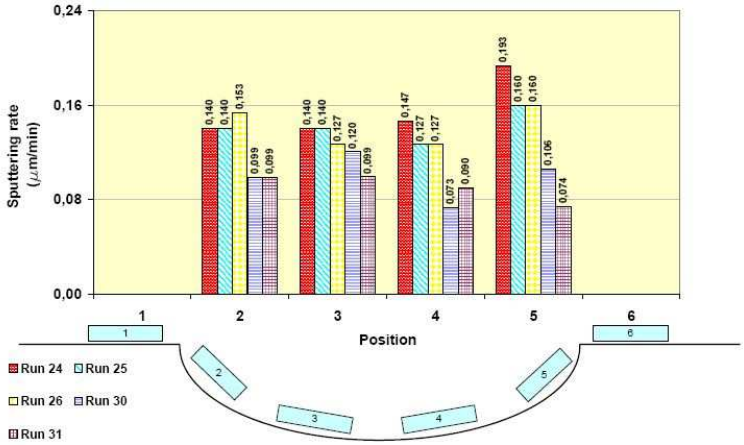

Figure 6.18: *Sputtering rate of the niobium target, for different positions around the equator and five different runs. Sputtering parameters are summarized in table 6.4*

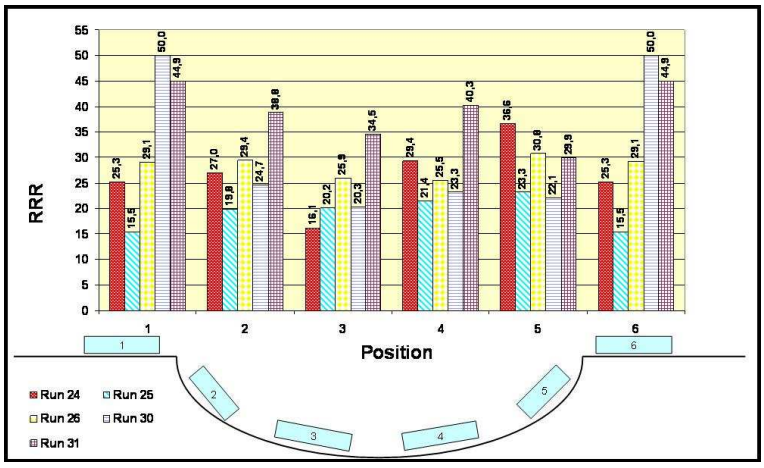

Figure 6.19: *RRR values of the niobium film on quartz sample, for different positions around the equator and five different runs. Estimated error for RRR is 5. Data are obtained with the four point probe method explained in chapter 4.*

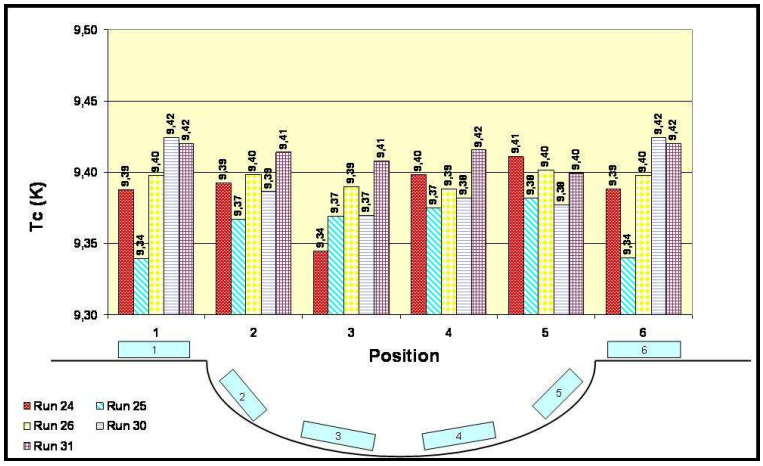

Figure 6.20: *Critical temperature Tc of the niobium film on quartz sample, for different positions around the equator and five different runs. Estimated error for Tc is 0.05K. Data are obtained with the four point probe method explained in chapter 4.*

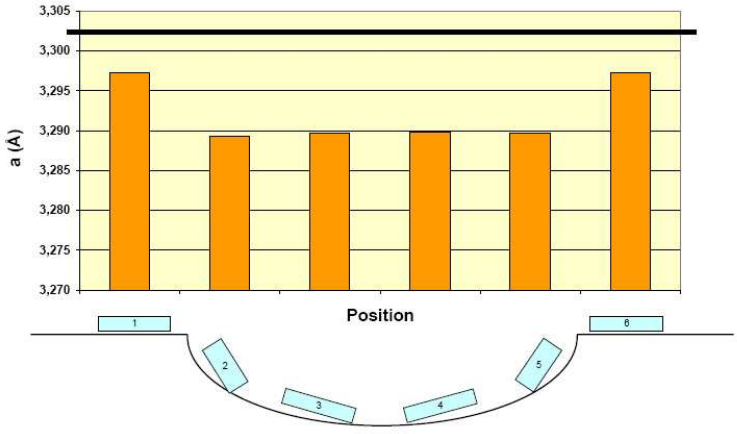

Figure 6.21: *Lattice parameter value versus position for the standard coating of niobium thin film on quartz substrates. a is calculated with the Bragg formula from X-ray diffraction spectra. The black line is leveled with the a lattice parameter of bulk niobium.*

ferences are due to the distinct cooling speed of the two methods. At the moment data collected in table 6.5 are reasonably more accurate. Niobium unbiased film on quartz

Run	Position	RRR	ΔRRR	Tc (K)	ΔTc (K)	Thickness
30	eq.Up	25	0.3	9.36	0.09	1.807
	eq.Down	23	0.6	9.42	0.03	1.094
31	eq.Up	34	1.7	9.40	0.08	1.985
	eq.Down	32	0.7	9.35	0.11	1.805

Table 6.5: *Summary of the Tc and RRR values measured for quartz samples coated with the standard cylindrical magnetron. Samples have been placed in the cell just above (Up) and below (Down)the equator position. Data are obtained with the second four point probe method explained in chapter 4.*

shows a needle-shaped grain structure with an average longitudinal dimension of 300-350 nm (figure 6.22). AFM measures reveal a roughness RMS-Ra-peak to peak respectively of 4.37-3.47-29.38nm.

An example of hardness and elastic module values for standard niobium coating on quartz are reported in figure 6.23. Due to the low indentation depth, this results could be influenced by the superficial oxide layer properties that is usually more than 10 nm thick.

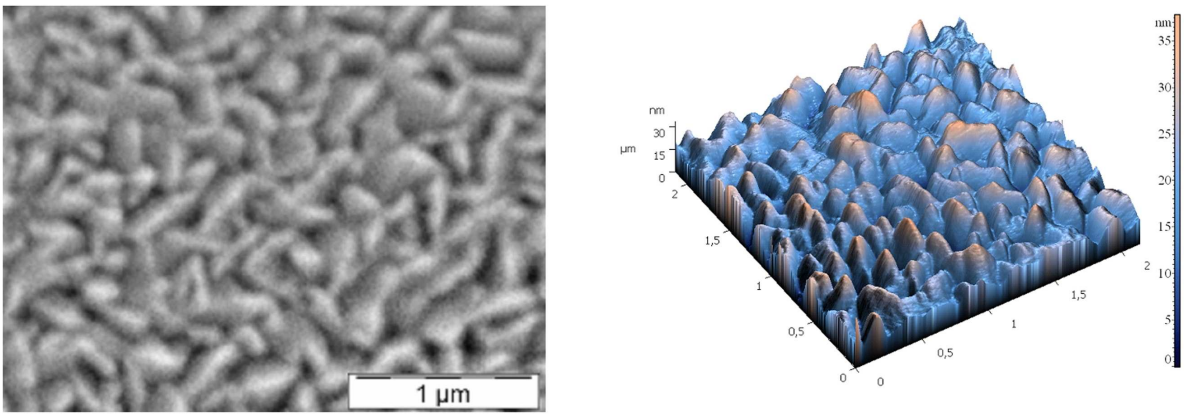

Figure 6.22: *SEM-AFM Surface morphological analysis on Nb thin films: (on the left) Nb on quartz standard coating run 30 (SEM SE 20 kV 40000x); (on the right) Nb on quartz standard coating run 30 (Contact Mode AFM). Coating parameters are summarized in table 6.4.*

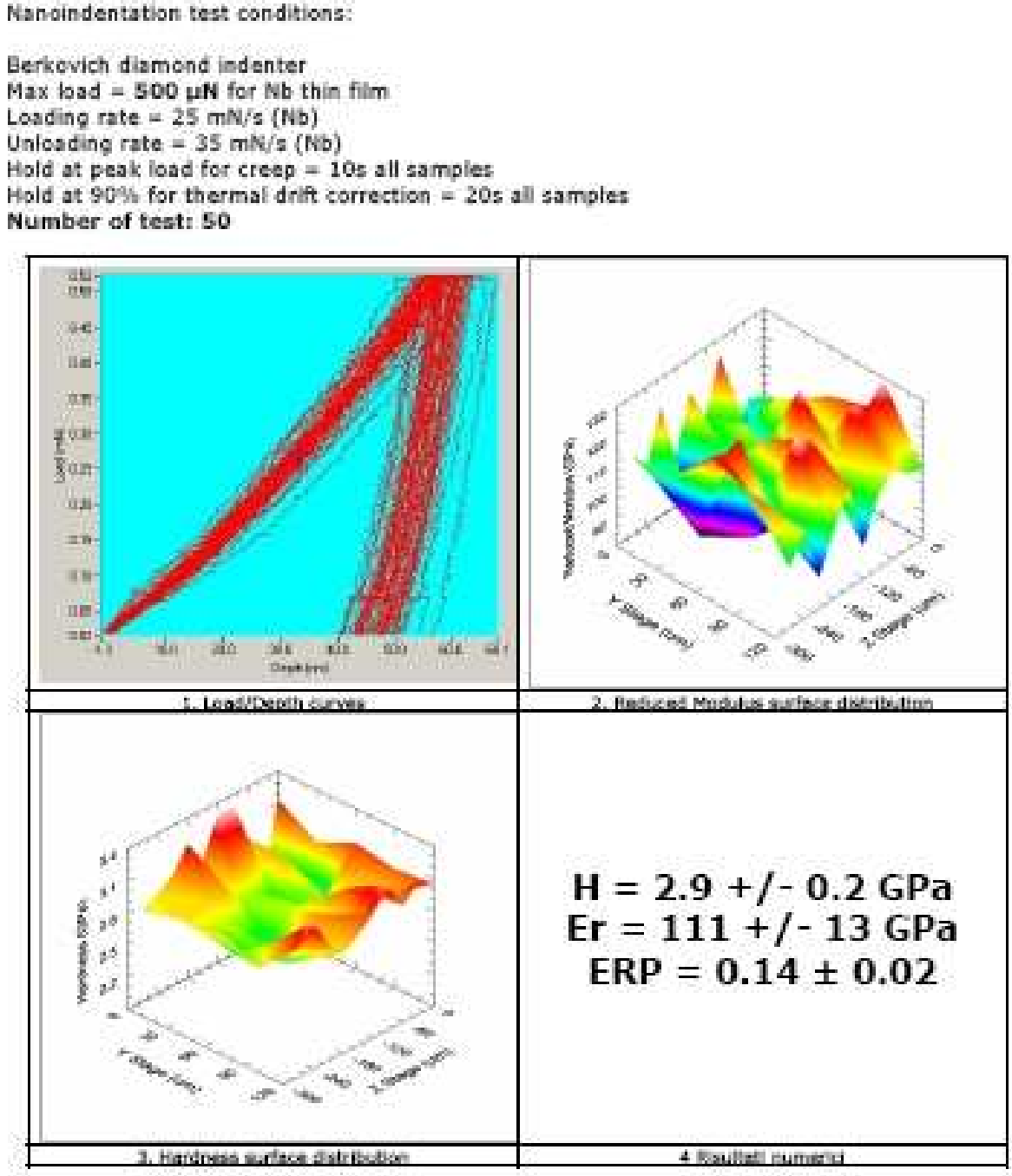

Figure 6.23: *Nanoindentation of niobium thin film on quartz substrate: 1.Load/Depth curve, 2.Reduced Modulus surface distribution, 3.Hardness surface distribution, 4.Numerical results.*

Coating of 1,5 GHz copper cavities

Two copper cavities, fabricated by spinning and CF100 flanged on both sides, have been coated. They are two 1.5GHz tesla-type cavity, signed with L1 and L2 identification name. These two cavities have been coated and etched several times but only the last treatments before each measure are reported.

L1 cavity has been coated and then measured twice. Coating parameters are collected

Run	I_{cell} (A)	p_{cell} (mbar)	$time_{cell}$ (min)	I_{tube} (A)	p_{tube} (mbar)	$time_{tube}$ (min)	cavity
27	3	$1.8{\cdot}10^{-3}$	15	1	$1.5{\cdot}10^{-3}$	2	L2
28	3	$2{\cdot}10^{-3}$	15	1	$2{\cdot}10^{-3}$	2	L1

Table 6.6: *Summary of the coating parameters used in runs 27 and 28, for coating L1 and L2 1.5GHz copper cavities applying the standard technique.*

in table 6.6. RF test have been executed as described in chapter 5. Errors on the Q and Eacc values are respectively 13% and 5% and have been calculated with the software created by Powers [93], assuming that:

- the linearity of the power meter is ± 2%
- percentage error on the pickup-Q Q_{pk} 11%

Starting from L1, this cavity has been processed as follows:

- Stripping from the previous coating
- 1 hour electropolishing
- High Pressure Water Rinsing (HPWR) 1 hour at 100 bar
- 15 minutes chemical etching
- 5 minutes passivation
- High Pressure Water Rinsing (HPWR) 1 hour at 100 bar
- Standard coating run28 keeping the cavity at 150°C
- HPWR 1 hour at 100 bar
- rf test (figure 6.25)
- High Pressure Water Rinsing (HPWR) 1 hour at 100 bar
- 2nd rf test (figure **??**)

Figure 6.25 shows the excitation curve of the L1 resonator; plotted is the quality factor Q_0 as a function of the accelerating electric field Eacc. The cavity has been measured at 4.2K and at the beginning the quench was clearly visible at 2MV/m. After the first curve, the cavity has been conditioned and it reached 8.8MV/m with a Q_0 of $1.9{\cdot}10^8$. The test stopped at 4.2K because liquid helium wasn't enough and the coupler was too short for the 1.8K test. In the second L1 rf measure the coupler antenna length covers the range between 10^7 and $3.5{\cdot}10^{10}$. At 1.8K the registered Q_0 is $3.4{\cdot}10^9$ and the maximum accelerating field

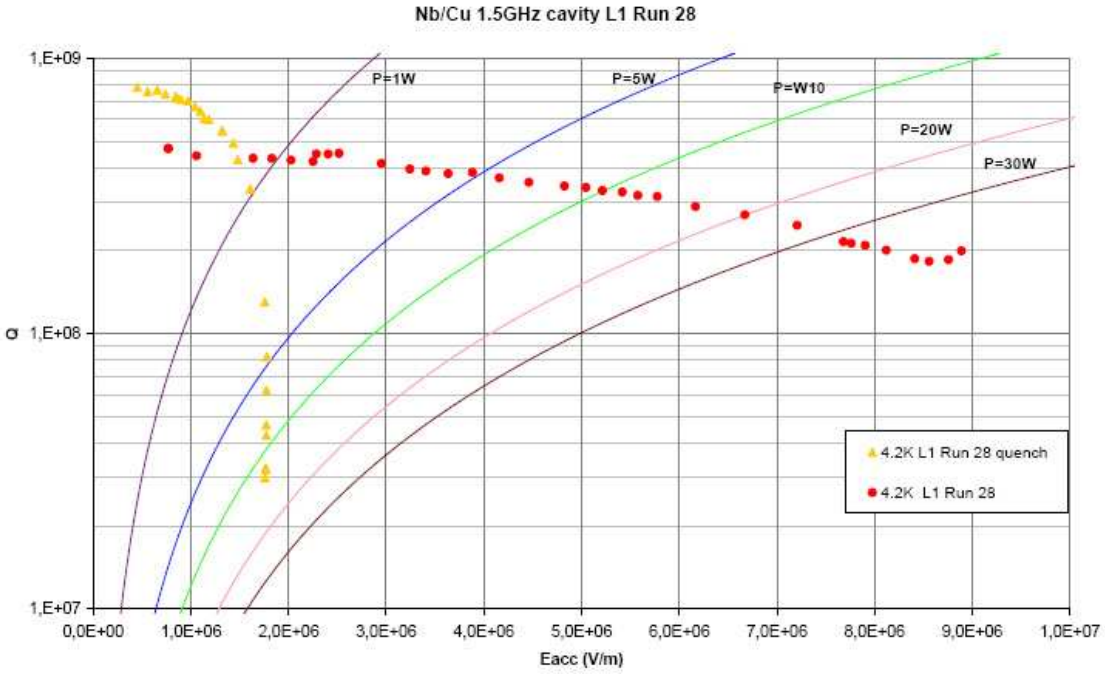

Figure 6.24: *Excitation curves of electropolished niobium on copper one-cell 1.5 GHz cavity named L1. Coating parameters are summarized in table 6.6, run 28 .*

is 8.9MV/m. The Q slope is clearly visible and more emphasized at 1.8K than at 4.2K. The cavity quenches around 20W of forwarded power. Cooling the cavity from 4.2K to 1.8K implies a gain of a factor of 1.

Even if it is still far from the best niobium on copper cavities performances, the L2 cavity reaches 14MV/m with a Q_0 of $2.7 \cdot 10^8$ at 1.8K (figure 6.26). It starts from a Q_0 of $2.4 \cdot 10^9$ and it quenches around 90W of forwarded power. The various cavity treatment steps for arriving at such performance are illustrated in the next list:

- Stripping from the previous coating
- 1 hour electropolishing
- High Pressure Water Rinsing (HPWR) 10 min at 100 bar
- 15 minutes chemical etching
- 5 minutes passivation
- High Pressure Water Rinsing (HPWR) 30 min at 100 bar
- Standard coating run 27 keeping the cavity at 150°C
- HPWR 1 hour at 100 bar
- rf test (figure 6.26)

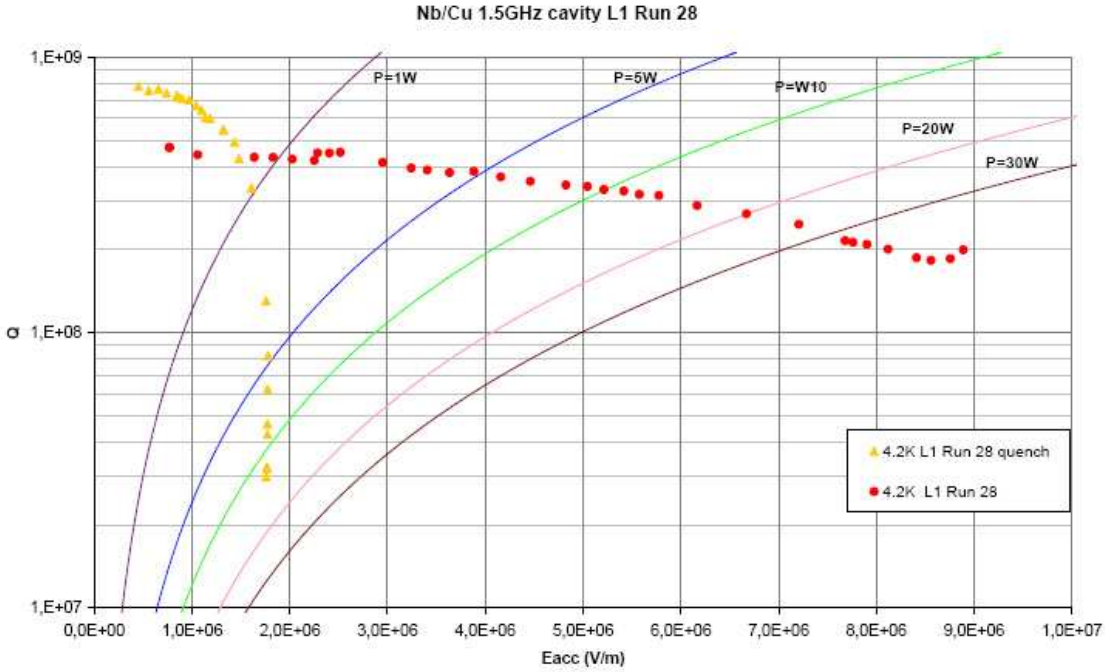

Figure 6.25: *Excitation curves of electropolished niobium on copper one-cell 1.5 GHz cavity named L1. Coating parameters are summarized in table 6.6, run 28 .*

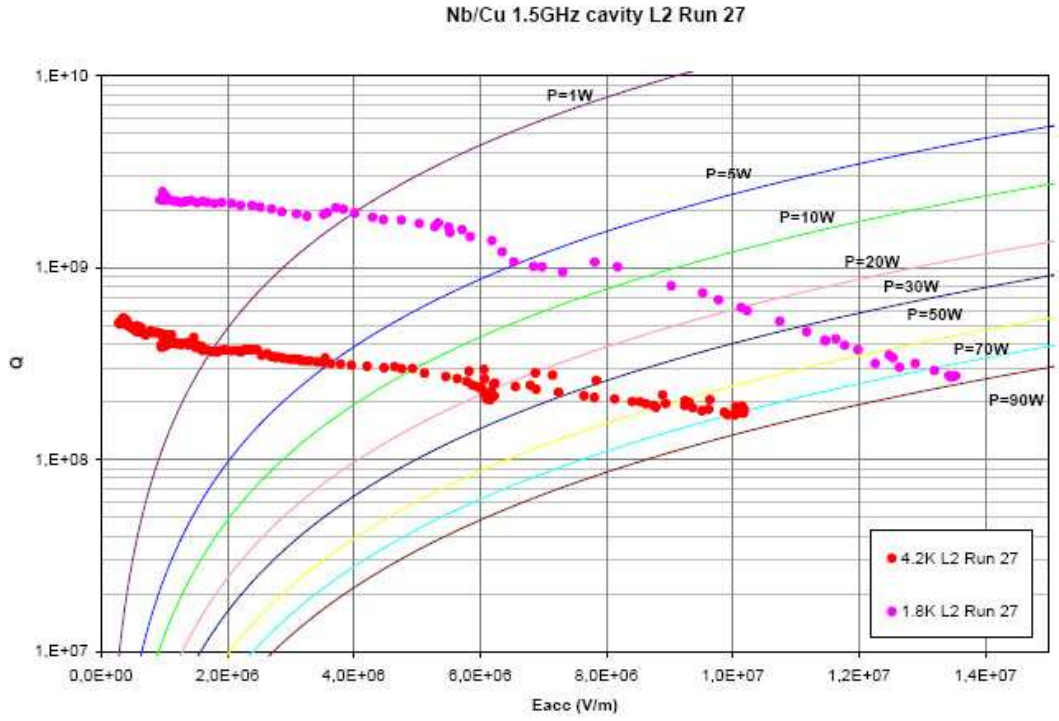

Figure 6.26: *Excitation curves of electropolished niobium on copper one-cell 1.5 GHz cavity named L2. Coating parameters are summarized in table 6.6, run 27.*

Chapter 7

Shaped Cathodes

In this chapter the attention is focalized on two cavity shaped cathode built with the aim of removing the angle effect and increase the sputtering rate. A niobium ring, 48.5 mm maximum diameter and 27 mm high, has been positioned around the cathode tube, leveled with the cavity cell. The magnetic field is produced by a 2 cm high NdFeB permanent magnet located in the middle of the cell, inside the cathode, centered with the niobium ring. This configuration aims to reduce the deposition angle and to increase the area where the magnetic field is perpendicular to the electric field. The other developed idea consists of ten cavity shaped cloves cathode coaxial with the cavity. A stainless steel tube, coaxial with the cavity as well, is biased positively and it works as ion attractor and as support for the whole cathode system. The bias grid can be placed behind the cathode thanks to the plasma conductivity that grants an increase of the plasma voltage inside and outside the cathode. Advantages of this configurations are: substrate-cathode distance reduction and parallelism; a higher cathodic area and the absence of the shadowing effects due to the grid [103, 92].

7.1 *Increasing the RRR and building of new configuration*

The possible methods to increase the RRR value of the Nb films are:

- inducting an ionic bombardment of the growing film;
- spread of the inner solid mass, that can be of an interstitial type or through the vacuums;
- creating a cavity-shaped cathode;
- increasing the ionization efficiency of the magnetron.

For each method the following aspects have been considered:

- the fundamental theory;
- the scientific community knowledge about the technique analyzed;

- all test performed by the candidate to verify the efficiency of the technique and the applicability for cavity coatings.

7.1.1 *Impurities and sputtering rate*

The fraction f_i of impurities of the species i trapped into the film during sputtering is:

$$f_i = \frac{N_i \alpha_i}{N_i \alpha_i + R} \tag{7.1}$$

where N_i is the number of atom of species i that bombards the film unit area in the unit time , α_i is the relative stiking factor and R is the deposition rate of the film.
There are three ways to reduce the value of f_i:

- increasing the sputtering rate R;
- decreasing the number of atoms of the species i that arrive on the surface (for example decreasing the basis vacuum of the system);
- decreasing the value of α_i, that means decreasing the probability of adhesion of the species i.

The deposition rate can be increased, maximizing the probability of ionization of the electrons: the longer the way completed by the electrons is, the greater is the number of ionized collisions that they make. The strength, that makes the negative charges to spiralize around the magnetic field lines, is maximum when the electric and the magnetic fields form a 90° angle (see section 2.4.1).

To obtain greater sputtering rates it is therefore necessary to build some configurations in which the area of the cathode where the electric and magnetic fields are perpendicular, is maximum: a target with a modified shape is one of the possible methods to obtain this condition.

7.1.2 *Orthogonal incidence: the angle effect on the film properties.*

Studies conduct on Nb films coating through magnetron sputtering technique at different target-substrate angles, show that the morphologic and physic properties vary with the angle [104]. If we increase the incidence angle of the atoms with the perpendicular to the substrate:

- the superficial roughness rises, showing a maximum at 75°;
- the superconducting critical temperature decreases;
- the RRR value decreases;
- the film shows preferential growing directions that differ from the normal one.

An hypothesis consolidated by simulations (see figure 7.6) is that, for the incidence angles superior to 75°, the sputtered atoms arrive grazing the surface and promotes the pulling down of the dendritic columnar structures.

Figure 7.1: *Sampleholder for 10x10 mm quartz substrates. It allows changing the deposition angle systematically.*

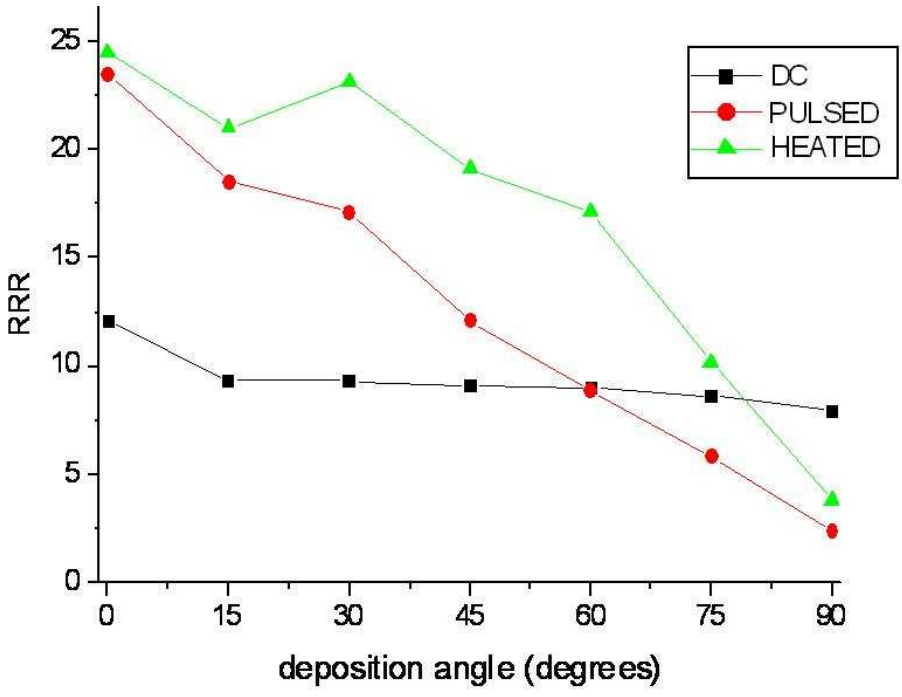

Figure 7.2: *RRR trend with angles of films sputtered at different target-substrate angles during three distinct configurations.*

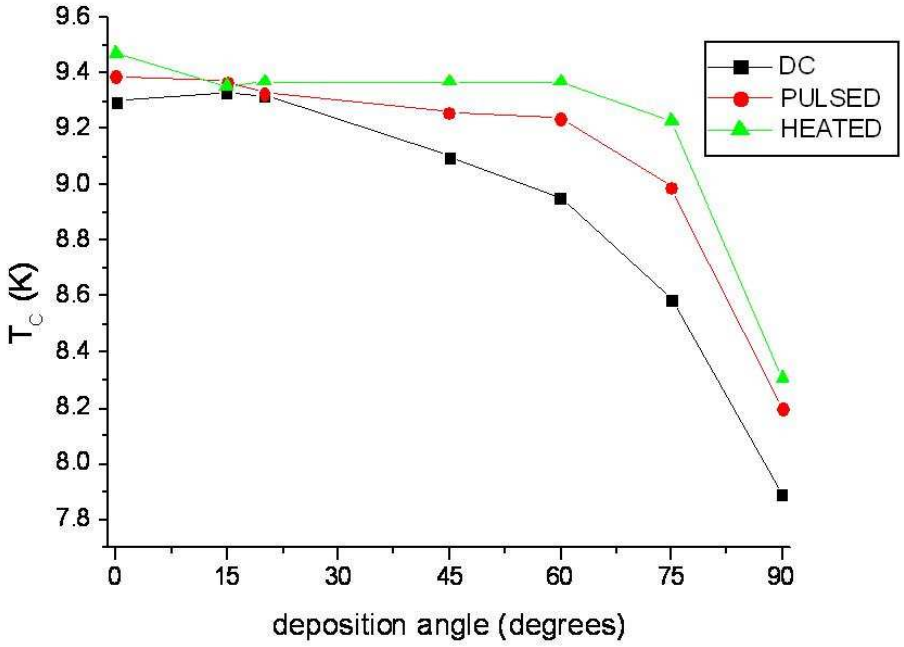

Figure 7.3: *Superconducting critical temperature trend with angles of films sputtered at different target-substrate angles during three distinct configurations.*

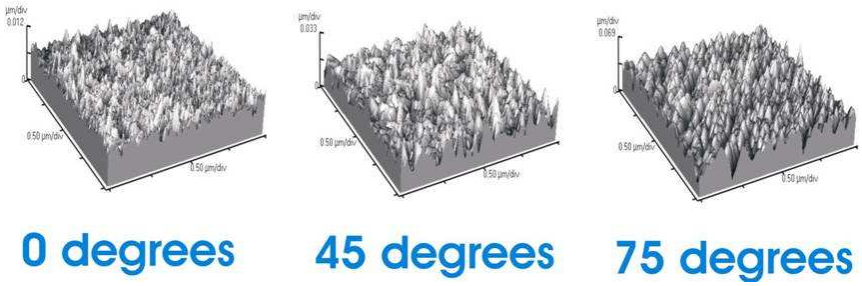

Figure 7.4: *AFM topographic images of films growth with different target-substrate angles.*

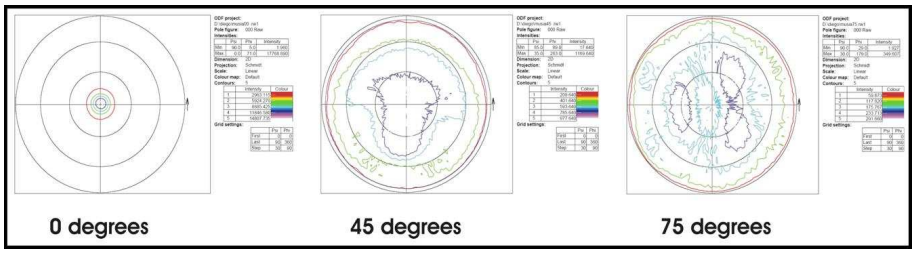

Figure 7.5: *X-ray texture obtain from films growth with different target-substrate angles.*

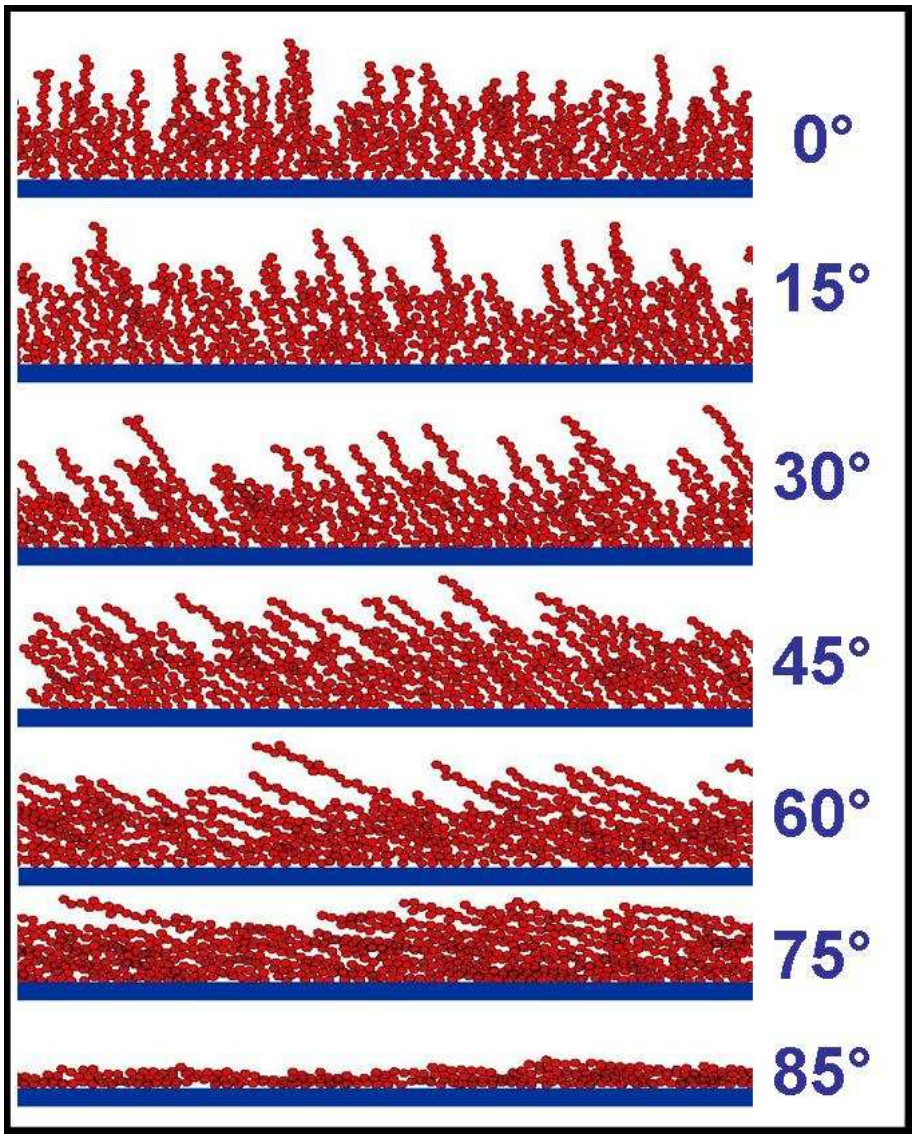

Figure 7.6: *Simple simulations of the film growth from a linear source with target-substrates angle of 0°,15°,30°,45°,60°,75°,85° respectively.*

7.2 *Ring shaped cathode*

7.2.1 *Building up of innovative planar magnetrons with high sputtering rate*

The electric field lines, in proximity of a conductive negative electrode, enter perpendicularly to the surface and they have a constant density. Therefore, it's easy to understand that the condition "electric field perpendicular to magnetic field" is equal to "magnetic field parallel to the surface of the target".

In the conventional circular planar magnetrons, the magnetic field is generated by a distribution of magnets placed under the target. As we can see in the simulation displayed in figure 7.7, the target area where the magnetic field lines are parallel to the surface, is limited.

To understand how the sputtering rate behaves, two 2" targets have been built and

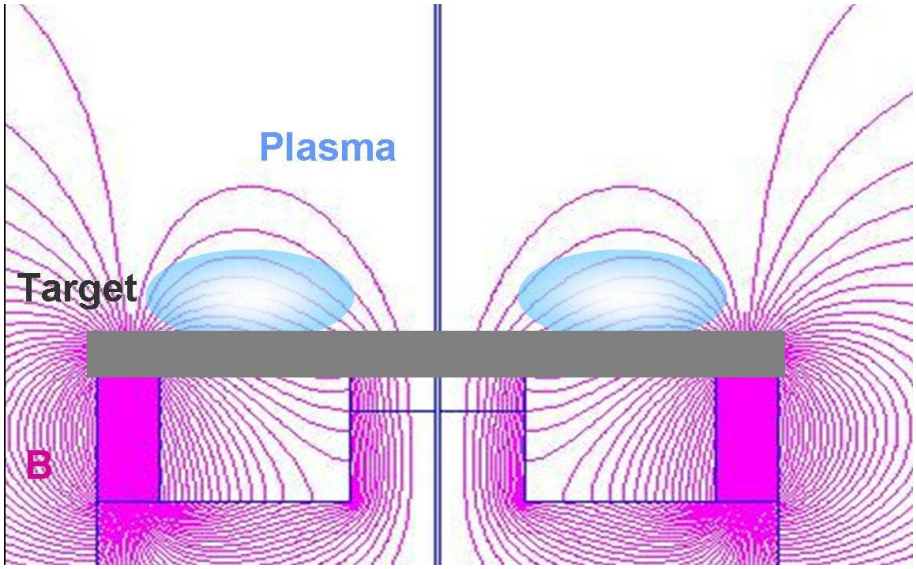

Figure 7.7: *Section of the circular magnetron with a planar target. The magnetic field line simulation is calculated with Pandira code [105].*

modified so that the surface follows the magnetic field lines. Since it was necessary to use an already existing configuration of magnets, the first step has been the measurement of the magnetic field intensity, in order define where the magnetic field lines are horizontal precisely. The adopted technique consists on a mapping the intensity of the field on the top of the target, by gaussmeter probe, maintained in a vertical position. When the probe reveals a vertical field value equal to zero, it means that all the lines of the magnetic field are parallel to the target (see figure 7.8).

Once experimentally determined the shape of the magnetic field, three 2" Nb targets have been built (figure 7.9):

1. "Planar target": 3 mm, planar;

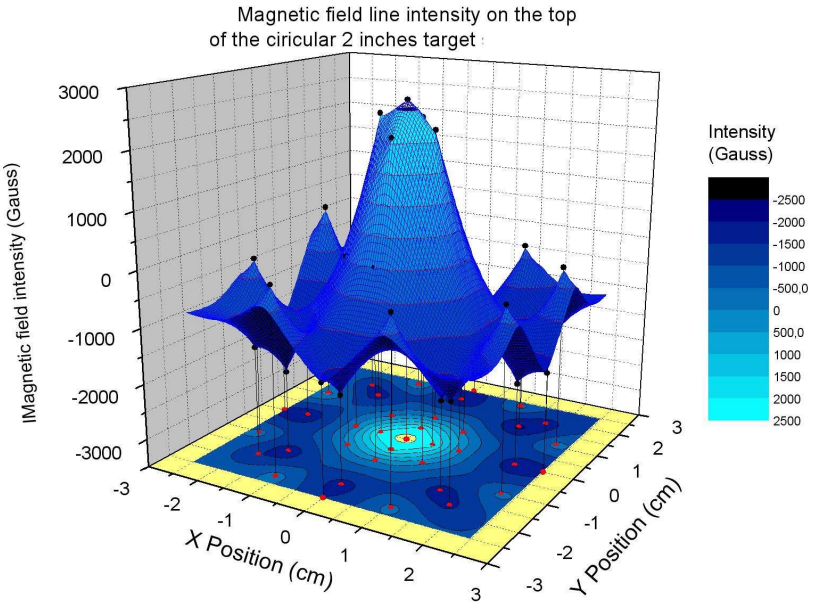

Figure 7.8: *Magnetic field intensity versus position, 10 mm above the taget.*

2. "Squared target": with a toroid of 12mm inner diameter , 26mm outer diameter and 12 mm high.

3. "Rounded target": with a toroid, rounded R5 of 12mm inner diameter, 26mm outer diameter and 9mm high.

The two toroidal targets have been built at different height so that they follow the simulated magnetic field line as better as they could.

Figure 7.10 and 7.11 report two simulations of the different targets and of their position

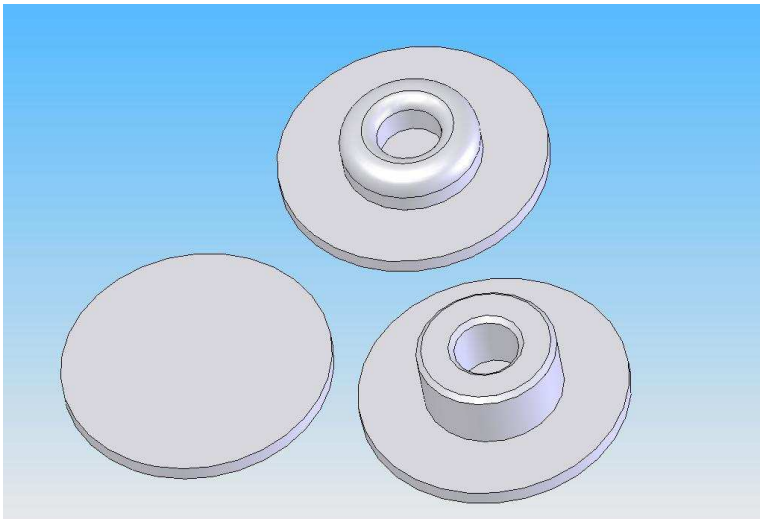

Figure 7.9: *Technical drawings of the three shaped 2" Nb targets: planar, squared and rounded.*

in the field, produced by the permanent magnets.

For each target some current-voltage curves at pressures of 1.1×10^{-2} e 2.5×10^{-2}

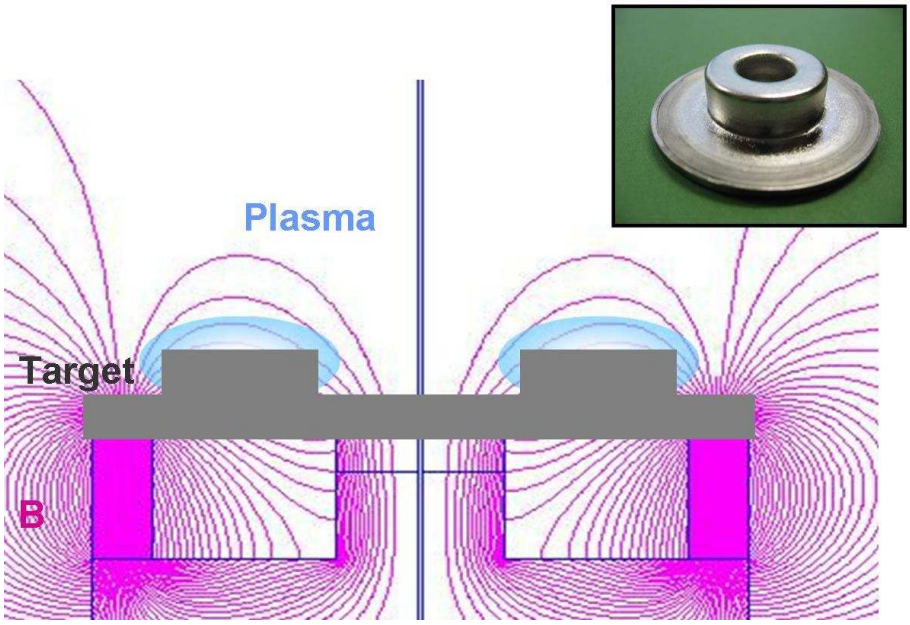

Figure 7.10: *Section of the circular magnetron with a squared target. The magnetic field line simulation is calculated with Pandira code [105]. A picture of the squared target on the right.*

mbar have been noted down. These points have been fitted with the formula I=aV^n using the Microcal Origin® 7.0 programme in order to estimate the ionizing coefficient n. The collected data and the relative fit are reported in figure 7.12 and 7.13. There is an evident improvement of the ionizing efficiency changing from the planar target to the toroidal one. In fact there are:

- progressive increasing of the n value (table 7.1);
- rising of the current between the cathode and the anode at an equal applied potential;
- plasma threshold tension decreasing.

Pressure ($10^{-2}mbar$)	**n value**		
	Planar target	**Squared target**	**Rounded target**
1.1	4.8	4.5	6.2
2.5	6.9	8.3	9.0

Table 7.1: *Values of the n coefficient from the I=aV^n fit. For different target and different process pressure.*

The rounded 8 mm target is the one characterized by the maximum efficiency of ionization because it presents the greater superficial area, parallel to the lines of the magnetic field. This is easy to guess also visibly, looking at the pictures 7.14 of the three different plasmas: in the case of the round target the plasma completely permeates the surface,

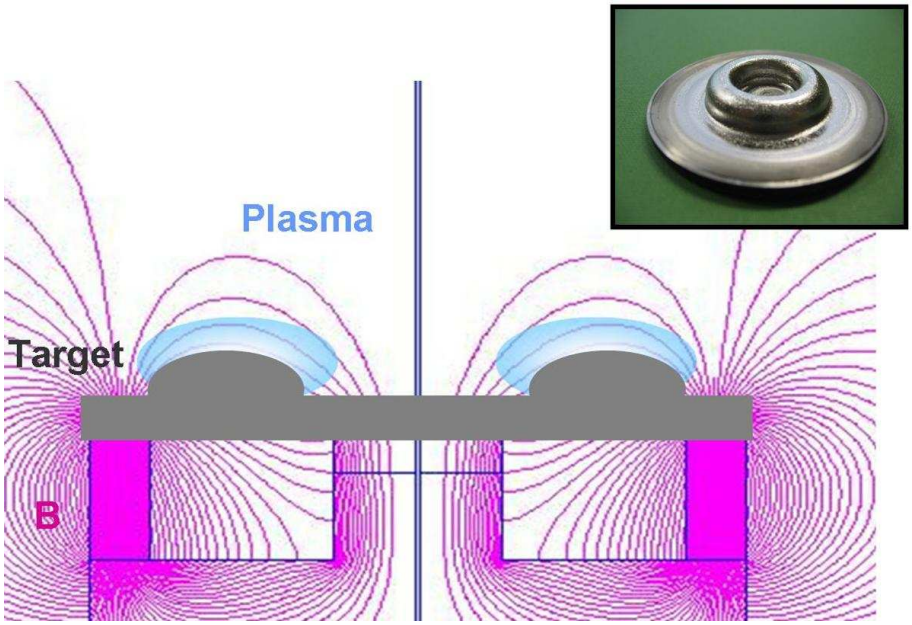

Figure 7.11: *Section of the circular magnetron with a rounded target. The magnetic field line simulation is calculated with Pandira code [105]. A picture of the rounded target on the right.*

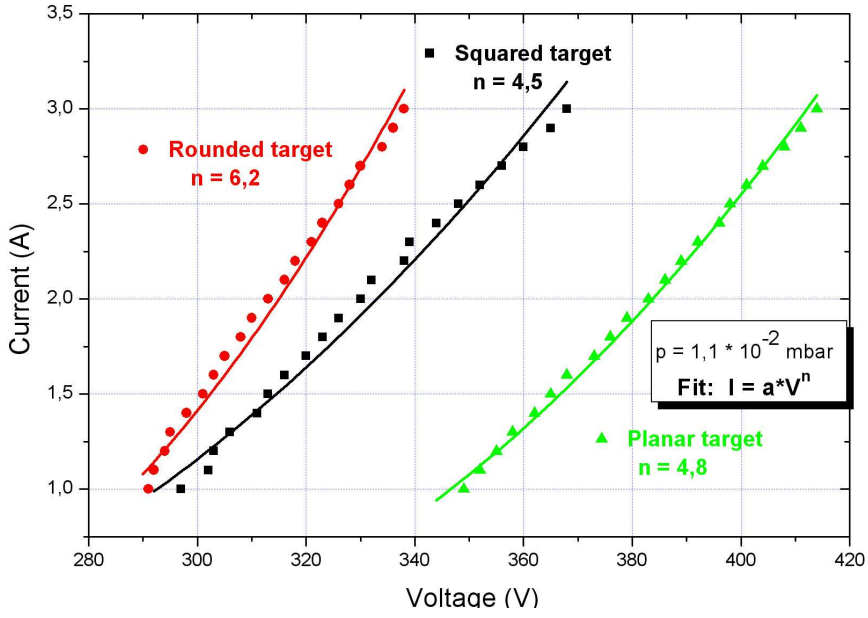

Figure 7.12: *I-V curves for the three shaped targets at* 1.1×10^{-2} *mbar.*

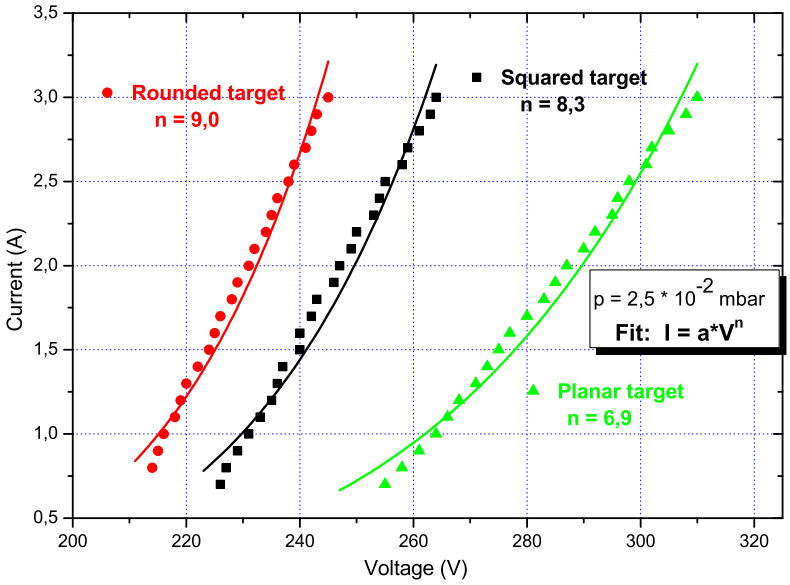

Figure 7.13: *I-V curves for the three shaped targets at* 2.5×10^{-2} *mbar.*

while in the case of a square target, the formation of two independent crowns of plasma, is remarkable (during the acquisition of the characteristic curves of the square target, it has been noticed that the ignition of the two crowns of plasma occurred at slightly different voltages). The only problem encountered has been the cooling of the bulk target at high currents.

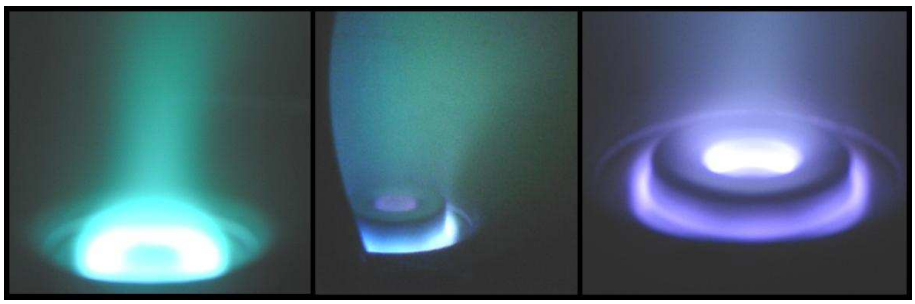

Figure 7.14: *From the left, pictures of the planar, squared and rounded target during the sputtering process.*

In conclusion, it has been shown that the planning of targets with a maximized superficial area where the electric and magnetic fields are perpendicular, leads to an improvement of the efficiency of the ionization and, therefore, of the sputtering rate.

7.2.2 *Planning of a shaped cathode*

One way to make the atoms arriving perpendicularly to the inner surface of a cavity, is building a cathode that presents the same shape of the substrate. The standard CERN deposition occurs moving the magnet along the Nb cathode during the beam tube coating. For the cell, instead, the magnet has to be positioned at the equator level and, once ignited the glow discharge, the deposition happens simultaneously over the whole surface. In this way, the deposition occurs at angles that vary from 0° to 35°, according to the cavity zone [75].

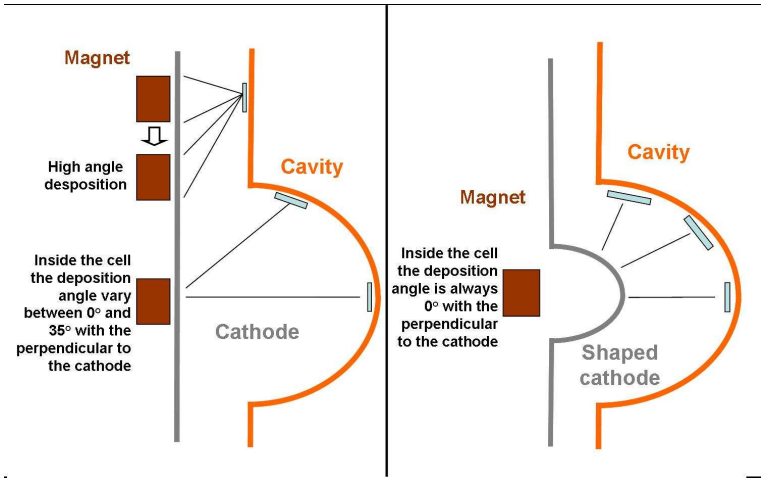

Figure 7.15: *Schematic view of the deposition angles for the standard cathode (left) and the modified cathode (right).*

To solve this problem, the cathode should have a sort of protuberance level with the cell as displayed in figure 7.15.

Through the Pandira® software the magnetic field shape around the magnet has been simulated; the magnet is closed between two iron circles. The programme is able to calculate the magnetic field line shape once defined the dimensions, the direction and the magnetization curve of the magnets used (in our case Nd-Fe-B): the code list is exposed in appendix A.

In the cylindric section of figure 7.16 the cavity inner surface and the cathode shape are sketched on the magnetic field lines simulation. 100G is the minimum field intensity to guarantee the ignition of the glow discharge with pressure and stream parameters proper to have an acceptable sputtering rate. The calculations point out that the ring can't have a diameter larger than 50mm because the field is lower than 100G at 25mm far from the cathode axis. It's also worth noting how the field lines faithfully follow the equatorial ring surface, so an homogenous erosion of the target is expected. Once defined the optimum dimensions, the niobium 48,5 mm outer ring to place around the cylindrical cathode, has been planned with Solid Works 2004® software (see figure 7.17).

The shaped cathode has been built to increase the sputtering rate and to reduce

Magnet	$\Phi_{internal}$	8mm
	$\Phi_{external}$	20mm
	h	20mm
Iron cilinders	$\Phi_{internal}$	9mm
	$\Phi_{external}$	23mm
	h	8.5mm

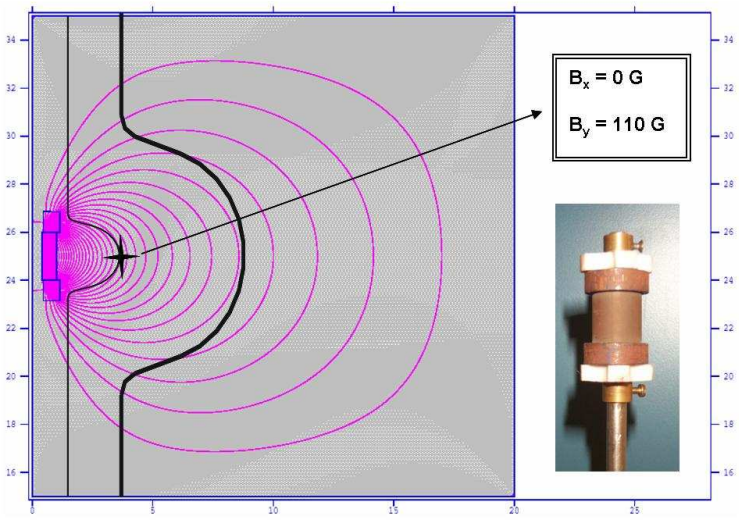

Figure 7.16: *Magnetic field lines Pandira® simulation for the 2cm high NdFeB magnet used in the standard-CERN coating technic.*

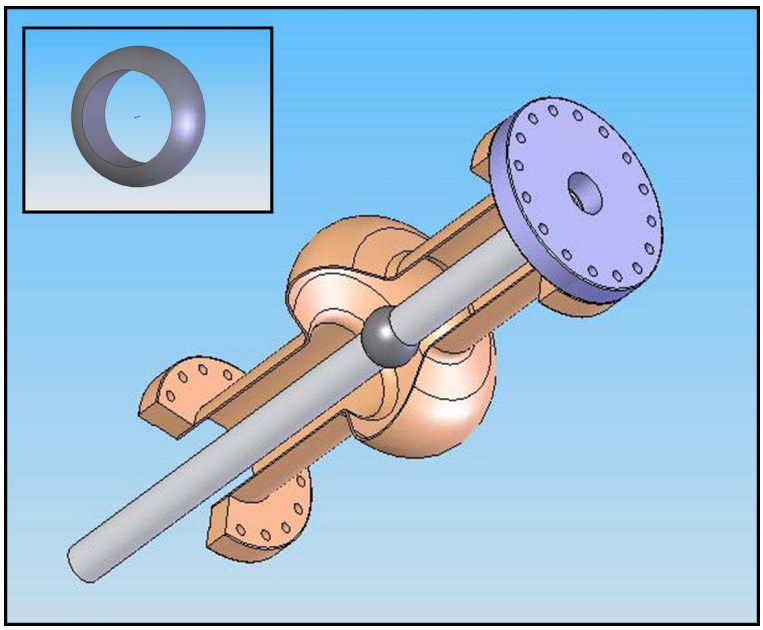

Figure 7.17: *Technical 3D drawing of the cathode with the niobium ring.*

the problem of the angle. The Nb ring has been spinned and placed around the cathode, leveled with the cavity equator. The ring has a 48,5 mm diameter and a 27 mm height (See Fig. 4-20) and is provided with two openings that guarantee a good pumping of the space volume inside it.

At the same time, cylindrical magnets that produce a more intense magnetic field have been studied and several magnet have been ordered with the intention to build shaped cathodes with greater equatorial diameters.

Since magnetic fields perpendicular to the electric ones on the cathode surface have shown to guarantee a greater sputtering rate, before choosing the magnet shape, a series of simulations have been performed with the Pandira® software. In figure 7.18 some results of the simulations done are reported and they have been useful to determine the shape necessary to guarantee a magnetic field parallel to the target.

7.2.3 *Description of the coating set up and process parameters*

To test the ring shaped cathode, three depositions on quartz samples have been made: the first run has been done using only the inner magnet (Run 1), in the second run two coils, placed around the cavity and coaxial to it, substitute the inner magnet (Run 2). The third run combine both configurations adding the two coils to the inner magnet (Run 3).

During Run 1, the plasma is very localized but it hardly seems to erode the exterior surface of the niobium ring due to the magnetic field low intensity. For this reason a combined use of the magnet and two external coils have been tested. The coils are placed at a G =115 mm distance (figure 7.19) and they works with a current of 3A. Since the coils sustain the plasma on the whole length of the cathode (post-magnetron configuration), two niobium wings have been added at the cathode extremities. The wings act as an electrostatic mirror and increase the confinement of the electrons (RUN 3, see table 7.2).

Since the first deposition, the problem of the Nb ring excessive heating has arisen, due to the insufficient thermic contact with the cooled tube and of the low thermic conductivity of the Nb of (7 W/(m·K)). The temperature of 1500°C reached by the ring (it delivers a white light) prevents to continue the sputtering. The glow discharge switches off: probably the high heat produced on the target cause a thermal expansion and loss of the electric contact or a reduction of the magnet efficiency.

7.2.4 *Results of ringed shaped cathode*

To estimate the ionization efficiency and the sputtering rate of the shaped cathode, three I-V curves of the different magnetic field configurations have been collected (figure 7.20). All data, analyzed with Microcal Origin® 7.0 Pro Programme has been fitted according to the Thornton [48] formula; the exponent value for the shaped cathode could be compared with those obtained for the simple cylindrical magnetron in figure 6.9.

Observing the experimental data, it comes out that the efficiency of ionization for the shaped cathode with the sole magnet is similar to the efficiency of the simple cylindri-

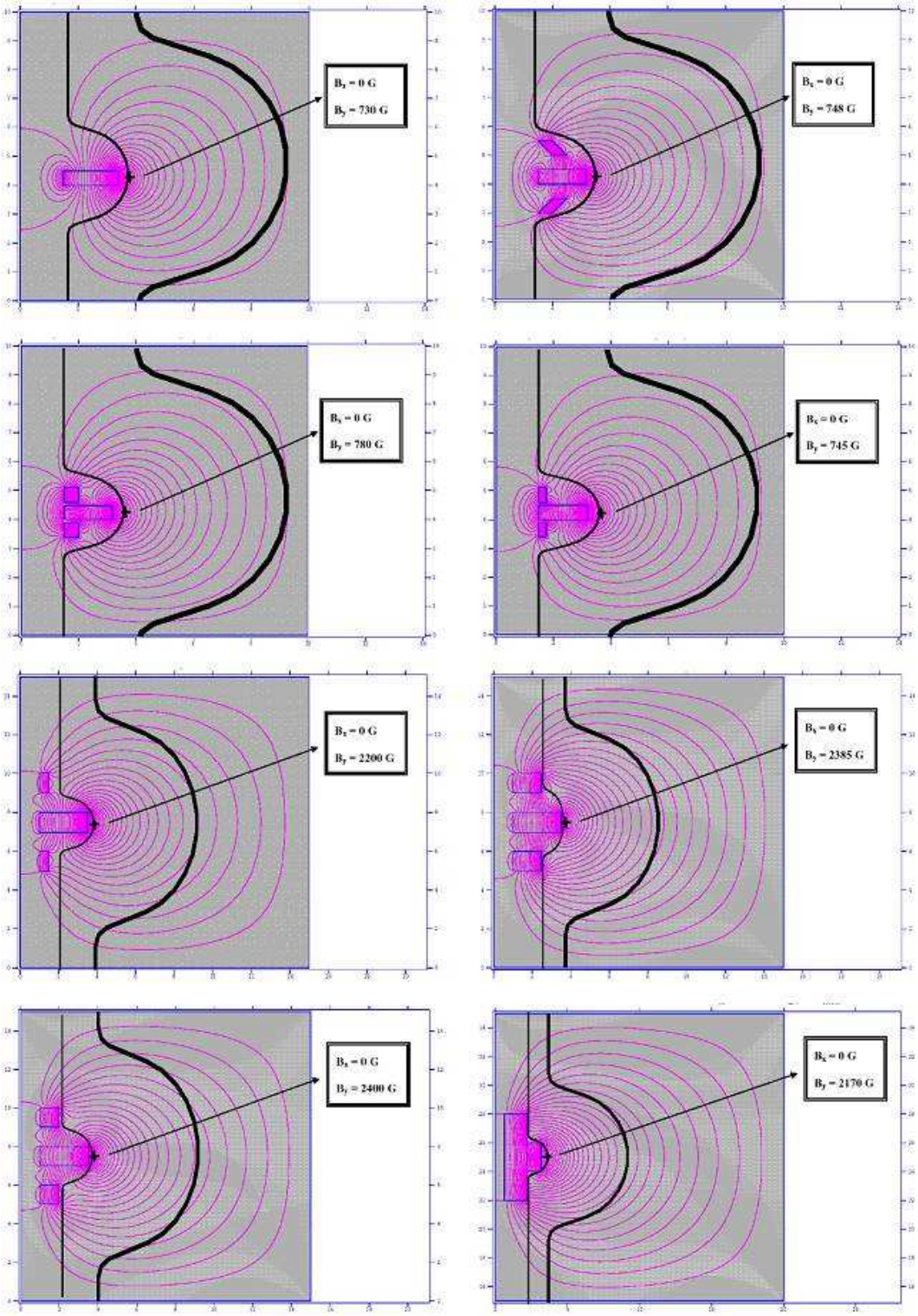

Figure 7.18: *Results from the Pandira® simulations of magnetic fields from different magnet shapes and dimensions.*

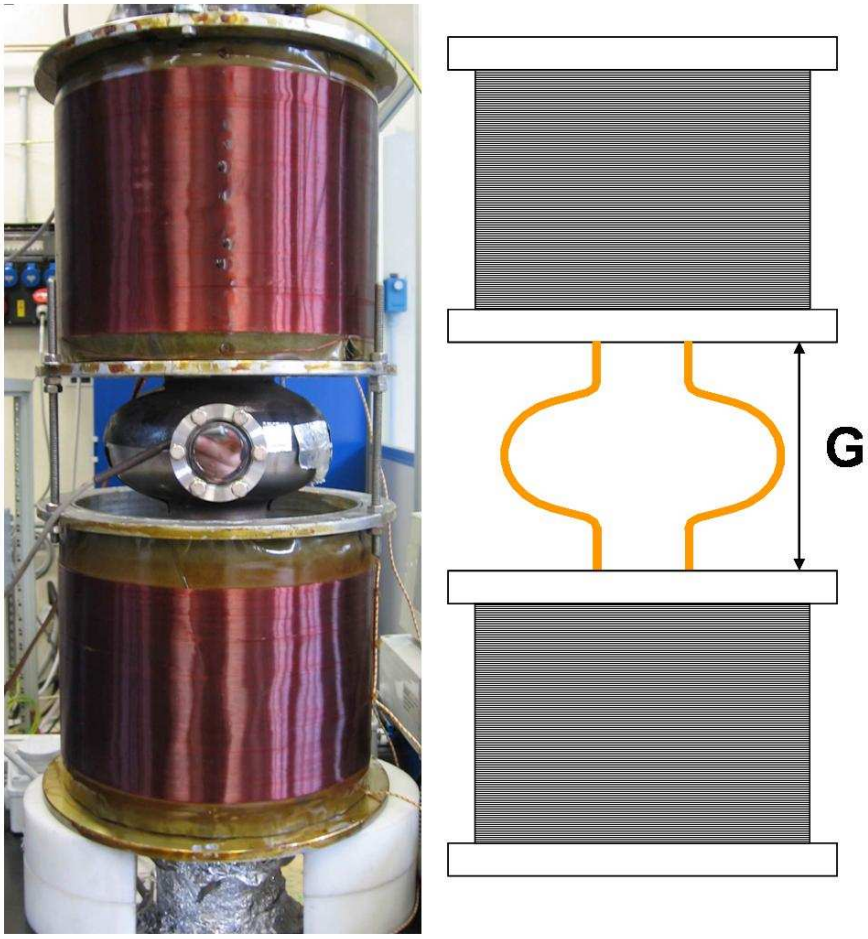

Figure 7.19: *Picture and sketch of the two coils mounted to gain magnetic field intensity in the cavity cell center.*

Run	**Deposition time**	**Argon pressure (mbar)**	**Cathode current**	**Coils current**
1 (magnet)	1h coating of beam tube and cell	$1{\cdot}10^{-2}$	1A	/
2 (magnet+coils)	11min coating of the cell	$1.5{\cdot}10^{-3}$	3A	2A
3 (magnet+coils+wing)	11min coating of the cell	$1.5{\cdot}10^{-3}$	5A	3A

Table 7.2: *Summary of the coating parameters for the three of the ring shaped cathode.*

cal magnetron (figure 6.9). Greater efficiencies can be obtained, instead, with the post-magnetron configuration or with the simultaneous use of coils and magnets. Figures 7.21

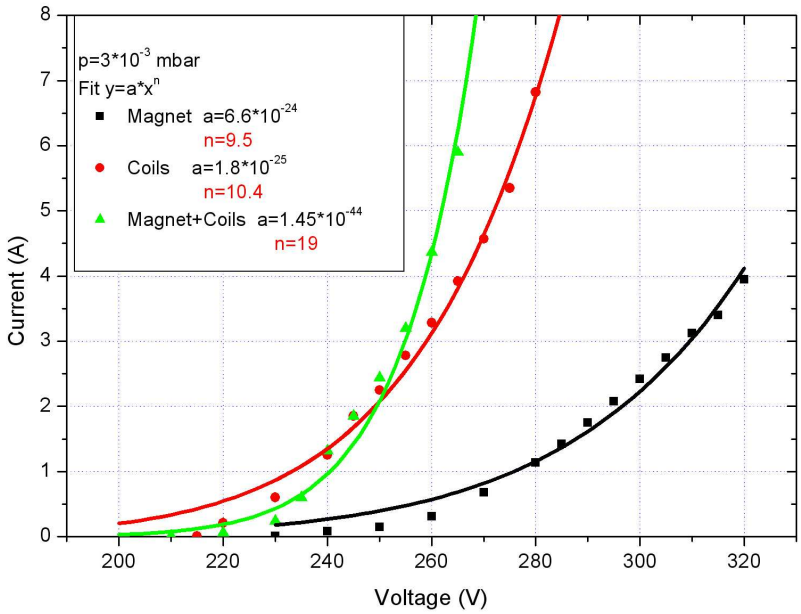

Figure 7.20: *I-V curves for the three different coating configurations (table 7.2). The magnet is left leveled with the cavity cell.*

and 7.22 collects all RRR and Tc results of the three ringed shaped cathode tests. The RRR vary from 3 to 20 and there is gradual improvement as long as the cathode is sputtered. Best RRR and Tc results at the equator are 13 and 9.36K. Tc higher than Nb bulk means a compressive stress of the crystal lattice, confirmed also by X-ray diffraction cell parameter measure a = 3.29Å respect to the bulk value a_0 =3.303Å (figure 7.23). In addition texture analysis have been performed on (110) peak, the most intense in Nb powder diffractogram, in order to investigate the occurrence of preferential orientation during film growth. Texture results are collected in chapter 9 and compared with texture from different sputtering configurations. Film thickness measurement analysis (figure 7.24) show that, this configuration work as expected. For run 1, where the upper beam tube have been coated, the sputtering rate at the equator is as higher as at the iris. Thickness difference between the film on equator position up and down is a systematic error probably due to a screening of the lower sample from the screw used to fix the quartz substrate. An error on the magnet centering respect to the equator center has been checked several time and excluded because it is possible to see the plasma position trough a window on the equator of the stainless steel cavity shaped chamber.

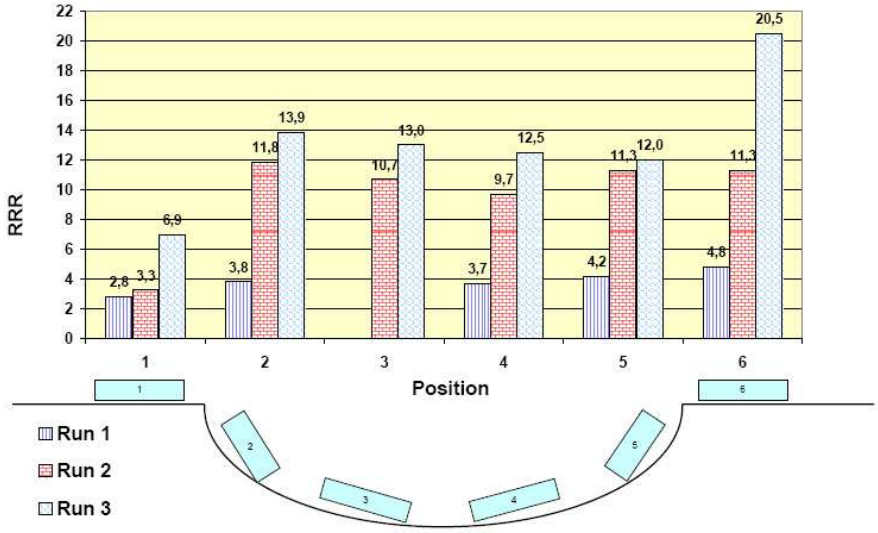

Figure 7.21: *RRR values of the niobium film on quartz sample, for different positions around the equator and three different runs of the ring shaped cathode configuration. Data are obtained with the four point probe method explained in chapter 4.*

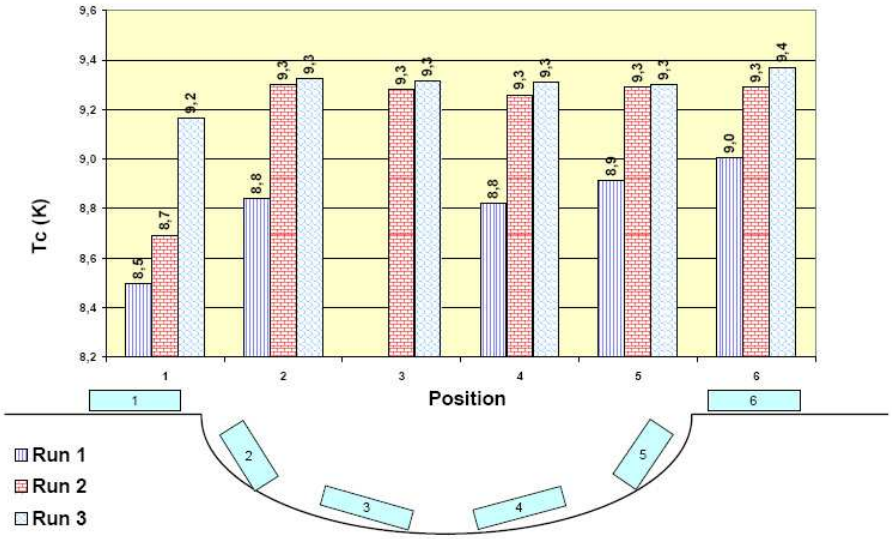

Figure 7.22: *Critical temperature Tc of the niobium film on quartz sample, for different positions around the equator and three different runs of the ring shaped cathode configuration. Data are obtained with the four point probe method explained in chapter 4.*

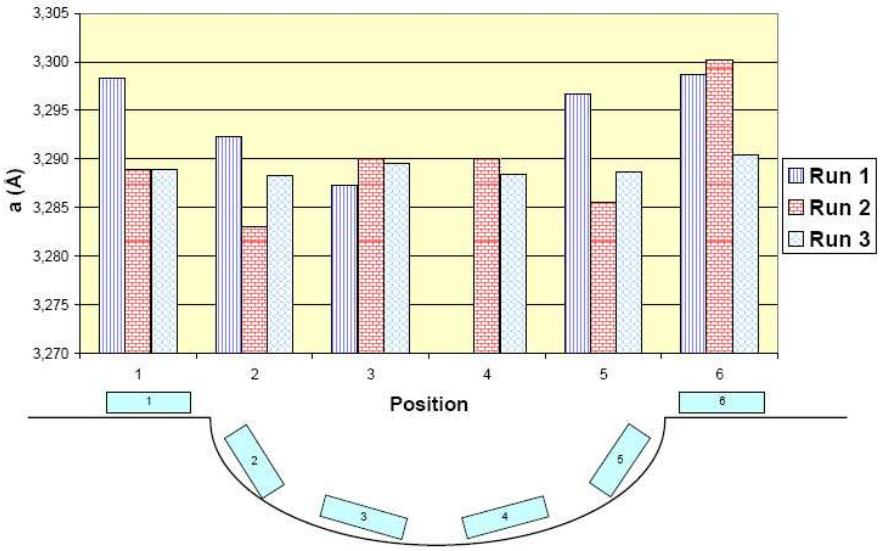

Figure 7.23: *Lattice parameter value versus position of niobium thin film on quartz substrates. Samples are coated using the ringed shaped cathode. a is calculated with the Bragg formula from X-ray diffraction spectra.*

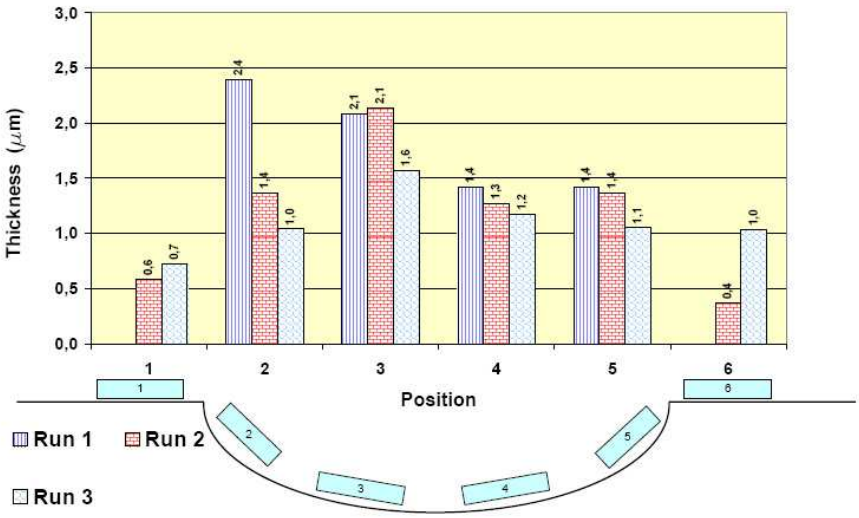

Figure 7.24: *Sputtering rate of the niobium ring shaped target, for different positions around the equator and three different runs. Sputtering parameters are summarized in table 7.2.*

7.3 *Large area cavity shaped cathode*

7.3.1 *Implemented studies*

The bias technique is highly reliable in fact over 50 Quarter Wave Resonators are installed and working at LNL for ALPI. Bias sputtering of 1,5 GHz cavities was developed at CERN around 1985, it consisted on a rotating cavity shaped cathode [99]. Its low ratio cathode/substrate area determines a very low sputtering rate (1μm /day). One way to improve the film quality is increasing the sputtering rate by enlarging the sputtering area respect to the cathode one. Another way is to keep the cathode parallel to the substrate all along the cavity shape.

Following to depositions carried out with ring shaped cathode, it was necessary to find out a cathode that contains all the positive characteristics of both configurations. First off all, we studied a very simple bias diode sputtering configuration, made up by three planar electrodes, in order to understand if it is possible to take advantage of the bias technique without positioning the grid between the cathode and the substrate. In particular, placing the grid behind the cathode could avoid shading problems and bring the cathode nearer to the substrate.

The system scheme can be seen in figure 7.25; the electrodes are niobium flat plates 60x30mm large and 2mm thick. Pictures of the plasma created were taken varying systematically the deposition parameters and the distances between cathode electrode and bias (B), as described in table 7.3.

It was noticed that as bias voltage increases from 0 to 150V, the plasma luminous

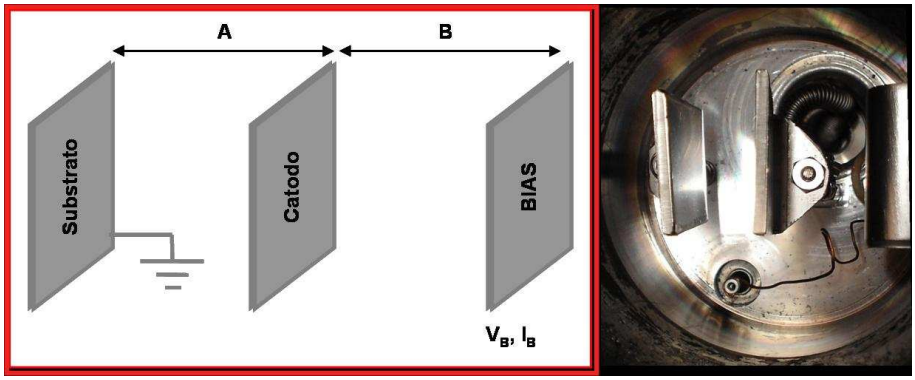

Figure 7.25: *Schematic of the test with planar electrodes to study the biased electrode position effect on the glow discharge. The picture on the right shows the three electrodes mounted on the vacuum system.*

intensity increases remarkably near to the substrate, even though the anode is not placed between cathode and substrate (figure 7.29).

Figure 7.26 and 7.27 show pictures of the system, taken from the top, during the sputtering process. Pictures were taken maintaining the exposition time , the aperture diaphragm and the sensitivity unchanged. Optimum pressures for the use of this system are from 10^{-1} to 1 mbar.

test	**A** (mm)	**B** (mm)	**p** (mbar)	$\mathbf{V}_{bias}$ **V**
1	20	20	1	0
2	20	20	1	50
3	20	20	1	100
4	20	20	0.1	0
5	20	20	0.1	50
6	20	20	0.1	100
7	20	20	1	0
8	20	20	1	50
9	20	20	1	100
10	20	20	0.1	0
11	20	20	0.1	50
12	20	20	0.1	100

Table 7.3: *Summary of the coating parameters used for bias diode coating with the planar electrode tests.*

This mentioned bias positive effect seems to happen both when the cathode is equidistant from substrate and bias electrodes (A=B=20 mm) and when the cathode is nearer to the bias that to the substrate (A=20, B=12 mm), cathode-substrate distance being equal.

The placement of two external coils producing a 200G central magnetic field parallel to the electrons guarantees a sputtering rate increase of a factor of 2.

7.3.2 *Description of the coating set up and process parameters*

The results obtained allowed us to start designing a cathode that has all the following characteristics:

- a positive electrode that allows re-sputtering of the growing film;
- a cavity-shaped surface that promotes deposition with orthogonal incidence along the whole surface;
- a large sputtering area exposed to the substrate that guarantees a high sputtering rate.

This new configuration comes from the idea of using a 1,3 GHz sliced cavity as cathode. The cavity was sliced through spark erosion in 12 slices (figure 7.28) but only 8 were assembled, with the help of supports and isolators . Only 8 slices have been assembled because the dimensions are compatible with the size of the external cavity and they combine a large cathode area, a minimum overlapping among slices and a relative ease of insertion.

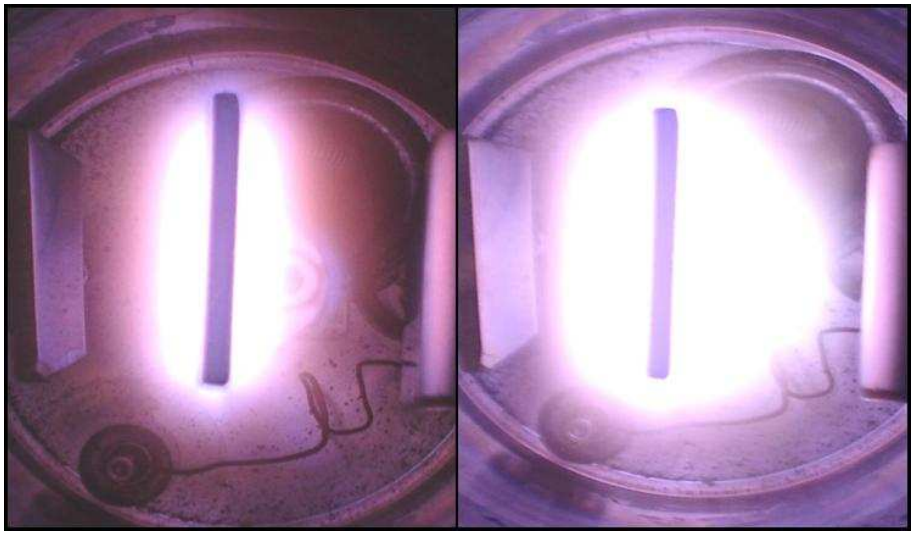

Figure 7.26: *Picture of the bias diode sputtering with planar electrodes. The cathode electrode is the one in the middle. Referring to table 7.3, on the right test 1 and on the left test 3 are depicted.*

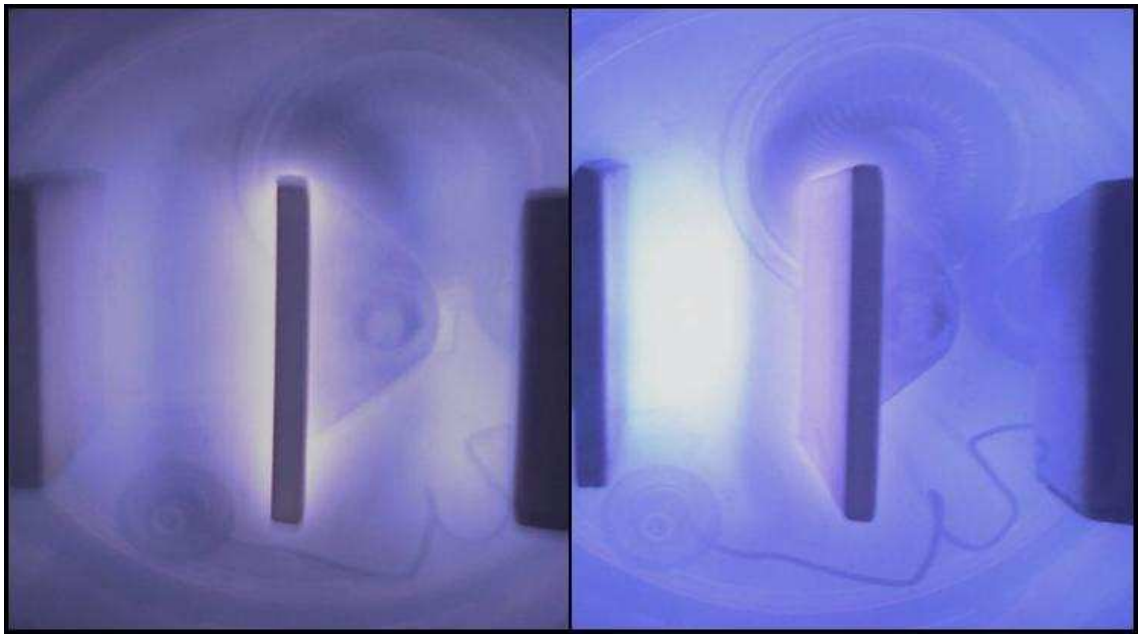

Figure 7.27: *Picture of the bias diode sputtering with planar electrodes. The cathode electrode is the one in the middle. Referring to table 7.3, on the right test 4 and on the left test 6 are depicted.*

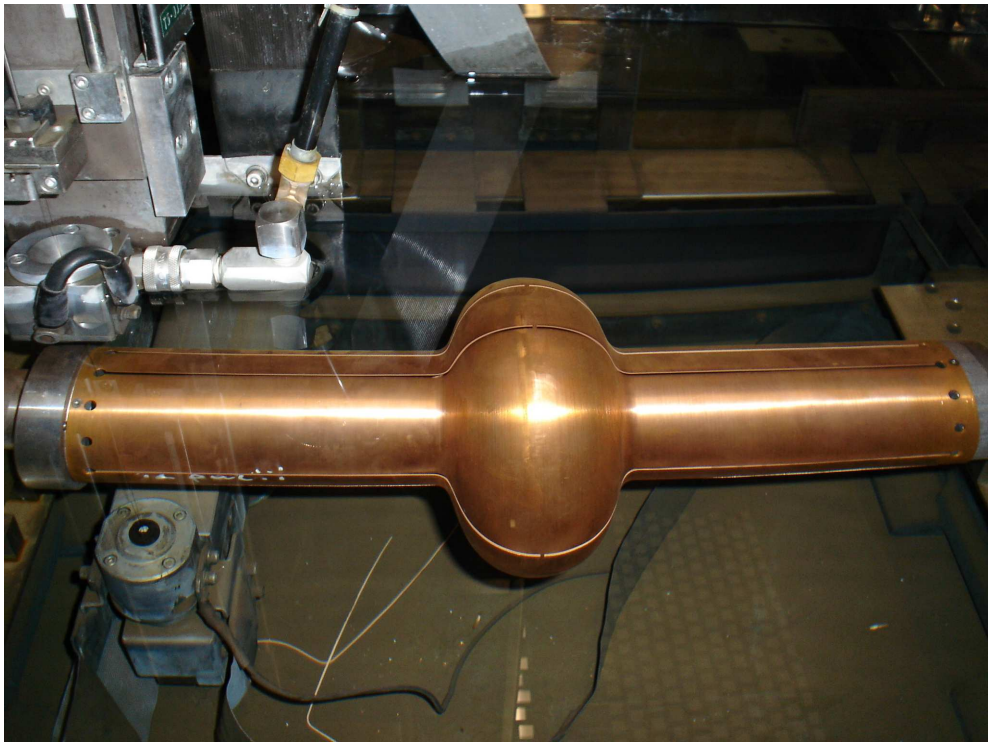

Figure 7.28: *The copper cavity mounted on the electromachine; it has been cut in 12 slices.*

The bias electrode is not placed between cathode and substrate, but it passes through the target (figure 7.29). The first prototype is completely made of copper, then the niobium cavity has been cut and tested.

7.3.3 *Results of large area cathode*

Tests aim at determining optimal deposition parameters and homogeneity of deposition along the axial and circular directions of the cavity. This last direction is critical as the sharp parts of the cathode like the edges, for the so called "corona effect", tend to concentrate charges and increase the sputtering rate locally. It must then be evaluated if the inhomogeneity can affect cavity performances.

Several deposition has been done to test the stability of the system and its applicability to coating a 2 μm niobium films onto cavities. At the moment best parameters to avoid the system collapsing or experiencing a short circuit are: a constant current of 0.5A, corresponding to a voltage of 336 V at the argon pressure of 7.7x10$_{-2}$mbar for 70 minutes, with e bias voltage of 120 V. Two attempts of magnetron sputtering has been experimented with two coils set around the beam tubes; this kind of configurations is under development. The system has shown a good mechanical and electrical stability after 70 minutes deposition. After four runs the cloves are still well shaped but they show no sign of recrystallization.

The main reason for the poor film results is the formation of a high ionized plasma inside the cathode instead of outside it, on the substrate side. The number of cloves or their size should be reduced to open the way from the biased bar to the substrate. In

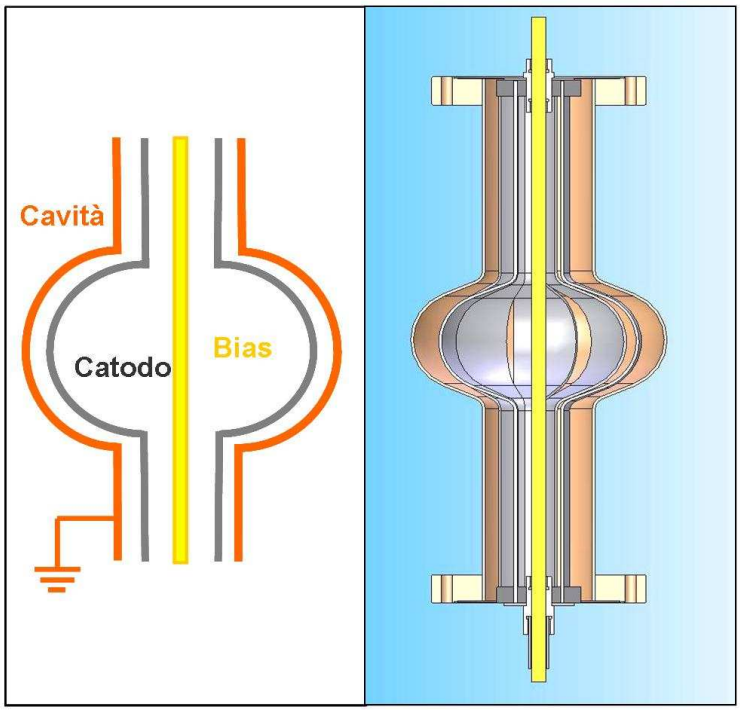

Figure 7.29: *The schematic of the large area cavity shaped cathode configuration with the central bias electrode is represented on the left. The structure section is presented on the right. The biased electrode is the yellow bar in both figures.*

figure 7.26 is clearly visible that the plasma need a way to communicate from one side to the other of the cathode.

Few samples has been characterized. RRR still very small (from 2 to 4) has been obtained on the equator position because the cathode need several runs to be conditioned and cleaned. Even if the cloves insertion is still difficult the purpose of the Large Area Shaped Cathode is to verify if the large cathode parallel to the substrate can improve the cavity performance. Morphological studies of films are under development.

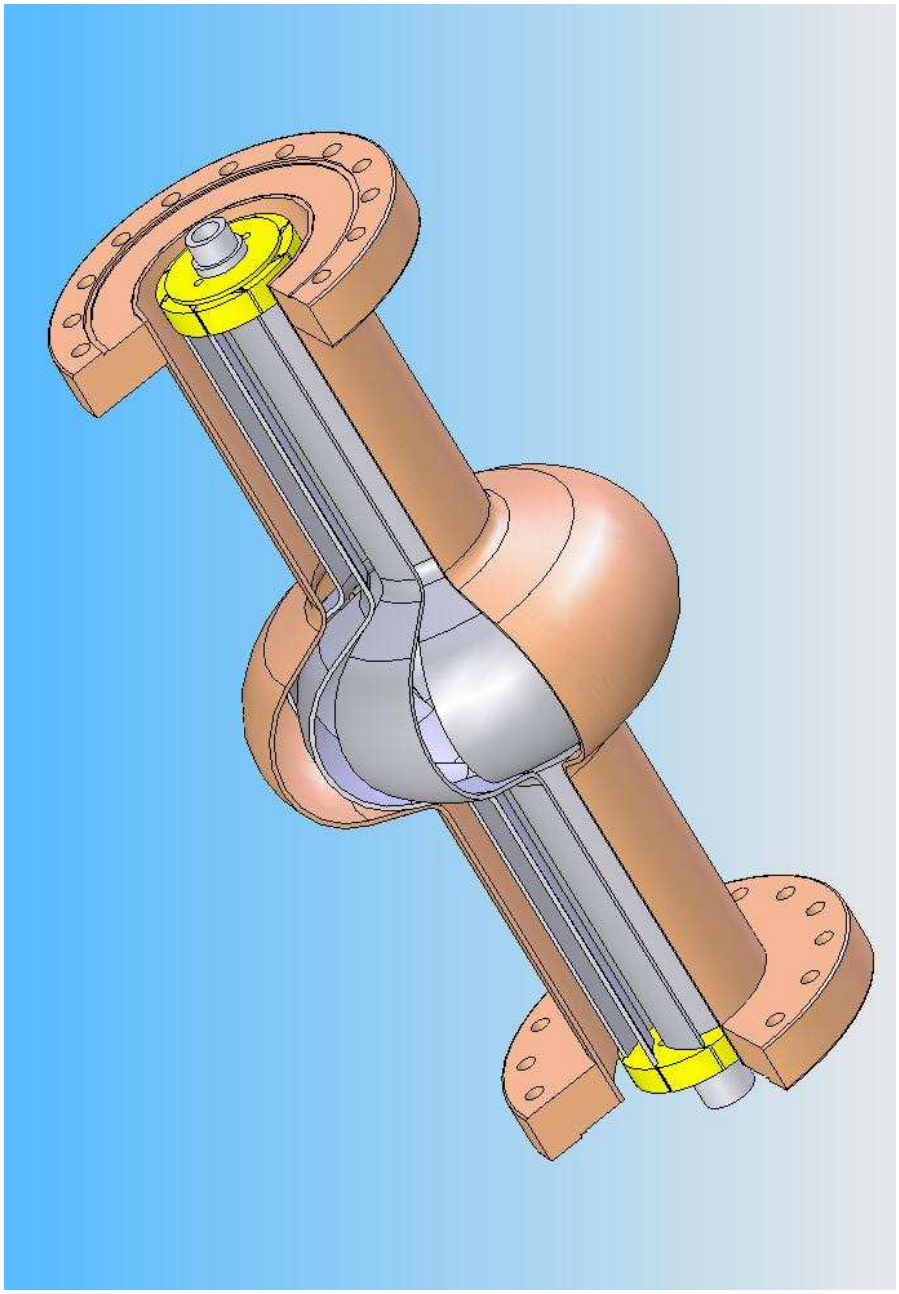

Figure 7.30: *Schematic view of the large area cavity shaped Cathode.*

Chapter 8

Bias Magnetron Sputtering

A positive bias applied to the grid placed between target and substrate promotes ionic bombardment of the growing film. The main feature of this technique is the impurities resputtering of the film surface. A mixed bias magnetron sputtering system for coating Nb onto Copper 1.5GHz cavities is presented, underlining some details of the constructions and explaining all the results [106, 107].

8.1 *Ionic Bombardment*

8.1.1 *Bias effect on the film properties*

When applying the DC bias sputtering technique the voltage difference between the plasma and the substrate increase. On one hand the bias increases the superficial mobility of the atoms that reaches the surface, on the other hand, it aids the re-sputtering of the physisorbed species.

The formula 2.12 of impurities of the type i entrapped in the film, becomes:

$$f_i = \frac{\alpha_i N_i - \beta}{\alpha_i N_i - \beta + R} \tag{8.1}$$

where β is a function of the bias current, due to the impurity ions.

When β increases, also the purities of the film increases because the ionic bombardment aids the impurity atoms release from the growing film. Usually they arrive to the substrate with a low energy (for example the atoms of the residual gases in the chamber) and they are, therefore, weakly linked.

Poitevin's work has shown that the application of a bias voltage higher than 80 V in some DC deposition systems considerably improves the TiN [108] film properties:

- greater density
- smoother surface
- minor quantity of oxygen included in the film
- minor resistance

Kay documented that the bias voltage has a great influence on the Nb film characteristics [52]. The weak ionic bombardment promoted allows the reduction of the imperfections and the concentration of noble gas in the film. It's clearly pointed from various experiments that the applications of a bias improve the film quality until 100-200 V, over these values there is a progressive degradation of the properties [109]. The positive effects deriving from the application of a bias potential have already been exploited into the INFN laboratories in Legnaro for the sputtering of Nb on more than 40 QWR resonant copper cavities.

8.1.2 *Planning of a biased grid for coating cavities*

The bias electrode, applied to increase the plasma discharge voltage, could be used both in the diode configuration and the magnetron configuration, even if in the last one the plasma ionization efficiency is already increased through a magnetic field. If the cavity is grounded, the biased electrode could be placed between it and the cylindrical cathode. The positive biased electrode is connected to another power amplifier, it acts as a new anode in the system (figure 8.1) and:

- it should be placed near the cathode
- it should not create any shadowing between the cathode and the substrate
- it cannot be larger than the beam tube inner diameter.

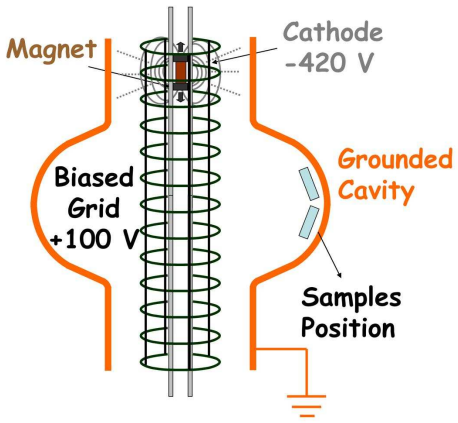

Figure 8.1: *Scheme of the magnetron bias configuration.*

The solutions adopted is a grid, made by a conductive and mechanically resistant material. The grid will be heated by the cathode irradiation and by the electronic bombardment. The grid obviously reaches high temperature mainly in correspondence to the magnetic field, due to the high temperature of the particles of the plasma in that zone. The materials adopted are: titanium, stainless steel and niobium. The starting project implies the using of a stainless steel net, formed by strings of 2mm of diameter with squared links of 50mm along the cut-off and 25mm in proximity to the equator (to guarantee a greater uniformity

of field near the cell). To obtain a cylindrical shape the net has been first rolled and then TIG welded. Great care have been taken in order to reduce the welding sizes so they cannot cause any screening of the substrate (figure 8.2).

A technological problem that has been solved concerns the grid support and how to

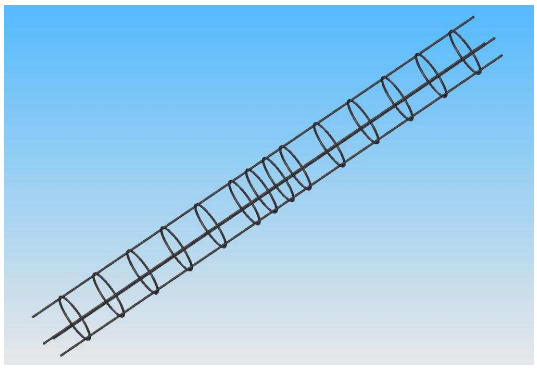

Figure 8.2: *The stainless steel grid.*

connect it to the cathode. The support should guarantee that the grid is at a constant distance along the whole surface of the target and it should ensure a good electric isolation between the two electrodes and the cavity. The solution adopted is depicted in figure 8.3: two discs cling, through three isolators, to the niobium wings that are screwed to the cathode ends.

The important variables to control in this configuration are the cathode current and

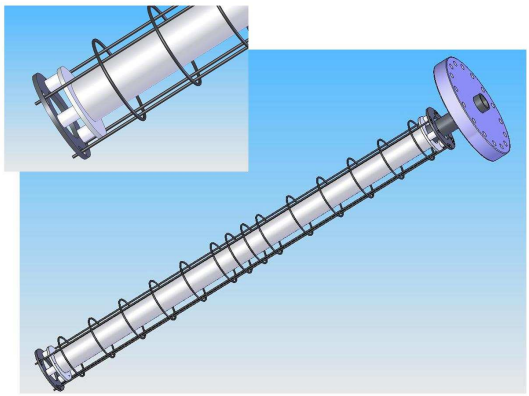

Figure 8.3: *The stainless steel grid clung to the cathode. A details of the two discs cling, through three isolators, to the niobium wings that are screwed to the cathode ends.*

voltage, but also the voltage applied to the net and the relative current (respectively called bias voltage and bias current). Two electric circuits that realize the desired potential distribution ; they are conceptually the same although the currents distributed by the power supplies are different.

Monitoring the potential difference between cathode and anode during deposition is important. In order to compare the different behaviour of the two circuits, the following test has been executed. The three electrode voltages have been set and then, connecting

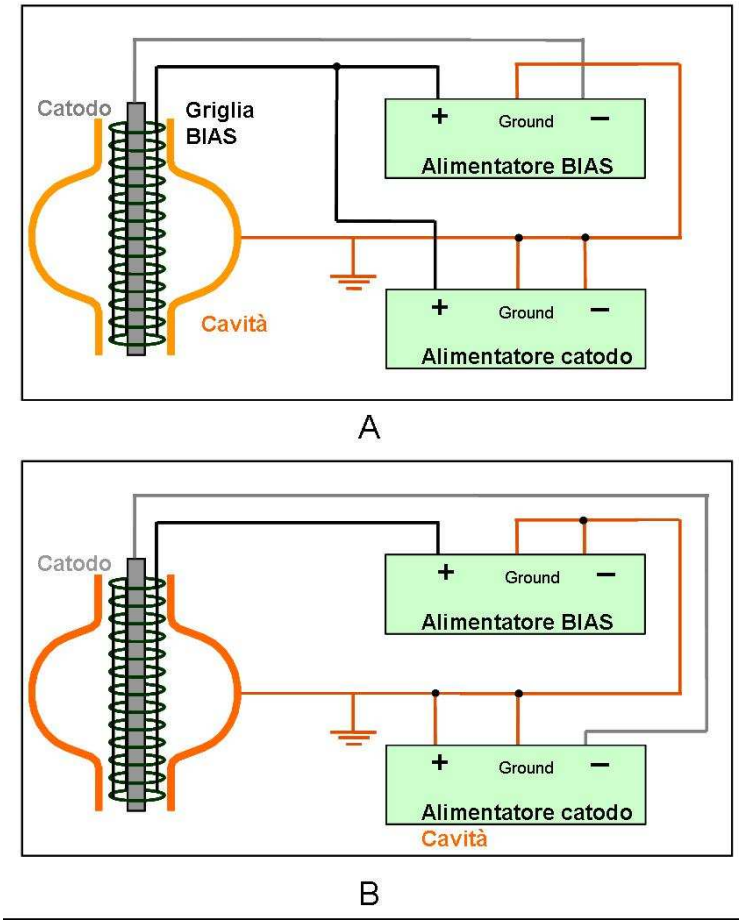

Figure 8.4: *Schematic of two electric circuits to connect the cavity, the cathode and the biased grid. A and B are conceptually the same although the currents distributed by the power supplies are different (see table 8.1).*

the power supplies in the two different ways, the power supply parameters, necessary to guarantee the distribution of potentials, have been collected in table 8.1. This procedure has allowed to optimize the parameters during the depositions.

Circuit	**Cathode Power Supply**			**Grid Power Supply**			**Potential diff.**	
	Current (A)	Voltage (V)	Power (W)	Current (A)	Voltage (V)	Power (W)	Cathode-Grid	Grid-Cavity
A	0.84	400	336	0.10	100	10	100	400
B	1.63	300	489	1.38	100	138	100	400
A	1.92	450	864	0.30	100	30	100	450
B	3.15	350	1102	2.72	100	272	100	450

Table 8.1: *Summary of the coating parameters for the three of the ring shaped cathode.*

8.1.3 *Biased magnetron sputtering configuration: the construction*

The gird is mounted around the cathode discs, tied up to the Nb wings by three ceramic isolators and then connected to the power supply. During the first run the stainless steel grid (figure 8.3) have been tested but after test, leveled with the equator, one of the steel rod of the net resulted interrupted, apparently fused.

Eventual off-axis magnet magnetization could concentrate the electrons on one side of the cathode making only one of the rods being bombarded by all of them. The melting of the rods is avoided by rotating the magnet around its axis (figure 8.5). Moreover, it has been noticed that the isolators were covered by a thin film. To avoid a short-circuit between the cathode and the grid, the system of isolation has been changed in order to use screened isolators. In the chamber, the melting of materials different from niobium has to be completely avoid since it can contaminate the film during the deposition.

The second planned grid is made of palatinate titanium. It is a flat rhombus meshed

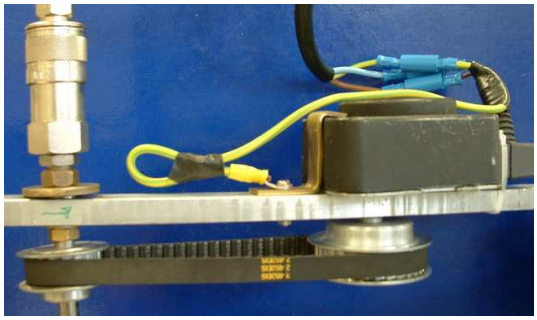

Figure 8.5: *This actuator avoid the melting of the rods by rotating the magnet around its axis.*

net of 75 mm of diameter, with mesh 10 mm large. Titanium (Tmelting = 1670° C)has a melting temperature higher than the stainless steel (Tmelting = 1420° C). This grid

didn't fuse but its insertion in the cavity beam pipe (Ø 78 mm) has been very difficult. A titanium grid with a smaller diameter makes the insertion easier, but the difficulty to center it provoked again the fusion of the net during deposition test. In addition, the mesh is even thicker that the first one causing shadowing during niobium sputtering.

The third and definitive more efficient grid configuration used stainless steel rods (SS)

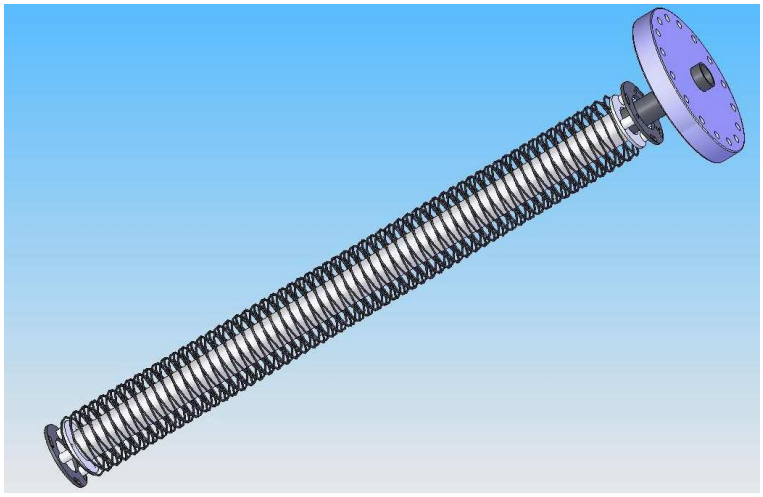

Figure 8.6: *Titanium grid 3D technical drawing.*

and the second and actual version uses niobium rods. The niobium tube is surrounded by six vertical rods isolated from the cathode by ceramic cylinders **??**. Twelve springs keep the rods tight and avoid heating deformations.

The idea to add some springs to stretch the bars in spite of the thermic extension and the magnet rotation have been tested several times and alll results reported in the following sections refers to this configuration.

8.2 *Description of the coating set up and process parameters*

The aim of the present research activity is to verify the influence of applied bias voltage on microstructural and functional properties of MS-PVD Niobium thin films for superconducting resonant cavities for particle accelerators.

To start the I-V curves of the magnetron sputtering system with the six niobium biased rods, have been acquired. Data, collected at different pressures and bias voltages, are displayed in figures 8.11 and 8.12. Data are fitted and the n parameters, that give information about the ionization efficiency of the plasma, have been calculated. At 100V or 150V bias the n parameter doesn't change much, instead at 200V n clearly decreases.

Rising the bias voltage from 100V to 200V the electron current on the grid doesn't show relevant changes, meaning that it is on the asymptotic part of the I-V curve.

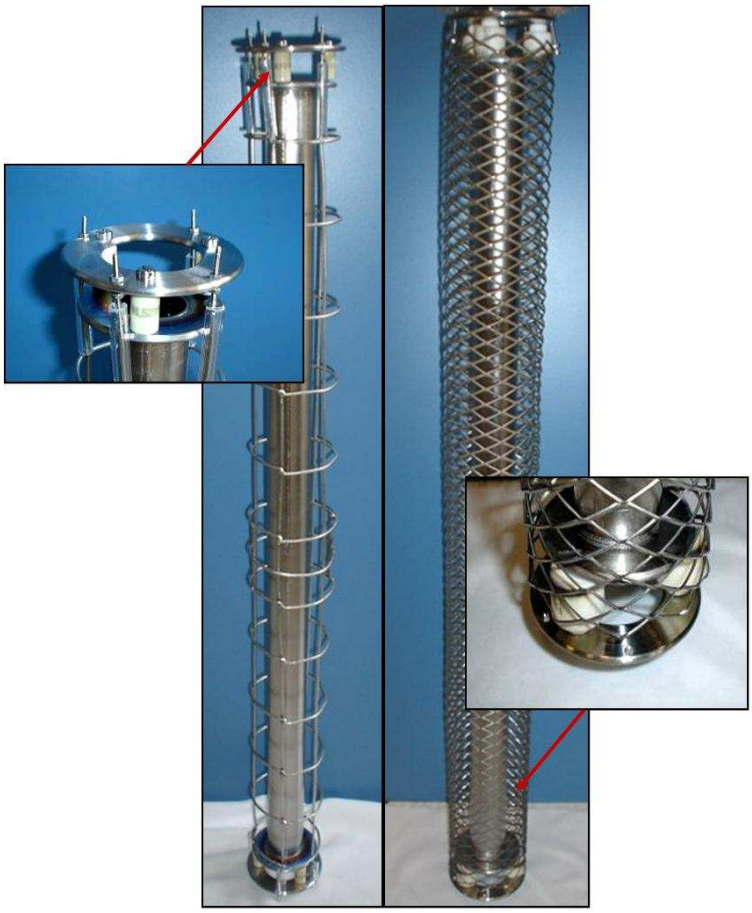

Figure 8.7: *The stainless steel grid (on the left) and the titanium grid (on the right) realized for the magnetron bias project. The two details show two different kind of isolators used to support the grid.*

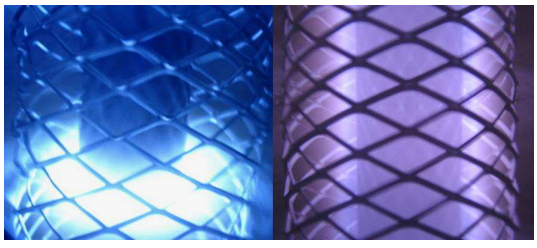

Figure 8.8: *Pictures of the plasma discharge in the bias magnetron configuration. On the left the plasma is confined by an internal magnet. On the right the plasma is spread along the cathode due to the magnetic field of two external coils as in figure 7.19.*

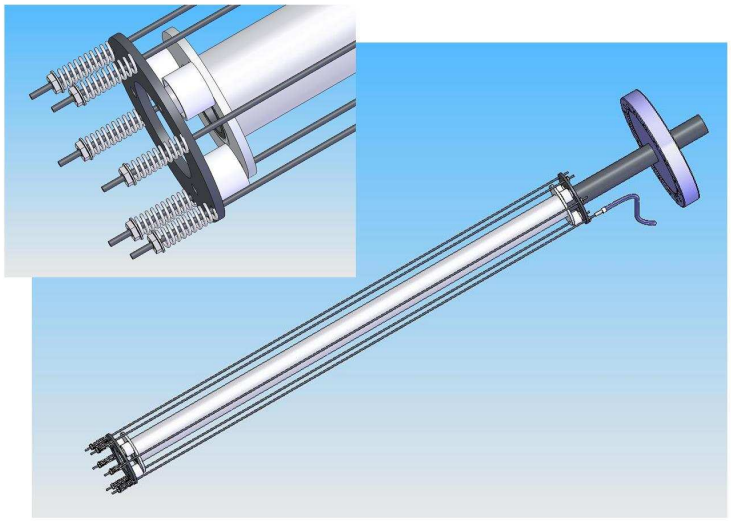

Figure 8.9: *Six vertical niobium rods are kept tight by twelve springs to avoid heating deformations.*

Figure 8.10: *Pictures of the plasma discharge in the bias magnetron configuration. The plasma is confined by an internal magnet leveled with the cavity cell.*

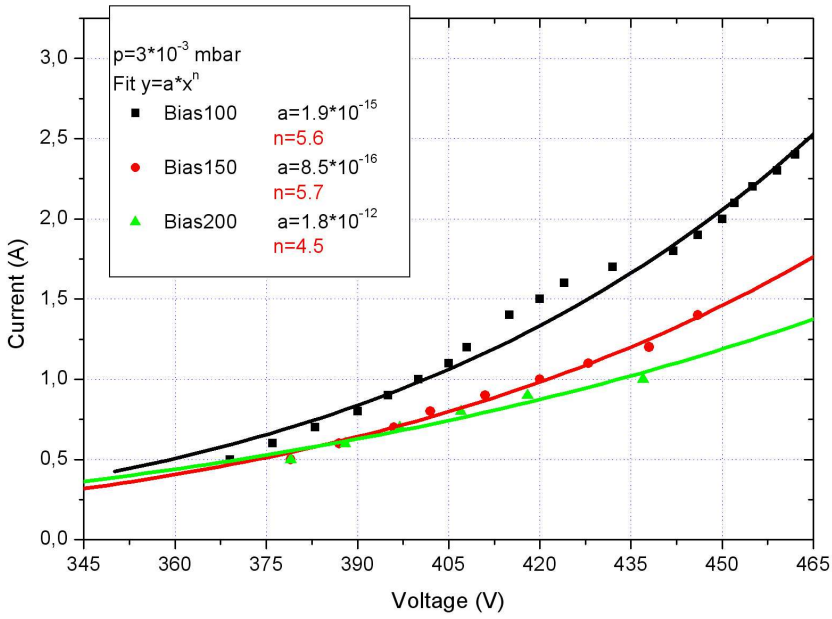

Figure 8.11: *I-V curves for different bias voltages applied. The magnet is leveled with the cell equator and the pressure is* $3{\cdot}10^{-3}$.

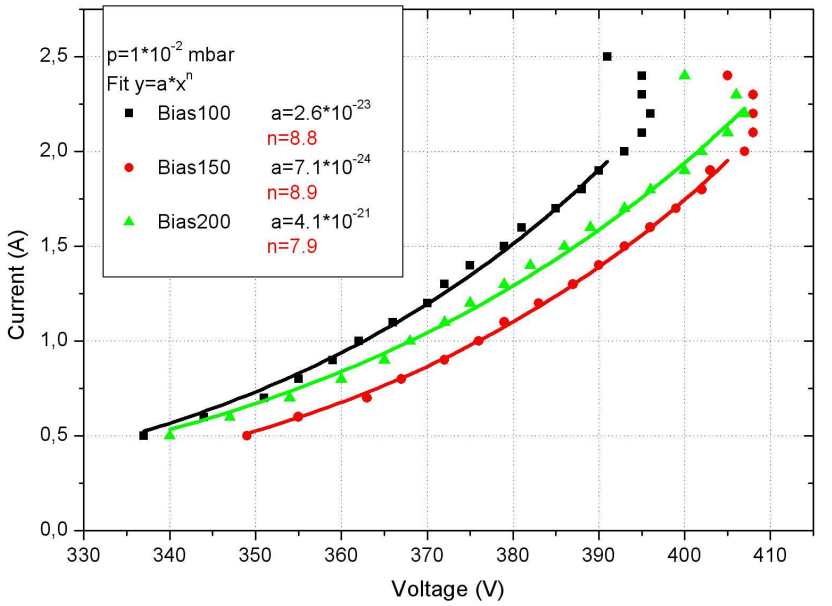

Figure 8.12: *I-V curves for different bias voltages applied. The magnet is leveled with the cell equator and the pressure is* $1{\cdot}10^{-2}$.

8.2.1 *First results of bias magnetron sputtering configuration*

Results of the bias magnetron sputtering technique have been compared with CERN type standard deposition . Coating parameters for the bias magnetron test are summarized in table 8.2, while standard coating parameters are collected and commented in section 6.4.1. Best RRR between 29 and 35 in the cell and 47 above and below the iris have been

Run	I_{cell} (A)	p_{cell} (mbar)	$time_{cell}$ (min)	I_{bias} (A)	V_{bias} (V)
16B	7.5	$5{\cdot}10^{-3}$	10	1.24	100
17B	7	$4.4{\cdot}10^{-3}$	20	1	100

Table 8.2: *Summary of the coating parameters used in runs 16B and 27B, to test the bias magnetron sputtering technique.*

obtained after sputtering with the niobium rods configuration. Maximum Tc obtained at the equator is 9.3K, meaning a compressive stress of the crystal lattice, confirmed also by X-ray diffraction cell parameter measure a = 3.30 Å. A comparison between RRR of CERN type niobium films and and those obtained with the BIAS technique is shown in figure 8.13. This results show no improvement or worsening of the film stress respect to MC standard deposition.

Texture analysis on biased results have been performed on (110) peak, the most intense in Nb powder diffractogram, in order to investigate the occurrence of preferential orientation during film growth. Texture figures show an homogeneous grain orientation growth, mainly perpendicular to the substrate, all along the cavity cell.

Film thickness measurement show that the grid shadowing doesn't affect the sputtering rate in any position all along and around the cell.

Probable limiting factors are the impurities coming from the all the stainless steel immersed in the plasma; in fact they could partly mask the benefit effects of the applied bias. Impurity content analysis hasn't been executed yet.

Film of 2μm thick on the equator have been obtained after 20 minutes sputtering. Films positioned on both iris regions are 0.4 μm thicker that the equator films.

Impurity content non quantitative SIMS analysis reveal no significant presence of other metal elements than niobium.

8.2.2 *Last results of bias magnetron sputtering configuration*

The main objective of the present section is to evaluate the bias effect on the morphological, microstructural and mechanical properties of Nb films and to correlate this information with the superconducting properties.

Two different sample set were produced, (i) adopting CERN deposition parameters and (ii) with an applied bias voltage of 100V; coatings were deposited both on quartz substrate, commonly used to perform superconductive properties measurements, and OFHC

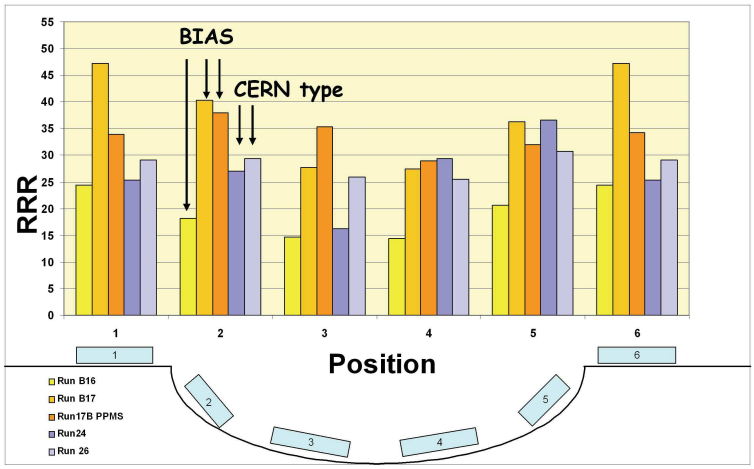

Figure 8.13: *Comparison between RRR of CERN type and BIAS technique niobium thin films.*

Cu substrate, in order to understand how the substrate influence the thin film structure and properties.
Four different sets of samples were produced, both varying the applied bias voltage and the nature of the substrate (Copper or Quartz). For the standard samples we refer to run 30 and run 31 summarized in table 6.4, while the coating parameters applied to the bias magnetron sputtering runs are collected in table 8.3. [110]

Run	I_{cell} (A)	p_{cell} (mbar)	$time_{cell}$ (min)	I_{bias} (A)	V_{bias} (V)
20B	7	$4{\cdot}10^{-3}$	20	1	100
21B	7	$5{\cdot}10^{-3}$	20	1	100

Table 8.3: *Summary of the coating parameters used in runs 16B and 27B, to test the bias magnetron sputtering technique.*

Surface Morphology and Coatings Microstructure

In-plane SEM analysis reveals a strong tendency of the film in replicate the grain structure of the copper substrate. The analysis at different magnitudes shows a needle-shaped grain structure from both biased (Figure 3a) and unbiased (Figure 3c) coatings on Copper substrate, with grain average longitudinal dimension of 350 nm.

AFM images (figure 8.14b and figure 8.14d) confirm a crystallite elongated structure with an average dimension of 300-350 nm. Superficial roughness results are reported in table 8.15: bias technique produce more rough film than the standard one.

Figure 8.16 show SEM observation after FIB sectioning of biased (figure 8.16a) and unbiased (figure 8.16b) thin Nb films on oxidized copper. A coarser microstructure is observed for the unbiased coating, with large columnar grains that extend all the way

through the film depth; finer grains are visible in the case of the biased coating. Further analysis are needed to prove whether such microstructural features do, as one would guess, influence the coating residual resistivity, but superconducting experimental measurements on Nb/Cu systems are not straightforward, due to the high conductivity of the substrate.

Figure 8.16(e-f) shows a detail of the biased coating on Cu substrate, detected by TEM after FIB lamella thinning, of the surface oxide layer, whose thickness of 12 nm is slightly higher than previously reported results (5-8 nm, [7]).

Figure 8.16c-d show the deleterious effects of a wrong substrate surface preparation by electropolishing without any chemical polishing after it. In this case, no SUBU etching treatment was adopted, and superficial defects remain after electropolishing, with noteworthy effects on coating RF properties. A possible cause of wrong parameters setting could be an erroneous exposure of sample surface to the cathode, for example sample backside should be always screened because it can influence the electric field. Chemical treatment can help smoothing the pitting due to a wrong electropolishing. The choice of the electropolishing parameters, setting and mixture is well explained in ref [17]. Also in this case the use of FIB techniques resulted to be important for interfaces characterization.

In-plane SEM analysis reveals significant differences between biased (figure 8.14e) and unbiased (Figure 8.14g) films, also confirmed by AFM analysis (figure 8.14f and figure 8.14h).

Niobium unbiased film on quartz shows a needle-shaped grain structure with an average longitudinal dimension of 300-350 nm, while biased coating on quartz shows a coarser round-shaped structure ($>$ 400nm).

Superficial roughness results are reported in table 8.15: also in this case bias technique produce a rougher film than the standard one.

Nanoindentation and Microhardness values (Korsunsky Model), reported in table 8.17, are consistent. Depth-Force data show a systematic displacement breakdown (horizontal line in Figure 5b) at 10-15 nm of penetration depth: this behaviour could be associated to the brittle failure of the oxidized superficial layer, observed also by FIB/TEM analysis.

It is noteworthy that lower hardness values and Elastic modulus values were measured in case biased Nb on quartz substrate, compared to the same coating on Copper substrate: this behaviour is likely due to microstructural changes due to a re-sputtering effect related to the low conductivity of quartz substrate, which leads to lower film density and coarser grain size, as confirmed by the microstructural differences detected by SEM-AFM (figure 8.14e-h).

As a further confirmation, Nb biased film on quartz substrate has a peculiar nanoindentation behaviour: results have low repeatability (see table 8.17) and more test have been necessary to increase the statistical validation, as a consequence of a rough and coarse surface.

In case of micro-hardness testing different deformation mechanism under indentation is observed for the same coatings on different substrates: indentation marks show an evident sinking-in (figure 5c-d) for high applied loads ($>$ 100gf) in case of Cu substrate, whilst they

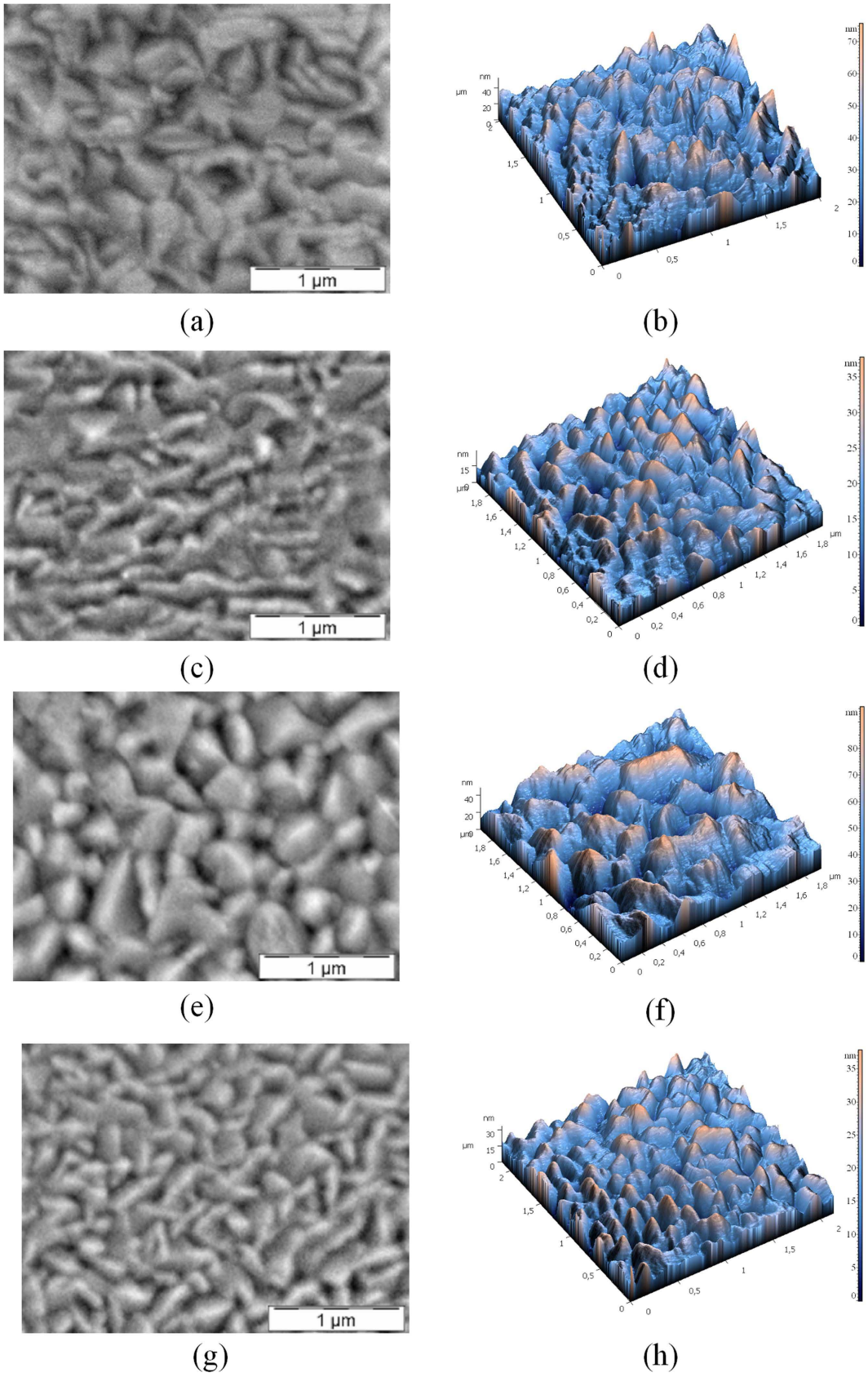

Figure 8.14: *SEM-AFM Surface morphological analysis on Nb thin films:(a) Nb on Cu BIAS type (SEM SE 20 kV 40000x);(b) Nb on Cu BIAS type (Contact Mode AFM);(c) Nb on Cu CERN type (SEM SE 20 kV 40000x);(d) Nb on Cu CERN type (Contact Mode AFM);(e) Nb on quartz BIAS type (SEM SE 20 kV 40000x);(f) Nb on quartz BIAS type (Contact Mode AFM);(g) Nb on quartz CERN type (SEM SE 20 kV 40000x);(h) Nb on quartz CERN type (Contact Mode AFM)*

Deposition mode	ID (#)	Substrate	Average Thickness [μm]	Roughness: RMS-Ra-peak to peak [nm]
Biased MS-PVD Nb film	R20/797	Quartz	2,5±0,2	7,98 -6,41- 48,77
	R20/796	Copper	2,2±0,2	7,21 - 7,75 - 52,57
Unbiased MS-PVD Nb film	R30/804	Quartz	1,81±0,08	4,68 – 3,78 – 33,59
	R30/803	Copper	1,1±0,3	4,37 – 3,47 – 29,38

Figure 8.15: *Results summary for morphological characterisation of the films.*

show an evident piling-up in case of quartz substrate (Figure 8.18e-f): this effect disappears at lower applied loads: the different behaviour can be attributed to the different properties of the substrates which are in fact mechanical constraints which regulate coatings' plastic flow during indentation: for these reasons, the application of energy based models (such as the model of Korsunsky [89]) is much more effective than geometry-based models (such as Chicot-Lesage [87] or Jonsson-Hogmark [86]), because they cannot take into account geometrically different plastic flows due to substrate effects; this has been already reported in literature [85]. Only niobium films on quartz has been analyzed with the resistive methods. Two runs of sputtering with the bias technique show a similar values of RRR for all films around the equator (figure 8.19). Unbiased technique shows such a difference in RRR due to the different time of sputtering (15 min for Run 30 unbiased and 20 min for Run 31 unbiased). Time of sputtering has a strong influence on the film purity and consequently on RRR: the higher is the sputtering time, the purer is the gas in the chamber and the cleaner is the atoms flux arriving on the substrate, due to the getter property of the growing niobium.

Discussion

The goal of the present work was to evaluate the influence of applied bias voltage on microstructural properties, mechanical properties and functional performances of MS-PVD Nb coatings for superconducting applications.

Comparing RRR results for the two techniques and the same sputtering time (Run 20 biased, Run21 biased and Run31 unbiased), unbiased samples shows higher RRR around 34. There is a systematic decreasing of the RRR from the sample positioned just above the equator and the sample just below the equator. Biased films show higher critical temperature than unbiased films (figure 8.20) but most of them are included in the error bars. Equator up and down films don't show significant differences for all tests. All film reveal a critical temperature higher than bulk niobium.

Thickness difference (figure 8.21) between the film on equator position up and down could be due to a screening of the lower sample from the screw used to fix the quartz substrate. An error on the magnet centering respect to the equator center has been checked

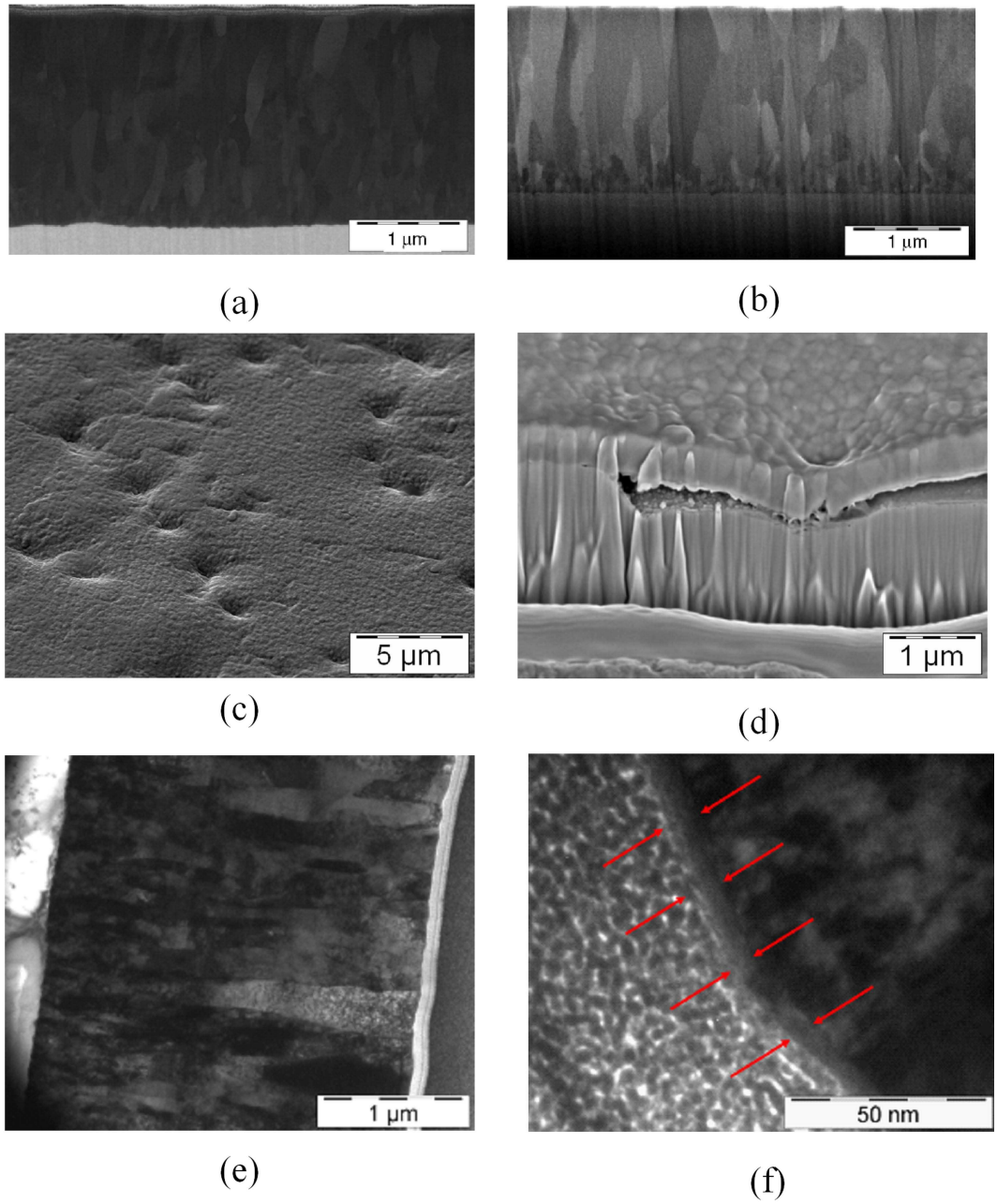

Figure 8.16: *Focussed Ion Beam (FIB) based analysis of surfaces and interfaces of Nb thin films: (a) Nb on Cu BIAS type (FEG-SEM SE 3 kV 80000x, after FIB sectioning); (b) Nb on Cu CERN type (FEG-SEM SE 3 kV 80000x, after FIB sectioning); (c) In-plane observation of surface defects induced by wrong substrate preparation, Nb on Cu BIAS type (FEG-SEM SE 5 kV 10000x); (d) Cross-section observation of surface defects induced by wrong substrate preparation (FEG-SEM SE 5 kV 40000x); (e) Nb on Cu BIAS type (TEM BF 25000X after FIB lamella thinning): (f) Detail of the surface oxide layer, Nb on Cu BIAS type (TEM BF 660000X after FIB lamella thinning.*

Sample code	Description	Nanoindentation		Standard micro-indentation
		H (GPa)	E (GPa)	H (GPa) Korsunsky model
R20/796	Nb on Cu BIAS type	3,10 ± 0,58	101,5 ± 23,61	2,51 ± 0,15
R20/797	Nb on quartz BIAS type	1,63 ± 0,30	76,22 ± 48,99	1,75 ± 0,12
R30/803	Nb on Cu CERN type	2,59 ± 0,35	108,68 ± 11,65	2,38 ± 0,15
R30/804	Nb on quartz CERN type	2,19 ± 0,31	95,95 ± 26,31	2,01 ± 0.10

Figure 8.17: *Nanoindentation and Microhardness Results.*

several time and excluded because it is possible to see the plasma position trough a window on the equator of the stainless steel cavity shaped chamber.

Thickness difference between sample on equator position up and down, directly influences the film RRR because resistivity decrease with the increasing of the average grain dimension with thickness. RRR directly depends on film thickness (grain dimensions), defects, impurities and grain boundary scattering. In this case higher RRR doesn't coincide with higher thickness and bigger grain dimensions of the film. This probably suggests a higher impurities concentration: bias apparatus is made up with six small ceramic break on the top and the bottom of the cathode and six niobium RRR 100 bars. Such amount of additional matter in the chamber could bring impurities inside it: bars are surrounded by plasma during deposition and they could evaporate just enough to deposit less pure niobium on the growing film, while ceramic break are far from the plasma but they are porous so they could bring powder inside the chamber. In addition the argon ionic bombardment of the growing film increase the concentration of nobel atoms embedded in the lattice.

Differences from run to run, due to changes in the cathode shape (erosion) and cathode purity are not so relevant and they are included in the RRR error bars.

Significant differences in coatings microstructure were observed both in case of biased and unbiased coatings and in case of either copper or quartz substrate (usually adopted for RRR measurements).

In particular, biased coating on quartz substrate showed different surface morphology (higher grain size and surface roughness, observed by SEM and AFM), compared to the other produced coatings.

This is likely due to a re-sputtering effect, coming from the lower conductivity of the quartz substrate, which influences the plasma distribution, and then the sputtering yield, in the proximity of the substrate.

Focussed Ion Beam (FIB) analysis also confirms that biased films on copper have finer grain size than unbiased film, while the use of FIB techniques sample preparation, coupled with TEM observation, gave a much deeper understanding of coatings microstructure at nanoscale: in particular the presence surface oxide layer was observed, and an estimation of its thickness was performed. It has to be underlined that at present no other technique can give equivalent morphological and microstructural thin films characterization, includ-

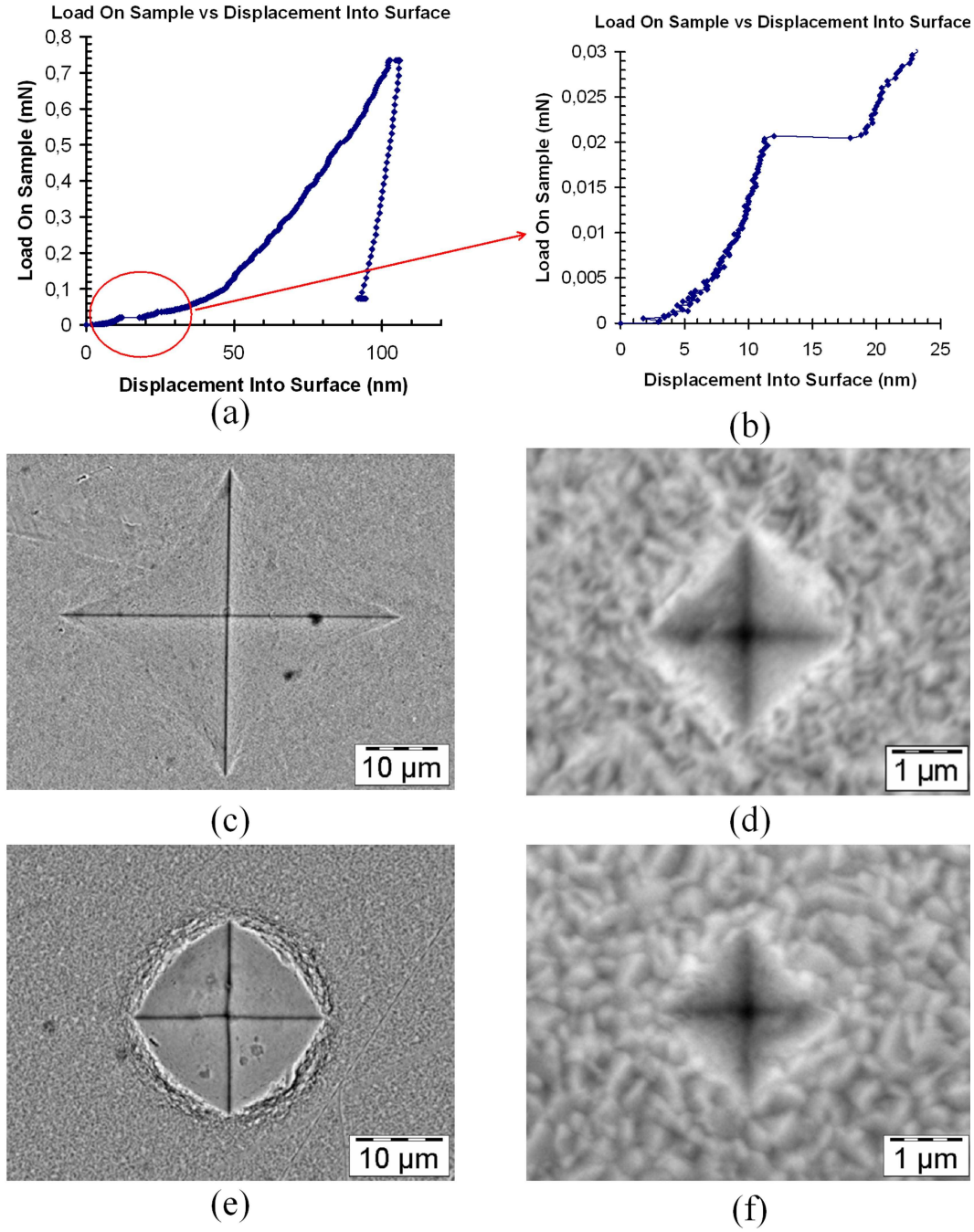

Figure 8.18: *Nanoindentation and microindentation testing on Nb thin films:(a) Load-depth (L-d) curve in case of Nb coating on Cu CERN type; (b) Detail of the L-d curve highlighting brittle failure of the surface oxide layer at depth 9-11 nm; (c) Vickers micro-indentation mark (SEM 20kV SE 2000x), Nb coating on Copper substrate CERN type, applied load 100 gf: a strong sinking-in is visible; (d) Vickers micro-indentation mark (SEM 20kV SE 20000x), Nb coating on Copper substrate CERN type, applied load 100 gf; (e) Vickers micro-indentation mark (SEM 20kV SE 2000x), Nb coating on quartz substrate CERN type, applied load 100 gf: a strong piling-up is visible; (f) Vickers micro-indentation mark (SEM 20kV SE 20000x), Nb coating on quartz substrate CERN type, applied load 1 gf*

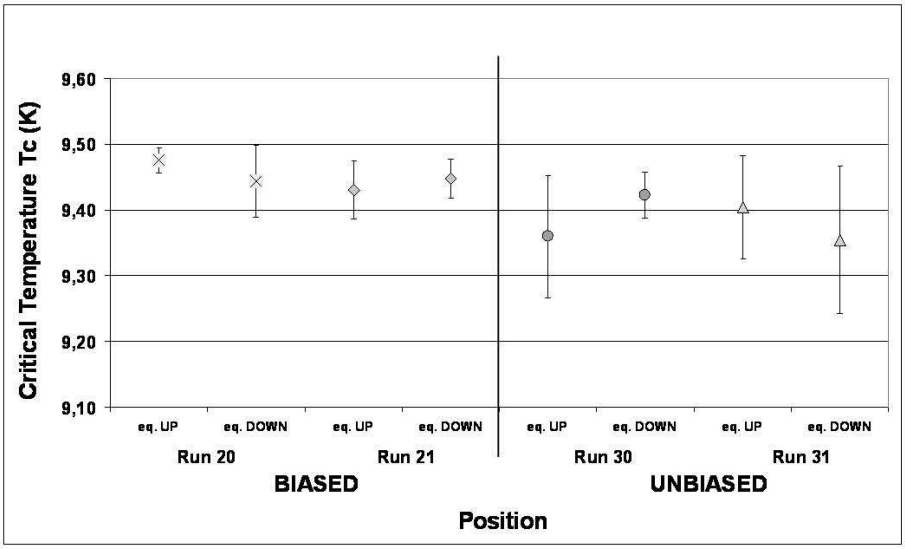

Figure 8.19: *RRR values of the niobium film on quartz sample, for different positions around the equator (eq. UP, eq. DOWN) and two different runs for each deposition techniques (Biased, Unbiased)*

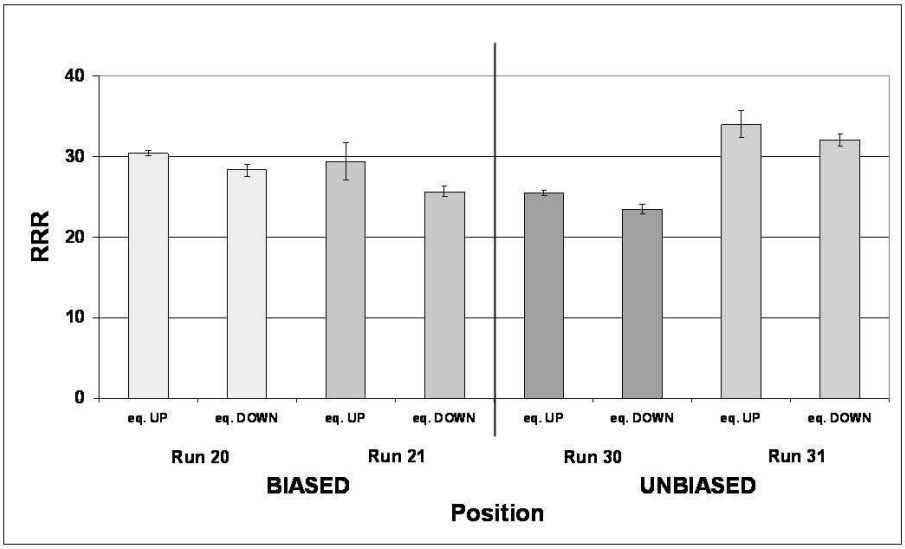

Figure 8.20: *Critical temperature Tc of the niobium film on quartz sample, for different positions around the equator (eq. UP, eq. DOWN) and two different runs for each deposition techniques (Biased, Unbiased)*

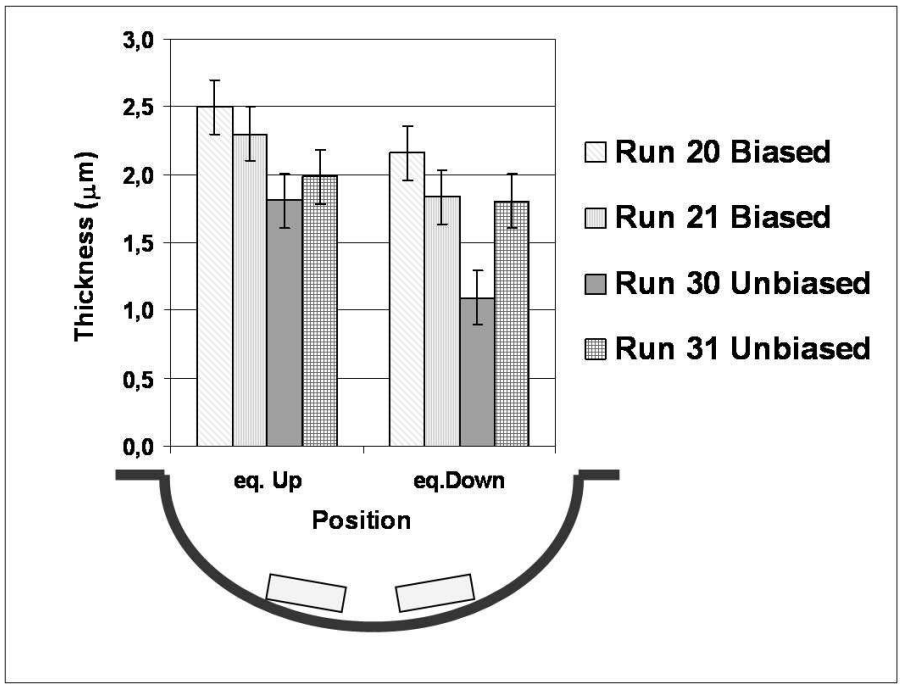

Figure 8.21: *Thickness values of the niobium film on quartz sample, for different positions around the equator (eq. UP, eq. DOWN) and two different runs for each deposition techniques (Biased, Unbiased)*

ing speed of analysis, site-specific morphology and composition and crystal orientation.

It is noteworthy that contrasting microstructural characteristics were observed on biased and unbiased coatings on different substrates: biased Nb films on copper showed higher roughness, finer grain size, compared to the unbiased on the same substrate, while opposite results were obtained for coatings on quartz substrate: such results suggest that attention should be paid to the use of RRR results (obtained for coatings on quartz substrate) for deducing conclusions on cavity performances.

Anyhow, RRR measurements play a fundamental role as a threshold experimental investigation technique, giving essential comparative information on the basic quality of coatings (such as level of impurities) obtained for different deposition conditions.

Such microstructural features were also clearly deducted from surface indentation testing, performed by Vickers micro-indentation (and the application of Korsunsky model for intrinsic hardness evaluation) and by Nanoindentation: biased Nb coating on quartz showed lower intrinsic hardness, lower apparent elastic modulus, and higher scatter of experimental data, as a consequence of a less dense microstructure and a higher surface roughness.

It has to be underlined that many previous experiments have evidenced the existing relationship between surface mechanical properties of coatings and their microstructure. As an example, Matthews et al [91] have shown for several sputtered thin films that a linear relationship exists between hardness, elastic modulus and coating density. Hardness measurement together with models to extrapolate the true film hardness [85, 87, 86, 89]

and its elastic modulus [90], therefore give useful information on the film microstructure, even in the case of coatings with functional applications.

In addition, nanoindentation testing also allowed an indirect (and cheaper) evaluation of the presence and thickness of a surface oxide layer (figure 8.18b), which has been already correlated to coating's superconducting performances [111].

On the other hand, the use of micro-indentation testing could significantly reduce costs for quality control of sputtered Nb coatings for superconducting applications, once the correlation with microstructure is known.

Coating of 1,5 GHz copper cavities with the bias configuration

RF test carried out on two cavities get the results shown in figure 8.22. The Standard CM receipe applied on a copper cavity show a Q_0=2.6·10^9, the cavity quenches at 13 MV/m. The second coating with the BMP technique has been applied on the same cavity after stripping, electropolishing, chemical etching and HPWR. The cavity positioned on cryogenic stand undergoes several leak problem and in fact it quenched at very low field.

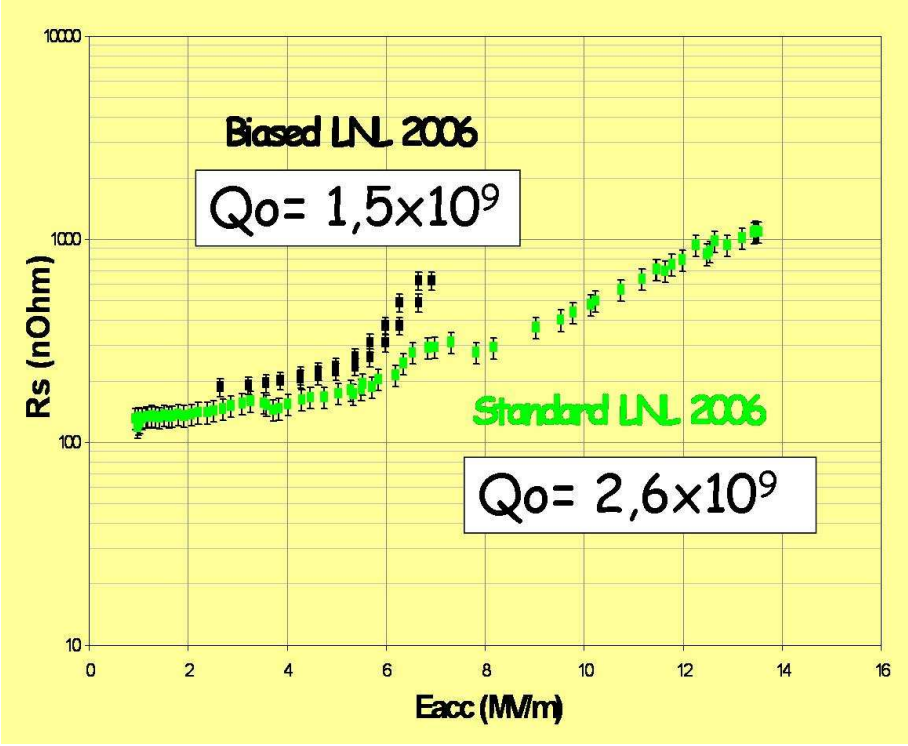

Figure 8.22: *RF test results for 1,5GHz tesla type monocell niobium on copper cavities [112].*

Conclusions

The main purpose of the present paper is to illustrate three different and new configurations for coating niobium into 1.5 GHz copper cavities. Several approaches have been studied to improve the sputtered niobium film properties: making niobium atoms impinging perpendicularly the substrate surface; promoting the effect of plasma bombardment of the growing film in order to remove impurities weakly bonded to the surface; increasing the sputtering area and the plasma ionization efficiency in order to increase the sputtering rate.

Different magnetron sputtering configurations have been built and tested: Ring shaped cathode; Biased Magnetron Sputtering Configuration; Large Area Cavity Shaped Cathode .

The ring shaped cathode has been optimized with several magnetic field simulations and the best results have been obtained in the post-magnetron configurations with two coils. Even if texture analysis reveals different orientations in the film growth, improvements in the film homogeneity have been obtained: thickness is relatively constant along the cell and Tc and RRR also. New magnets have been simulated in order to improve and optimize the cathode shape.
The "large area cavity shaped cathode" idea of ten cavity shaped cloves coaxial with the cavity is still in progress. Some tests have confirmed the mechanical stability of the structure but still film results are poor. The main reason is the formation of a high ionized plasma inside the cathode instead of outside it, on the substrate side. The number of cloves will be reduced to let the biased bar and the substrate communicate.

Best results have been obtained with pulsed biased magnetron sputtering with the six rods configuration but improvement of the film purity is compulsory for emphasizing the benefit of the ion bombardment.

Results of the bias magnetron sputtering configurations has been compared with those obtained with the standard CERN technique. They show slight differences: the former configuration gets few improvements and no worsening of the films RRR and Tc respect to MC standard depositions. The same assertion could be done for the cell parameters, related to the film stress, that show no relevant variation. The lower sputtering rate of the BIAS technique underline a probable percentage of resputtering of the biased film due to the positive grid.

The biased niobium films coated on copper and quartz grow with different microstruc-

ture, therefore superconducting measurement of niobium films on quartz could not reflect precisely the actual Niobium on Copper film properties. Even if biased niobium on copper films are harder and denser than the unbiased one, still their small grain dimensions and consequently their low RRR seem to make the biased technique similar with the standard one from the RF point of view. Preliminary RF tests seem to confirm this. Morphological characterizations (especially FIB techniques) are essential for determining the coating technique improvements and the coating quality before the rf tests. In fact rf tests need a more complex cryogenic and electronics apparatus. Furthermore, a correlation between coatings microstructure and indentation response has been observed, so the use of micro- and nano-indentation techniques can be an effective and low cost way for quality control also in case of functional coatings, such as Nb thin films for superconducting resonant cavities. Combination of morphological and RF characterization provide a deeper understanding of thin film behaviour and give useful indications for coating production process optimization.

To test step by step the development on the RF system, a 3-cell bulk niobium 1.3 GHz cavity has been prepared and measured three times. At the beginning the aim was comparing bulk niobium and thin film cavities but spinned niobium surface treatment are not yet sufficiently developed to obtain good and comparable results. Cavity cryogenic stand instability and coupler antenna problems still sap measurement reproducibility but several tests have been already completed successfully.

Niobium films have however not yet achieved their potential ultimate performance, contrary to what has been obtained with niobium sheet cavities, and this hinders at present their use for electron linacs although their cost is far inferior. Anyway several ways haven't been explored yet, many studies are under development and niobium films on copper cavities are still a challenge for SRF applications.

Appendix A

Pandira® code

POISSON, SUPERFISH is a group of codes that solve Poisson's equation and are used to compute field quality for both magnets and fixed electric potentials and RF cavity codes that calculate resonant frequencies and field distributions of the fundamental and higher modes. The group includes: POISSON, PANDIRA, SUPERFISH, AUTOMESH, LATTICE, FORCE, MIRT, PAN-T, TEKPLOT, SF01, and SHY.

POISSON solves Poisson's (or Laplace's) equation for the vector (scalar) potential with nonlinear isotropic iron (dielectric) and electric current (charge) distributions for two-dimensional Cartesian or three-dimensional cylindrical symmetry. It calculates the derivatives of the potential, the stored energy, and performs harmonic (multipole) analysis of the potential.

PANDIRA is similar to POISSON except it allows anisotropic and permanent magnet materials and uses a different numerical method to obtain the potential. It works with either 2-D Cartesian coordinates or axially symmetric cylindrical coordinates. The programs generate a triangular mesh fitted to the boundaries of different materials in the problem geometry

The following example is the code to simulate the magnetic field of a cylindrical NdFeB magnet, with 63,5mm external diameter and 30mm internal diameter, closed between two smaller iron cylinders as in figure below.

```
Dirichlet boundary at Z = 0
&reg kprob=0,dx=0.5,mode=0,
```

- information about the mesh width, therefore here is defined the simulation precision

```
kmax=150,\\
lmax=150,\\
```

- symmetry definition (cylindrical)

```
icylin=1,
```

- contour conditions definition

```
nbslo=0, nbsup=0, nbsrt=0, nbslf=0, ktype=1
```

- the magnetic field is calculated along a straight line. Here are the line coordinates

```
YMINF=5.5 XMAXF=14 \&\\
```

- calculation zone limits

```
; air-zone
&po x= 0.00,y= 15.00 &
&po x= 0.00,y=35.0 &
&po x= 20.0,y=35.0 &
&po x= 20.0,y=15.0 &
&po x= 0.00,y= 15.00 &
```

- magnet coordinates

```
; Magnet
&reg mat=7,mshape=1,mtid=1 &
&po x=2.7,y=24 &
&po x=2.7,y=26 &
&po x=3.2,y=26 &
&po x=3.2,y=24 &
&po x=2.7,y=24 &
```

- first iron cylinder coordinates

```
; Ferro Sopra
&reg mat=8,mshape=-1,mtid=3 &
&po x=1.5,y=4.5 &
&po x=1.5,y=5 &
&po x=3.2,y=4.5 &
&po x=1.5,y=4.5 &
```

- second iron cylinder coordinates

```
; Ferro Sotto
&reg mat=9,mshape=-1,mtid=3 &
&po x=1.5,y=4 &
&po x=3.175,y=4 &
&po x=1.5,y=3.5 &
&po x=1.5,y=4 &
```

- magnet materials and magnetization parameters

```
; NdFeB
&mt mtid=1,
aeasy=90, gamper=1,
hcept=-11500,bcept=12400 &
```

- iron magnetic properties

```
; Ferrite properties
&mt mtid=3,
BMU=0.19996 0.05
0.25007 0.15
0.30006 0.27
0.35005 0.38
0.40004 0.49
0.45002 0.56
0.50001 0.65
0.55 0.71
0.59999 0.77
0.64998 0.84
0.69997 0.9
0.80007 0.98
0.90005 1.06
1.00003 1.12
1.50004 1.32
2.00005 1.42
2.50007 1.48
3.00008 1.52
3.5001 1.55
4.00011 1.57
4.50012 1.58
5.00014 1.59
5.50015 1.605
6.00016 1.615
6.50018 1.625
7.00019 1.63
8.00022 1.64
9.00024 1.645
10.00027 1.65
15.00041 1.67
20.00054 1.7
25.00068 1.72
30.00082 1.735
...
```

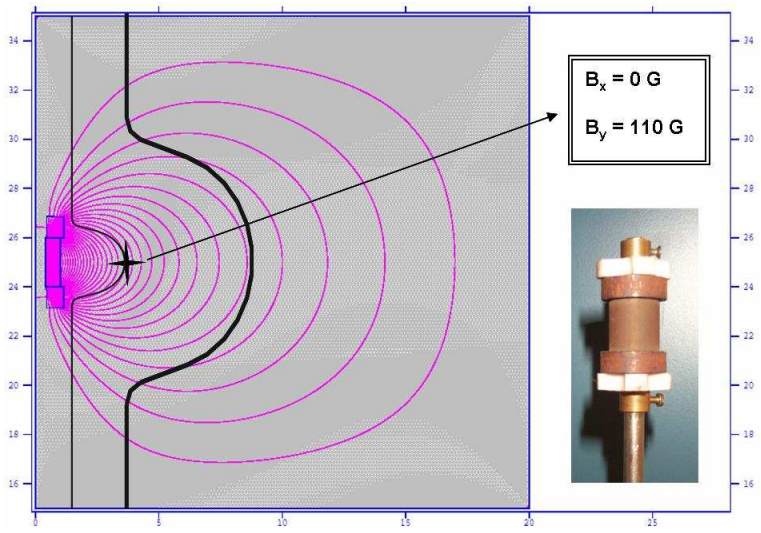

Figure A.1: *Result of the magnetic field simulation listed above.*

List of Tables

List of Figures

Bibliography

[1] G. Bisoffi et al., *ALPI QWR and S-RFQ operating experience*, in: Proceedings of the 13th Workshop on RF Superconductivity, Peking University, Beijin, China, 2007.

[2] G. Wu, L. Philips, *Thin Film Coatings for RF Superconductivity*, in: Proceedings of the 1st Thin Film Workshop, Jefferson Lab, VA, 23606, 2004.

[3] H. Padamsee, J. Knobloch, T. Hays, *RF Superconductivity for Accelerators*, John Wiley & Sons, Plenum Press, San Diego, 1998.

[4] W. De Sorbo, *Effect of Dissolved Gases on Some Superconducting Properties of Niobium*, Phys. Rev. 134 (1964) A1119.

[5] S. Calatroni, C. Benvenuti, V. Ruzinov, *Diffusion of oxygen during bake-out*, in: Proceedings of the 10th Workshop on RF Superconductivity, KEK, Tsukuba, Japan, 2001, PR025.

[6] G. Eremeev, H. Padamsee, *Temperature Map Studies on Nearly Oxide-Free, Thin-Oxide and Standard-Oxide Cavities*, in: Proceedings of the 13th Workshop on RF Superconductivity, Peking Univeristy, Beijin, China, 2007, WE101.

[7] J. Halbritter, *Transport in superconducting niobium films for radio frequency applications*, J. Appl. Phys. 97 (2005) 083904.

[8] J. Bardeen, L. Cooper, J. R. Schrieffer, *Theory of superconductivity*, Physical Review 108 (1957) 1175.

[9] A. Pippard, Proc . Roy. Soc A203 (1953) 98.

[10] J. Waldram, *Surface Impedance of Superconductors*, Adv. Phys. 13.

[11] B. Bonin, *Materials for superconducting cavities*, in: *Superconductivity in Particle Accelerators*, S. Turner, CERN, May 1996, p. 191, CERN 96-03.

[12] K. Saito, P. Kneisel, *Temperature Dependence of the Surface Resistance of Niobium at 1300 MHz - Comparison to BCS Theory*, in: Proceedings of the 9th Workshop on RF Superconductivity, Santa Fe, New Mexico, USA, 1999.

[13] J. Halbritter, *Calculation of the BCS surface resistance*, Z. f.Phys. 238 (1970) 466.

[14] F. Palmer, *Surface resistance of Superconductors - Examples from Nb - O system*, in: Proceedings of the 3th Workshop on RF Superconductivity, Argonne, USA, 1988, ANL-PHY-88-1, pag 309.

[15] B. Bonin, H. Safa, J. Charrier et al., *Flux trapping in superconducting cavities*, in: Proceedings of the 3rd EPAC, 1992, p. 1295.

[16] W. T. Singer, X. Singer, H. Wen, *Influence of interstitials on properties of high purity niobium for RF*, Materiaux & Techniques 7-8-9.

[17] V. Palmieri, *Fundamentals of electrochemistry-the electrolytic polishing of metals: application to copper and niobium*, in: Proceedings of the 11th Workshop on RF Superconductivity, Lübeck, Germany, 2003, WETO2.

[18] V. Palmieri, *Advancements on Spinning of Seamless Multicell Reentrant Cavities.*, in: Proceedings of the 11th Workshop on RF Superconductivity, Lübeck, Germany, 2003, TuP26.

[19] V. Palmieri, *Progress on Spun Seamless Cavities.*, in: Proceedings of the 12th Workshop on RF Superconductivity, Cornell University, Ithaca, NY, USA, 2005, TuP68.

[20] W. Singer, H. Kaiser, X. Singer, G. Weichert, I. Jelezov, P. Kneisel, T. Fujino, K. Saito, *Hydroforming of superconducting tesla cavities*, in: Proceedings of the 10th Workshop on RF Superconductivity, KEK, Tsukuba, Japan, 2001, FA009.

[21] V. Palmieri, R. Preciso, V. Ruzinov, Ital. Pat. Appl. RM91 (1991) A000616.

[22] V. Palmieri, R. Preciso, V. Ruzinov, American Pat Appl07-930.

[23] V. Palmieri, *Seamless cavities: the most creative topic in RF Superconductivity*, in: V. Palmieri, A. Lombardi (Eds.), Proceedings of the 8th Workshop on RF Superconductivity, Abano, Italy, 1997, vol.3.

[24] H. Padamsee, IEEE Trans. Magnetics 19 (1983) 1322.

[25] W. Weingarton, *Progress in thin film techniques*, in: Proc. Of 7th workshop on RF superconductivity, Gif-sur-Yevette, France, 1995.

[26] T. Wang et al., *DC field emission studies,10th workshop on RF superconductivity*, in: Proceedings of the 10th Workshop on RF Superconductivity, KEK, Tsukuba, Japan, 2001.

[27] C. Durand, P. Bosland, J. Mayer, *Non Quadratic RF Losses in Niobium Sputter Coated Accelerating Structures*, Appl. Superconductivity,IEEE Trasactions on 5 (1995) 1107.

[28] J. Halbritter, J. Supercond. 8 (1995) 691.

[29] I. Kulik, V. Palmieri, Part. Accel. 60 (1998) 257.

[30] B. et al., in: Proceedings of the SRF2001 Workshop, S. Noguchi ed.

[31] B. et al., in: Proc. of the SRF2003 Workshop, D. Proch ed.

[32] M. Malev, D. Weisser, *Oxygen desorption during niobium sputtering for superconducting RF accelerators*, NIM in physics research A 364 (1995) 409.

[33] J. Halbritter, in: Proceedings of the 10th Workshop on RF Superconductivity, KEK, Tsukuba, Japan, 2001.

[34] J. Halbritter, Supercond. Sci. Technol. 12 (1999) 883.

[35] S. Calatroni, *20 years of experience with the Nb/Cu technology for superconducting cavities and perspectives for future developments*, in: Proceedings of the 12th Workshop on RF Superconductivity, Cornell University, Ithaca, NY, USA, 2005.

[36] V. Palmieri, *A DC Post-magnetron configuration for niobium sputtering into 1.5 GHz Copper monocells*, in: Proceedings of the 7th Workshop on RF Superconductivity, Gif-sur-Yevette, France, 1995, p. 485.

[37] G. Lanza, *Superconduttività in radiofrequenza applicata alle cavità acceleratrici: deposizione per sputtering di film sottili di niobio e relativa correlazione fra morfologia, microstruttura e proprietà elettriche* (2004).

[38] G. e. a. Fortuna, in: Proceedings of EPAC92, Vol. 170, 1992.

[39] M. e. a. Porcellato, Nucl. Instr. and Meth. A 382 (1996) 121.

[40] A. Porcellato et al, in: Proceedings of the 8th HIAT Conference, Argonne (USA), 1998, p. 228.

[41] R. Russo et al., Supercond. Sci. Technol. 18 (2005) L41.

[42] R. Russo, *Report of ARCO Project*, in: Proc. Of 10th workshop on RF superconductivity, Tsukuba, Japan, 2001.

[43] R. Russo, L. Catani, A. Cianchi, D. DiGio, R. Nietubyc, M. Sadowski, M. Bruchon, B. Visentin, B. Ruggiero, *Nb coating of copper cavities by UHV cathodic arc*, in: Proceedings of the 13th Workshop on RF Superconductivity, Peking Univeristy, Beijin, China, 2007, WE101.

[44] G. Wu, *Energetic Deposition of Niobium Thin Film in Vacuum*, Ph.D. thesis, Faculty of the Virginia Polytechnic Institute and State University (2002).

[45] G. Wu et al., *Studies of niobium thin film produced by energetic vacuum deposition*, Thin Solid Films 489 (2005) 56.

[46] L. Maissel, R. Glang, *Handbook of Thin Film Technology*, McGraw-Hill, New York, 1970.

[47] J. Thornton, A. Penfold, *Cylindrical magnetron sputtering*, J. Wossen and W.Kern, Academic Press, San Diego, 1978.

[48] J. Thornton, *Coating deposition by sputtering*, in: S. Rossnagel, J. Cuomo, W. Westwoood (Eds.), Handbook of plasma processing technology, Noyes publications, 1990, p. 196.

[49] D. Hoffman, R. McCune, *Microstructural control of plasma sputtered refractory coatings*, in: S. Rossnagel, J. Cuomo, W. Westwoood (Eds.), Handbook of plasma processing technology, Noyes publications, 1990, p. 483.

[50] B. Movchan, A. Demchishin, *Study of the structure and properties of thin vacuum condenstaes of nickel, titaniom, tungsten, aluminium oxide, and zirconium oxide*, Fiz.Metal.Metalloved 28 (1969) 653.

[51] L. Maissel, P. Schaible, *Thin Films Deposited by Bias Sputtering*, J.Appl.Phys. 36 (1965) 237.

[52] E. Kay, G. Heim, *Model of Bias Sputtering Applied to the Control of Nb Film Properties*, J.Appl.Phys. 49 (9) (1978) 4862.

[53] A. Dirks, H. Leamy, *Columnar microstructure in vapour deposited thin films*, Thin Solid Films 47 (1977) 219.

[54] A. Dirks, H. Leamy, *Microstructure and magnetism in amorphous rare-earth transition metal thin films*, I. Microstructure J. Appl. Phys. 49 (1978) 3430.

[55] J. Thornton, *Influence of apparatus geometry and deposition conditions on the structure and topography of thick sputtered coatings*, Journ. of Vacuum Sci. and Tech. 11 (1974) 666.

[56] A. C. Raghuram, R. F. Bunshah, Journ. of Vacuum Sci. and Tech. 9 (1974) 1389.

[57] G. Orlandi, C. Benvenuti, S. Calatroni, F. Scalambrin, *Expected dependence of Nb-coated RF cavity performance on the characteristics of niobium*, in: Proceedings of the 6th Workshop on RF Superconductivity, CEBAF, USA, 1993, p. 718.

[58] G. M. Schucan, C. Benvenuti, S. Calatroni, *Niobium films produced by magnetron sputtering using an Ar-He mixture as discharge gas*, note 94-23.

[59] C. Benvenuti et. al., *Rare gas trapping in sputtered Nb films*, in: Proceedings of the 7th Workshop on RF Superconductivity, Gif-sur-Yevette, France, 1995, p. 473.

[60] V. Palmieri, *Spinning of Tesla-type cavities: status of art*, in: Proceedings of the 9th Workshop on RF Superconductivity, Santa Fe, New Mexico, USA, 1999, THA001.

[61] L. Lilje, *Experimental Investigations on Superconducting Niobium Cavities at Highest Radiofrequency Fields*, Ph.D. thesis, University of Hamburg (2001).

[62] K. Saito, *Surface smoothness for high gradient niobium sc rf cavities*, in: Proceedings of the 11th Workshop on RF Superconductivity, Lübeck, Germany, 2003.

[63] S. Calatroni, C. Benvenuti, M. Hakovirta, H. Neupert, M. Prada, A.-M. Valente, *CERN studies on niobium-coated 1.5GHz copper cavities*, in: Proceedings of the 10th Workshop on RF Superconductivity, KEK, Tsukuba, Japan, 2001.

[64] T. Higuchi et al., *Centrifugal Barrel Polishing of L-band Niobium Cavities*, in: Proceedings of the 10th Workshop on RF Superconductivity, KEK, Tsukuba, Japan, 2001.

[65] T. Higuchi, K. Saito, *Hydrogen Absorption in Electropolishing of Niobium*, in: AIP Conference Proceeding, Vol. 671, 2003, pp. 203–219.

[66] D. Turley, L. Samuels, J. Iron and Steel Inst 186 (1957) 211.

[67] D. Turley, L. Samuels, Metallography 14 (1981) 275.

[68] P. Jacquet, Metal Finishing 47 (5) (1949) 48.

[69] V. Palmieri, F. Stivanello, S. Stark, C. Roncolato, M. Valentino, *Besides the standard niobium bath chemical polishing*, in: Proceedings of the 10th Workshop on RF Superconductivity, KEK, Tsukuba, Japan, 2001, PR016.

[70] N. Steinhau-Kühl, R. Bandelmann, A. Matheisen, H. Morales Zimmermann, M. Schmökel, V. Palmieri, V. Rampazzo, *Update on the JRA1 project results of electro-polishing of multi-cell superconducting resonators*, in: Proceedings of the 13th Workshop on RF Superconductivity, Peking Univeristy, Beijin, China, 2007, poster.

[71] C. Roncolato, F. Stivanello, V. Palmieri, *Recent improvements on surface treatments for superconducting cavity*, LNL Annual Report (2004) 175–176.

[72] H. Samour et al., *Anodic polarisation of Nb in various oxiacids media and ion NaOH*, Indian J. of Chem. 17A (1979) 237–241.

[73] C. Z. Antoine et al., *The role of atomic hydrogen in Q degradation of Nb superconducting cavities*, in: Proceedings of the 5th Workshop on RF Superconudctivity, Hamburgh, Germany, 1991, pp. 616–634.

[74] C. Z. Antoine et al., *RF material investigation by sample analysis*, in: V. Palmieri, A. Lombardi (Eds.), Proceedings of the 8th Workshop on RF Superconductivity, Abano, Italy, 1997, pp. 899–917.

[75] C. Benvenuti, S. Calatroni, I. Campisi, P. Darriulat, M. Peck, R. Russo, A.-M. Valente, *Study of the surface resistance of superconducting niobium films at 1.5 GHz*, Physica C 316 (1999) 153–188.

[76] J.-P. Birabeau, J. Guerin, Patent no 88 09820, Institut National de la Proprie´te´ Industrielle, 1993.

[77] *Encyclopaedia of electrochemistry of elements, Vol. II*, A.J. Bard, M. Deklev ed., New York, 1974, and references therein.

[78] *Columbium and Tantalum*, in: Wiley Series on the science and technology of materials, F.T. Sisco & E. Epremian ed., NY, 1963.

[79] C. Antoine, A. Aspart, M. Berthelot, Y. Gasser, J. Poupeau, F. Valin, *Morphological and Chemical studies of Nb Samples after Various Surface Treatment*, in: Proceedings of the 9th Workshop on RF Superconductivity, Santa Fe, New Mexico, USA, 1999, p. 295, NM LA-13782-C.

[80] A. Boucheffa et al., *Kapitza conductance of niobium for superconducting cavities in the temperature range 1.6 - 2 K*, in: Proceedings of the 7th Workshop on RF Superconductivity, Gif-sur-Yevette, France, 1995, p. 659.

[81] H. Safa et al., in: Proceedings of the 7th Workshop on RF Superconductivity, Gif-sur-Yevette, France, 1995, p. 649.

[82] P. Darriulat, C. Durand, P. Janot, N. Rensing, W. Weingarten, P. Bosland, J. Gobin, J. Martignac, *Dependence of the surface resistance of Niobium coated copper cavities on the coating temperature*, in: Proceedings of the 7th Workshop on RF Superconductivity, Gif-sur-Yevette, France, 1995, p. 467.

[83] P. Kneisel, B. Lewis, in: Proceedings of the 7th Workshop on RF Superconductivity, Gif-sur-Yevette, France, 1995, p. 311.

[84] B. Anue et al., Phy. Rev. Special Topics. Accelerators And Beams 3, 092001.

[85] D. Beegan, M. Laugier, Surface & Coatings Technology 199 (2005) 32–37.

[86] Vingsbo, S. Hogmark, B. Jonsson, A. Ingemarson, Materials Science and Engineering ASTM STP 889 (1986) 257.

[87] D. Chicot, J. Lesage, Thin Solid Films 245 (1995) 123.

[88] D. Tabor, The Hardness of Metals, Clarendon Press, Oxford,U.K., 1951.

[89] A. Korsunsky, M. McGurk, S. Bull, T. Page, Surface & Coatings Technology 99 (1998) 171–183.

[90] W. Oliver, G. Pharr, *Low-pressure magnetron sputtering*, J. Mater. Res. 19 (1).

[91] C. Rebholz, A. Leyland, A. Matthews, C. Charitidis, S. Logothetidis, D. Schneider, Thin Solid Films 514.

[92] G. Lanza, J. Bermudez, A. Frigo, H. Padamsee, V. Palmieri, D. Tonini, Physica C: Superconductivity; Proceedings of the 12th International Workshop on RF Superconductivity 4 (1-2) (2006) 102–107.

[93] T. Powers, *Theory and practice of cavity RF test systems.*, in: Proceedings of the 12th Workshop on RF Superconductivity, Cornell University, Ithaca, NY, USA, 2005, SuP02.

[94] V. Palmieri, R. Parodi, A. Porcellato, S. Ruzinov, V.and Stark, *Computer based measuring system for 160 and 1500 MHz resonators*, LNL Annual Report (1994) 216.

[95] C. Durand, V. Palmieri, A. Porcellato, S. Stark, *RF-Superconducting Cavity measurement*, LNL Annual Report (1996) 300.

[96] C. Durand, V. Palmieri, R. Preciso, S. Stark, F. Stivanello, W. Venturini, *RF Characterization of small scale cavities*, in: V. Palmieri, A. Lombardi (Eds.), Proceedings of the 8th Workshop on RF Superconductivity, Abano, Italy, 1997, LNL-INFN (Rep) 133/98 p. 941.

[97] S. Stark, *GUARD - modular software for complex system monitoring and data sharing*, LNL Annual Report.

[98] B. Visentin, *Cavity baking: a cure for the high accelerator field Q_0 drop*, in: Proceedings of the 9th Workshop on RF Superconductivity, Santa Fe, New Mexico, USA, 1999.

[99] G. Arnolds-Mayer, C. Benvenuti, D. Bloess, G. Cavallari, E. Chiaveri, M. Hauer, N. Hilleret, M. Minestrini, V. Palmieri, L. Ponto, F. Scalambrin, W. Weingarten, *On niobium coated copper cavities at 500 MHz* (1986).
URL `http://preprints.cern.ch/cgi-bin/setlink?base=preprint&categ=CM-P&id=CM-P00059313`

[100] G. Lanza, D. Tonini, G. Keppel, V. Rampazzo, M. Negrato, G. Torzo, V. Palmieri, Superconducting niobium coated copper accelerating cavities: investigation of cylindrical magnetron sputtering configurations, in: INFN-LNL Annual Report 2004, Legnaro, Padova, Italy, 2004.

[101] D. Shuman, Microscopy and Analysis Issue 95.

[102] D. Chicot, I. Hage, P. Démarcéaux, J. Lesage, Surf. Coat. Technol. 81 (1996) 269–274.

[103] G. Lanza, J. Brmudez, A. Frigo, H. Padamsee, V. Palmieri, D. Tonini, *New Magnetron Configurations for Sputtered Nb onto Cu*, in: INFN-LNL Annual Report 2005, Legnaro, Padova, Italy, 2005.

[104] D. Tonini, *orfologia di film di niobio depositati per sputtering a differenti angoli target-substrato* (2003).

[105] J. Billen, L. Young, *Poisson Superfish - Pandira*, Tech. rep., Los Alamos National Laboratory, LA-UR-96-1834 Revised November 5.

[106] G. Lanza, E. Bemporad, F. Carassiti, A. Frigo, A. Minarello, H. Padamsee, V. Palmieri, M. Sebastiani, *Bias Magnetron Sputtering For Niobium Thin Films*, in: INFN-LNL Annual Report 2006, Legnaro, Padova, Italy, 2006.

[107] A. Frigo, G. Lanza, H. Padamsee, V. Palmieri, Bias magnetron sputtering for niobium thin films, in: Proceedings of the International Workshop on: Thin Films and New Ideas for Pushing the Limits of RF superconductivity, to be published.

[108] M. Poitevin, G. Lemperiere, J. Tardy, Thin Solid Films 97 (1) (1982) 69–77.

[109] E. Kay, P. Ziemann, *Correlation between the ion bombardment during film growth of Pd films and their structural and electrical properties*, J. Vac. Sci. Technol. A 1 (2).

[110] E. Bemporad, F. Carassiti, G. Lanza, H. Padamsee, V. Palmieri, M. Sebastiani, Superconducting and microstructural studies on sputtered niobium thin films for accelerating cavities applications.

[111] A. Daccà, G. Gemme, L. Mattera, R. Parodi, Appl. Surf. Sci. 126 (1998) 219–230.

[112] G. Lanza, V. Palmieri, N. Patron, C. Pira, S. Stark, F. Carassiti, M. Sebastiani, H. Padamsee, *Different sputtering configurations for coating 1,5 GHz copper cavities*, in: Proceedings of the 13th Workshop on RF Superconudctivity, Peking University, Beijin, China, 2007.

Acknowledgments

To prof. Padamsee my warmest thanks for making this PhD possible and for giving me the great opportunity to go on with my studies on sputtering and superconducting cavities.

To all Rome3 group, and to prof.Bemporad and Marco Sebastiani in particular, for the important, valuable and useful collaboration on sample characterization.

To Sergio Calatroni for the experience at CERN and for all the fruitful discussions.

To Larry Philips and Tom Powers for their visits at Legnaro and for all their important advices.

Grazie a mamma e papà, sempre pronti a venirmi in aiuto e darmi coraggio. E grazie alla sister che ha saputo quando era ora di tenermi al telefono e che anche stavolta ha contribuito alla stesura di questa tesi.

Alla mia migliore amica Valentina, che più di ogni altra mi conosce, mi ascolta e mi capisce al volo. Prima o poi torneremo ad Istanbul a bere birra sul tetto, con i gabbiani che volano sulle cime della moschea blu.

A Niccolò, che c'eri quando questo è iniziato e che, a modo tuo, ci sei sempre stato. Per tutte le volte che abbiamo, riso, scherzato, giocato, parlato, litigato, cucinato o ci siamo persi dietro un banco di sardine.

A tutto il gruppo di capoeira: Giovanni, Marilisa, Luca, Carlotta e Grazia con cui gioco, canto e mi diverto e mi sfogo: "Vamos jogar Capoeira!"

A Dario che mi è stato vicino in uno dei momenti più difficile della mia vita, che in Australia tu possa trovare tutto l'amore e la serenità che meriti.

A Mirco che per un breve periodo era qui con me e mi hai coccolata, ridato il sorriso e la fiducia in me stessa.

Per quanto riguarda il laboratorio, Andrea Frigo viene per primo in quanto coautore di tutto il lavoro di questi tre anni. Ci siamo messi a dura prova e l'abbiamo superata!

Subito dopo Silvia D. con cui ho condiviso gioie e dolori di questi tre anni, essere in due ha alleviato le frustrazioni ed è stato bello riderci sempre su!

Un grazie particolare a Sergey che con pazienza mi ha spiegato come lavorare con la radiofrequenza, e poco a poco ha aiutato me e Silvia a fare funzionare un laboratorio. Senza di te non avremmo mai cominciato e sei un aiuto costante e prezioso.

A tutto il gruppo di superconduttività: Silvia M., Vanessa, Cristian, Giorgio, Oscar , Paolo, Fabio, Fabrizio, Antonio, Alessandro, Marigo, Gastone, Michele ed Enzo. Alle persone con cui lavoro da anni e a quelle appena arrivate, grazie ragazzi per la collaborazione costante, il divertimento, la passione e l'entusiasmo che trovo ogni mattina quando varco la porta del laboratorio!